Fraunhofer MEVIS

Universität Bremen

Dissertation
submitted to the
Faculty of Physics
University of Bremen, Germany
for the degree of
Doctor of Natural Sciences (Dr. rer. nat.)

Adaption in Dynamic Contrast-Enhanced MRI

Ina Nora Kompan

Referees:
Prof. Dr. Matthias Guenther
PD Dr. Wolfgang Dreher
Date of colloquium: 25.03.2015

It was the best of times, it was the worst of times,
it was the age of wisdom, it was the age of foolishness,
it was the epoch of belief, it was the epoch of incredulity,
it was the season of Light, it was the season of Darkness,
it was the spring of hope, it was the winter of despair, …

CHARLES DICKENS

Abstract

In breast DCE MRI, dynamic data are acquired to assess signal changes caused by contrast agent injection in order to classify lesions. Two approaches are used for data analysis. One is to fit a pharmacokinetic model, such as the Tofts model, to the data, providing physiological information. For accurate model fitting, fast sampling is needed. Another approach is to evaluate architectural features of the contrast agent distribution, for which high spatial resolution is indispensable. However, high temporal and spatial resolution are opposing aims and a compromise has to be found. A new area of research are adaptive schemes, which sample data at combined resolutions to yield both, accurate model fitting and high spatial resolution morphological information. In this work, adaptive sampling schemes were investigated with the objective to optimize fitting accuracy, whilst providing high spatial resolution images.

First, optimal sampling design was applied to the Tofts model. By that it could be determined, based on an assumed parameter distribution, that time points during the onset and the initial fast kinetics, lasting for approximately two minutes, are most relevant for fitting. During this interval, fast sampling is required. Later time points during wash-out can be exploited for high spatial resolution images.

To achieve fast sampling during the initial kinetics, data acquisition has to be accelerated. A common way to increase imaging speed is to use view-sharing methods, which omit certain k-space data and interpolate the missing data from neighboring time frames. In this work, based on phantom simulations, the influence of different view-sharing techniques during the initial kinetics on fitting accuracy was investigated. It was found that all view-sharing methods imposed characteristic systematic errors on the fitting results of K^{trans}. The best fitting performance was achieved by the scheme "modTRICKS", which is a combination of the often used schemes keyhole and TRICKS.

It is not known prior to imaging, when the contrast agent will arrive in the lesion or when the wash-out begins. Currently used adaptive sequences change resolutions a fixed time points. However, missing time points on the upslope may cause fitting errors and missing the signal peak may lead to a loss in morphological information. This problem was addressed with a new automatic resolution adaption (AURA) sequence. Acquired dynamic data were analyzed in real-time to find the onset and the beginning of the wash-out and consequently the temporal resolution was automatically adapted. Using a perfusion phantom it could be shown that AURA provides both, high fitting accuracy and reliably high spatial resolution images close to the signal peak.

As alternative approach to AURA, a sequence which allows for retrospective resolution adaption, was assesses. Advantages are that adaption does not have to be a global process, and can be tailored regionally to local sampling requirements. This can be useful for heterogeneous lesions. For that, a 3D golden angle radial sequence was used, which acquires contrast information with each line and the golden angles allow arbitrary resolutions at arbitrary time points. Using a perfusion phantom, it could be shown that retrospective resolution adaption yields high fitting accuracy and relatively high spatial resolution maps.

Contents

Introduction

Cancer has been a scourge of mankind since time immemorial. The history of this "monster hungrier than the guillotine" has been described by Siddhartha Mukherjee in his book "The Emperor of All Maladies" [Mukherjee2010]. The following historical facts and quotes are taken from his "biography of cancer".

Throughout the history of human civilization, evidence of cancer has been found. The oldest documentation of cancer was discovered on a papyrus, dating back to 2500 BC, written by the Egyptian physician Imhotep. In his medical instructions, he adviced women to examine their breasts for a "bulging mass, cool, hard and dense, which spreads over the breast". As therapy he claimed that "there is none". In 400 BC, the ancient Greek historian Hereductus gave records of Atossa, queen of Persia, who suffered from a bleeding lump in her breast. A Greek slave removed her breast, healing the disease. Even more evident proof of cancer occurring in ancient times was found during the examination of mummies from Egypt and the Atacama dessert. In the preserved bodies, malignant abdominal and bone tumors were discovered.

As long as mankind has been inflicted by cancer, it has also been fighting it. The earliest approach of treating tumors was to surgically remove them. In medieval times, painful mastectomies were practiced employing knives and acid. With the invention of anesthetics and antiseptics in the middle of the 19th century, surgical techniques became more refined. When X-rays and other types of ionizing radiation were discovered at the end of the 19th century, it was found that tumor cells can be destroyed by targeting them with radiation. A new era of cancer treatment, the radiation therapy, was born. However, after some years it became evident that high dose radiation itself causes cancer when healthy tissue is exposed. Another strategy in the war against cancer was to employ chemical substances, which selectively target cancer cells, but spare the patients. In 1947, the American pediatrist Sidney Farber was the first to treat children suffering from leukemia with chemotherapy. He succeeded in achieving a temporal remission of tumor cells. Since these first attempts, many chemicals were identified which have destructive effects on cancer cells. Additionally, hormones were found to act on certain tumor cells with hormonal receptors, such as breast, cervical and prostate tumors. Currently, a relative new form of therapy using anti-angiogenic drugs is in development, targeting tumor perfusion and restricting blood supply [Jackson2005]. These therapies are currently undergoing clinical trials.

Today, cancer is one of the leading causes of death. In the year 2010, in Germany 477,300 people were diagnosed with cancer. In women, breast cancer is the cancer with the highest mortality, in men it is lung cancer [DKFZ2014]. Worldwide, 8,2 million cancer deaths and 32,6 million people living with cancer were recorded in 2012 [IARC2014]. However, whilst before 1980 more than two thirds of all cancer patients died, today half

of the patients are still alive five years after thier cancer diagnosis and have high chances of permanent cure [DKFZ2014].

One reason for the decreasing mortality is due to the therapies described above, which have been optimized for different types of tumors, often applied in combinations with each other. However, to a large extent, the decline of mortality rates is based on the early detection of tumors at a stage where therapies are still effective. Another reason is the assessment of response to therapy, which allows an early change of the applied therapy if no response is detected. The latter two would not be feasible without advanced imaging technologies such as ultrasound, computer tomography (CT), positron emission tomography (PET) and magnetic resonance imaging (MRI). The focus of this thesis is cancer diagnosis and monitoring of response to therapy using MRI.

To generate MR images, a strong magnetic field is used to manipulate the magnetic properties of hydrogen nuclei within the body. Advantages of MRI above other imaging modalities are a high and flexible soft tissue contrast, no usage of ionizing radiation or radioactive tracers and the ability to provide functional information.

For beast cancer diagnosis, dynamic contrast-enhanced (DCE) MRI has become a standard method for lesion detection and classification. In DCE MRI, a contrast agent is administered and a series of MR images is acquired. Tissue in which contrast agent is present shows signal enhancement. In general, tumors exhibit different enhancement characteristics than healthy tissue. The amount of contrast agent accumulated in tumors is higher, areas accessible to contrast agent are larger and dynamic processes occur faster.

Two different analysis methods of DCE MRI data are currently used, one investigating the dynamic enhancement characteristics, the other depicting morphological information of the contrast agent distribution. In the dynamic approach, the signal time curves of suspicious regions of interest are extracted and pharmacokinetic models, for example the Tofts model [Tofts1991] are fitted to the data. The resulting functional parameters which reflect the underlying vasculature, such as the interstitial space v_e, the contrast agent (CA) onset time τ and the vascular permeability K^{trans}, are used for distinction between benign and malignant lesions. For accurate model fitting, imaging at a high temporal resolution is of importance [Henderson1998]. On the other hand, architectural features of contrast agent distribution are important for lesion characterization as well [Kuhl2005]. For example heterogeneous enhancement patterns and irregular margins are indicators for malignant tumors. The morphological evaluation requires a high spatial resolution.

An inherent problem of MRI is, that high spatial resolution images require long acquisition times. Therefore, high temporal and spatial resolution are interfering goals, especially for images with a large coverage including both breasts and the axillary lymph nodes. Since contrast agent is normally administered only once, a trade-off between kinetic and morphological information has to be found.

Most studies acquire images at a constant temporal resolution. However, different phases of the dynamic signal time curves $S(t)$ are governed by different physiological processes. A typical measured dynamic signal time curve consists of a baseline before contrast agent onset, a fast upslope until a peak is reached, followed by a slower wash-out

phase. Some time points have more relevance than others for the extraction of a certain parameter from $S(t)$. Therefore, it is not clear if equidistant sampling is the optimal approach.

There are some publications indicating that combining high and low temporal resolution acquisitions within the same DCE MRI investigation can be of advantage for diagnostic accuracy [Vomweg2004], [Veltman2008], [Pinker2009], [Jansen2010], [Mann2011]. These adaptive sequences are suitable for DCE MRI because they yield the combined diagnostic information of both, fast and slow sampling, being accurate dynamic information and high spatial resolution morphological images. All of them have in common that data are acquired at high temporal resolution during the fast initial kinetics (IK) of the contrast agent. At later time points during the wash-out (WO) the sampling scheme changes to higher spatial resolution images to allow for morphological evaluation when there is still a high concentration of CA present in the lesion.

However, adaptive sequences are a relatively new area of research and many aspects are still insufficiently investigated. In this thesis, problems and unanswered questions regarding adaptive sequences are approached from various angles.

First, it is theoretically derived where fast sampling is needed for accurate model fitting and where high spatial resolution is sufficient and can be exploited for morphological analysis.

To achieve high temporal resolution during the required intervals, the amount of acquired data has to be reduced. This can be done in many different ways, all potentially having undesired effects on the image quality. Based on simulations, different acceleration strategies are compared with respect to their influence on fitting accuracy.

Since contrast agent is injected only once and kinetic curves can vary largely, it is not known prior to imaging when contrast agent arrives within the region of interest and when the signal peak is reached. To overcome this problem, two different approaches are implemented. One approach is to analyze acquired data during dynamic imaging to detect the mean onset and peak time and to adapt sampling requirements in real-time.

The other approach is to employ an acquisition method which allows for retrospective reconstruction at arbitrary time points and resolutions. This way, resolution adaption can be regionally optimized throughout heterogeneous regions. In the following, a brief outline of the chapters in this thesis is given:

Thesis Outline

Chapter 1: A brief review of vascular physiology is given, including the vascular system, angiogenesis, the physiology of tumors and the passage of injected contrast agent.

Chapter 2: The basic principles of magnetic resonance imaging are explained, including image generation, the k-space formalism and image reconstruction techniques.

Chapter 3: The method of DCE MRI is introduced. Data acquisition techniques

and analysis methods such as pharmacokinetic modeling are described. Furthermore, studies concerning the trade-off between spatial and temporal resolution in DCE MRI are summarized in a review.

Chapter 4: Optimal sampling design is applied to the Tofts model, which is often used for quantitative analysis of DCE MRI data. By that, it is investigated at which time intervals high frequency sampling is required for accurate model fitting. For a distribution of realistic parameter values, it is shown that high frequency sampling is required during the first two minutes after contrast agent onset. Later time points can be exploited for high spatial resolution imaging, yielding morphological information.

Chapter 5: The cost of fast imaging during the time intervals, at which high temporal resolution is required, is image degradation. In this chapter, a dynamic numerical phantom is generated and different accelerating imaging strategies are simulated during the first two minutes after the onset time. Their effects on model fitting accuracy are studied and compared.

Chapter 6: A perfusion phantom is introduced which is used for data acquisition in chapter 8 and chapter 9. The experimental setup, the quantitative analysis and the reproducibility of the phantom is described.

Chapter 7: The prototype of an automatic resolution adaption (AURA) sequence for DCE MRI is presented. Acquired data are evaluated in real-time for onset time and peak detection of contrast agent and temporal resolution is adapted automatically by changing the spatial resolution. The AURA sequence is validated using the perfusion phantom and compared to a fast and a slow sequence with temporally equidistant sampling intervals.

Chapter 8: Phantom data are acquired using a 3D golden angle (GA) radial sequence. This allows for retrospective reconstruction of images at arbitrary time points and resolutions. By that, the maximal feasible spatial resolution throughout the signal time curves can be achieved whilst preserving fitting accuracy. The adaption process is optimized for different areas of similar onset and peak times within a region of interest.

Chapter 9: The main findings of this research are summarized, critically discussed, and concluded. Potential applications and further research are discussed.

1 Basics of Vascular Physiology

1.1 The Vascular System

Perfusion describes the act of a fluid such as blood flowing through an organ or tissue to supply it with oxygen and nutrients and to remove metabolic products such as carbon dioxide. The complex structure of the human vascular system enables the perfusion of organs in an efficient way. In figure 1.1 a), the human vascular system is schematically described. The blood flows in a closed circuit, with the heart functioning as engine.

The vascular system consists of an arterial component which is built up like a tree and a venous component, which has the shape of an inverse tree, going from small to large structures. From the heart, blood is pumped into the aorta which branches into large arteries (diameter of approximate 1-4 mm) serving as delivery system to the different regions of the body. Having arrived in the organ of interest, the arteries divide into smaller arterioles (diameter of approximately 0.05 mm) and then branch into many small capillaries (diameter of approximately 5-30 μm). Here, in the capillary bed, the

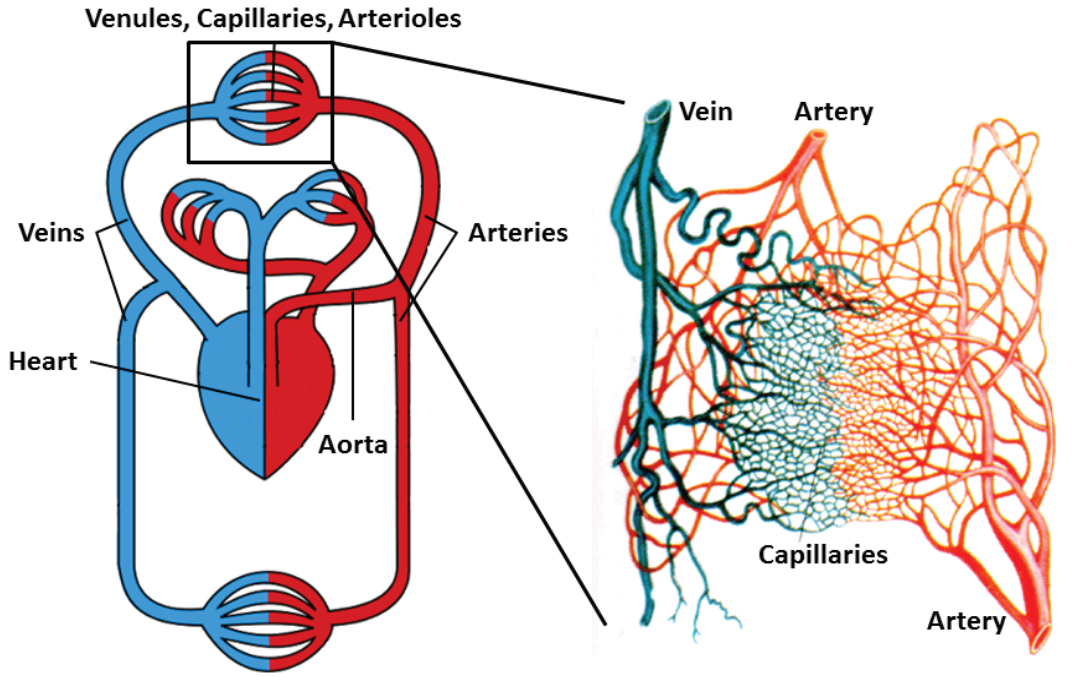

Figure 1.1: Schematic description of a) human vascular circuit [biologie.oncampus2013] and b) capillary bed [Brockhaus1989].

exchange of the nutrients and metabolic products between the vascular system and the tissue cells takes place. For that purpose, the capillaries have permeable vessel walls. All vessel diameters are taken from [Nichols1990]. In the capillary bed, the end of the arterial and the venous tree join. From the capillaries, blood is transported via larger venules and large veins back to the heart. A more detailed schematic image of the capillary bed in between delivering arteries and veins can be seen in figure 1.1 b).

1.2 Angiogenesis and Vessel Structure

Angiogenesis, the formation of new vessels, is required during the vascular development of an embryo and in the case of wound healing. Angiogenesis is a very complex multistep phenomenon. To trigger the angiogenic process, cells release pro-angiogenic growth factors (cytokines), such as vascular endothelial growth factor (VEGF) and fibroblast growth factor (FGF). They stimulate the existing vasculature to form new vessels as it is schematically shown in figure 1.2.

Normal vasculature is built up in a hierarchical order. A histological image of healthy vasculature is shown in figure 1.3 a) in comparison to tumorous vaculature in b), which will be described in section 1.3. Capillaries have a membrane which is smooth and shows highly controlled transport.

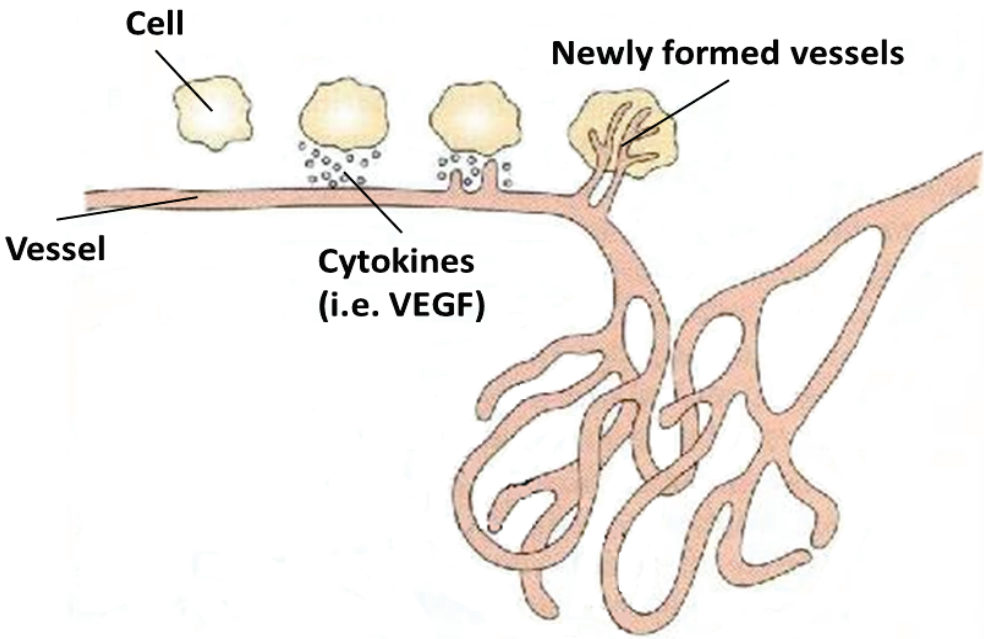

Figure 1.2: Schematic description of the process of angiogenesis. (adapted from [Jackson2005])

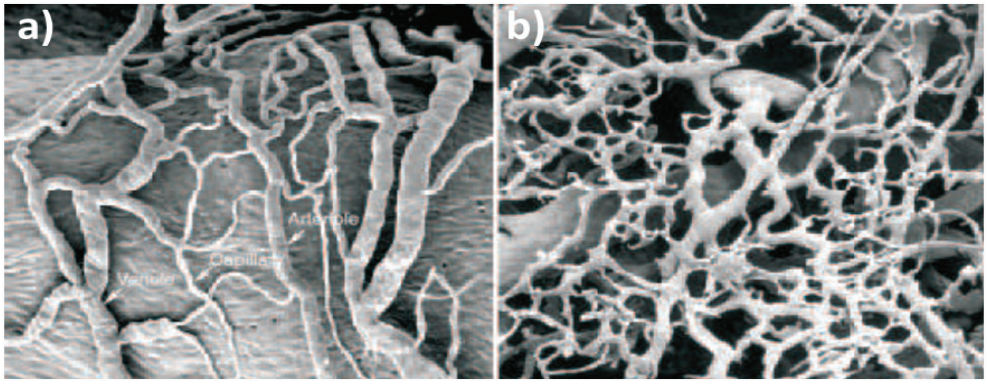

Figure 1.3: Microscopic images of a) normal and b) tumor vasculature. Tumor vasculature is less organized than normal vasculature. [Walker-Samuel2007]

1.3 Tumor Physiology

The earliest detectable tumors, called cancer in situ, are in the order of 1 mm in size. These tumors are avascular, they can maintain themselves without vascular supply. To grow and form metastasis, a tumor requires nourishment, which can only be delivered via blood vessels. Therefore, tumor growth is associated with angiogenesis.

Tumor cells release cytokines to stimulate the existing vasculature to form new blood vessels, which grow towards the tumor. The morphology of tumor neovasculature is different to that of normal vasculature. Its structures are highly chaotic, heterogeneous, irregularly distorted and entangled, without hierarchical branching. A histological image of tumor vasculature is shown in figure 1.3 b). But not only the shape of vasculature differs from that of normal tissue. Tumor capillary membranes are extremely coarse and fragile, which makes them very leaky and increases their permeability to plasma proteins and macromolecules. In addition, vasculature throughout a tumor is normally highly heterogeneous with areas of low vascular density, mixed with regions of high angiogenic activity known as 'hot spots'. As a general rule it applies that the more aggressive a tumor is, the more bizarre its neovasculature.

1.4 The Passage of Contrast Agent

In imaging methods such as magnetic resonance imaging, contrast agent (CA) is administered intravenously. Once CA is injected, it travels through the vasculature as described above for blood until it reaches the capillary bed. Inside the vasculature, it is confined to the blood plasma and cannot cross blood cell membranes. Having arrived in the capillary bed, its small molecular size permits leakage through the capillary wall into the extracellular regions of the tissue. Due to their size, CA molecules cannot cross tissue cell membranes, therefore intracellular areas are not accessible to them. When the CA concentration in the capillaries decreases due to leakage into the tissue and renal

excretion, the contrast agent diffuses back from the tissue to the capillaries. This process continues until all contrast agent is renally excreted.

Due to the altered capillary structure in tumors and their increased permeability, CA behavior in tumors differs from that in normal tissue. In tumorous tissue the exchange between the capillary bed and the tissue generally takes place more rapidly than in healthy tissue and the volume of the accessible tissue volume increases. Due to the heterogeneous tumor vasculature, CA distribution within the tissue is consequently as well more heterogeneous than in healthy tissue.

2 Basics of Magnetic Resonance Imaging

Magnetic resonance imaging (MRI) is a cross-sectional imaging method based on the phenomenon of nuclear magnetic resonance (NMR). It is an emission tomography method, measuring a signal coming directly from within the body. The employed electromagnetic waves have energies of about 10^{-6} to 10^{-8} eV, which is a non-ionizing radiation.

An important advantage of MRI is the large amount of information that can be obtained in the images. Contrast depends on many different intrinsic parameters of the measured tissue. By adjusting measurement parameters the effects of these intrinsic parameters will be enhanced or suppressed. This makes MRI a very flexible technique, allowing tailored contrast to answer the clinical question of interest. In general, MRI is a non-invasive technique. Only in some applications contrast agent is used.

In this chapter the basic principles of magnetic resonance imaging will be introduced, based on literature from [Haacke1999], [Liang2000], [Bernstein2004] and [Guenther1999].

2.1 Nuclear Magnetic Moments and Macroscopic Magnetization

When placed in an external magnetic field $\vec{B}_0$, the intrinsic magnetic moments $\vec{\mu}$ of the hydrogen proton spins interact with the external field and align with $\vec{B}_0$. In the following the term *spin system* shall refer to a large number of protons as found in an object. Due to the laws of quantum mechanics, the z-component of $\vec{\mu}$ can take only two discrete orientation, such that $\vec{\mu}$ forms the angles $\theta = \pm 54.44°$ with $\vec{B}_0$. These two states are called *spin up* and *spin down*. Since $\vec{\mu}$ is not aligned with $\vec{B}_0$, it experiences a torque and performs a nuclear precession with the *Larmor frequency* ω_0:

$$\omega_0 = \gamma \cdot B_0, \tag{2.1}$$

where γ is the gyromagnetic ratio of ^1H with the value $\gamma = 2\pi \cdot 42.58\ \mathrm{MHzT}^{-1}$. The state spin up has a lower energy level than the state spin down. According to the Boltzmann distribution, more spins populate the state spin up. Therefore, the z-components of the microscopic magnetic moments of all N_s spins within a system sum to a macroscopic magnetization $\vec{M}$. The magnitude of $\vec{M}$ is given by:

$$M = \frac{\gamma^2 \hbar^2 B_0 N_s}{4 k_B T}, \tag{2.2}$$

where $\hbar = 6.6 \cdot 10^{-34}/2\pi$ Js is Planck's constant, $k_B = 1.38 \cdot 10^{-23}\ \mathrm{JK}^{-1}$ is the Boltzmann constant and T is the temperature of the object. The stronger the external field B_0,

the lower the temperature T and the higher the number of spins in the object, hence the larger the resulting macroscopic magnetization. For a detailed description it shall be referred to [Haacke1999].

2.2 RF Excitation

An radiofrequency (RF) pulse $\vec{B}_1$ is an in the radiofrequency oscillating magnetic field perpendicular to $\vec{B}_0$, which is applied for a brief time period in the order of milliseconds. For the remainder of this thesis it is assumed that $\vec{B}_0$ is aligned along the z-axis. The RF pulse is said to be in resonance with the spin system, when its oscillation frequency ω_{RF} is equal to the Larmor frequency ω_0:

$$\omega_{RF} = \omega_0 = \gamma \cdot B_0. \tag{2.3}$$

When the condition $\omega_{RF} = \omega_0$ is met, the system is excited, having the following effects on $\vec{M}$. Due to the presence of $\vec{B}_1$, the magnetization is not aligned with the external magnetic field anymore. It experiences a torque and precesses around the field. This can be expressed in the following equation of motion:

$$\frac{d\vec{M}(t)}{dt} = \gamma\vec{M}(t) \times \vec{B}_{res}(t), \tag{2.4}$$

where $\vec{B}_{res}(t) = \vec{B}_0 + \vec{B}_1(t)$. For simplification the coordinates are transformed into the rotating frame of reference (x', y', z'), where the axis $z' = z$ and x' and y' rotate with ω_{RF} around the z-axis. In the rotating frame of reference, equation 2.4 becomes:

$$\frac{d\vec{M}(t)}{dt} = \frac{d\vec{M}'(t)}{dt} + (\vec{\omega}_{RF} \times \vec{M}'(t)), \tag{2.5}$$

where $\vec{M}'(t)$ is the magnetization vector as observed in the rotating frame. Combining equations 2.4 and 2.5, $\frac{d\vec{M}'(t)}{dt}$ can be rewritten as:

$$\frac{d\vec{M}'(t)}{dt} = \gamma\vec{M}'(t) \times \vec{B}_{eff}(t), \tag{2.6}$$

with

$$\vec{B}_{eff}(t) = \vec{B}_{res}(t) + \frac{\vec{\omega}_{RF}}{\gamma}. \tag{2.7}$$

The effective magnetic field $\vec{B}_{eff}(t)$ is the field $\vec{M}'$ 'sees'. When the resonance condition $\omega_{RF} = \omega_0$ is met, the longitudinal field apparently vanishes and $\vec{B}_{eff}$ seems stationary in the x'-y'-plane.

For example for an RF pulse along x', the magnetization precesses around the x'-axis, describing a tipping down motion. The flip angle α is defined as the angle of $\vec{M}'$ with the z'-axis. When the RF pulse is turned off, $\vec{M}'$ is not aligned with $\vec{B}_0$ anymore and

precesses around the z'-axis with the Larmor frequency given in equation 2.1. The z'-component of $\vec{M}'$ is called longitudinal magnetization M'_z, the component aligned with the x'-y'-plane is called transverse magnetization M'_{xy}. M'_{xy} combines the x'- and y'-components of $\vec{M}'$ in such that $M'_{xy} = M'_x + iM'_y$. From now on, the magnetization will always be assumed in the rotating frame of reference and the $'$-notation will be dropped for simplicity.

According to Faraday's law of electromagnetism a change of magnetic flux within a closed current loop generates electric voltage. A coil placed perpendicular to $\vec{B}_0$ can therefore detect a voltage from an RF excited object due to the precession of the magnetization. This measured signal is proportional to the transverse magnetization, which again is proportional to the local spin density.

2.3 T_1-, T_2-, T_2^*-Relaxation and the Bloch Equation

When the RF pulse is switched off, the system will, according to the laws of thermodynamics, return to a state of equilibrium. This means that M_z returns to the alignment parallel to $\vec{B}_0$. This recovery process is called *longitudinal relaxation* or T_1*-relaxation*. Another phenomenon that can be observed is the T_2*-relaxation*. Ideally, the moment the RF pulse is switched off, all the local magnetization vectors are coherent in phase, precessing at the Larmor frequency. However, in reality, due to dipole-dipole interactions within the spin system, this coherence is lost with time. This dephasing results in a decay of the transversal component of the magnetization $M_{xy}(t)$ and thus in a signal loss. This process is also known as *transversal relaxation* or *spin-spin relaxation*. Additionally, in reality the main magnetic field $\vec{B}_0$ is not a perfectly homogeneous field due to technical imperfections and due to susceptibility effects when the object placed in the field. These field inhomogeneities lead to additional dephasing. The T_2^**-relaxation* describes the combined effects of dephasing due to spin-spin interactions as well as B_0 inhomogeneities and susceptibility effects.

When the relaxation processes are taken into account for the description of the trajectory of $\vec{M}$, equation 2.4 has to be extended by relaxation terms:

$$\frac{d\vec{M}(t)}{dt} = \gamma\vec{M}(t) \times \vec{B}_{res}(t) - \frac{1}{T_1}(M_z^0 - M_z(t))\vec{z} - \frac{1}{T_2}M_{xy}(t), \tag{2.8}$$

where M_z^0 is the equilibrium value of the magnetization in z-direction. This relation was empirically found by Felix Bloch and is known as the *Bloch equation* [Bloch1946]. The solutions for M_z and M_{xy} are given by:

$$M_z(t) = M_z(0)e^{-\frac{t}{T_1}} + M_z^0(1 - e^{-\frac{t}{T_1}}) \tag{2.9}$$

$$M_{xy}(t) = M_{xy}(0)e^{-\frac{t}{T_2}}. \tag{2.10}$$

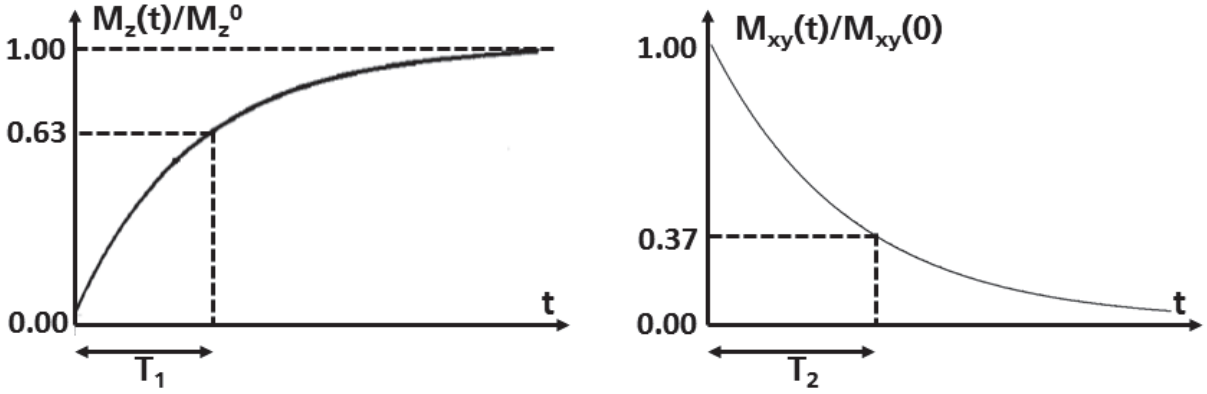

Figure 2.1: Relaxation curves: a) T_1-relaxation: The longitudinal component of the magnetization $M_z(t)$ exponentially regrows towards its equilibrium value M_z^0. b) T_2-relaxation: The transverse component of the magnetization $M_{xy}(t)$ exponentially decays.

The T_1-relaxation time T_1 is defined as the time after which the longitudinal magnetization, excited by a flip angle of 90°, has recovered 63% $(1 - \frac{1}{e})$ of the equilibrium value M_z^0. The T_2-relaxation time T_2 is the time after which the transverse magnetization has decayed to 37% of the initial transverse magnetization value $M_{xy}(0)$. The exponential relaxation curves are shown in figure 2.1.

The values of T_1 and T_2 depend on tissue composition and surroundings. In biological tissue typical T_1-relaxation times are 300 ms-1500 ms and T_2 is on the order of 30 ms-150 ms.

2.4 Concepts of Imaging

So far, the measured signal is the sum of signals from all spins within the object. Spatial localization of the signal is done by using gradient fields, which introduce a spatial dependency of the Larmor frequency. Two methods are normally used called *slice selection* and *frequency encoding*. A mathematical formalism known as k-space is employed for image reconstruction. Here, these concepts are introduced. For a more detailed description it shall be referred to [Haacke1999] or [Bernstein2004].

2.4.1 Gradient Fields

A gradient field $\vec{G}$ is an inhomogeneous field whose z-component varies linearly along a specific direction. $\vec{G}$ has the general shape

$$\vec{G} = (G_x, G_y, G_z) = (\frac{\partial B_z}{\partial x}, \frac{\partial B_z}{\partial y}, \frac{\partial B_z}{\partial z}). \tag{2.11}$$

Gradient amplitudes are measured in mT/m and are typically in the order of $30mT/m$. The magnetic field $\vec{B_G}$ at location $\vec{r}$ can be expressed as

$$\vec{B}_G(\vec{r},t) = \vec{G}(\vec{r},t) \cdot \vec{r} = G_x(x,t) \cdot x + G_y(y,t) \cdot y + G_z(z,t) \cdot z. \tag{2.12}$$

Gradient fields are applied in addition to the main magnetic field. The resulting field $\vec{B}$ is

$$\vec{B} = (\vec{B}_0 + \vec{G}(\vec{r},t) \cdot \vec{r}). \tag{2.13}$$

This leads to position dependent Larmor frequencies $\vec{\omega}(\vec{r},t)$ and accumulated phases $\phi(\vec{r},t)$:

$$\omega(\vec{r},t) = \gamma\vec{B}(\vec{r},t) = \gamma(\vec{B_0} + \vec{G}(\vec{r},t) \cdot \vec{r}), \tag{2.14}$$

$$\phi(\vec{r},t) = \gamma \int_0^\tau (\vec{B_0} + \vec{G}(\vec{r},t) \cdot \vec{r})dt. \tag{2.15}$$

2.4.2 Slice Selection

The excitation of spins within a specific slice can be achieved with a method called *slice selection (ss)*. For that, a gradient field called *slice selection gradient* and an RF pulse are applied simultaneously. The ss gradient is applied along a direction perpendicular to the slice of interest. Here, this direction is assumed to be the z-axis. The ss gradient makes the precession frequency of the spins vary linearly along the z-axis. Due to the resonance condition, the applied RF pulse excites only the spins at frequencies $\omega_{RF} \pm \frac{\Delta\omega_{RF}}{2}$, where $\Delta\omega_{RF}$ is the bandwidth of the RF-pulse. Due to the linear variation of the slice selection gradient the excited spins are contained within a slice.

The slice thickness Δz can be either changed by varying the strength of the gradient or altering the bandwidth of the RF pulse:

$$\Delta z = \frac{\Delta\omega_{RF}}{\gamma \cdot G_z}. \tag{2.16}$$

The slice selection gradients introduce a linear phase shift across the slice thickness. It can be removed by applying a *refocusing gradient*, a gradient of opposite polarity to that of the slice selection gradient and half of its area.

2.4.3 Frequency Encoding

Slice selection confines the measured signal to one specific slice. Within that slice, spatial localization is performed employing two gradient fields $\vec{G}_x$ and $\vec{G}_y$ along the x-axis and y-axis, both played after the slice excitation.

$\vec{G}_y$ is turned on for a brief time period T_y, leading to position-dependent Larmor frequencies along the y-axis during the time interval $0 < t < T_y$. After T_y, $\vec{G}_y$ is switched off and the magnetization vectors at different y-locations have accumulated a linear position-dependent phase:

$$\phi(y) = \gamma \int_0^{T_y} G_y(t)ydt. \tag{2.17}$$

When $\vec{G}_y$ is turned off, all magnetization vectors precess at the same Larmor frequencies, but the accumulated phase remains locked in. After the time T_y, $\vec{G}_x$ is applied for a longer time T_x, imposing a linear frequency dependency along the x-axis. During the time interval $0 < t < T_x$, data are read out by an analog-to-digital converter (ADC) at N_x acquisition times t_{acq}, each lasting for the dwell time $t_{dwell} = T_x/N_x$. The accumulated phase due to $\vec{G}_x$ at the time t_{acq} is given by:

$$\phi(x) = \gamma \int_0^{t_{acq}} G_x(t) x dt. \tag{2.18}$$

The transverse magnetization resulting from the combined effects of both gradients at the acquisition time t_{acq} is given by:

$$M_{xy}(\vec{r}, t_{acq}) = M_{xy}(\vec{r}, 0) \cdot e^{(i\gamma \int_0^{t_y} G_y(t) y dt)} \cdot e^{(i\gamma \int_0^{t_{acq}} G_x(t) x dt)}. \tag{2.19}$$

The measured signal S is proportional to the integral of the transverse magnetization over the excited slice:

$$S(t_{acq}, G_y) = \int_{slice} |M_{xy}(\vec{r}, 0)| \cdot e^{(i\gamma \int_0^{t_y} G_y(t) y dt)} \cdot e^{(i\gamma \int_0^{t_{acq}} G_x(t) x dt)} dx dy. \tag{2.20}$$

This process is repeated for multiple varying gradient strengths $\vec{G}_y$. The encoding along the x-axis during readout is normally called *frequency encoding* and $\vec{G}_x$ is often referred to as *readout gradient*. The step-by-step encoding along the y-axis is called *phase encoding*. To obtain an image from the acquired signal, the spatially encoded data have to be decoded. Decoding is done with the help of the mathematical concept of k-space, which will be discussed in section 2.6.

2.5 2D and 3D Imaging

The combination of slice selection and spatial encoding gradients in two dimensions is said to be 2D imaging. A 3D volume can be acquired slice by slice. However, it is also possible to either excite a large volume, called *slab*, instead of a thin slice or omit slice selection completely and instead to apply a third spatial encoding gradient G_z along the z-axis. Equation 2.20 then can be extended to:

$$\begin{aligned} &S(t_{acq}, G_y, G_z) = \\ &\int_{slab} |M_{xy}(\vec{r}, 0)| \cdot e^{(i\gamma \int_0^{t_{acq}} G_x(t) x dt)} \cdot e^{(i\gamma \int_0^{t_y} G_y(t) y dt)} \cdot e^{(i\gamma \int_0^{t_z} G_z(t) z dt)} dx dy dz. \end{aligned} \tag{2.21}$$

With this true 3D imaging method the whole volume to image is excitated with every acquisition.

2.6 *k*-space Formalism

2.6.1 Basic Principle

The *k*-space formalism is a mathematical concept which makes storing and decoding of acquired data easier.

The coordinates of k_x, k_y and k_z of the three-dimensional *k*-space are defined as:

$$k_x = \frac{\gamma}{2\pi} \int_0^\tau G_x(t)dt \tag{2.22}$$

$$k_y = \frac{\gamma}{2\pi} \int_0^\tau G_y(t)dt \tag{2.23}$$

$$k_z = \frac{\gamma}{2\pi} \int_0^\tau G_z(t)dt. \tag{2.24}$$

(k_x, k_y, k_z) is said to be the *sampling trajectory of k-space*. Substituting for k_x, k_y and k_z in equation 2.21 yields:

$$S(k_x, k_y, k_z) = \int_{slab} |M_{xy}(\vec{r}, 0)| \cdot e^{i2\pi k_x x} \cdot e^{i2\pi k_y y} \cdot e^{i2\pi k_z z} dxdydz. \tag{2.25}$$

This notation makes it possible to save and sort the acquired data in the *k*-space-matrix $S(k_x, k_y, k_z)$.

Equation 2.25 has the form of a three-dimensional Fourier transformation (FT). The transverse magnetization $M_{xy}(x, y, z)$ can be calculated by applying the inverse Fourier transformation to the *k*-space data. If relaxation effects are not taken into account $M_{xy}(x, y, z)$ is proportional to the local proton spin density $\rho(x, y, z)$. More general, the application of the inverse Fourier transform to $S(k_x, k_y, k_z)$ yields the image $I(x, y, z)$:

$$I(x, y, z) = \int_{slab} S(k_x, k_y, k_z) \cdot e^{-i2\pi k_x x} \cdot e^{-i2\pi k_y y} \cdot e^{-i2\pi k_z z} dk_x dk_y dk_z. \tag{2.26}$$

For two-dimensional imaging using slice selection only a two-dimensional *k*-space with coordinates (k_x,k_y) is defined. All the *k*-space properties discussed for 3D imaging are also valid for 2D imaging.

Figure 2.2 illustrates the meaning of *k*-space. In figure 2.2 a) an example of acquired 2D *k*-space data and the resulting image after two-dimensional FT are shown. In figure 2.2 b) an image reconstructed only from the low *k*-space values, near the center, is displayed. It can be seen that the center of *k*-space represents the low frequencies and characterizes the contrast in the image. Figure 2.2 c) shows an image which is reconstructed from only the outer *k*-space data. These high frequency data determine fine structures such as sharp edges.

The amplitudes, shapes and durations of G_x, G_y and G_z determine how *k*-space is traversed. The location in *k*-space is given by the 0th gradient moment, which is the area under the gradient-time curve. Aside from sampling data points on a Cartesian grid, which is used as standard, non-Cartesian trajectories, such as 2D or 3D radial or

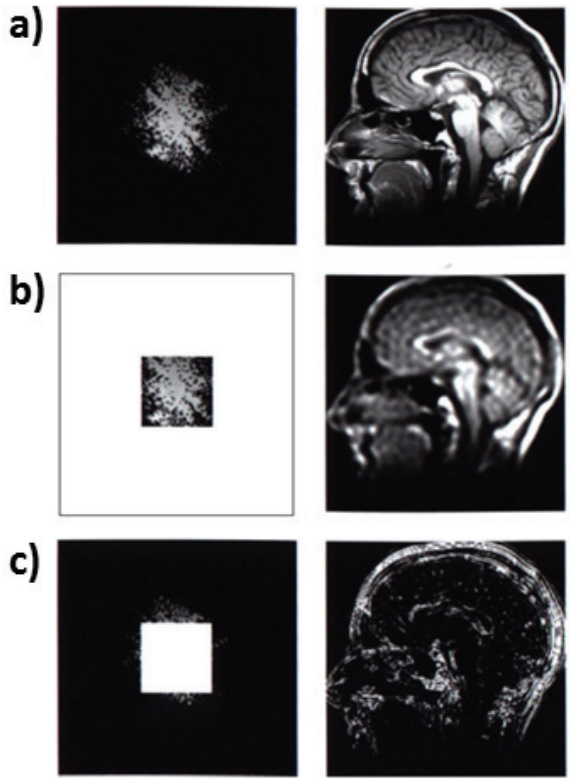

Figure 2.2: a) On the left hand side a 2D k-space dataset is shown. On the right hand side the 2D FT of the k-space data yields the image of sagittal slice through the head. b) Only the center parts of k-space data from a) are used. The resulting image shows the contrast and the coarse structures of image a). c) Only the outer parts of k-space data from a) are used. The resulting image shows the fine structures of image a) [Siemens2003].

spiral trajectories are possible. Figure 2.3 shows examples of a 2D Cartesian (a), radial (b) and a spiral trajectory (c). The advantage of Cartesian sampling is, that for reconstruction the Fourier transform can be performed using the fast Fourier transform (FFT) algorithm, which is highly efficient in computation [Cooley1965]. Non-Cartesian sampling points require a more sophisticated reconstruction. Usually, a *gridding* algorithm is employed, which interpolates the non-Cartesian points onto a Cartesian grid. The gridding process will be discussed in detail in section 2.9.2.

The sampling pattern of k-space also determines the image field of view and the resolution. These issues will be addressed in more detailed in the following sections.

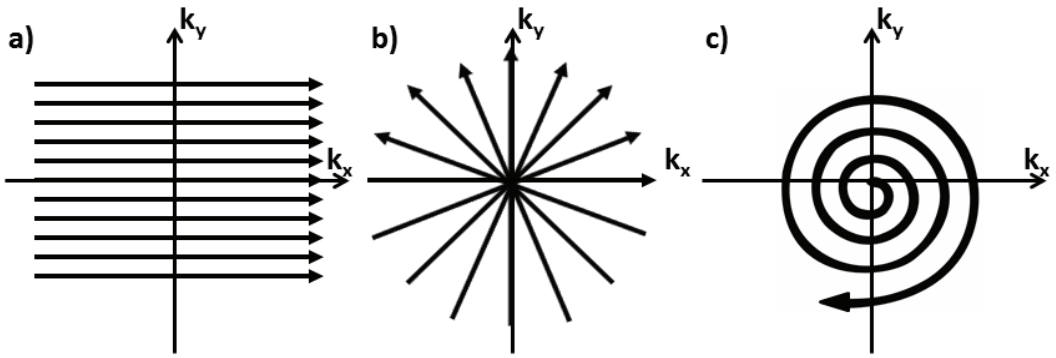

Figure 2.3: 2D k-space can be traversed in different ways. Examples: a) Cartesian trajectory, b) radial trajectory, c) spiral trajectory.

2.6.2 Field of View (FOV) and Nyquist Criterion

It shall be assumed that the k-space data $S(k_x)$ is of infinite extent and continuously sampled. The FT of $S(k_x)$ shall be the image $I(x)$. For simplicity, only one dimension along the x-direction is considered here. However, the extension to higher dimensions is straightforward.

In reality, data can be sampled only at discrete time intervals Δt which correspond to discrete k-space sampling intervals $\Delta k = \frac{\gamma}{2\pi} G_x \Delta t$. Mathematically, measuring discrete values $S_d(k_x)$ in k-space is equivalent to a multiplication of the continuous data $S(k_x)$ with a Shah function $\text{Ш}(\frac{k_x}{\Delta k_x})$ with delta peaks equispaced at distance Δk_x:

$$S_d(k_x) = S(k_x) \cdot \text{Ш}(\frac{k_x}{\Delta k_x}). \tag{2.27}$$

According to the convolution theorem this corresponds to a convolution $*$ with the FT of $\text{Ш}(\frac{k_x}{\Delta k_x})$ in the image domain. Since the FT of $\text{Ш}(\frac{k_x}{\Delta k_x})$ is again a Shah function $\text{Ш}(k_x \Delta k_x)$ with peak to peak distance $\frac{1}{\Delta k_x}$, the effect on the resulting image $I_d(x)$ is:

$$I_d(x) = I(x) * \text{Ш}(k_x \Delta k_x). \tag{2.28}$$

Therefore, the consequence of discrete sampling is that the image becomes a series of copies of the image at distance $\frac{1}{\Delta k_x}$. The effects of discrete sampling are summarized in figure 2.4. For imaging only one replica is used, the other copies are discarded. The imaging field of view in x-direction (FOV_x) is defined as the spacing between the replicas:

$$FOV_x = \frac{1}{\Delta k_x}. \tag{2.29}$$

If the object to be imaged is larger than the FOV, the replicas overlap and can cause image artifacts. This is known as *aliasing*. The *Nyquist Criterion* states that aliasing

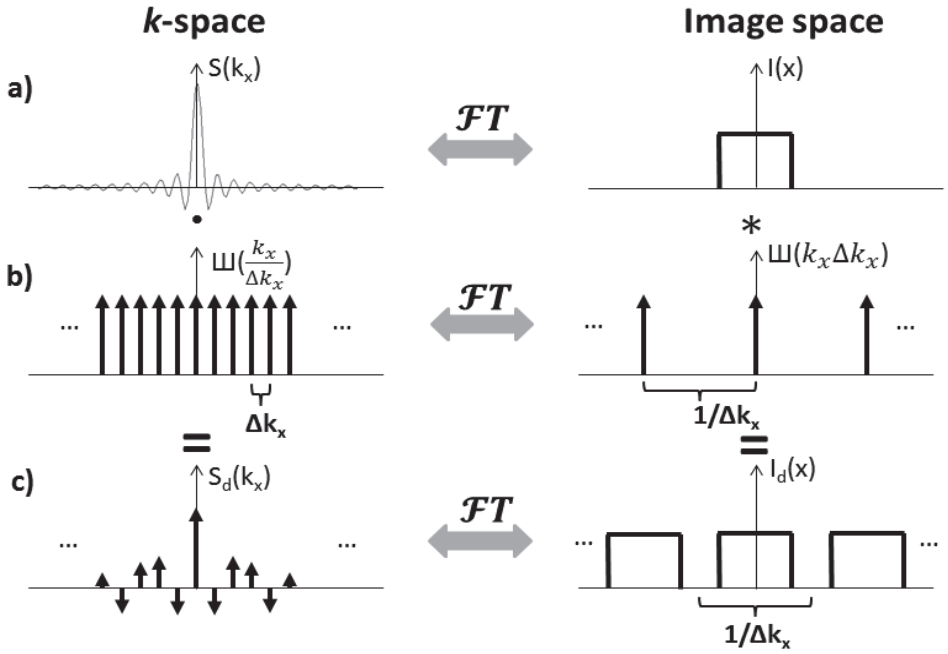

Figure 2.4: The effects of discrete sampling in k-space: a) Left: The ideal case of continuously sampled data $S(k_x)$, right: The resulting image $I(x)$ after FT. b) Left: Discrete sampling at distance Δk_x is mathematically expressed by multiplication with a *Shah*-function $\text{Ш}(\frac{k_x}{\Delta k_x})$, right: In the image domain this corresponds to a convolution $*$ with a *Shah* function $\text{Ш}(k_x \Delta k_x)$. c) Left: Discretely sampled data $S_d(k_x)$, right: The image is a series of copies of the original image at distance $\frac{1}{\Delta k_x}$. (adapted from [Haacke1999])

artifacts do not occur when the FOV is larger than the object to be imaged [Nyquist1928]. If the extent of the object to be imaged in x-direction is A, the Nyquist Criterion in x-direction is met if:

$$FOV_x > A \text{ or } \Delta k_x < \frac{1}{A}. \tag{2.30}$$

If data are sampled such that Δk_x is too large to fulfill the Nyquist criterion, the dataset is said to be *under-sampled*. If Δk_x of a dataset is smaller than needed to fulfill the Nyquist criterion, it is called *oversampled*.

For Cartesian acquisition the distance between the k-space samples is equidistant. In that case, aliasing results in a wrap-around artifact, folding back the front parts of the object into the back of the image and vice versa.

For non-Cartesian trajectories aliasing artifacts have a more complicated appearance. The k-space samples are not equidistantly spread anymore, which means that for some frequencies the Nyquist criterion might be fulfilled, while for others it is not. For example, in radial acquisitions, high frequencies are sampled with a lower density than frequencies near the k-space origin. In that case, the Nyquist criterion is satisfied for the

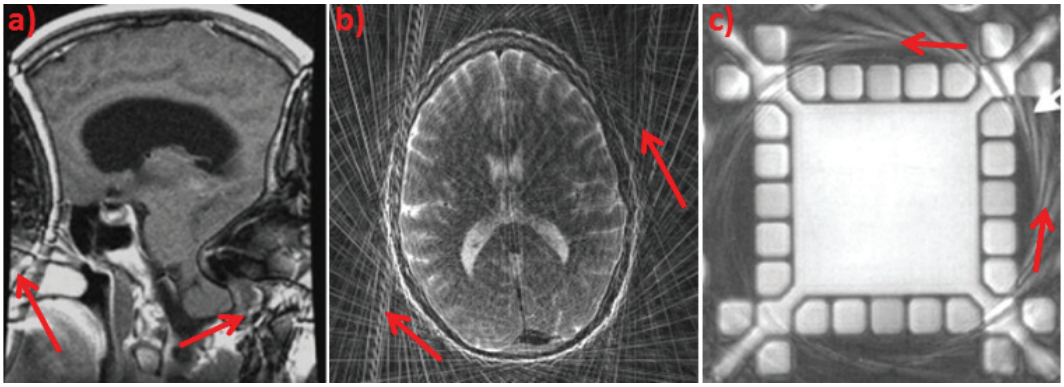

Figure 2.5: Examples of the appearance of aliasing artifacts for an a) Cartesian trajectory [mri-info], b) radial trajectory [AGILE2011], c) spiral trajectory [Bernstein2004].

low but not for the high frequencies and aliasing results in streaking artifacts. For spiral trajectories aliasing shows as swirl artifacts. Examples for the appearance of aliasing artifacts for different k-space trajectories are shown in figure 2.5.

Nyquist Criterion for 3D Radial *k*-space Data

The Nyquist criterion for 3D radial k-space data is derived, which will be needed for this thesis.

It is assumed for each profile that k_{max} is the maximal distance from k-space center, as indicated in figure 2.6. Furthermore it is assumed that all data points are sampled at equidistant solid angles. To determine the Nyquist criterion only the data points on the surface of a sphere of radius k_{max} that surrounds all data points have to be considered. Due to geometrical reasons these are the data points with the largest distance between two adjacent samples. For points located on the surface the two-dimensional Nyquist criterion can be expressed as:

$$(\Delta k)^2 < \frac{1}{A^2}, \tag{2.31}$$

where Δk is the distance between two adjacent data points and A is the largest extent of the object to be imaged. No aliasing occurs when the distances at the periphery of k-space Δk fulfill the Nyquist criterion.

The area $(\Delta k)^2$ can be written in terms of the solid angle $\Delta\Omega$:

$$(\Delta k)^2 = k_{max}^2 \Delta\Omega. \tag{2.32}$$

Combining equations 2.31 and 2.32 yields:

$$k_{max}^2 \Delta\Omega < \frac{1}{A^2}. \tag{2.33}$$

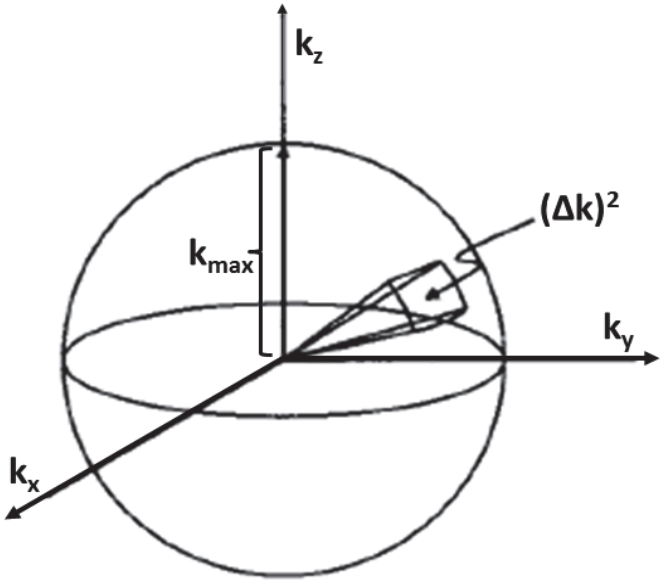

Figure 2.6: Derivation of the Nyquist criterion of a 3D radial sequence: The distance between two adjacent points Δk is maximal on the surface of the sampling sphere at distance k_{max} from the k-space center. The Nyquist criterion can be expressed as: $(\Delta k)^2 < \frac{1}{A^2}$, where A is the maximal extent of the object to be imaged. (adapted from [Bernstein2004])

The solid angle of the whole sphere is 4π sr. Therefore, the number of required profiles N_{pr} is given by:

$$N_{pr} = \frac{4\pi}{\Delta\Omega}. \tag{2.34}$$

Combing equations 2.33 and 2.34 yields the Nyquist criterion:

$$N_{pr} = 4\pi(k_{max}A)^2. \tag{2.35}$$

For a given matrix size M this can be rewritten as:

$$N_{pr} = 4\pi(M/2)^2. \tag{2.36}$$

For Cartesian sampling with the same isotropic resolution the number of phase encoding steps is $(2k_{max}A)^2$. The number of acquired samples to fulfill the Nyquist criterion is therefore smaller by a factor π compared to a 3D radial acquisition.

2.6.3 Resolution, Point Spread Function (PSF) and Gibbs Ringing

In general, the resolution Δx is defined as the smallest distance between two objects, where they can be still recognized as two separate objects. For a quantitative description of the resolution of an MRI image, the Point Spread Function (PSF) is useful.

Consider an object $\rho(x)$ and the image of the object $I(x)$. Again, only the one-dimensional case in x-direction is considered, but extension to higher dimensions is straightforward. The relation between $\rho(x)$ and $I(x)$ can be written as:

$$I(x) = \rho(x) * PSF(x), \tag{2.37}$$

where PSF is the Point Spread Function, and $*$ indicates a convolution. If $\rho(x) = \delta(x)$, where $\delta(x)$ is the one-dimensional *delta*-function then $I(x)$ is the PSF. The PSF describes the amount of blurring in the image.

The resolution of an image can be quantified by the width of the PSF. If the PSF is a *rect*-function, then the resolution is given by the width W of the function. If the PSF is not a *rect*-function, then the effective width W_h can be defined as the width of an approximating *rect*-function that has the same height and area as the PSF:

$$W_h = \Delta x = \frac{1}{PSF(0)} \int_{-\infty}^{\infty} PSF(x)dx, \tag{2.38}$$

where PSF(0) is the maximum point of the PSF. To derive an approximation of the PSF in MR images, the process of data acquisition within a finite measurement time is investigated.

So far we have assumed acquisitions of infinite duration. However, in reality data acquisition can take only a finite time, and consequently the data need to be cut off. Mathematically, measuring data $S_f(k_x)$ over a finite amount of time corresponds to multiplication of the infinite k-space data with a *rect*-function $rect(\frac{k_x}{W})$ of width W :

$$S_f(k_x) = S(k_x) \cdot rect(\frac{k_x}{W}). \tag{2.39}$$

According to the convolution theorem this corresponds to a convolution of the data in the image domain with the FT of the *rect*-function. The FT of the function $rect(\frac{k_x}{W})$ is the function $sinc(\pi W k_x)$. Consequently, the finite sampling has the following effect on the image $I(x)$:

$$I_f(x) = I(x) * sinc(\pi W x)), \tag{2.40}$$

where $I_f(x)$ is the resulting image. The *sinc*-function blurs each image point of $I(x)$. The effects on finite sampling are summarized in figure 2.7. With regard to equation 2.37, the PSF of an image can be approximated by the function $sinc(\pi W k_x)$. Substituting this in equation 2.38 for the PSF, the resolution Δx yields:

$$\Delta x = \frac{1}{2k_{x,max}} = \frac{FOV_x}{N_x}. \tag{2.41}$$

The higher the frequencies acquired in k-space, the larger the effective width W_h of the PSF, hence the less the blurring and the higher the resolution.

Another effect from the convolution with the *sinc* function is the phenomenon of *Gibbs ringing*, which is indicated in figure 2.7. It is caused by the sidelobes of the *sinc*-function

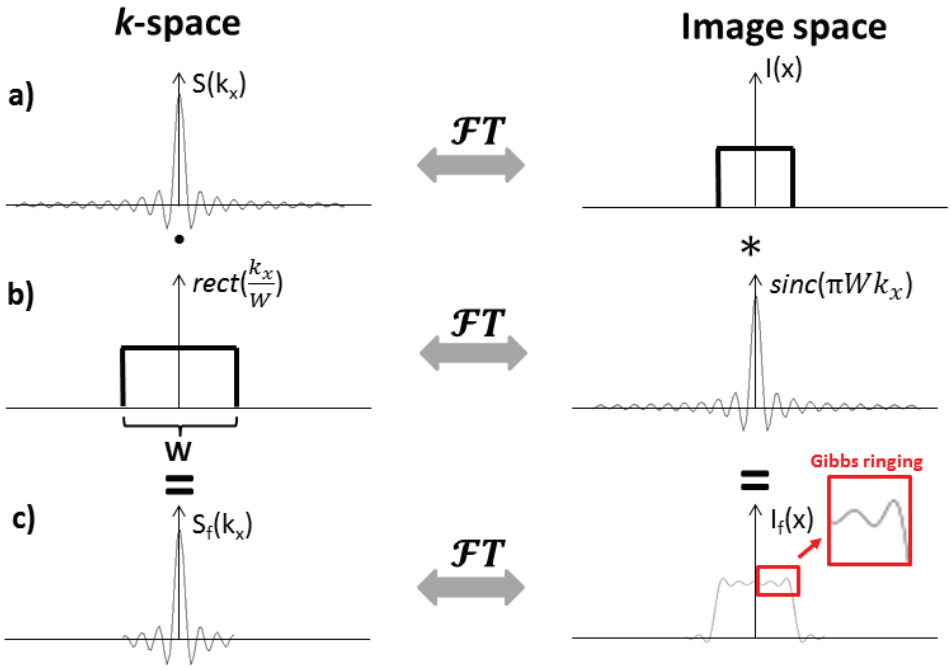

Figure 2.7: The effects of finite sampling in k-space: a) Left: The ideal case of data sampled over an infinite period of time $S(k_x)$, right: The resulting image $I(x)$ after FT. b) Left: Finite sampling is mathematically expressed by multiplication with a *rect*-function $rect(\frac{k_x}{W})$, right: In the image domain this corresponds to a convolution $*$ with a *sinc* function $sinc(\pi W k_x)$. c) Left: Data sampled over a finite time period $S_f(k_x)$, right: The resulting image $I_f(x)$ is blurred by the *sinc*-function. In the magnified region Gibbs ringing is visible. (adapted from [Haacke1999])

and becomes visible as rings or stripes especially around sharp edges. At low resolutions this artifact can become significant. It can be corrected for by multiplication of the k-space data with a smoothing window function such as the Hamming window. The Hamming window suppresses the high frequencies and attenuates Gibbs ringing, but also reduces the spatial resolution by making the PSF wider.

2.7 MRI Pulse Sequences

An *MR imaging sequence* is the composition and timing of RF pulses, gradient fields and data acquisition used for image generation. The timing of RF pulses and gradient waveforms can be displayed in an imaging scheme called *pulse sequence diagram*. An example of a pulse sequence diagram can be seen for example in figure 2.9. Plenty of different pulse sequences exist in MRI. In the following, a basic gradient recalled echo

(GRE) sequence is introduced.

2.7.1 Gradient Recalled Echo (GRE) Sequence

Formation of a Gradient Echo

The formation of a *gradient echo (GRE)* is explained using a one-dimensional experiment along the x-axis shown in figure 2.8. The extension to higher dimensions is straightforward. After the RF excitation, a constant gradient along the x-axis with the amplitude -$G_{Deph}(x,t)$ is switched on for a duration τ. Local magnetization vectors with different x-locations precess at different frequencies $\omega(x,t)$ during this time. The precession frequencies are described as:

$$\omega(x,t) = -\gamma \cdot G_{deph}(x,t) \cdot x. \tag{2.42}$$

Assuming the initial phase to be 0°, the phases accumulated at time τ can be written as:

$$\phi(x,\tau) = -\gamma \int_0^{\tau} G_{Deph}(x,t) \cdot x \cdot dt = -\gamma G_{Deph}(x,t) \cdot x \cdot \tau. \tag{2.43}$$

At time τ a second gradient $G_{Reph}(x,t)$ of same strength and duration but different polarity is switched on. The accumulated phase is now:

$$\phi(x,\tau) = -\gamma G_{Reph}(x,t) \cdot x \cdot \tau + \gamma \int_{\tau}^{2\tau} G_{Reph}(x,t) \cdot x \cdot t. \tag{2.44}$$

At time $t = 2\tau$ the local magnetization vectors are rephased and a signal echo is measured. The time between the RF pulse and the occurrance of the gradient echo is known as the *echo time* TE.
In general, GRE are formed when the 0th gradient moment is zero for all components. B_0-inhomogeneities and susceptibility effects are not eliminated by gradient echoes. Consequently, the GRE signal still decays with T_2^*.

Basic 2D GRE sequence

The pulse sequence diagram of a basic 2D gradient echo sequence is displayed in figure 2.9. During an RF pulse of flip angle α a slice selection gradient G_z is switched on to excite only a specific slice along the z-axis. To compensate for phase dispersion throughout the selected slice a refocusing gradient of opposite polarity and half its area succeeds the slice selection gradient (A).

In (B) the G_y gradient is applied. For each of the presented G_y gradients the slice has to be excited by a new RF pulse. The effect of the G_y gradient in k-space is to move the k-space position along the k_y- axis. Positive and negative gradients lead to positive and negative k_y-locations. In general, both polarities are needed since the Fourier integral given in equation 2.25 requires both, negative and positive values. In practice, this process can be abbreviated for example using half-Fourier imaging methods [Noll1991].

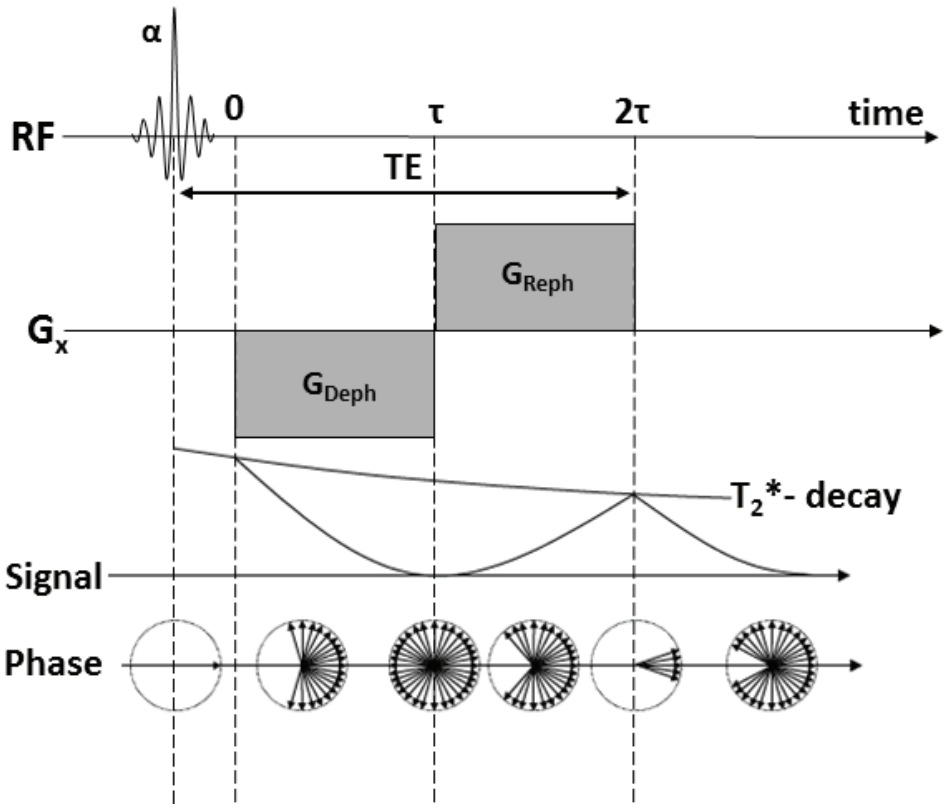

Figure 2.8: The formation of a gradient echo: The gradient G_{Deph} dephases the local magnetization vectors, the gradient G_{Reph} of opposite polarity rephases them again. When the areas of both gradients add up to zero, a gradient echo is formed. The measured echo signal still decays with T_2^*-relaxation (adapted from [Guenther1999]).

Frequency encoding using a G_x gradient and data acquisition with an ADC are shown in (C) and (D). Prior to data acquisition a G_x prephaser gradient of opposite polarity and half area of the readout gradient is turned on. This is needed for full k-space coverage from positive to negative values. In k-space it serves as a 'prewinder', moving the k_x-position to the negative maximum -$k_{x,max}$. The frequency encoding G_x gradient results in the trajectory of a straight line from -$k_{x,max}$ to $k_{x,max}$ at a given k_y location. During signal acquisition a gradient-recalled echo is formed when the area under the prephaser gradient time curve equals the area under the readout gradient at $k_x = 0$. With equal gradient magnitudes of prephaser and readout gradient the echo occurs at half of the frequency encoding duration. After data acquisition a *spoiler gradient* (E) is applied to dephase all of the residual transversal magnetization. The spoiling process will be described more detailed later in this section.

This *sequence block* is repeated until all k_y lines are collected. The time between two

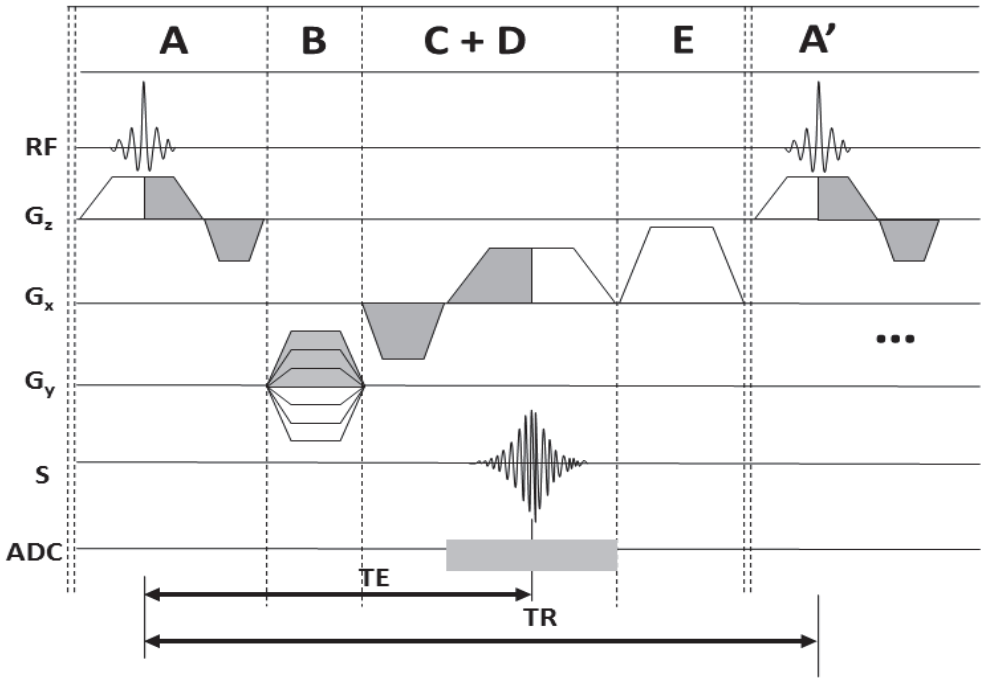

Figure 2.9: Pulse sequence diagram of a basic 2D GRE sequence: (A) RF pulse, slice selection and slice refocusing gradient, (B) G_y gradient, (C) G_x-rephaser and G_x readout gradient, (D) Data acquisition with an ADC, (E) spoiler gradient (adapted from [Guenther1999]).

adjacent excitations of the same slice is known as *repetition time* (TR). For N_y k_y-lines, the total measurement duration t_{tot} of the sequence becomes:

$$t_{tot} = N_y \cdot TR. \tag{2.45}$$

Spoiled GRE sequence in the steady-state

To encode multiple phase encoding steps a series of identical RF pulses with flip angle α, evenly spaced over time with period TR, is applied to the spin system:

$$\alpha - TR - \alpha - TR - \alpha - TR - ... \tag{2.46}$$

After a certain number of repetitions the transverse and longitudinal components of the magnetization M_{xy} and M_z reach a dynamic equilibrium, known as *steady-state*. The steady-state describes a periodic behavior of the magnetization with period TR.

GRE sequences can be classified by the value of the transverse magnetization before each new RF pulse. If $M_{tr} = 0$ the sequence is called a *spoiled* GRE sequence. If $M_{tr} \neq 0$ the sequence is said to be a steady-state free precession (SSFP) sequence. In this thesis a spoiled GRE sequence is used, therefore it will be the focus of the remainder of this section.

The condition $M_{tr} = 0$ can be achieved by choosing TR to be at least $5T_2^*$. In this case, the transverse magnetization automatically decays nearly to zero due to T_2^* decay. However, the disadvantage is, according to equation 2.45, that with a long TR the total measurement time of the sequence becomes large. A more practical way is to dephase or *spoil* M_{xy} before each new RF pulse. *Spoiling* can be achieved either with *spoiler gradients* or using *RF spoiling*, or a combination of both. Spoiler gradients are large gradients applied at the end of each sequence block. They dephase the transverse magnetization prior to each new RF pulse. With RF spoiling, the residual magnetization is killed by cycling the phase of each RF excitation pulse according to a predetermined schedule. The mechanisms of spoiling will be described in more detail at the end of this section. For now, it will be assumed that the transverse magnetization is zero before each new RF excitation.
The steady-state is reached when a counterbalance between the loss of longitudinal magnetization due to tipping and regrowth due to T_1-relaxation is established. The steady-state of M_z of a spoiled GRE sequence is said to be *incoherent*. Mathematically, the created transverse magnetization at each data acquisition and therefore the received signal of a spoiled GRE sequence can be determined as follows. The following notation will be used: The indices '1, 2, 3, ...' describe the number of the RF pulse, the indices '-' and '+' stand for 'just before the RF pulse' and 'just after the RF pulse'. M_z^0 describes the equilibrium value of the magnetization.

Each RF pulse tips the longitudinal magnetization by flip angle α. For example for the first RF pulse $M_{z,1}$ after tipping has the value:

$$M_{z,1}^{+} = M_{z,1}^{-} cos\alpha. \tag{2.47}$$

During the TR interval between the two RF pulses at time points t_1^+ and t_2^- M_z regrows due to T_1-relaxation. This is given according to the solutions of the Bloch equation by:

$$M_{z,2}^{-} = M_{z,1}^{+} e^{-\frac{TR}{T_1}} + M_z^0(1 - e^{-\frac{TR}{T_1}}) = M_{z,1}^{-} cos\alpha E_1 + M_z^0(1 - E_1), \tag{2.48}$$

with $E_1 := e^{-\frac{TR}{T_1}}$.
For a system in steady-state the longitudinal magnetization just before two RF excitations is the same. Therefore, the condition for the steady-state is:

$$M_{z,1}^{-} = M_{z,2}^{-}. \tag{2.49}$$

The elimination of $M_{z,2}^{-}$ in equation 2.48 and rewriting yields:

$$M_{z,1}^{-} = M_z^0 \frac{(1 - E_1)}{1 - E_1 cos\alpha}. \tag{2.50}$$

The measured signal S, which is proportional to the transverse component after flipping M_z into the transverse plane by α, is caused by the rephasing of the magnetization vectors at echo time TE:

$$S = \frac{M_z^0 sin\alpha(1 - E_1)}{1 - cos\alpha E_1} e^{-\frac{TE}{T_2^*}}. \tag{2.51}$$

	TR»T_1, α«θ_E	TR»T_1, $\alpha \approx \theta_E$	$TR \lesssim T_1$, α«θ_E	$TR \lesssim T_1$, $\alpha \approx \theta_E$
$TE << T_2^*$	ρ-weighting	ρ-weighting	ρ-weighting	T_1-weighting
$TE \approx T_2*$	ρ-T_2^*-weighting	ρ-T_2^*-weighting	ρ-T_2^*-weighting	T_1-T_2^*-weighting

Table 2.1: Relationship between TR, TE, α and the image contrast in a spoiled GRE sequence

The flip angle α that maximizes the signal S is called the *Ernst angle* θ_E.

$$\theta_E = arccos(E_1) = arccos(e^{-\frac{TR}{T_1}}). \tag{2.52}$$

The Ernst angle monotonically increases as the ratio $\frac{TR}{T_1}$ increases. Mathematically, the approach to steady-state can be described as:

$$S_j = M_0 sin\theta[\frac{1-E_1}{1-cos\theta E1} + (cos\theta E_1)^{j-1}(1 - \frac{1-E_1}{1-cos\theta E1})]e^{-\frac{TE}{T_2^*}}, \tag{2.53}$$

where j indicates the jth RF pulse.

Contrast of spoiled GRE sequences

As equation 2.51 indicates, spoiled GRE images are weighted by a factor of $e^{-\frac{t}{T_2^*}}$. This makes them prone to signal loss, especially in regions with high B_0- or susceptibility-inhomogeneities, for example near metallic implants. If TE is chosen to be short relative to T_2^*, then the term $e^-(\frac{TE}{T_2^*})$ tends to 1 and no weighting by T_2^* remains.

For small flip angles α the term $cos\alpha$ in equation 2.51 approaches the value 1 and the E_1-dependence cancels out. In the case of short echo times TE and small flip angles the signal is only dependent on M_0, which is proportional to the proton spin density ρ_0. The signal is said to be *proton density weighted*. If a small echo time TE and a larger flip angle, preferably around the Ernst angle, are employed, the E_1-factor becomes dominant and the signal is weighted by the factor $e^{-\frac{TR}{T_1}}$. The signal is said to be T_1-*weighted*. The relationship between the choice of TR, TE and α and the resulting contrast is summarized in table 2.1.

Fast imaging with spoiled GRE sequences

An advantage of spoiled gradient echo sequences is that they can be used for fast imaging, especially as needed for the coverage of large 3D volumes. Fast GRE sequences employ small flip angles between $\alpha = 2°$ and 70°. Small flip angles have the advantage that most longitudinal magnetization is undisturbed while there is still an appreciable amount of transversal magnetization. Short TR times can be used because there is no long T_1-relaxation.

Mechanisms of Spoiling

Gradient Spoiling

At the end of a TR period residual transverse magnetization can remain. In a sequence where TR is repeated multiple times, this residual magnetization can interfere with the desired magnetization in the subsequent data acquisition and lead to imaging artifacts. *Spoiler gradients* are used to kill the unwanted remaining magnetization. They are usually gradients of large 0th gradient moments applied at the end of a sequence to dephase the residual transverse magnetization whilst leaving the longitudinal magnetization undisturbed.

Considering and arbitrary voxel in which the transverse residual magnetization $\vec{M}_{tr}(\vec{r})$ remains at the end of an TR period. Within this voxel the magnetization is the sum of many local magnetization vectors. When a spoiler gradient $\vec{G}_{sp}$ is applied, these vectors fan out with frequencies dependent on their location along the spoiler gradient direction. The acquired phase $\phi(r)$ of the spoiler gradient $\vec{G}_{sp}$ at time t after the starting time $t = 0$ of the spoiler is given by the product of the gradient moment and the voxel dimension along the gradient direction:

$$\phi(r,\tau) = \gamma \int_0^\tau \vec{G}_{sp}(r,t)\vec{r}dt = \gamma \int_0^\tau G_{sp}(r,t)rdt = \gamma r A_{sp}, \tag{2.54}$$

where A_{sp} is the 0th moment of the spoiler gradient. The phase dispersion across the whole voxel $\Delta\phi$ is:

$$\Delta\phi(r) = \gamma \Delta r A_{sp}, \tag{2.55}$$

where Δr is the voxel dimension in direction of $\vec{G}_{sp}$. The minimal moment needed to spoil the unwanted magnetization is normally determined experimentally. The spoiler gradient moment is incremented and the resulting images are monitored for the occurrence of artifacts. For most applications, the minimal phase dispersion across the voxel must be at least 2π [Bernstein2004]. Since the polarity of the spoiler gradients can be chosen flexibly, they should be selected such that they do not counteract the preceding gradients. For example if the spoiler is applied along the same direction as a readout gradient, it should be of the same polarity. The spoiler gradient is preferably applied along the axis with the largest voxel dimension, since here the largest phase dispersion can be achieved for the same gradient moment. The magnetization is killed to a large extent if the spoiler moment is large enough. However, if only small amount of transverse magnetization is left undestroyed, it can build up to a steady-state value after multiple repetitions. Therefore, it is recommended to vary the moment of the spoiler gradient with each excitation to prevent this build up.

RF Spoiling

RF spoiling is done by applying a phase offset to each new RF pulse. This prevents a build up towards the steady-state of a residual transverse magnetization. The phase is

cycled according to a predetermined schedule. A commonly used schedule is:

$$\phi_j = \phi_{j-1} + j\phi_0, \tag{2.56}$$

where j is the index of the jth RF pulse, ϕ_j is the phase of the jth RF pulse and the starting value ϕ_0 can be chosen freely. $\phi_0 = 117°$ has been shown to lead to efficient spoiling [Bernstein2004]. In general, efficient spoiling can be achieved by combining both, RF and gradient spoiling.

2.8 Noise in MR Images

2.8.1 Signal-to-Noise Ratio (SNR)

In this section the origin and quantification of noise in MR images will be introduced. All measurements exhibit unstructured or structured noise, which can corrupt image quality and lead to misinterpretations of image features. Unstructured noise, also called *white noise*, is caused by random thermal fluctuations in the electronics of the receiver coil and in the sample. White noise is typically Gaussian distributed with a mean value of 0 and noise variance σ^2, which is given by:

$$\sigma^2 = 4k_B T \cdot R \cdot BW_{read}, \tag{2.57}$$

where R is the combined effective resistance of the object, the receive coil and the electronics, and BW_{read} is the readout bandwidth of the receive coil. The receiver bandwidth is defined as the range of frequencies over which a signal is recorded. The noise variance is the same for signals of all measured frequencies. Structured noise is systematic and appears for example as streaking artifacts, Gibbs ringing or other image artifacts. This section focuses only on unstructured noise.

When the data are acquired, noise is inflicted on the k-space data. By applying the discrete inverse FT to the noisy k-space data, the image noise is obtained. The mean of the image noise is still 0 and the image noise variance σ_I^2 is given by

$$\sigma_I = \frac{\sigma}{\sqrt{N}}, \tag{2.58}$$

where N is the number of acquired k-space samples. The FT distributes the Gaussian noise uniformly across the image and hence the standard deviation σ_I is the same for all image locations.

The signal-to-noise ratio (SNR) is a measure for the effect of noise on image quality and is defined as:

$$SNR := \frac{S_{voxel}}{\sigma_I}, \tag{2.59}$$

where S_{voxel} the voxel signal. The dependence of the SNR on all of user-selective parameters for 3D imaging are summarized in the formula:

$$SNR \propto \Delta x \Delta y \Delta z \sqrt{\frac{N_{acq} N_x N_y N_z}{BW_{read}}} S(TR, TE, \alpha). \tag{2.60}$$

For 2D imaging the SNR dependence is analogous, however without the factor $\Delta z\sqrt{N_z}$. Therefore, 3D imaging is more SNR efficient than 2D imaging. The given parameters are in the following relation to other parameters:

$$T_s = N_x \Delta t = \frac{N_x}{BW_{read}}, \tag{2.61}$$

where T_s is the total sampling period and Δt is the time to measure each individual sample. Another relationship is:

$$FOV_x = N_x \Delta x \ , \ FOV_y = N_y \Delta y \ , \ FOV_z = N_z \Delta z. \tag{2.62}$$

Therefore, many variations of equation 2.60 exist. If one of the parameters is changed, the effect on other parameters has to be considered due to the interconnections amongst them.

2.8.2 Measuring SNR

In MRI it is common practice to work with magnitude images. Each voxel is calculated from the square root of the sum of squares of the real and imaginary voxel signals. The noise in the real and imaginary components are each Gaussian distributed. The non-linear procedure of reconstructing the magnitude image changes the noise distribution to a Rician distribution [Rice1945]. In the case of large SNRs the Rician distribution approaches again a Gaussian distribution with non-zero mean. In image areas without any signal, for example the background, the Rician distribution becomes a Rayleigh distribution [Gudbjartsson1995].

To measure the SNR, the voxel signal S_{voxel} and the standard deviation σ_I of the noise distribution have to be estimated. On magnitude images one approach is done as follows. S_{voxel} is approximated by measuring the mean signal from a homogeneous region in the tissue of interest. σ_I can be estimated by measuring the standard deviation σ_{bg} of an image region in the background. However, due to the Rayleigh distribution a correction factor of 1.5 has to be applied in order to obtain the standard deviation of the underlying Gaussian distribution. The image noise becomes:

$$\sigma_I = \sigma_{bg} \cdot 1.5. \tag{2.63}$$

Alternatively, σ_I can be determined from the non-zero mean signal S_{bg} of the background as follows:

$$\sigma_I = S_{bg} \cdot 0.8. \tag{2.64}$$

The presented method is easy to implement, as long as large homogeneous regions occur in the data. If systematic errors and structured noise corrupts the data too much, it can be problematic to find homogeneous regions. In that case, different methods can be used, for example as proposed by Sijbers *et al* [Sijbers1998].

SNR of Radial *k*-space Data

For the content of this thesis, the effect of non-Cartesian radial k-space sampling on the SNR is of interest. This is described for example in [Newbould2006]. In radial acquisitions, data near the k-space center are oversampled, which increases the SNR in this region. Therefore, noise is not 'white' anymore. The noise variance is greater for higher frequencies. This *colored noise* leads to the loss of SNR near fine structures in the resulting image.

2.9 Reconstruction

2.9.1 Fourier Reconstruction

The 2D or 3D k-space signal is the FT of the transverse magnetization. Therefore, image reconstruction can be achieved by applying the 2D or 3D inverse FT (IFT) to the k-space data. Since discrete k-space values are sampled, the discrete FT (DFT) has to be used. If the data are sampled on a Cartesian trajectory, the inverse DFT can be performed with a series of Fast FTs (FFT) [Cooley1965]. The FFT is an algorithm that is computationally faster than the standard DFT. It is fastest for input data of length of a power of 2. If the input data length is not a power of 2, data can be symmetrically appended with zeros. This procedure is called *zero filling* or *zero padding*. Even if no new information is added, zero filling increases the matrix size by interpolation with a *sinc*-function. This has a smoothing effect on the image, improving the apparent resolution.

Multiple Coils

If multiple coils are used for data acquisition, the individual coil images $I_j(x, y)$ are reconstructed as described above, where j is the coil index. Afterwards they are combined to the image $I(x, y)$ as follows:

$$I(x,y) = \sqrt{\sum_{j=1}^{N_j} \frac{|I_j(x,y)|^2}{\sigma_j}}, \tag{2.65}$$

where N_j is the total number of coils and σ_j is the noise variance (section 2.8). After the combination $I(x, y)$ is a magnitude image, which does not consist of complex numbers anymore. Methods which yield better SNR are available such as [Roemer1990], which are currently used as standard procedures.

2.9.2 Gridding Reconstruction

Due to advantages such as imaging speed or SNR efficiency, k-space trajectories are acquired, which do not fall onto a Cartesian grid. These are for example radial or spiral

trajectories as it was described in section 2.6. Since the FFT can straightforwardly only be applied to Cartesian data, the reconstruction process has to be modified. One approach is to interpolate the non-Cartesian data and resample them onto a Cartesian grid and then to apply the FFT. This method is called *gridding*. In the following, the gridding process, which is used in this thesis, will be explained in detail.

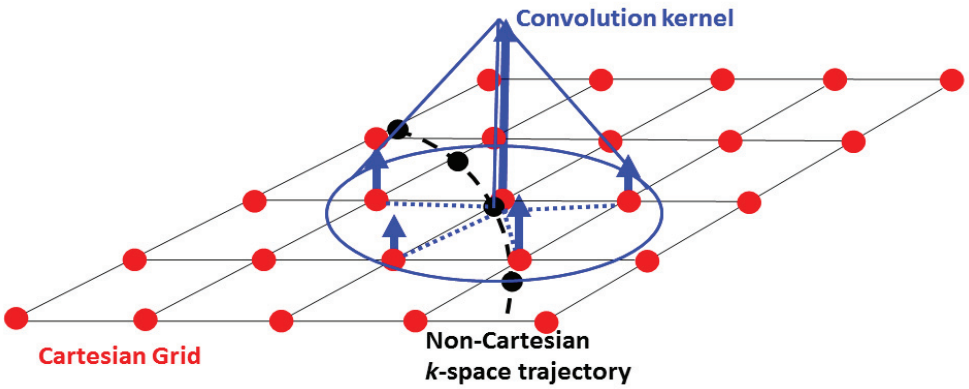

Figure 2.10: Basic principle of gridding: The acquired data (black) lie on a non-Cartesian trajectory. Each non-Cartesian data point is convolved with a convolution kernel (blue) and the resulting distance-weighted values are accumulated. The result is resampled onto a Cartesian grid (red). (adapted from [Pauly2005]

Basic Gridding Algorithm

The basic problem can be formulated as follows: Non-uniformly spaced data points in k-space are given. The aim is to obtain k-space data on a rectilinear grid by interpolating the given non-uniform k-space data. The basic principle of gridding is illustrated in figure 2.10. Each of the non-uniform sample points is convolved with a gridding kernel and the values are accumulated for all sample points. Then the result is resampled onto a Cartesian grid and a FFT is performed.

Mathematically, the gridding algorithm can be described as follows. Here, the operations for gridding of 2D data are shown, but the extension to 3D is straightforward. Consider a 2D image function $I(x, y)$ with FT $S(k_x, k_y)$:

$$S(k_x, k_y) = \int_{-\infty}^{\infty} I(x, y) e^{i2\pi(k_x x + k_y y)} dx dy \tag{2.66}$$

and a sampling function Ψ consisting of delta funtions at the positions $\vec{k}_j$:

$$\Psi(k_x, k_y) = \sum_{j=1}^{P} \delta^2(k_x - k_{x_j}, k_y - k_{y_j}). \tag{2.67}$$

The non-Cartesian sampled data $S_\Psi(k_x, k_y)$ is given by:

$$S_\Psi(k_x, k_y) = S(k_x, k_y) \cdot \Psi(k_x, k_y). \tag{2.68}$$

In the gridding process, each sampled data point is convolved with a kernel $C(k_x, k_y)$. After the convolution, the sampled and convolved data $S_{\Psi C}(k_x, k_y)$ becomes:

$$S_{\Psi C}(k_x, k_y) = S_\Psi(k_x, k_y) * C(k_x, k_y), \tag{2.69}$$

where $*$ represents a two-dimensional convolution. Eventually the data $S_{\Psi C}(k_x, k_y)$ are resampled onto a unit spaced Cartesian grid by multiplication with a two-dimensional *Shah* function Ш, defined as the sum of equally spaced two-dimensional delta functions, resulting in the data $S_{\Psi C\text{Ш}}(k_x, k_y)$:

$$S_{\Psi C\text{Ш}}(k_x, k_y) = S_{\Psi C}(k_x, k_y) \cdot \text{Ш}(\frac{k_x}{\Delta k_x}, \frac{k_y}{\Delta k_y}). \tag{2.70}$$

In summary:

$$S_{\Psi C\text{Ш}}(k_x, k_y) = [(S(k_x, k_y) \cdot \Psi(k_x, k_y)) * C(k_x, k_y)] \cdot \text{Ш}(\frac{k_x}{\Delta k_x}, \frac{k_y}{\Delta k_y}). \tag{2.71}$$

After applying the inverse FT to $S_{\Psi C\text{Ш}}$ the reconstructed image $I_{\Psi C\text{Ш}}$ becomes:

$$I_{\Psi C\text{Ш}}(x, y) = [(I(x, y) * \psi(x, y)) \cdot c(x, y)] * \text{Ш}(\frac{x}{FOV_x}, \frac{y}{FOV_y}), \tag{2.72}$$

where $\psi(x, y)$ is the FT of $\Psi(k_x, k_y)$, $c(x, y)$ is the FT of $C(k_x, k_y)$ and the FT of the *Shah* function Ш is again a *Shah* function, with the distance FOV between the delta peaks.

The effects on the image of each of these steps are illustrated in figure 2.11. The ideal image $I(x, y)$ is first blurred by the convolution with the FT of the finite discrete sampling function $\psi(x, y)$ and aliasing artifacts show as side-lobes. If the Nyquist criterion is fulfilled, the aliasing artifacts are located outside the object. The process of multiplying the sampled data with the FT of the kernel $c(x, y)$ is called *apodization* and causes undesired shading in the image. However, it has the desirable effect to suppress the side-lobes. The rectilinear resampling to the Cartesian grid by the convolution with $\text{Ш}(\frac{x}{FOV_x}, \frac{y}{FOV_y})$ causes replicas of the image. Depending on how the FOV is chosen, side-lobes from the next replicas can interfere with the objects of interest.

There are many options how to implement the gridding algorithm and how to handle the described influence of the gridding operations on the image. Here, the choice of the gridding kernel, the density of the Cartesian grid and a correction of the shading during the apodization called *deapodization*, as used in this thesis, will be explained. Furthermore, the gridding algorithms require a correction for the non-uniform density of the samples.

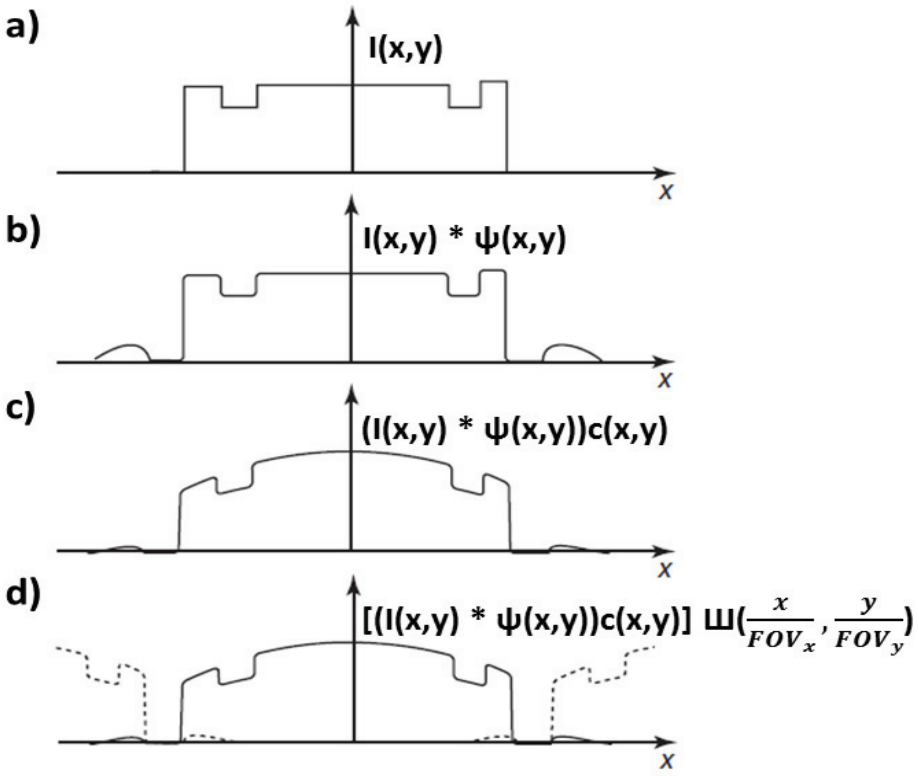

Figure 2.11: Effects of gridding on the image: a) Ideal image $I(x, y)$. b) The convolution with the FT of the sampling function $\psi(x, y)$ blurs the image and results in aliasing side-lobes. c) The multiplication with the FT of the kernel function $c(x, y)$ causes shading of the image. d) The resampling onto the Cartesian grid by the convolution with $\text{Ш}(\frac{x}{FOV_x}, \frac{y}{FOV_y})$ generates replicas of the image. (adapted from [Pauly2005]

Gridding Kernel and Deapodization

As described above, the convolution with the kernel $C(k_x, k_y)$ in k-space is a multiplication with the apodization function $c(x, y)$ in image space. The ideal choice of the gridding kernel would be a finite kernel, that suppresses all the side-lobes. Jackson *et al* [Jackson1991] found that a kernel in the shape of a Kaiser-Bessel function can yield nearly optimal results in terms of computation time and side-lobe suppression. The 1D Kaiser-Bessel function is defined as:

$$C(k) = \frac{1}{w} I_0(\beta(1 - \frac{2k}{w})^2) rect(\frac{2k}{w}), \tag{2.73}$$

where I_0 is the zero-order modified Bessel function of the first kind, w is the width of the kernel and β is a scaling parameter, that determines the curve shape. The inverse

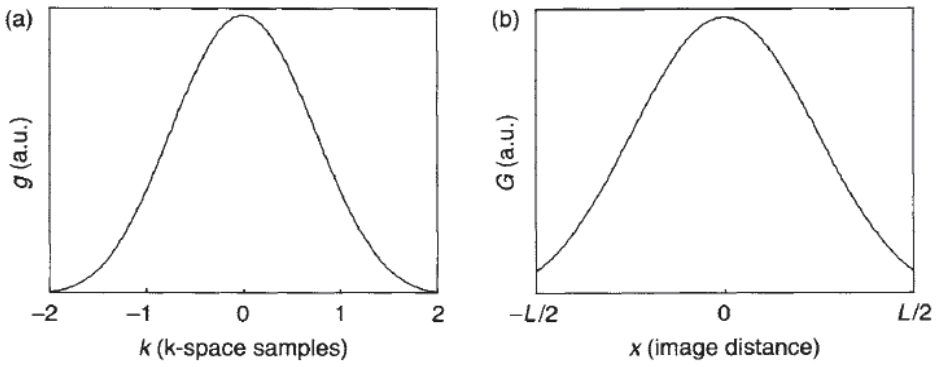

Figure 2.12: a) Kaisel-Bessel window, b) FT of the Kaiser-Bessel window [Bernstein2004].

w	1.5	2.0	2.5	3.0	3.5	4.0	4.5	5.0
β_{1X}	1.9980	2.3934	3.3800	4.2054	4.9107	5.7567	6.6291	7.4302
β_{2X}	6.6875	9.1375	11.5250	13.9086	16.2734	18.5547	–	–

Table 2.2: Optimized parameters β of the Kaisel-Bessel function for kernel window widths w for a $1X$ and a $2X$ grid. [Jackson1991]

FT of the Kaiser-Bessel function can be calculated analytically and is given by:

$$c(x) = \frac{sin(\sqrt{\pi^2 w^2 x^2 - \beta^2})}{\sqrt{\pi^2 w^2 x^2 - \beta^2}}. \tag{2.74}$$

The Kaiser-Bessel function and the corresponding FT are displayed in figure 2.12. In [Jackson1991], the parameter β was optimized for several kernel widths w such that the apodization function has sharp edges. The resulting parameter values are shown in table 2.2. The meaning of the $1X$- and $2X$-grid used in the table is explained in the next subsection. w is typically chosen to be 2-4 data sample points and a trade-off between steep rolling-off or computation time. In more than one dimension, the kernel can be treated as separable function in all dimensions.

The shading in the object, caused by the apodization, results in significant loss in image quality. It can be removed by dividing the image by the apodization function at the end of the gridding process. This is called *deapodization*. The gridding algorithm including deapodization can be written as:

$$I_{\Psi C \text{Ш} D}(x,y) = \frac{1}{(c(x,y))}\{[(I(x,y) * \psi(x,y)) \cdot c(x,y)] * \text{Ш}(\frac{x}{FOV_x}, \frac{y}{FOV_y})\}. \tag{2.75}$$

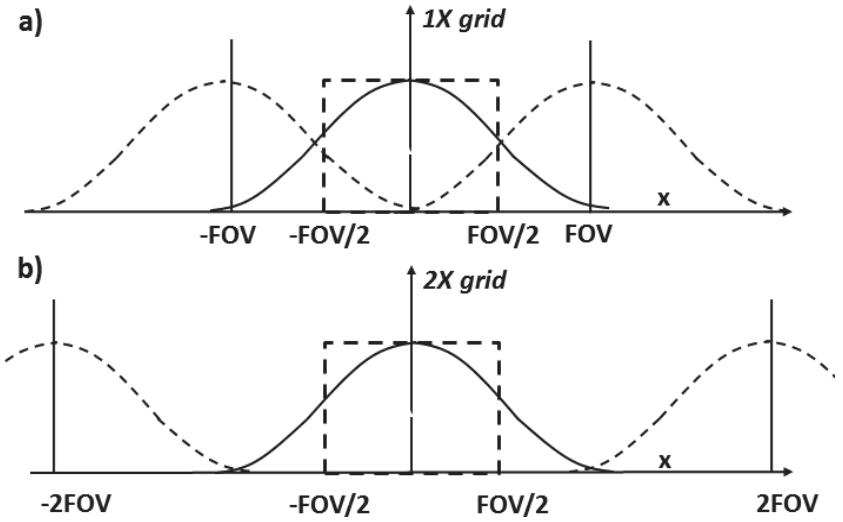

Figure 2.13: Oversampling of the Cartesian grid size: a) *1X Grid*: There is no transition band between the object and the adjacent side-lobes folding into the image FOV. b) *2X Grid*: The FOV is twice as large as in a). The object and the adjacent side-lobes get 'pushed' apart, allowing for a transition band [Pauly2005].

Cartesian Grid Size and Oversampling

Aliasing side-lobes corrupt image quality, since the adjacent replica fold back into the image. When the Cartesian grid is as dense as determined by the underlying data (*1X Grid*), there is no space for a transition band, where no adjacent side-lobes fold into the object, as can be seen in figure 2.13 a).

O'Sullivan *et al* proposed to sample more finely onto a denser grid, for example a *2X Grid*, which is twice as dense as the *1X Grid*[OSulllivan1985]. This is possible since there is no restriction about the density of the Cartesian raster. According to equation 2.29 sampling twice as dense, with an *oversampling factor* of 2, results in a FOV of twice the size. This allows for a transition band and reduces aliasing artifacts significantly. This is visualized in figure 2.13 b). In general, using an oversampling factor of α changes the rectilinear sampling function $\text{Ш}(\frac{x}{FOV_x}, \frac{y}{FOV_y})$ to $\text{Ш}(\frac{x}{\alpha FOV_x}, \frac{y}{\alpha FOV_y})$ and equation 2.75 to

$$I_{\Psi C \text{Ш} D}(x,y) = \frac{1}{(c(x,y))}\{[(I(x,y) * \psi(x,y)) \cdot c(x,y)] * \text{Ш}(\frac{x}{\alpha\ FOV_x}, \frac{y}{\alpha\ FOV_y})\}. \quad (2.76)$$

An oversampling factor of $\alpha = 2$ is sufficient for the Kaiser-Bessel kernel and additionally attenuates the apodization shading because it is spread over a larger FOV. The periphery of the large FOV can be discarded by cutting out only the center part of the image.

A major limitation of oversampling is the increased computational memory. With an oversampling factor of 2 the number of points in each dimension double which is a cubic increase in memory usage for three dimensions.

Smaller oversampling factors can be achieved with the same results when the kernel is optimized with a continuous trade-off between memory issues and computational time. Acceptable results have been demonstrated by Beatty *et al* with a oversampling factor of 1.25 [Beatty2005].

Density Compensation

Dependent on the trajectory, the density of non-Cartesian samples can vary. The spatial density of data points in k-space shall be given by the density function $\rho(k_x, k_y)$. With gridding reconstruction, each sample is convolved with a kernel and the resulting values for all sample points are accumulated. This leads to an over-representation of k-space samples lying in an area of high sample density. This is for example the case for the k-space data in the center of radial acquisitions. In the image domain this corresponds to a convolution with the FT of the density function $\rho(k_x, k_y)$, which causes image artifacts and needs to be corrected for.

There are two possibilities to compensate for the density: *Pre-compensation* and *post-compensation*. Pre-compensation is done before the gridding process by weighting every data point with $\frac{1}{\rho(k_x,k_y)}$. Therefore, $\rho(k_x, k_y)$ needs to be known before the gridding algorithm starts. With density pre-compensation, equation 2.71 becomes:

$$S_{\Psi\rho C\text{Ш}}(k_x, k_y) = [(S(k_x, k_y)\frac{\Psi(k_x, k_y)}{\rho(k_x, k_y)}) * C(k_x, k_y)] \cdot \text{Ш}(\frac{k_x}{\Delta k_x}, \frac{k_y}{\Delta k_y}). \tag{2.77}$$

Post-compensation is done after the gridding by weighting every calculated grid-point with $\frac{1}{\rho(k_x,k_y)}$. $\rho(k_x, k_y)$ does not have to be known prior to gridding and can be calculated during the gridding process. With density post-compensation, equation 2.71 becomes:

$$S_{\Psi C\rho\text{Ш}}(k_x, k_y) = [(S(k_x, k_y) \cdot \Psi(k_x, k_y)) * C(k_x, k_y)] \cdot \frac{1}{\rho(k_x, k_y)} \cdot \text{Ш}(\frac{k_x}{\Delta k_x}, \frac{k_y}{\Delta k_y}). \tag{2.78}$$

Post-compensation has the disadvantage that large density changes that happen on a scale smaller than the kernel width, are blurred. This is for example the case for radial trajectories in the center of k-space. In this thesis, where a 3D radial trajectory is gridded, pre-compensation is preferred.

The density compensation function (DCF) is defined as $DCF(k_x, k_y) := \frac{1}{\rho(k_x,k_y)}$. For pre-compensation, given a k-space trajectory, the DCF can be calculated based on the geometry of the samples or using Voronoi diagrams, which numerically approximate the area of volume of each sample. This area or volume of each point yields the density function. Drawbacks of Voronoi diagrams are long calculation times and the handling of the periphery points that take infinity area and reasonable values need to be estimated.

Summary the gridding process

A summary of the gridding process as implemented in this thesis is given in the flow chart in figure 2.14.

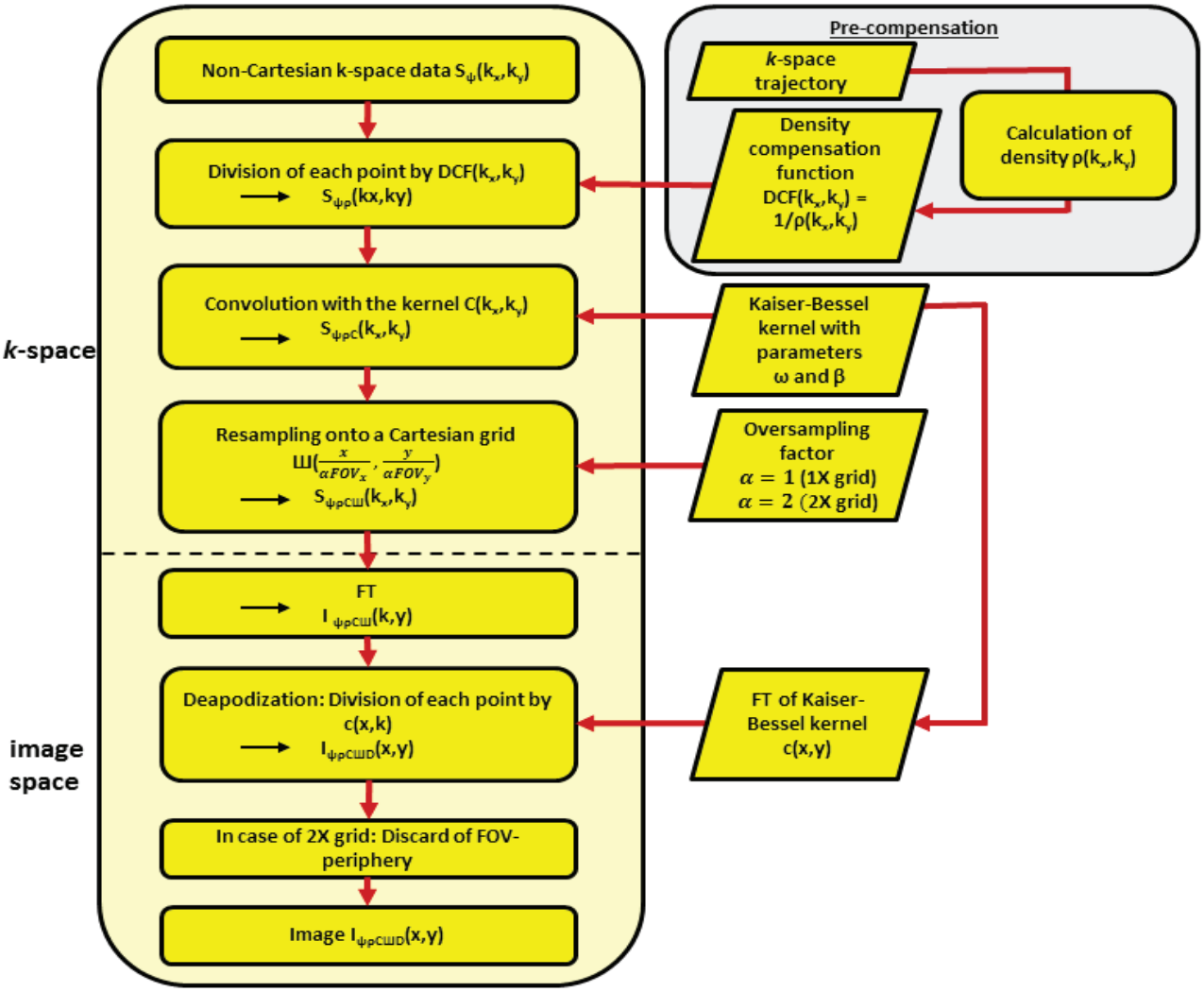

Figure 2.14: Summary of the gridding process. Here, the density of k-space samples is accounted for by pre-compensation.

3 Dynamic Contrast-Enhanced (DCE) MRI in Oncology

Dynamic contrast-enhanced (DCE) MRI is a minimal-invasive method to image and quantify the physiology of tissue perfusion, requiring only a contrast agent (CA) injection. In oncology, DCE MRI is used in clinical routine for lesion diagnosis, detection and classification, and to monitor and predict response to treatment.

3.1 Basic Principle

The basic principle of DCE MRI is illustrated in figure 3.1. After the administration of a bolus of CA, a series of dynamic T_1-weighted images is acquired. Contrast agent has the effect to locally shorten T_1-relaxation times. Therefore, whilst CA travels though the body, as described in section 1.4, signal enhancement occurs. These signal changes over time are monitored and evaluated qualitatively or quantitatively.

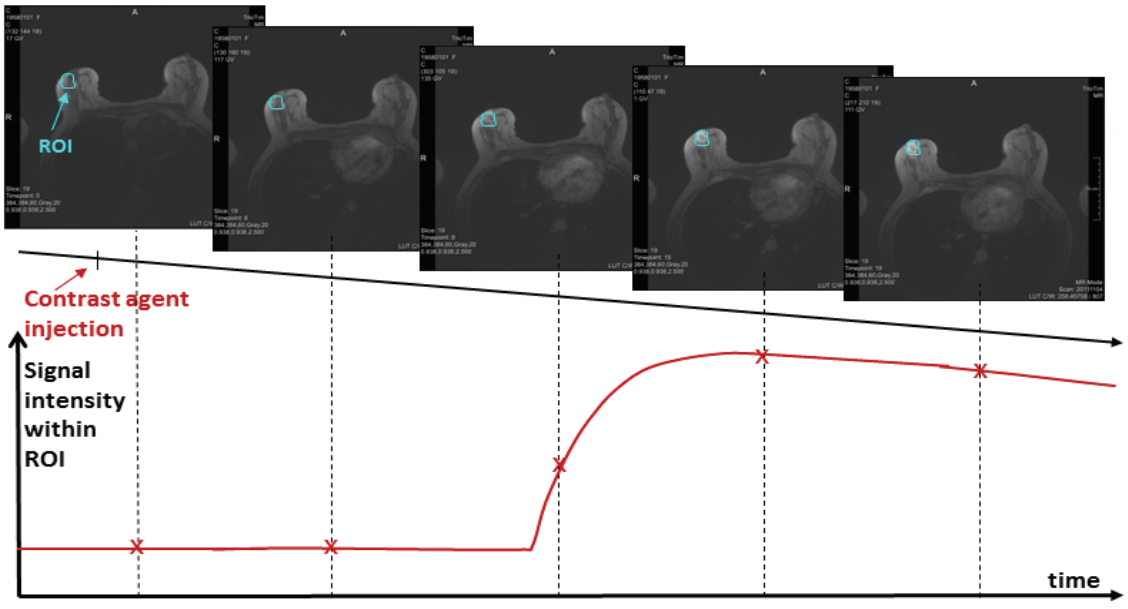

Figure 3.1: Basic principle of DCE MRI: Contrast agent is injected and the resulting signal changes in a T_1-weighted time series are monitored.

3.2 Contrast Agents in DCE MRI

A bolus of contrast agent is administered intravenously in a peripheral vein. To assure reproducibility, automated pressure power injection systems are employed. A typical dose of contrast agent is 0.1 mMol/kg body weight, injected at a rate of 4 ml/s for a duration in the order of a second. To make the bolus stay coherent during its passage, a chaser injection of saline at the same flow rate flushes the contrast agent.

In clinical DCE MRI low molecular weight paramagnetic gadolinium chelates are used as contrast agents. Multiple types of contrast agents exist which differ in their chelates. An often used contrast agent in DCE MRI is Gd-DTPA ('Magnevist').

Gadolinium ions are paramagnetic and interact with nearby hydrogen nuclei. This leads to a decrease in the T_1- and T_2^*-relaxation times in the tissue water in proximity to the contrast agent. The resulting effect for imaging is signal enhancement in T_1-weighted and signal loss in T_2^*-weighted images. The amount of signal increase/loss is correlated with the concentration C of CA present in the tissue. The relationship between $T_1(t)$ and $C(t)$ is given by [Rosen1990]:

$$C(t) = \frac{1}{r_1}\left(\frac{1}{T_1(t)} - \frac{1}{T_1(0)}\right), \tag{3.1}$$

where $T_1(0)$ is the native T_1-relaxation time of the tissue before contrast agent arrival and r_1 is the relaxivity of the contrast agent. The relaxivity is a measure for the strength of the effect of the CA on T_1 given in $\mathrm{mMol}^{-1}\mathrm{s}^{-1}$.

3.3 Mechanisms and Characteristics of Enhancement

The degree and pattern of enhancement in DCE MRI images reflects many different physiological mechanisms. An inspection of the signal time curves allows for estimation of physiological parameters. However, contrast depends as well on other factors such as native 'pre-contrast' T_1-relaxation time $T_1(0)$ prior to contrast agent arrival, CA dose, imaging sequence parameters, image scaling factors and technical scanner properties.

A measured dynamic signal curve typically consists of four distinct phases: pre-contrast baseline, upslope, maximum enhancement and washout. The upslope depends mainly on the capillary permeability and perfusion. The maximum enhancement is determined by the total CA concentration in the tissue. Wash-out is related to vascular permeability. Healthy tissue shows either slow or no enhancement and a slow wash-out. In malignant lesions, typically a steep upslope and a fast wash-out phase is measured.

A typical tumor signal time curve and its four phases can be seen in figure 3.2. Here, the wash-out phase is defined to start after peak signal when the signal has attenuated to 99% of the maximum value.

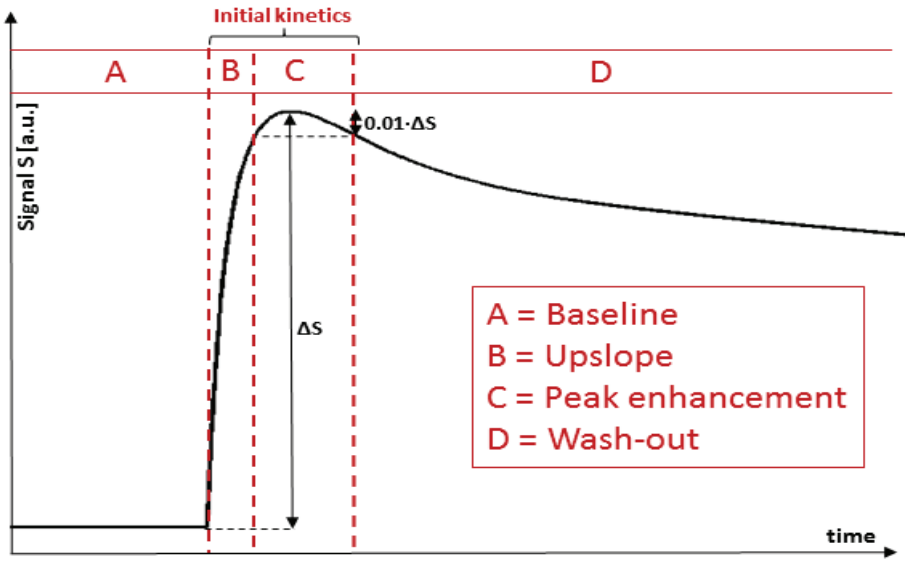

Figure 3.2: A typical malignant tumor signal time curve can be divided into four phases: A = Baseline, B = Initial upslope, C = Peak enhancement, D = Wash-out.

3.4 Analysis of DCE MRI Data: Qualitative and Quantitative Methods

A wide range of techniques for the analysis and post-processing of DCE MRI data exists. They vary from simple visual methods over semi-quantitative techniques to complex quantification using pharmacokinetic modeling (PK).

The analysis can be done on a region of interest (ROI) or voxel-by-voxel. Many methods are based on the former, in which an ROI is chosen that encompasses the lesion. Inside this ROI the mean intensity values are monitored. Advantages are the relatively easy usage and a high SNR due to averaging over multiple voxels. However, there is no standardized method to locate an ROI, making it an operator-dependent process. Furthermore, an ROI analysis is incapable of detecting the heterogeneity within a tumor.

On a voxel-by-voxel basis, the signal time curve of every image voxel is analyzed, resulting in parametric maps. This way, more information can be obtained than from ROI analysis, especially about the heterogeneity of a lesion. The disadvantages are high demands on the acquisition and analysis techniques. Since no averaging over many voxels is performed, the measured curves suffer from poor SNR. Furthermore, subject motion can have a significant impact. With sub-millimeter spatial resolution, even physiological motion can lead to errors.

In the following sections commonly used qualitative and quantitative analysis methods are introduced.

3.4.1 Qualitative Analysis

The simplest approach of DCE MRI data analysis is the visual inspection of the signal time curves within an ROI. Each curve is classified as type 1-5 [Jackson2005]. The different curve shapes and their characteristics are displayed in figure 3.3. In general, the higher the number, the more aggressive the lesion. Despite its simplicity this non-quantitative method shows good diagnostic performance in differentiating malignant from benign lesions and is the current clinical standard.

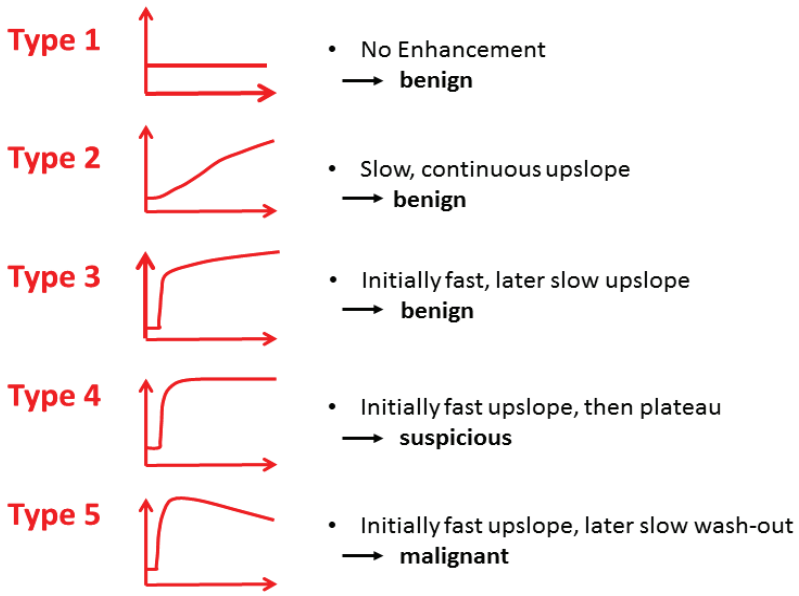

Figure 3.3: Curve types 1-5 for lesion characterization in DCE MRI (adapted from [Jackson2005]).

3.4.2 Semi-Quantitative Analysis

A semi-quantitative enhancement curve analysis is often used for diagnosis and lesion classification. Some examples semi-quantitative parameters are:

- Area under signal curve (AUC) within a certain time interval,
- area under gadolinium concentration curve (AUGC) within a certain time interval,
- relative enhancement at various time points,
- onset time,
- peak signal intensity,

- peak concentration,
- initial slope.

Even if this analysis is only semi-quantitative, it has proven to be valuable for the distinction between malignant and benign lesions and the grading and classification of tumors. Physiological differences between the vasculature of benign and malignant tumors can be large, therefore even relatively crude methods are sufficient to distinguish between them. Furthermore, semi-quantitative parameters are relatively simple to acquire and straightforward to calculate, and some of them have been shown to be very robust [Jackson2005].

However, semi-quantitative parameters depend on the acquisition protocol and vary with different sequence parameters. From scanner to scanner, tuning and scaling factors can vary. Even acquisitions from the same scanner can produce different results due to varying scaling factors. This makes the comparison of results difficult especially in multi-center studies. Also the physiological interpretation is problematic since many physiological processes contribute to the resulting parameters in an undefined manner.

3.4.3 Quantitative Analysis Using Pharmacokinetic Modeling

To overcome the drawbacks of semi-quantitative methods, a more quantitative analysis is beneficial, which better reflects the underlying physiology and is independent of the used MR scanner.

In MRI, pharmacokinetic (PK) models mathematically describe the distribution and elimination of contrast agent within the body. PK models can be fitted to the measured concentration time curves, providing quantitative parameters.

The CA distribution is governed by many different physiological processes, for example regional blood flow, blood volume, vessel shape and size, endothelial permeability, endothelial surface area and the volume fraction which is accessible to the contrast agent. An optimal analysis would allow for an independent measurement of all of these parameters. Ideally, models should include all of the parameters listed above and describe their effect on the flux of CA. This leads to very complex models with many unknown parameters which makes the fitting process difficult and instable. Therefore, a range of simplified models exist in which parameters are combined to reduce the number of unknown variables. These simplifications improve fitting but introduce an uncertainty to the results which makes them difficult to interpret. In the following, different PK models are described.

Conversion from MRI Signal to Tracer Concentration

Pharmacokinetic models describe the concentration $C(t)$ of contrast agent instead of the MRI signal $S(t)$. Therefore, the measured signal needs to be converted to CA concentration. For this conversion, T_1-values $T_1(t)$ are monitored over time. This can be achieved for example by using multiple flip angles [Wang1987], which is described in section 5.2. The relationship between $T_1(t)$ and $C(t)$ is given by equation 3.1.

Modeling of DCE MRI Data

In the following section, theoretical considerations of PK modeling are presented and an overview of existing models is given. Special emphasis is put on the Tofts model which is used in this thesis.

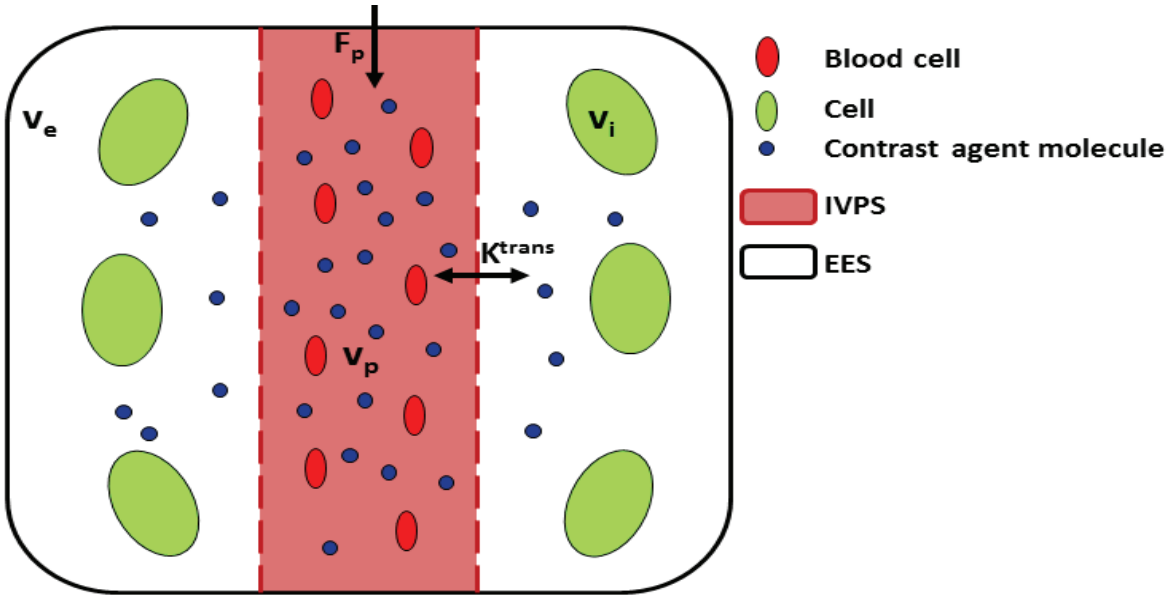

Figure 3.4: Schematic illustration of a simplified capillary-tissue system (adapted from [Koh2011]).

Simplified Capillary-Tissue System

To describe the complex exchange processes of the contrast agent within the tissue, simplifications have to be made. A simplified capillary-tissue system can be seen in figure 3.4 [Koh2011]. Such a system can be a voxel or a cluster of voxels of volume V_{tiss}. The capillary-tissue system is compartmentalized into distribution spaces of the tracer. The passage of the CA was described earlier in section 1.4. The compartment describing the whole vasculature is called the *intravascular space* (IVS) and the compartment made up only of the blood plasma is called *intravascular plasma space*($IVPS$). Inside the tissue, CA can only access the *extravascular, extracellular space* (EES). Due to its size CA cannot enter the *intracellular space* (ICS). The absolute volumes of the $IVPS$ V_p, EES V_e and ICS V_i within the tissue system can be expressed as relative fractions of V_{tiss}, where v_p is the fractional blood plasma volume, v_e is the fractional extravascular extracellular volume and v_i is the fractional intracellular volume.

The capillary-tissue system is assumed to comprise only of these three compartments such that:

$$v_p + v_e + v_i = 1 \tag{3.2}$$

The fractional whole blood volume of the intravascular space is given by:

$$v_b = \frac{v_p}{(1 - Hct)}, \tag{3.3}$$

where Hct is the hematocrit of blood. The blood plasma flow F_p delivering the system is assumed to be constant. The rate exchange across the capillary wall is given by the transfer constant K^{trans}. Transport across the wall is assumed to be isodirectional and passive.

The tracer concentration of the whole capillary-tissue system is denoted as $C_{tiss}(t)$, the concentration in the EES is given as $C_e(t)$ and the concentration in the plasma as $C_p(t)$. The whole blood concentration $C_b(t)$ is related to the plasma concentration by $C_p(t) = C_b(t)/(1 - Hct)$.

Convolution Function

The relation between $C_{tiss}(t)$ and $C_p(t)$ can be described by the following equation:

$$C_{tiss}(t) = K^{trans} C_p(t) \star R(t) = K^{trans} \int_0^t C_p(t - \tau) R(\tau) d\tau, \tag{3.4}$$

where $\star$ is the convolution operator and $R(t)$ is the *impulse residue function* describing the response of the system to an impulse function of tracer input [Koh2011]. Equation 3.4 is only valid under the assumption that the system is time-invariant, reacting with the same response at all times. Also a linear system has to be assumed in which the net residue function is a superposition of all single residue functions weighted according to their height. When $C_{tiss}(t)$ and $C_p(t)$ are measured, then K^{trans} and $R(t)$ can be determined. This deconvolution can be performed by *model-fitting*. For model fitting, a mathematical function is derived based on a tracer kinetic model. This model is fitted to the sampled tissue concentration curve, providing tissue parameters. In the following, examples of PK models are given.

The Tofts Model

The early works from [Tofts1991], [Brix1991] and [Larsson1989] are combined in the *general kinetic (GK) model* or *Tofts model*. In the Tofts model, two *well-mixed* compartments with a homogeneous tracer concentration throughout the volume are assumed: the vascular and the organ compartment. 'Well-mixed' means that the compartments show instantaneously a homogeneous tracer concentration throughout the volume. The model is based on a rate equation describing the flux of tracer via the capillary wall from one compartment to the other.

The changes in tissue concentration $C_{tiss}(t)$ due to changes in the EES concentration $C_e(t)$ can be expressed as:

$$\frac{dC_{tiss}(t)}{dt} = K^{trans}(C_p(t) - C_e(t)). \tag{3.5}$$

It is assumed that the flux across the capillary wall is proportional to the concentration difference between the EES and the IVS. K^{trans} stands for the volume transfer constant between the IVS and the EES. Dependent on the physiological conditions, K^{trans} can have different meanings [Tofts1999]. In high-permeability situations where $PS >> F_p$, the flux across the capillary wall is *flow-limited* and K^{trans} is equal to the blood plasma flow F_p. In the case of high plasma flow, where $F_p >> PS$, the flux of the tracer is *permeability-limited* and K^{trans} equals the permeability-surface area product PS. For a general *mixed* case where both F_p and PS contribute to flux across the membrane, K^{trans} takes the value EF_p, where E is the *extraction fraction* defined as the fraction of tracer that is extracted from v_p in a single capillary transit with $E = 1 - e^{-\frac{PS}{F_p}}$. In summary:

$$\begin{aligned} K^{trans} &= F_p \text{ (flow-limited)}, \\ K^{trans} &= PS \text{ (permeability-limited)}, \\ K^{trans} &= EF_p \text{ (flow- and permeability-limited)}. \end{aligned} \tag{3.6}$$

In normal tissue the vascular volume makes up about $v_p \approx 5\%$ of the whole tissue volume. Therefore, in the Tofts model the approximation is made that tracer is only present in the EES with $v_p \approx 0$. This leads to:

$$C_{tiss}(t) \approx v_e C_e(t) \tag{3.7}$$

Combining euqation 3.5 and 3.7 yields:

$$\frac{dC_{tiss}(t)}{dt} = K^{trans}(C_p(t) - \frac{C_{tiss}(t)}{v_e}) = K^{trans}C_p(t) - k_{ep}C_{tiss}(t) \tag{3.8}$$

where $k_{ep} = K^{trans}/v_e$ denotes the backflux rate constant.
The differential equation 3.8 can be rewritten in integral form:

$$C_{tiss}(t) = K^{trans}\int_0^t C_p(t)e^{-\frac{K^{trans}(t-t')}{v_e}}dt' = K^{trans}C_p(t) \star e^{-k_{ep}t} \tag{3.9}$$

Comparing equation 3.4 and 3.9 reveals that for the Tofts model the residue function takes the form $R(t) = e^{-k_{ep}t}$. C_p cannot be measured directly with DCE MRI. However, the tracer concentration $C_A(t)$ within a large feeding artery supplying the system, also called arterial input function (AIF), can be sampled. It is assumed that

$$C_p(t) \approx \frac{C_A(t)}{(1 - Hct)} \tag{3.10}$$

is a valid approximation. Substituting $C_p(t)$ in equation 3.9 yields:

$$C_{tiss}(t) = K^{trans}\frac{C_A(t)}{(1 - Hct)} \star e^{-k_{ep}t} \tag{3.11}$$

The Extended Tofts Model

The *extended Tofts model* accounts for the case when v_p is not negligible anymore [Tofts1997]. This is for example true for some tumors where the blood volume strongly increases. In this case the tissue concentration can be written as:

$$C_{tiss}(t) = v_e C_e(t) + v_p C_p(t) \tag{3.12}$$

A derivation analogous to the Tofts model leads to the integral form:

$$C_{tiss}(t) = v_p C_p(t) + K^{trans} C_p(t) \star e^{-k_{ep}t} = v_p \frac{C_A(t)}{(1-Hct)} + K^{trans} \frac{C_A(t)}{(1-Hct)} \star e^{-k_{ep}t} \tag{3.13}$$

The Tofts and Kermode Model

The Tofts model was first applied to DCE MRI data in the context of measuring leakage through the blood brain barrier in a brain tumor [Tofts1991]. Here, the AIF is assumed to be a bi-exponential decay:

$$C_A(t) = D(a_1 e^{-m_1 t} + a_2 e^{-m_2 t}), \tag{3.14}$$

where D is the dose of contrast agent in mMol·kg^{-1}, a_1 and m_1 characterize the exchange between the vasculature and the whole-body EES and a_2 and m_2 describe the elimination of contrast agent by the kidneys. Weinmann *et al* [Weinmann1984] measured averaged values of a_1, m_1, a_2 and m_2 in healthy volunteers [Tofts1991] to be:

$$\begin{aligned} a_1 &= 3.99 \frac{kg}{l}, \\ m_1 &= 0.144 min^{-1}, \\ a_2 &= 4.78 \frac{kg}{l}, \\ m_2 &= 0.0111 min^{-1}. \end{aligned} \tag{3.15}$$

Given $C_A(t)$, the solution to equation 3.8 within the lesion can be derived [Tofts1991] to be:

$$C_{tiss}(t) = D[b_1 e^{-m_1 t} + b_2 e^{-m_2 t} + b_3 e^{-m_3 t}], \tag{3.16}$$

with

$$\begin{aligned} m_3 &= \frac{K^{trans}}{v_e}, \\ b_1 &= \frac{K^{trans} a_1}{(m_3 - m_1)}, \\ b_2 &= \frac{K^{trans} a_2}{(m_3 - m_2)}, \\ b_3 &= -(b_1 + b_2). \end{aligned} \tag{3.17}$$

Other Models

Besides compartmental models such as the Tofts model *distributed parameter models*, *tracer dilution models* and *reference region models* exist.

Distributed Parameter (DP) models account for the fact that v_e and v_p are in reality not well-mixed. In their *tissue homogeneity (TH) model* Johnson and Wilson [Johnson1966] assume that C_p is not just a function of time but as well a function of the distance along the axial length of the capillary $C_p(x,t)$. $C_e(t)$ is still assumed to be well-mixed. The resulting differential equations are difficult to solve.

St. Lawrence and Lee [Lawrence1998] simplified the TH model in their *adiabatic approximation tissue homogeneity (AATH) model* with the assumption that $C_{tiss}(t)$ changes slowly in comparison to $C_p(t)$. With this adiabatic approximation an analytical solution can be found when the mean transit time is used as additional fitting parameter. An advantage of the St. Lawrence and Lee model over the Tofts model is that it allows for simultaneous estimation of blood blow F_p and permeability surface area product PS.

The quality of a PK model fit depends on the accuracy of the measured AIF. Since AIF measurement is difficult, *reference region (RR) models* have been proposed. Instead of directly sampling $C_A(t)$, model parameters are derived by reference to literature values from other normal tissues. This can be done using a single [Kovar1998] or multiple reference tissues [Yang2004].

In contrary to the Tofts model, *tracer dilution models* do not assume well-mixed compartments, neither an equilibrium between tissue and blood concentrations. Meier and Zierler *et al* [Meier1954] and Griebel *et al* [Griebel2004] describe a distribution of transit times of contrast agent through a capillary network, yielding the blood flow, the blood volume and the mean transit time.

Additionally, models such a the *Shutter-speed model* [Li2005] exist, which take water exchange between the intracellular and extracellular space into account.

Arterial Input Function (AIF)

All described models, with exception of RR models, require the blood plasma tracer concentration $C_p(t)$. However, it is not possible to measure $C_p(t)$ of capillaries with DCE MRI. Instead, the AIF $C_A(t)$ of a large supplying vessel is sampled. Since whole blood concentration is measured, to obtain plasma concentration, the AIF has to be divided by $(1 - Hct)$.

Even if AIF measurements are feasible with a suitable imaging protocol, it is still challenging to perform an accurate and reproducible AIF measurement. High temporal resolution is needed and a feeding artery has to be located in FOV. Low SNR and partial volume effects for small arteries cause additional errors, which propagate into modeling.

One alternative is to administer a low-dose prebolus for AIF measurement [Kershaw2011]. Population-averaged solutions as shown by Weinmann *et al* [Tofts1991] or Walker-Samuel *et al* [Walker-Samuel2007] are convenient, but only an approximation, since a high inter-patient variability can occur. Also for the same patient the AIF can

vary for example as a function of injection timing and dose, the heart output rate, regional variance and the kidney function [Jackson2005].

To overcome the difficulties in AIF measurements, reference region (RR) methods have been proposed. Without direct sampling of the AIF, PK parameters or the AIF itself can be estimated by normalization against a reference tissue, for example muscle with known literature values for PK parameters. This can be done using one or more reference regions. RR models have been shown to provide robust results when compared to AIF sampling [Yankeelov2007].

Sources of Error in Quantitative DCE MRI

Many sources of error corrupt the quantification of DCE MRI data. Uncertainties arise from the chosen model, the measurement of the tissue signal and the AIF, conversion from signal to concentration and general image artifacts.

For an accurate model fit, the temporal resolution and SNR have to be sufficiently high. In MRI, high temporal resolution is contradictory to high spatial resolution. The resulting limitations on the temporal resolution can result in fitting inaccuracies.

The conversion from signal to concentration is done via T_1 measurements. Errors in T_1 measurement can occur for example due to inaccurate flip angles when $T_1(0)$ is measured using a variable flip angle approach [Sung2013].

Furthermore, imaging artifacts can corrupt the acquired curves of the tissue signal and the AIF. For example motion artifacts can have a large impact, especially when PK modeling is done on a voxel-by-voxel basis.

As described in the previous section, measuring the plasma concentration $C_p(t)$ is potentially a large source of error in PK modeling.

To convert the measured CA concentration in whole blood to plasma concentration, the hematocrit Hct is required: $C_p(t) = C_A(t)/(1-Hct)$. An averaged value of $Hct \approx 0.4$ is normally used [Jackson2005]. However, Hct may vary in patients with advanced cancer. Also Hct in large vessels is different than in capillaries, where the packing of red blood cells is less dense.

Furthermore, the AIF is sampled in a large vessel, but the modeling takes place is the capillaries. Bolus dispersion may change the curve shape significantly when reaching the microvasculature.

Finally, an important factor leading to a potentially false interpretation of PK parameters is the choice of the model. Models always describe a simplification of the true physiology. The more approximations are made, the greater the degree of uncertainties in the interpretation becomes. These simplifications can lead to systematic errors in certain parameters since other parameters, which are omitted, are compensated for. However, including more parameters to better describe the complex processes leads to a more unstable fitting routine. A trade-off between the interpretation and the parameter stability has to be found.

3.5 Spatial and Temporal Resolution in DCE MRI: A Review

In DCE MRI both, high temporal and high spatial resolution are required. High temporal resolution is needed to monitor dynamic changes, high spatial resolution allows evaluation of the morphology and the heterogeneity of lesions. Many publications have addressed the issue how spatial and temporal resolution affect lesion quantification and diagnosis. Other works investigated the temporal requirements and accuracy of quantitative DCE MRI. Also many studies were concerned with the acceleration of imaging whilst still maintaining sufficient spatial information. In the following section these studies are summarized.

The Role of Spatial and Temporal Resolution for Diagnosis

In MRI high temporal and high spatial resolution are opposing aims. Many studies investigated which trade-off between the two is beneficial for diagnosis. To role of spatial resolution was shown to be important for example by the following studies. In 2001, Furman-Haran *et al* [Furman-Haran2001] purposely degraded the spatial resolution of images and evaluated them with a kinetic analysis at three different time points. They found that low spatial resolution degrades the appearance of malignant time curves. They concluded that it is essential to record the dynamic behavior at high spatial resolution for robust diagnosis. In 2005, Kuhl *et al* [Kuhl2005] investigated the trade-off between temporal and spatial resolution in breast DCE MRI by acquiring data from patients twice with a relatively high temporal/relatively low spatial resolution(256x256 matrix size, 69 seconds per acquisition) and a low temporal/high spatial resolution (400x512 matrix size, 116 seconds per acquisition). They found that an increased spatial resolution significantly improves diagnostic accuracy. The loss in kinetic information was shown to be diagnostically irrelevant due to a broad overlap between the classification of benign and malignant lesions. The results from Goto *et al* in 2007 [Goto2007] are in good agreement with [Kuhl2005]. The diagnostic performance of breast lesions with regard to enhancement patterns and morphological criteria for two different temporal/spatial resolutions was compared. The analysis of morphological features showed a significantly higher diagnostic performance. Goto *et al* suggested to omit dynamic information completely.

Other studies found that high temporal resolution has a large diagnostic relevance. Schabel *et al* [Schabel2010] performed pharmacokinetic modeling using the extended Tofts model on patients with biopsy-proven benign and malignant lesions. Data were acquired at high temporal resolution of $9.2-19.7$s. It was shown that classification based on K^{trans} and k_{ep} provides a significant accuracy for the identification of malignancies. In 2002 Wasser *et al* [Wasser2002] employed a high temporal resolution sequence to evaluate the response of breast cancer to neoadjuvant chemotherapy. Both, the tumor size and parameters of a two-compartment model were evaluated. A decrease in PK parameters was found to precede tumor size changes. It was concluded that high temporal

Reference	Δt	Evaluation/PK model	Accuracy
[Henderson1998]	AIF: $\leq$ 1s, Tissue: $\leq$ 16s	Tofts	error<10%
[Kershaw2006]	2.3s	AATH	errors: EF:15%, F:19%,PS:28%, v_e:35%,BV:36%
[Kershaw2010]	1.5s/6s	AATH	error<5%/ error<10%
[Planey2009]	<36.5s	RR	error<20%
[El-Khouli2009]	$\leq$ 45s	semi-quantit. benign/malignant discrimination	
[Heisen2010]	$15s - 85$s	Tofts	K^{trans}: -(4-25)% v_e: 1-10% error

Table 3.1: Summary of studies investigating the effects of temporal resolution and noise on the accuracy of PK parameters for different models.

resolution imaging provides a valuable tool to assess therapeutic effects of neoadjuvant chemotherapy.

It can be concluded that both, high spatial and temporal resolution have a large relevance for diagnostics. When high temporal resolution imaging is employed, it has to be kept in mind that a minimal temporal resolution is required. For example in [Kuhl2005], high temporal resolution was assumed to be 69s, which is not sufficient. Also alterations of the kinetic curves at low spatial resolutions due to spatial blurring have to be taken into account. It is the topic of current research to find out if one of the approaches is preferable to the other, but it seems that a combined solution may yield the best diagnostic results.

Temporal Requirements and Parameter Accuracy

Many studies investigated the temporal requirements needed for a certain evaluation method and the effects on the accuracy of the resulting parameters. The results of some of these studies are summarized in table 3.1.

In 1998 Henderson *et al* [Henderson1998] investigated the temporal sampling requirements for tracer kinetics modeling using the Tofts model of breast disease. They found that for the resulting error in kinetic parameters to be less than 10%, the AIF should be sampled at least every second and the signal time curve in the tissue should be sampled every 16s or less.

Kershaw *et al* [Kershaw2006] estimated the precision of fitting parameters extracted from fitting the AATH model to prostate and muscle tissue data. Using a temporal resolution of 2.3s they estimated precisions for parameters measured in the prostate gland to be 14% for extraction fraction, 19% for blood flow, 28% for permeability area product, 35% for the volume of the EES and 36% for blood volume. They additionally

found that the bolus arrival time of contrast agent in the tissue of interest is an important parameter contributing to fitting accuracy.

The important role of the bolus arrival time and its potentially large influence on model fitting accuracy has as well been shown by Laue *et al* [Laue2010].

In a study in 2010 Kershaw *et al* [Kershaw2010] addressed the question of temporal resolution and SNR requirements for accurate DCE MRI analysis using the AATH model. In a simulation study they examined the effects of temporal resolution, noise level and error in the measured AIF on the accuracy of AATH model parameters. A temporal resolution of 1.5s and a high SNR of noise standard deviation of 0.05 were found to ensure an error below 5% for all model parameters. The temporal resolution can be relaxed to 6s if a bias larger than 10% for the transit time is permitted. An 10% error in the measured height of the AIF first pass peak results in an error of at most 10% in each parameter.

The temporal requirements for the application of the reference region (RR) model to breast DCE MRI data were investigated by Planey *et al* [Planey2009]. They could show that the RR model yields less than 20% error in the extracted parameters for a temporal resolution $\leq$ 35.6s.

In 2008 Cheng *et al* [Cheng2008] investigated the influence of an inaccurately measured AIF on Tofts model parameters. They found that an error in the AIF bolus amplitude results in an inversely proportional error in K^{trans} and v_p, whilst v_e remains a robust fitting parameter.

El-Khouli *et al* [El-Khouli2009] studied the requirements of temporal resolution for characterizing breast lesions as benign or malignant based on the curve shape and the semi-quantitative parameters wash-in- and wash-out slope and washout percentage is tested. They found that a temporal resolution of at least 45s is required to achieve a good classification between benign and malignant values.

In 2010 Heisen *et al* [Heisen2010] investigated the influence of temporal resolution on PK parameter estimation of implanted prostate tumors on rat hind limb using the Tofts model. Images were subsequently downsampled to temporal resolutions in the range of 15-85s. Heisen *at al* demonstrated that, as temporal resolution decreases, K^{trans} is progressively underestimated (4%-25%) and v_e is progressively overestimated (1%-10%). This is in good agreement with [Buckley2002], where a systematic overestimation of K^{trans} has been shown to occur with fitting of the extended Tofts model whilst v_p is potentially underestimated.

Fluckinger *et al* [Fluckinger2012] compared the performance of the Tofts model and a 3 time point (3TP) analysis as a function of the temporal resolution. The error of the 3TP analysis remained constant with temporal resolution, whereas the Tofts model parameter errors linearly increased with decreasing temporal resolution. At a temporal resolution $\leq$ 20s the Tofts model outperformed the 3TP method, otherwise the 3TP analysis was more accurate.

In 2003 Dale *et al* examined the sensitivity of quantitative perfusion maps to sources of error in the images. They found that artifacts in the baseline images and flip-angle inaccuracies have the strongest effect on K^{trans} estimation accuracy.

In summary, many different studies have been conducted, which are difficult to compare since either the organ of interest (prostate, breast, muscle tissue), the image SNR (for example varying between Kershaw[2006] and Kershaw[2010]), the fitted model (Tofts, RR, AATH or analysis of semiquantitative parameters), the species (rats in [Heisen2010]) varied from study to study. This shows how sensitive the results are to the underlying conditions and analysis methods. However, from all of these studies an order of magnitude can be extracted, that for model fitting the temporal resolution should not be larger that 20-30 s for acceptable fitting results, but optimally should be smaller than 10 s. In most studies, a required temporal resolution for a maximal error of a certain parameter was investigated. However, it is still not clear how large errors are allowed to be for a certain analysis method to still provide accurate diagnostic results, whis is a topic of current research.

Imaging Acceleration Techniques

Conventional acquisition schemes are limited in achieving simultaneously high temporal and high spatial resolution. A number of approaches have been proposed to overcome this trade-off and accelerate imaging whilst maintaining spatial information. In most of these methods k-space data are omitted during acquisition. The missing data are estimated during post-processing by exploiting spatiotemporal correlations between the acquired and the missing data. Since there is usually a high redundancy in dynamic series, imaging can be highly accelerated by acquiring only a fraction of the data and estimating the rest. To better describe dynamic series of raw data the concept of the higher dimensional k-t-space is used. The k-t sampling pattern describes the order of data sampling at different time frames. Image acceleration techniques can be divided into methods with heuristically chosen k-t sampling patterns and methods with k-t sampling strategies based on prior knowledge or assumptions about the object [Tsao2010].

In the following, examples of studies employing heuristically chosen k-t-sampling patterns are presented, which are visualized in figure 3.5. In 1993, Jones *et al* [Jones1993] and van Vaals *et al* [Vaals1993] both suggested a *keyhole* k-space substitution method in which first a high spatial resolution reference image is acquired. During the dynamic acquisition only low frequency data in the phase-encoding direction around the center of k-space are acquired. During image reconstruction the missing high frequency data are substituted by the ones from the reference scan (figure 3.5 a)). [Plewes1995], [Spraggins1994], [Bishop1997] and [Oesterle2000] investigated the errors introduced by the keyhole technique. They all found that image degradation for keyhole is only expected for small objects. Here, the basic assumption of keyhole that all relevant dynamic information is located in the center, is not true. Therefore the minimum keyhole size used should be restricted by the inverse approximate minimum size of the expected lesion.

Many refined variations of the keyhole view-sharing technique have been developed. In 1995, Parrish *et al* [Parrish1995] proposed the CURE (continuous update with random encoding) technique. A random phase-encoding sampling strategy is employed to allow for a smoother update of k-space lines than for keyhole (figure 3.5 b)). Korosec *et al* [Korosec1996] developed a method referred to as TRICKS (time-resolved imaging

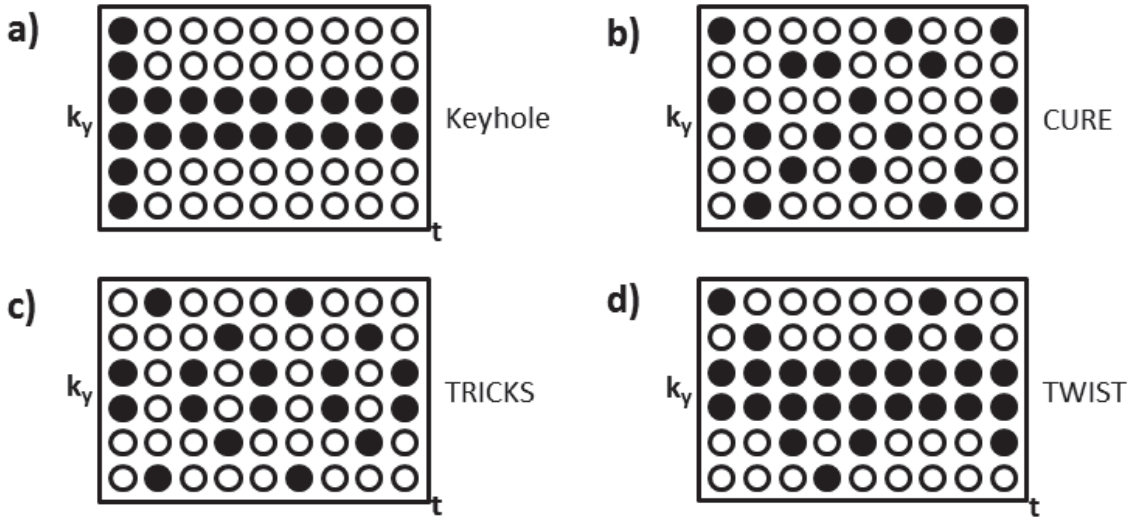

Figure 3.5: Schematic illustration of different view-sharing methods. For simplification only the k_y-axis is plotted. Data along the k_x-axis are supposed to be fully sampled. The black dots indicate data sampling (adapted from [Tsao2010]).

of contrast kinetics). k-space is divided into sections, each acquired at a different time frame. The k-space center section is sampled with the highest frequency. The missing k-space sections in each frame are filled by linear interpolation of the neighboring time frames (figure 3.5 c)). Time-resolved imaging with stochastic trajectories (TWIST) [Vogt2007] divides k-space into two sections A and B. Section A encompasses a circle around k-space center containing the low frequencies, whilst B consists of the high frequency regions outside the circle. Section A is completely sampled with each time frame, whilst B is undersampled in a temporally varying spiral fashion. The TWIST sequence has been optimized by Song *et al* [Song2009] for the application to MR renography. Furthermore, it has been succesfully applied in clinical settings with a temporal resolution < 20s for 3D breast coverage for example by [Tudorica2012] and [Herrmann2011].

All of the presented view-sharing methods have in common that some k-space data are omitted. The key idea is to sample the outer parts of k-space at least once but focus on the central parts of k-space since most contrast information is concentrated here. The missing data are recovered by interpolation from the acquired data, assuming that nearby data are similar. The artifacts arising from the interpolation depend on the size and frequency of the updated portions of k-space. The required frequencies are dependent on the size of the lesion which is not known *a priori*.

Other image acceleration methods incorporate prior knowledge or assumptions about the object into the choice of the k-t-sampling scheme. For example Hu *et al* [Hu1994] proposed in 1994 a FOV reduction. The assumption is made that signal intensity changes are localized to a small FOV during the dynamic scan. First a reference image of the whole FOV is acquired. Then dynamic data with a reduced FOV are acquired which

are combined with the reference image to yield difference images. To be able to apply this method, prior knowledge about the location of signal changes has to be given. In other methods such as UNFOLD [Madore1999], k-t-BLAST [Tsao2003] or k-t-SENSE [Tsao2003] sampling patterns are as well chosen based on prior knowledge or assumptions about the object. The basic idea is to apply the Fourier transform to the k-t-space to obtain the point spread function of the k-t-sampling pattern in the Fourier conjugate x-f-space. With prior knowledge it is possible to control the x-f-point spread function by adjusting the sampling pattern such that the signal contamination in the k-t-space is minimized [Tsao2010].

Parallel imaging methods such as SENSE [Pruessmann1999] and GRAPPA [Griswold2002] exploit the coil sensitivities to reduce undersampling artifacts and allow for acceleration of imaging. SENSE has been successfully applied in breast imaging [Friedmann2005].

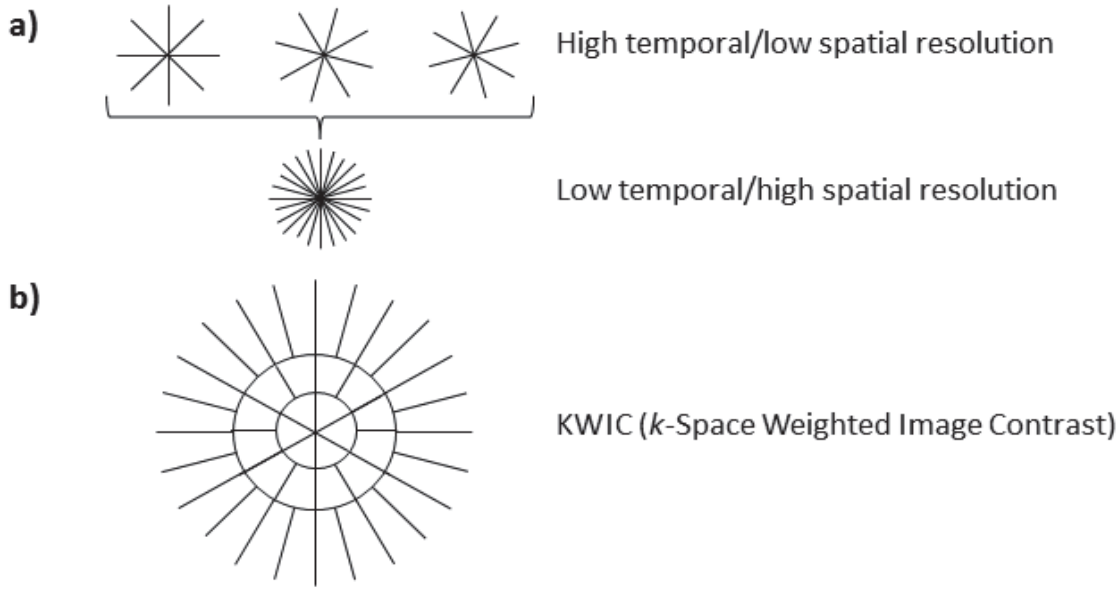

Figure 3.6: Schematic illustration of radial sampling methods in DCE MRI. a) Subapertures providing a high temporal resolution can be combined to a high spatial resolution image. b) With the KWIC method radial profiles are filtered to manipulate image contrast. (adapted from [Song2001] and [Song2004])

Radial Acceleration Techniques

Another approach which has been pursued is radial as opposed to Cartesian k-space sampling. In 2001, Song *et al* [Song2001] showed that by sampling k-space in a 2D radial fashion, image series of high temporal and high spatial resolution can be reconstructed retrospectively from the same dataset. Radial projections are acquired in an interleaved

fashion of subapertures such that single subapertures can be used to reconstruct low spatial/high temporal resolution images. By combining multiple subapertures, high spatial resolution images can be generated (figure 3.6 a)). The method was applied to breast DCE MRI data providing high temporal resolution kinetics and high spatially resolved architectural features of an enhancing lesion. In 2003, Song *et al* [Song2004] extended this method by applying a k-space weighted image contrast (KWIC) technique which enables the manipulation of image contrast using selective filtering (figure 3.6 b)). 3D TRICKS and projection reconstruction techniques were combined by Ramsey *et al* in 2006 [Ramsey2006] in a method called PR-TRICKS. This three-dimensional technique employs TRICKS in the k_z direction and a radial trajectory in the k_x-k_y-plane.
A disadvantage of radial trajectories with a uniform distribution of profiles as in [Song2001] is that images can be reconstructed only from a certain fixed number of profiles. Winkelmann *et al* [Winkelmann2007] suggested to acquire profiles at an azimuthal profile spacing of 111.256°. This *golden angle* is the optimal choice when an arbitrary number of profiles are combined, because the spokes are always arranged in a relatively uniform fashion. This method allows for flexible image reconstruction at arbitrary time points from one raw data set. Chan *et al* [Chan2009] extended the 2D golden angle method to 3D golden angle radial sampling by deriving multidimensional golden means.

Undersampled radial images reduce scan time whilst preserving spatial resolution. However, if the Nyquist criterion is not met, streaking artifacts corrupt image quality. To allow for a higher degree of undersampling Dougherty *et al* [Dougherty2007] combined a radial sampling scheme with non-Cartesian SENSE, additionally exploiting coil information. To remove streaking artifacts in undersampled radial images Martel *et al* [Martel2008] successfully applied independent component analysis. Furthermore, constrained reconstruction techniques have been successfully employed, using *a priori* knowledge or assumptions about the data to yield high quality images from undersampled dynamic k-space data. With constrained reconstruction methods such as [Fessler2004] imaging can be accelerated, however, at the price of high computational time during reconstruction.

In summary, radial techniques allow for flexible reconstruction of high spatial and high temporal resolution from the same data set. However, temporal blurring of rapid signal changes can corrupt image quality, since the center of k-space is traversed with each projection. Furthermore, the reconstruction process is not straightforward and advanced reconstruction techniques such as constrained reconstruction can be very time-consuming.

Combination of High Temporal and High Spatial Resolution Images

Instead of acquiring images at a constant temporal resolution during the whole dynamic imaging time, methods combining high and low spatial/temporal resolution within a single DCE MRI investigation have been proposed, as illustrated in figure 3.7. In 2004 Vomweg *et al* [Vomweg2004] combined high spatial and high temporal resolution scans during the time course of a single contrast agent administration. Observers investigated

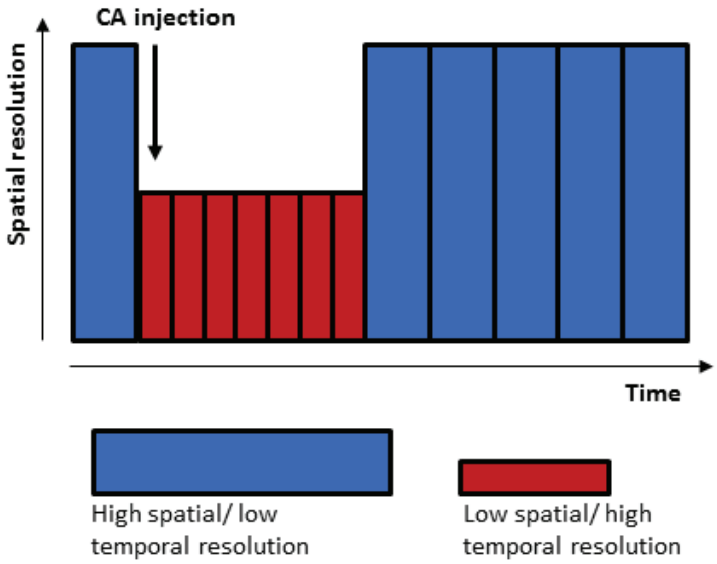

Figure 3.7: Schematic illustration of an adaptive imaging approach with both, high temporal/low spatial and lows spatial/high temporal acquisitions (adapted from [Jackson2005])

the data and found diagnostic improvement. Mann *et al* [Mann2006] published in 2006 a combined approach using the TWIST sequence during the first 2 minutes after contrast agent injection with a temporal resolution of about 7s. The TWIST sequence was preceded and followed by high spatial resolution acquisitions lasting 107s each. The evaluation of patient data indicated that the TWIST data are sufficient for correct lesion interpretation. In 2008 Veltman *et al* [Veltman2008] derived pharmacokinetic parameters from fast dynamic imaging at a temporal resolution of about 4s during the initial enhancement for a duration of approximately 90s. The low temporal resolution was achieved by acquiring only a few slices. Low spatial resolution images are followed by high spatial resolution scans at a temporal resolution of 86s. The combined evaluation of fast and slow dynamic series could be shown to significantly improve the diagnostic performance. Pinker *et al* [Pinker2009] employed in 2009 as well a combined protocol of high temporal and high spatial resolution. A high spatial resolution image is acquired before contrast agent administration. After contrast agent injection images at a temporal resolution of 12 s are acquired, followed by a high resolution image of 2 min duration, then again a high temporal resolution series with a temporal resolution of 13s. Finally, another high resolution image is acquired. That way both, the uptake and wash-out of contrast agent could be monitored with high temporal resolution. Combining morphological and dynamic information yielded accurate detection and assessment of breast lesions. Eventually, in 2010 Jansen *et al* [Jansen2010] sampled the early contrast kinetics with a temporal resolution of 7 s acquiring only a few slices for the first 90 s post-injection. It was shown to yield high diagnostic accuracy in distinguishing pathologically proved

breast tumors.

These studies show that the usage of combined resolutions is a very promising method for tumor diagnosis. It combines the information provided from high and low temporal resolution imaging within one DCE MRI investigation.

All of the presented sequences change their temporal resolutions at fixed predefined time points. However, contrast agent dynamics are patient-specific, depending on physiological conditions and the bolus timing. Therefore, rigid resolution changes may not be optimally tailored to each patient.

4 Optimal Sampling Design in Quantitative DCE MRI

4.1 Introduction and Motivation

All currently used adaptive sequences, as described in the introduction and in chapter 3, have in common that they acquire data rapidly during the fast initial kinetics. During the slower wash-out, the sampling scheme switches to higher spatial resolution images to allow for morphological analysis when there is still a high concentration of CA present in the lesion. However, to date there are no studies providing a proof that this approach improves quantitative evaluation of DCE MRI data.

In this work, the method of optimal sampling design is applied to the Tofts model to obtain optimal sampling schemes (OSS) with respect to fitting accuracy. The OSS is calculated for single Tofts model parameter sets and a distribution of PK parameters. The performance of the OSS with respect to fitting accuracy is compared to equidistant sampling schemes (EDS).

This work is based on a publication by Xie *et al* [Xie2008], in which an optimal sampling scheme for Arterial Spin Labeling (ASL) data is derived. Whereas ASL employs labeled blood as endogenous tracer, with which $S(t)$ can be repeatedly sampled at any time point, contrast agent is administered only once in DCE MRI. If a certain time point is missed, it cannot be recovered in a later measurement. Therefore, the methods of [Xie2008] have to be adapted for the application to DCE MRI.

4.2 Optimal Sampling Design Theory

A nonlinear function y is considered with independent variables in time t and a set of parameters $\vec{p} = (p_1, p_2, ..., p_M)$:

$$y(t) = f(t, \vec{p}). \tag{4.1}$$

An experiment is performed and equation 4.1 is fitted to the measured data points y_i with $i = 1, ..., N$. This can be performed using nonlinear regression methods by minimizing the goodness-of-fit parameter χ^2:

$$\chi^2(\vec{p}, t_i) = \sum_{i=1}^{N} (\frac{y_i - f(t_i; \vec{p})}{\sigma_i})^2, \tag{4.2}$$

where t_i is the measurement time and σ_i is the noise standard deviation of the i^{th} data point, respectively.

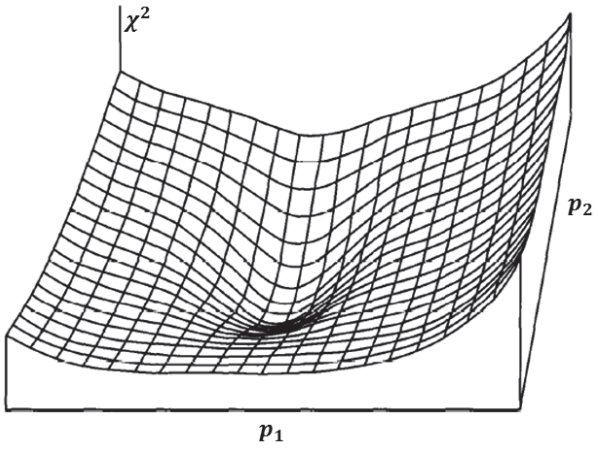

Figure 4.1: Example χ^2-function of two parameters p_1 and p_2. The parameters at the minimum yield the best fit ([Bevington2002)].

The χ^2-function describes a continuous hypersurface in an M-dimensional space. An example of a χ^2-function of two parameters p_1 and p_2 is shown in figure 4.1.
Optimal fitting results can be obtained from the parameters at the minimum of χ^2. This can be achieved by simultaneously setting the partial derivatives of χ^2 with respect to each parameter p_j to zero:

$$\frac{\partial\chi^2(\vec{p})}{\partial p_j} = -2\sum_{i=1}^{N}\frac{y_i - f(t_i;\vec{p})}{\sigma_i^2}\frac{\partial f(t_i;\vec{p})}{\partial p_j} = -2\sum_{i=1}^{N}\frac{y_i - f(t_i;\vec{p})}{\sigma_i^2}\cdot\zeta_{p_j} = 0, \tag{4.3}$$

with $j = 1, ..., M$. The sensitivity functions are defined as $\zeta_{p_j} := \frac{\partial f(t_i;\vec{p})}{\partial p_j}$. They characterize how sensitive χ^2 is to changes in the parameter p_j at a time point t_i. The higher the absolute value of $\zeta_{p_j}(t_i)$ is, the more relevant sampling at t_i becomes for accurate fitting.

For a nonlinear function there is no analytical solution to equation 4.3. Instead, the optimal solution to the problem can be found by using optimized search algorithms such as the Levenberg-Marquardt algorithm [Levenberg1944], [Marquardt1963]. The second order partial derivatives, describing the curvature of χ^2, are given by:

$$\frac{\partial^2\chi^2(\vec{p})}{\partial p_j\partial p_k} = 2\sum_{i=1}^{N}\frac{1}{\sigma_i^2}[\frac{\partial f(t_i,\vec{p})}{\partial p_j}\frac{\partial f(t_i,\vec{p})}{\partial p_k} - [y_i - f(t_i;\vec{p})]\frac{\partial^2 f(t_i;\vec{p})}{\partial p_j\partial p_k}]. \tag{4.4}$$

Close to the minimum of χ^2, the second order terms can be neglected due to $y_i - f(t_i;\vec{p}) \approx 0$, resulting in:

$$\frac{\partial^2\chi^2(\vec{p})}{\partial p_j\partial p_k} = 2\sum_{i=1}^{N}\frac{1}{\sigma_i^2}[\frac{\partial f(t_i,\vec{p})}{\partial p_j}\frac{\partial f(t_i,\vec{p})}{\partial p_k}] =: H_{jk}. \tag{4.5}$$

This matrix $\vec{H}$ of the second partial derivatives is called *Hessian* or *Fisher information matrix*. The inverse of the Hessian matrix $\vec{C} = \vec{H}^{-1}$ is called *covariance matrix*. When it is assumed that the correlation between the fit parameters is negligible, the off-diagonal elements of $\vec{H}$ can be ignored.

The variance $\sigma^2_{p_j}$ of parameter p_j can be obtained from the diagonal elements of $\vec{H}$ as follows [Bevington2002]:

$$\sigma^2_{p_j} = 2(\frac{\partial \chi^2}{\partial p_j^2})^{-1}. \tag{4.6}$$

χ^2 is a function of $\vec{p}$ and the sampling times $\{t_i\}$. In optimal sampling design it is the aim to distribute the sampling times $\{t_i\}$ such that the parameter uncertainties σ_{p_j} are minimized. This can be achieved either by minimizing the determinant $det(\vec{C})$ or maximizing $det(\vec{H})$ between all $\{t_i\}$. This optimization criterion, employing the determinant, is called D-optimality criterion. To find an optimal sampling scheme $\Omega = \{t'_1, ...t'_N\}$ according to the D-optimality criterion, the following inverse cost function Ψ is maximized:

$$\Psi(S) = det(\vec{H}), \tag{4.7}$$

where $S = \{t_1, ..., t_N\}$ is the sampling schedule. Ω is found when

$$\Psi(\Omega) = max_S\{\Psi(S)\}. \tag{4.8}$$

The OSS is calculated for a fixed parameter set $\vec{p}$ and varies from parameter set to parameter set. Therefore, the underlying parameter set needs to be known *a priori* in order to be able to calculate the OSS.

4.3 Methods

In the following, the methods of this chapter used to find optimal sampling schemes are described. All of the following calculations are implemented in Matlab 2012b (The MathWorks, Inc., Natick, Massachusetts, United States).

4.3.1 Model

An optimal sampling scheme Ω for Tofts model fitting is derived. Here, the Tofts model from equation 3.16 is used:

$$C(t) = \begin{cases} 0 & \text{for } t < \tau \\ D \cdot [b_1 e^{-m_1(t-\tau)} + b_2 e^{-m_2(t-\tau)} + b_3 e^{-m_3(t-\tau)}] & \text{for } t \geq \tau, \end{cases} \tag{4.9}$$

with

$$\begin{aligned} m_3 &= K^{trans}/v_e, \\ b_1 &= (K^{trans} \cdot a_1)/(m_3 - m_1), \\ b_2 &= (K^{trans} \cdot a_2)/(m_3 - m_2), \\ b_3 &= -(b_1 + b_2). \end{aligned} \tag{4.10}$$

$C(t)$ is a function of time t and the parameter set $\vec{p} = [K^{trans}, v_e, \tau]$. The parameters a_1, a_2, m_1 and m_2 of the arterial input function are set to the population-averaged values measured by [Walker-Samuel2007], as given in equation 3.15. A dose of D = 0.1 mMol/kg is assumed. The total dynamic imaging time is set to T_{tot}=8 min.

4.3.2 *A priori* Model Parameters

The optimal sampling scheme $\Omega(\vec{p})$ for a given set of parameters $\vec{p}$ can be determined using the D-optimality criterion as described in section 4.2. However, to be able to calculate the OSS, $\vec{p}$ has to be known *a priori*. In DCE MRI, contrast agent is administered only once. Therefore, the underlying parameter sets are not known prior to imaging. However, by assuming physiologically realistic PK parameter values, still an estimate of the OSS can be found.

Based on a literature review, which can be found in detail in appendix A, ranges of typical K^{trans} and v_e parameter values for benign and malignant lesions are chosen. They are summarized in table 4.1 a) and additionally illustrated in figure 4.1 b) as colored boxes. Due to an overlap between benign and malignant PK parameter values, an additional tissue type of *intermediate* PK values is introduced which describes regions where an overlap between benign and malignant PK parameters occurs.

Finding absolute values for the onset time τ from the literature is difficult since it strongly depends on the CA injection technique and timing with respect to the start of imaging. Moreover, it is dependent on the physiological condition of the patient. Therefore in this work the onset time is randomly set to $\tau = 1.5$ min. It is furthermore assumed that, within a lesion, the onset time can vary by $\Delta t = \pm 0.1$ min.
Two parameter sets $\vec{p} = [K^{trans}, v_e, \tau]$, each representing typical PK parameter values of benign and malignant lesions are considered here for OSS calculation:

$$\begin{aligned} \vec{p}_B &= [0.6\ \text{min}^{-1}, 0.3, 1.5\ \text{min}] \quad \text{(benign lesion)} \\ \vec{p}_M &= [2.0\ \text{min}^{-1}, 0.8, 1.5\ \text{min}] \quad \text{(malignant lesion)}. \end{aligned} \tag{4.11}$$

4.3.3 Optimal Sampling for Single Parameter Sets

In this chapter, optimal sampling schemes Ω for the Tofts model are derived according to section 4.2 for the parameter sets $\vec{p}_B$ and $\vec{p}_M$.

a)	K^{trans} [min^{-1}]	v_e [ ]
benign	$0.2 \leq K^{trans} < 1.0$	$0.2 \leq v_e < 0.4$
intermediate	$1.0 \leq K^{trans} < 1.5$	$0.4 \leq v_e < 0.6$
malignant	$K^{trans} \geq 1.5$	$0.6 \leq v_e < 0.9$

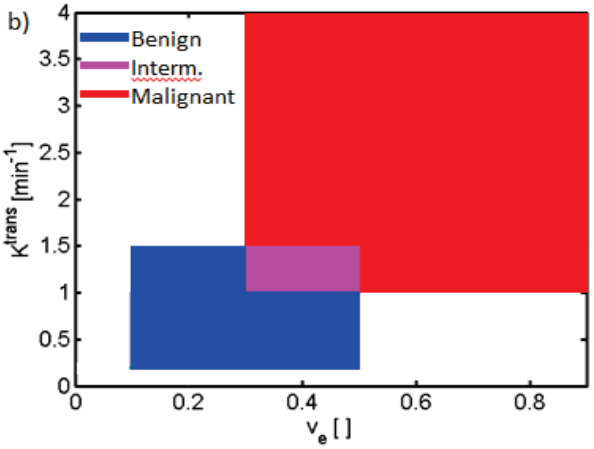

Table 4.1: a) Ranges of physiologically realistic PK parameter values for different tissue types. b) Graphical illustration of a).

Constraints and Assumptions of Sampling in DCE MRI

To determine an OSS for the application to DCE MRI, the following constraints and assumptions need to be considered:

- There is a natural ordering of the sampling times t_i, since contrast agent is administered only once:
  $0 < t_1 < t_2 < ... < t_N$,
  where N is the total number of samples.

- Imaging takes place during a time interval with a minimal time Δt_{min} needed to acquire an image. For two adjacent time points this imposes the constraint:
  $t_{i+1} - t_i \geq \Delta t_{min}$.

- For Cartesian acquisitions, image contrast is mainly determined by the central k-space lines. Therefore, it is assumed here that the actual imaging process occurs instantaneously during a single time point t_i within the interval.

Sensitivity Functions

It is beneficial for accurate model fitting to sample data at time points t_i at which the sensitivity functions have a high magnitude. They are given by

$$\zeta_K(t) = \frac{\partial C(t)}{\partial K^{trans}}, \zeta_v(t) = \frac{\partial C(t)}{\partial v_e}, \zeta_\tau(t) = \frac{\partial C(t)}{\partial \tau}. \tag{4.12}$$

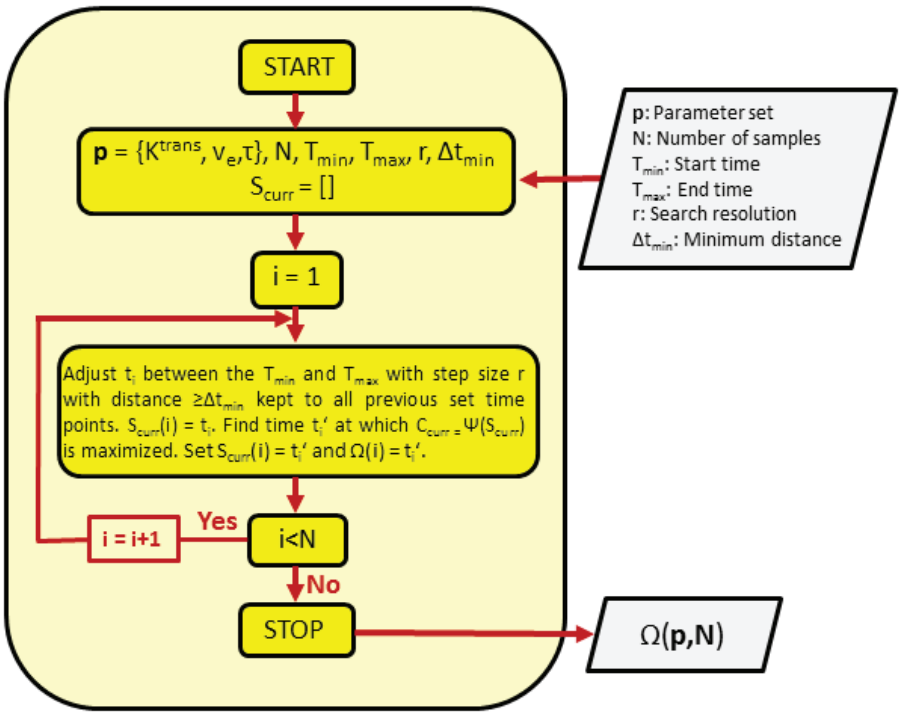

Figure 4.2: Flow chart of the algorithm to determine optimal sampling schemes for a single parameter set (adapted from [Xie2008])

Here, $\zeta_K(t)$, $\zeta_v(t)$ and $\zeta_\tau(t)$ are calculated using Mathematica 8 [Wolfram Research, Inc., Champaign, Illinois, USA].

In figure 4.4 the sensitivity functions $\zeta_K(t)$, $\zeta_v(t)$ and $\zeta_\tau(t)$ are plotted along with the concentration time curve $C(t)$ for each parameter set $\vec{p}_B$ and $\vec{p}_M$ to obtain an estimate where sampling is relevant. The analytical solutions of the sensitivity functions are given in appendix B.

Algorithm to Determine the OSS Using D-Optimality

To determine the optimal sampling scheme, a search algorithm is implemented which is illustrated in the flow chart of figure 4.2.

The algorithm takes as input an *a priori* known parameter set $\vec{p} = (K^{trans}, v_e, \tau)$, the total number of sampling points N, the total start time T_{min} and total end time T_{max} of imaging, the search resolution r and the minimal distance between neighboring time point Δt_{min}. The final output of the algorithm is the optimal sampling scheme $\Omega(\vec{p}, N)$ for the parameter set $\vec{p}$ and N sampling points.

The inverse cost function $\Psi = det(\vec{H})$ is to be maximized against all sampling schemes within the given constraints to minimize the parameter variance. S_{curr} describes the current sampling scheme and C_{curr} the current value of the inverse cost function $\Psi(S_{curr})$. The algorithm consists of a loop in which the sampling times t_i, with $i = 1, ..., N$, are

successively adjusted. The first sampling point t_1 is adjusted with step size r between T_{min} and T_{max} and with every step the current scheme $S_{curr}(1)$ is updated to t_1. The time t_1' is found at which the inverse cost function $C_{curr} = \Psi(S_{curr}(1))$ is maximized. $\Omega(1) = t_1'$ is set. For the next iteration $S_{curr}(1) = t_1'$ is set fixed and $S_{curr}(2)$ is adjusted analogously, however keeping the distance Δt_{min} to $S_{curr}(1)$. For all $i > 1$ it is proceeded analogously. The possible locations for t_i are constrained by keeping the minimal distance Δt_{min} to previously determined time points $S_{curr}(j)$ with $j < i$.

Here, a search resolution of $r = 1$ s, $T_{min} = 0$ min, $T_{max} = 8$ min and a minimal distance of $\Delta t_{min} = 10$ s is employed. The number of samples is varied from $N = 6$ to $N = 40$.

Comparison of the Performance of the EDS and the OSS

To be able to compare different sampling schemes in terms of resulting parameter stability, the following two measures are used.

(i) *Theoretical parameter accuracy*: The standard deviation σ_{p_j} of the parameter p_j can be theoretically estimated from the curvature of the χ^2-function close to the minimum. Under the assumption that there is no correlation between the fit parameters, the variance $\sigma_{p_j}^2$ of parameter p_j is given by equation 4.6. Combined with equation 4.5, this yields:

$$\sigma_{p_j} = \sqrt{2(\frac{\partial \chi^2}{\partial p_j^2})^{-1}} = \sqrt{1/\sum_{i=1}^{N} \frac{1}{\sigma_i}(\frac{\partial C(t_i)}{\partial p_j})^2} \tag{4.13}$$

In MRI, it can be assumed that the noise standard deviation $\sigma_i = \sigma$ is the same at all time points t_i. Here, the second derivative is evaluated at the true underlying parameter set $\vec{p}$. The resulting standard deviations σ_K, σ_v and σ_τ of the parameters K^{trans}, v_e and τ are compared for the OSS and the EDS for $N = 6, ..., 40$ and the two different noise standard deviations $\sigma_1 = 0.01$ and $\sigma_2 = 0.05$. The calculation is performed for $\vec{p}_B$ and $\vec{p}_M$.

(ii) *Measured fitting accuracy*: The concentration time curve $C(t)$ is generated with the underlying parameter set $\vec{p} = [K^{trans}, v_e, \tau]$. Gaussian noise with a standard deviation σ for each single measurement point $C(t_i)$ at sampling time t_i is added, resulting in the noisy concentration curve $C_\sigma(t)$. Using a Levenberg-Marquardt algorithm with the initial guess being the true parameter set $\vec{p}$, the Tofts model is fitted to $C_\sigma(t)$. This process is repeated $N_{rep} = 100$ times, resulting in a set $\{\vec{p}_{fit}\}$ of resulting parameter sets. From this set, the relative means K_{fit}, v_{fit}, τ_{fit} and standard deviations $\sigma_{K_{fit}}$, $\sigma_{v_{fit}}$, $\sigma_{\tau_{fit}}$ of the parameters K^{trans}, v_e and τ are calculated. This calculation is performed for $N = 6, ..., 40$ and two different noise standard deviations $\sigma_1 = 0.01$ and $\sigma_2 = 0.05$. It is repeated for the parameter sets $\vec{p}_B$ and $\vec{p}_M$.

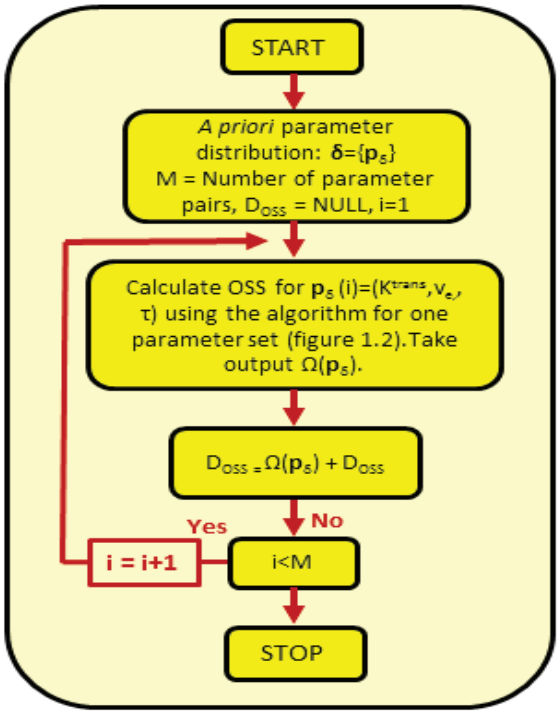

Figure 4.3: Flow chart of the algorithm to determine optimal sampling schemes for a distribution of parameter sets (adapted from [Xie2008])

Additionally, the χ^2-function of the parameter set $\vec{p}_M$ for K^{trans} and v_e at the true value $\tau = 1.5$ min and of the parameters K^{trans} and τ at the true value $v_e = 0.8$ is plotted for $N = 7$ and $\sigma = 0.01$ for the EDS and the OSS. This is done to visualize the varying χ^2-surface of different sampling schemes, leading to varying fitting stabilities.

4.3.4 Optimal Sampling for a Parameter Distribution

In the previous section optimal sampling schemes were derived for two fixed parameter sets $\vec{p}$. However, in reality tumors are heterogeneous structures comprising of a distribution of parameter sets, which varies from tumor to tumor dependent on type and stage. Therefore, a more feasible approach is to calculate the OSS for a distribution δ of PK parameters sets $\vec{p}_\delta$ as opposed to single parameter sets.

Here, the distribution δ is chosen to consist of equally weighted typical benign, intermediate and malignant values. This is for example a sensible choice if the clinical question of interest is the distinction between benign and malignant lesions. The assumed distribution δ is based on table 4.1: 0.2 $\text{min}^{-1} \leq K^{trans} \leq$ 2.5 min^{-1}, $0.2 \leq v_e \leq 1.0$. The onset time τ is varied between τ =1.5 min and 1.6 min. Each parameter is iterated with step size s = 0.01.

The flow chart in figure 4.3 describes the search algorithm which is employed to find

the OSS of an *a priori* given distribution of PK parameters. For all parameter sets $\vec{p}_\delta$ of the distribution δ, the OSS for N samples is calculated as described for a single parameter set (figure 4.2). The time points of all resulting optimal sampling times $\{t_i\}$ of each parameter set within $\vec{p}_\delta$ are recorded in a histogram $\vec{D}_{OSS}$. $\vec{D}_{OSS}$ displays the distribution of optimal sampling times throughout all parameter sets of $\vec{p}_\delta$. The optimal sampling scheme Ω_δ of the whole distribution is obtained by dividing the area under the resulting histogram into N equal parts. Here, Ω_δ is calculated for $N = 10$. $N = 10$ is chosen since according to figure 4.6 and 4.7 a constant parameter uncertainty is reached for the OSS of both tested parameter sets and noise standard deviations, as will be seen in the results section section.

4.4 Results

The methods described above were used to calculate the following sensitivity functions, optimal sampling schemes and comparisons of the EDS and the OSS.

4.4.1 Optimal Sampling for Single Parameter Sets

Sensitivity Functions

In figure 4.4 a) and b) the sensitivity functions $\zeta_\tau(t)$ (*green*), $\zeta_K(t)$ (*blue*) and $\zeta_v(t)$ (*red*) and the concentration time curves $C(t)$ (*black*) of the two parameter sets $\vec{p}_B$ and $\vec{p}_M$ are displayed. Both parameter sets exhibit a similar behavior.

It can be seen that $\zeta_\tau(t)$ has a peak of high magnitude with a maximum at a few seconds after the onset time τ with a narrow total width of about 0.5 min. When compared to $C(t)$, the peak of $\zeta_\tau(t)$ is located at the upslope of the concentration time curve. A smaller second peak starting at about 0.5 min after the onset time with a width of about 1 min can be seen for both parameters sets, being higher for $\vec{p}_M$. It correlates with the time of the initial fast downslope of $C(t)$ after the peak.

$\zeta_K(t)$ displays a peak starting at τ with a maximum at approximately 15 s after τ with a narrow total width of 1.0 min-1.5 min. The amplitude of $\zeta_K(t)$ is small compared to that of $\zeta_\tau(t)$ and $\zeta_v(t)$. Relative to $C(t)$, the peak of ζ_K occurs during the upslope and the initial fast downslope after the peak of $C(t)$.
Starting at τ, the magnitude of the peak of $\zeta_v(t)$ increases. From about 0.5 min on, $\zeta_v(t)$ is the sensitivity function with the highest magnitude, lasting until the end of the measurement. The relatively high maximum is found at about 1 min-1.5 min after τ. The decrease of ζ_v after the maximum with increasing time is slow, resulting in a high magnitude of $\zeta_v(t)$ until the end of the measurement.

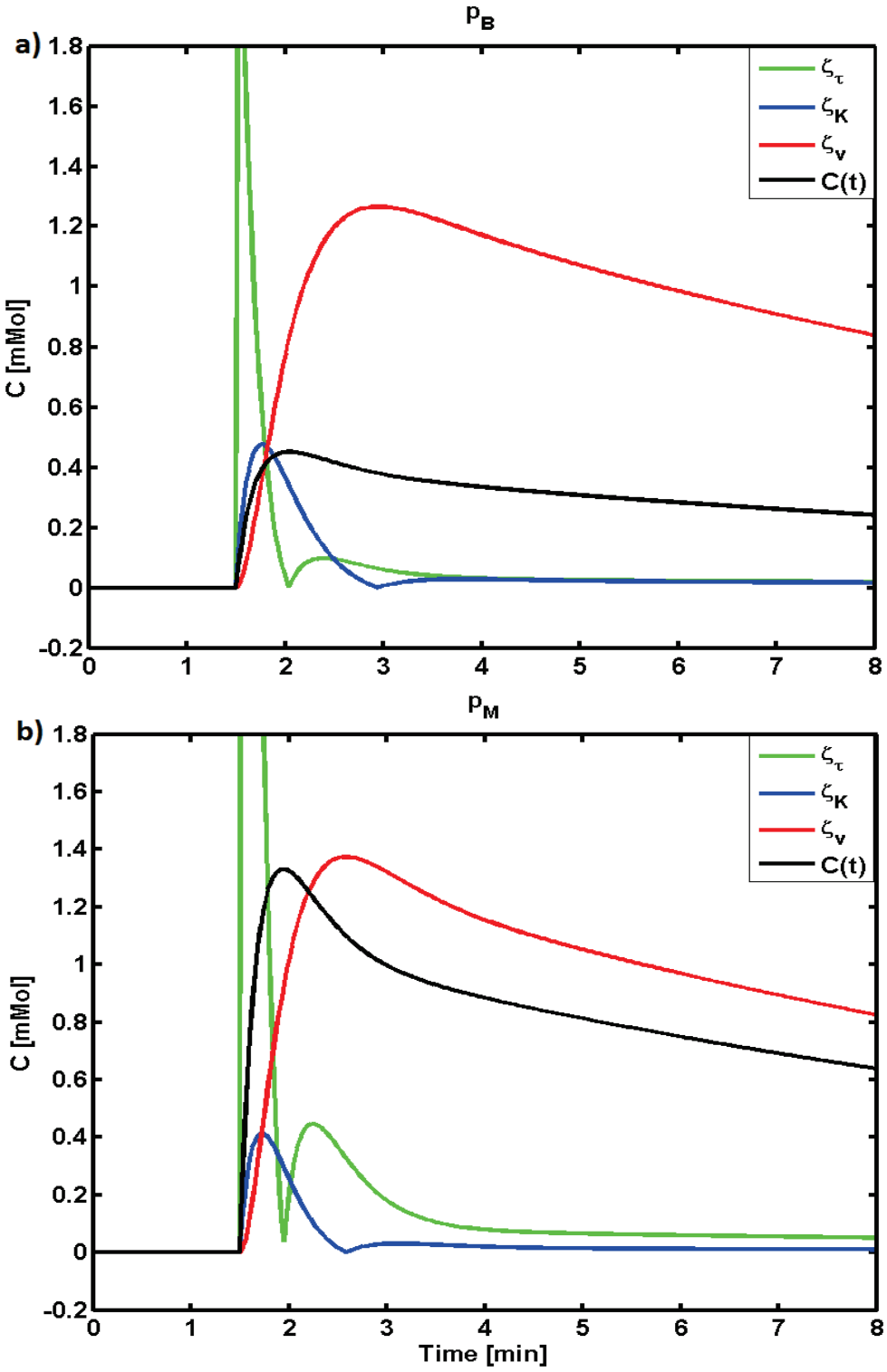

Figure 4.4: Sensitivity functions of the parameter sets a) $\vec{p}_B$ and b) $\vec{p}_M$. The following color scheme is used: $C(t)$ = black, $\zeta_\tau(t)$ = green, $\zeta_K(t)$ = blue, $\zeta_v(t)$ = red.

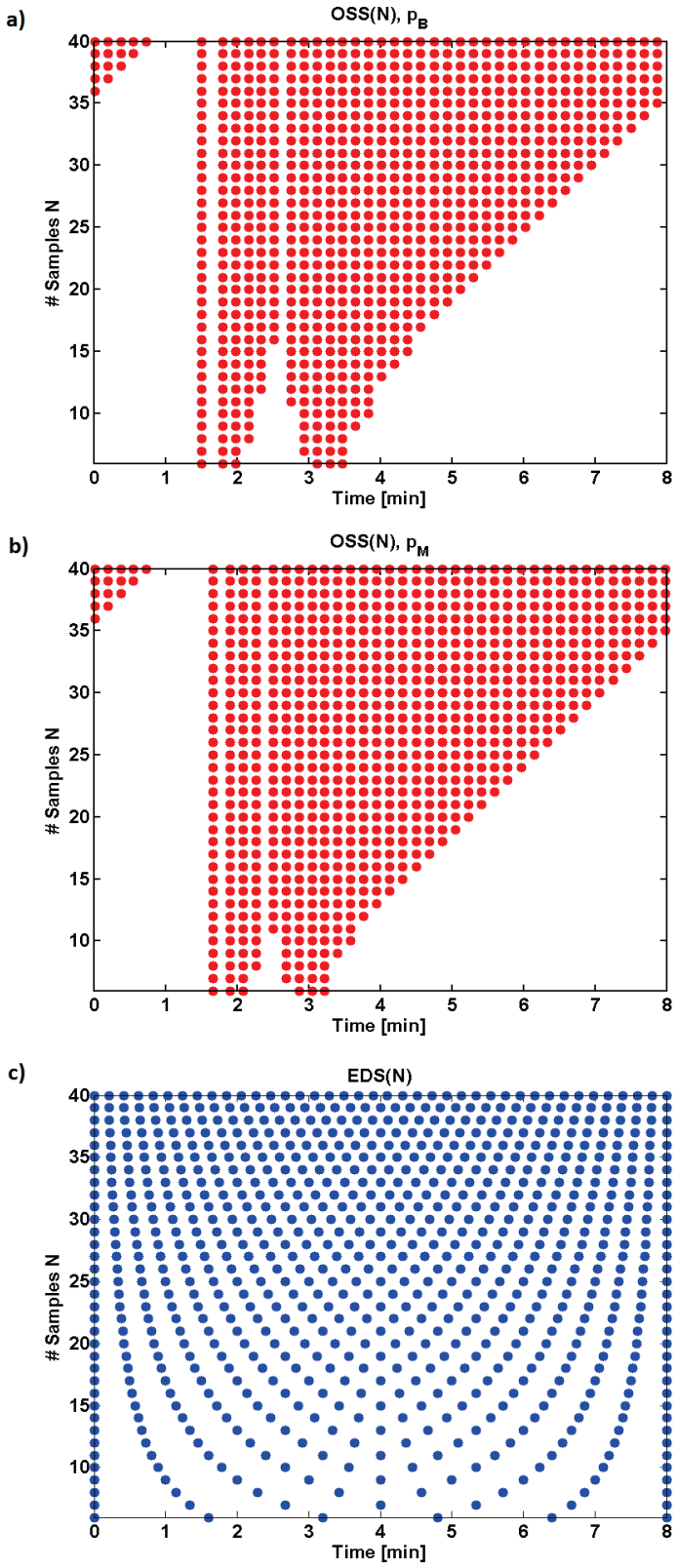

Figure 4.5: Optimal sampling schemes $\Omega(\vec{p}, N)$ in dependence of number of sampling points N for parameter set a) $\vec{p}_B$ and b) $\vec{p}_M$. c) Equidistant sampling schemes in dependence of N

OSS for Single Parameter Sets Using D-optimality

The output $\Omega(\vec{p}, N)$ of the OSS algorithm as a function of the number of samples N with $N = 6$ to $N = 40$ can be seen in figure 4.5 a) - b) for the parameter sets $\vec{p}_B$ and $\vec{p}_M$. In figure 4.5 c) equidistant schemes with $N = 6$ to $N = 40$ are also plotted for comparison. For $\vec{p}_B$ and $\vec{p}_M$ a similar behavior can be seen. For $N = 6$, three clusters of time points can be distinguished. The first is located at approximately $[\tau, \tau + 0.1 \text{ min}]$, the second approximately at $[\tau + 0.3 \text{ min}, \tau + 0.6 \text{ min}]$ and the third cluster at approximately $[\tau + 1.3 \text{ min}, \tau + 1.7 \text{ min}]$. With increasing N, the later clusters broaden and merge into a single cluster, for $\vec{p}_B$ at $N = 16$ and for $\vec{p}_M$ at $N = 11$. For higher N each new sample is added to the next possible higher time within the constraint. When $t = T_{max}$ is reached, the next sample points are placed at the baseline.

Comparison of the Performance of the EDS and the OSS

The results of the comparison of the parameter uncertainty of the EDS and the OSS using method (i) and (ii) are shown in figures 4.6 and 4.7. For the EDS (left) and OSS (right) the expected parameter standard deviations σ_k, σ_v and σ_τ (figure 4.6) and the mean and standard deviation of the fitting results (figure 4.7) of the parameters K^{trans} (blue), v_e (red) and τ (green) are plotted for $\vec{p}_B$ (a)- d)) and $\vec{p}_M$ (e)- h)), each for noise standard deviation σ_1=0.01 and σ_2=0.05. The following behavior is observed:

- For the larger noise standard deviation σ_2, the parameter standard deviations σ_K, σ_v and σ_τ (figure 4.6) and $\sigma_{K_{fit}}$, $\sigma_{v_{fit}}$ and $\sigma_{\tau_{fit}}$ (figure 4.7) are significantly higher than for σ_1 for both, the EDS and the OSS. It can additionally be seen that for σ_2, systematic fitting errors in K_{fit}, v_{fit} and τ_{fit} increase, especially for small N (figure 4.7).

- For small N, the parameter standard deviations σ_K, σ_v and σ_τ (figure 4.6), $\sigma_{K_{fit}}$, $\sigma_{v_{fit}}$ and $\sigma_{\tau_{fit}}$ and systematic errors of K_{fit}, v_{fit} and τ_{fit} (figure 4.7) of the EDS are large. For the OSS, they are significantly smaller. Only for a few single N, the EDS performs comparable, as can be seen for example in figure 4.6 a) for $N = 11$, where σ_τ of the EDS has a comparable value to that of the OSS.

- For the OSS, the parameter standard deviations of all parameters approach an approximately constant value σ'_K, σ'_v and σ'_τ after N'_{OSS} samples (figure 4.6). The same behavior can be seen in figure 4.7 for $\sigma_{K_{fit}}$, $\sigma_{v_{fit}}$, $\sigma_{\tau_{fit}}$ and K_{fit}, v_{fit} and τ_{fit}, approaching $\sigma'_{K_{fit}}$, $\sigma'_{v_{fit}}$, $\sigma'_{\tau_{fit}}$ and K'_{fit}, v'_{fit} and τ'_{fit} . The constant value depends on the parameter set and the noise standard deviation. With increasing noise standard deviation the constant values increase. With increasing malignancy, the constant values decrease.

- With increasing N the parameter standard deviations (figure 4.6) and fitting mean and standard deviations (figure 4.7) of the EDS decrease and approach that of the OSS. An exception to this behavior is $\vec{p}_B$ for σ_2 (figure 4.6 c)- d)), where σ_K and σ_τ of the EDS approach a smaller value than that of the OSS.

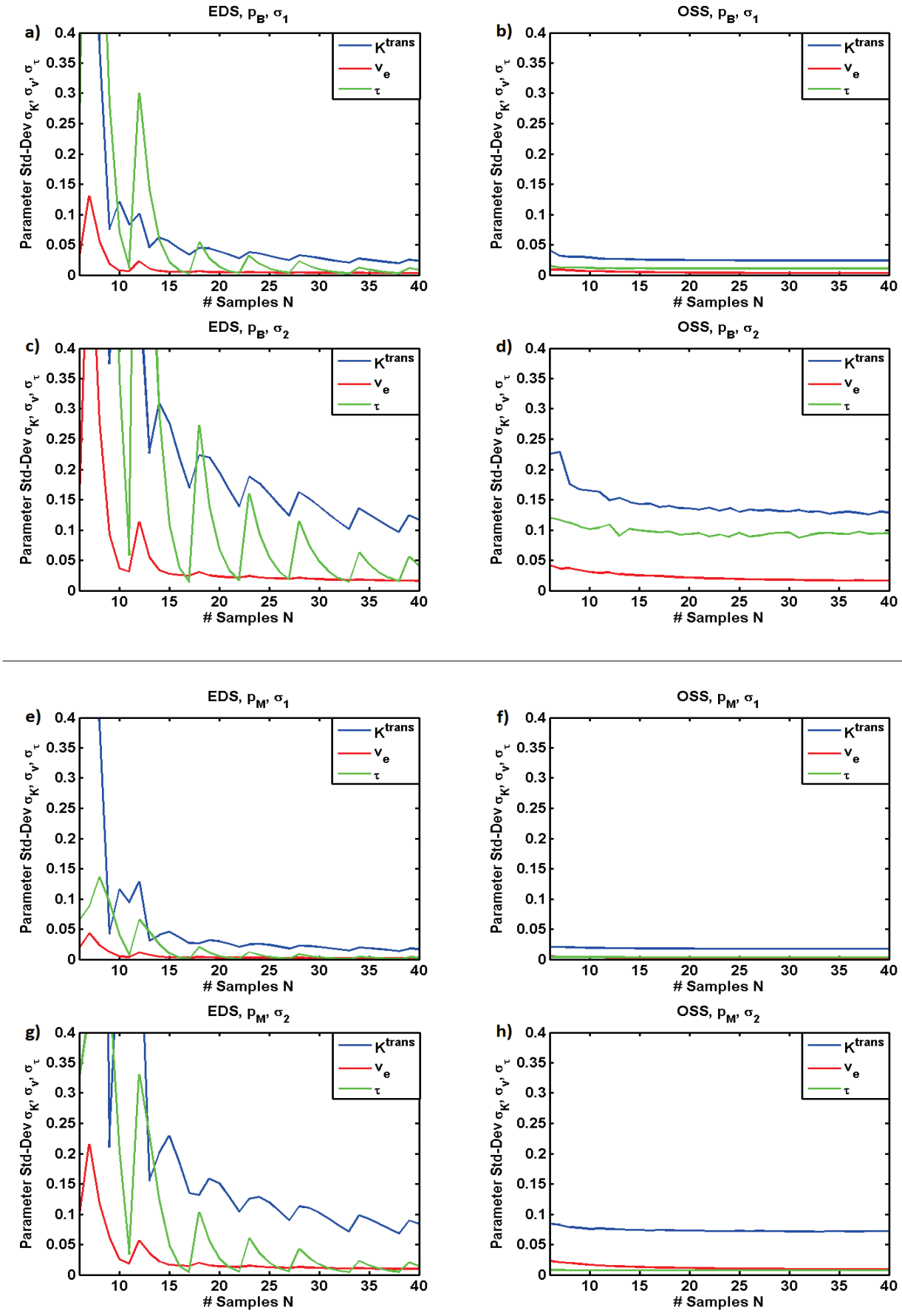

Figure 4.6: Comparison of the expected parameter standard deviation of the EDS (left) and OSS (right) estimated from the curvature of the χ^2-function for parameter sets $\vec{p}_B$ and $\vec{p}_M$, each for noise standard deviation σ_1=0.01 and σ_2=0.05.

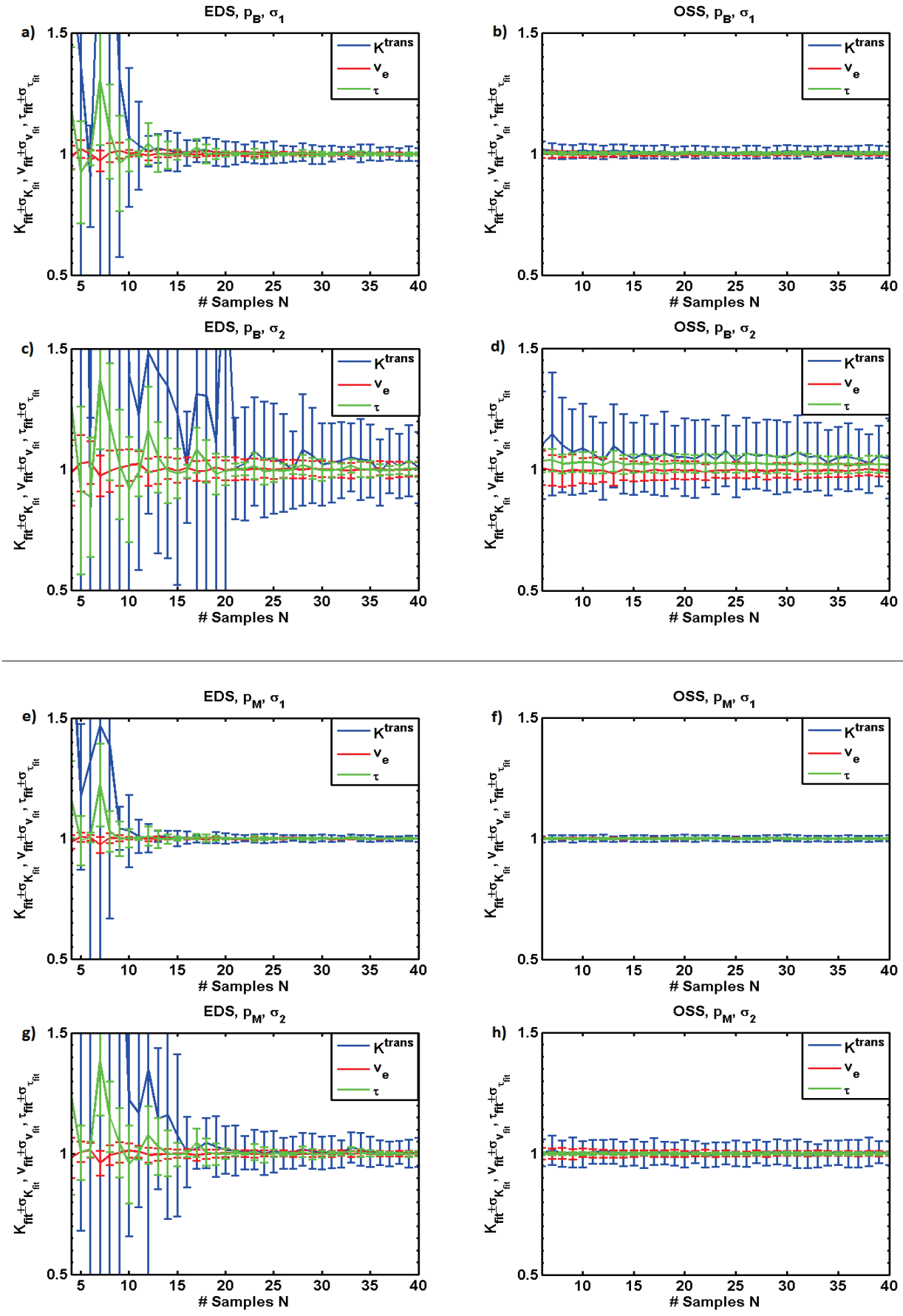

Figure 4.7: Comparison of the fitting accuracy of the EDS(left) and the OSS(right): The mean and standard deviation of $N_{rep} = 100$ fitting results is plotted for parameter sets $\vec{p}_B$ and $\vec{p}_M$, each for noise standard deviation σ_1=0.01 and σ_2=0.05.

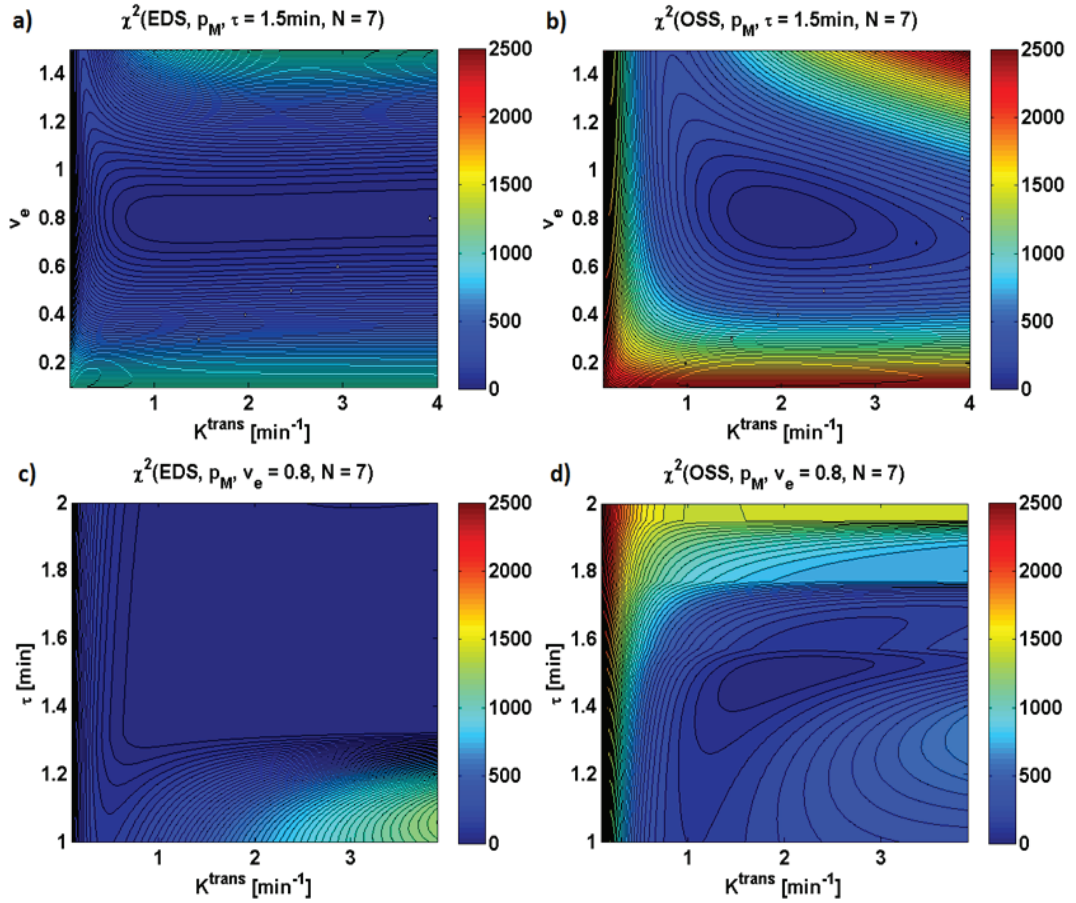

Figure 4.8: 2-D χ^2-function for $\vec{p}_M$, $N = 7$ and a) EDS for K^{trans} and v_e at true $\tau = 1.5$ min, b) OSS K^{trans} and v_e at true $\tau = 1.5$ min, c) EDS for K^{trans} and τ at true $v_e = 0.8$, d) OSS for K^{trans} and τ at true $v_e = 0.8$. The OSS exhibits steeper slopes than the EDS.

- The EDS displays for both methods (i) and (ii) a periodic 'zig-zag'-pattern, whilst the OSS shows a comparably smooth curve. The amplitude of the zig-zag-pattern decreases with increasing N. A correlation between the pattern of K^{trans} and τ exists.

- K^{trans} is the parameter with the highest parameter standard deviation σ_K and the highest mean error K_{fit} and standard deviation $\sigma_{K_{fit}}$ of the fitting parameters for the OSS and the EDS. v_e is the parameter with the smallest parameter standard deviation σ_v and the smallest mean error v_{fit} and standard deviation $\sigma_{v_{fit}}$ of the fitting parameters for the OSS and the EDS. For the OSS, τ is a stable parameter, for the EDS it is stable only for large N.

In figure 4.8 an example of the χ^2-function for the EDS (left) and the OSS (right) are shown for the parameter set $\vec{p}_M$ and $N = 7$. Comparing a) and b) it can be seen that for the OSS the valley around the true parameter set $(K^{trans}, v_e) = (2.0\ \text{min}^{-1}, 0.8)$ exhibits steeper slopes than for the EDS when going to other parameter pairs. This is especially evident for varying K^{trans}, showing a long broaden valley for the EDS.

Comparing c) and d) a similar pattern can be seen. For the OSS the minimum area around the true parameter set $(K^{trans}, \tau) = (2.0\ \text{min}^{-1}, 1.5\ \text{min})$ shows a more narrow and better distinct valley than for the EDS. The minimum area of the EDS displays a large plateau over a large range of values, especially for parameter sets with higher values than the true parameter set.

4.4.2 Optimal Sampling for a Parameter Distribution

The histogram $\vec{D}_{OSS}$ (black) and the resulting optimal sampling scheme Ω_δ (red) are shown in figure 4.9. It can be seen that the optimal sampling times are distributed such that high temporal resolution is required for the first 2 minutes after contrast agent arrival, followed by a single sampling time at about 3 minutes after the onset time. In the distribution 3 peaks can be distinguished, centered around $t_1 \approx \tau + 0.05$ min, $t_2 \approx \tau + 0.7$ min and $t_2 \approx \tau + 1.6$ min.

4.5 Discussion

In this chapter, optimal sampling design is applied to the Tofts model with respect to the evaluation of DCE MRI data. Under the constraints of DCE MRI data acquisition, optimal sampling schemes are derived for single PK parameter sets and a distribution of parameter sets. From the optimal sampling schemes it can be estimated where to sample with high temporal resolution to provide accurate model fitting. In the following, the employed methods and results will be discussed.

Sensitivity Functions

From the shape of the sensitivity functions it can be estimated how robust the individual fitting parameters are and at which time intervals high temporal resolution is required for accurate parameter fitting. The time intervals which do not contribute significantly to an improvement of fitting accuracy can be sacrificed to acquire high spatial resolution images.

Fitting with respect to a certain parameter becomes more robust when data are sampled at time points where the sensitivity function of that parameter is high. High temporal resolution is required in the following cases:

- The width of the high magnitude interval of the sensitivity function is narrow. In this case, fast sampling is necessary in order not to miss time points within the narrow interval.

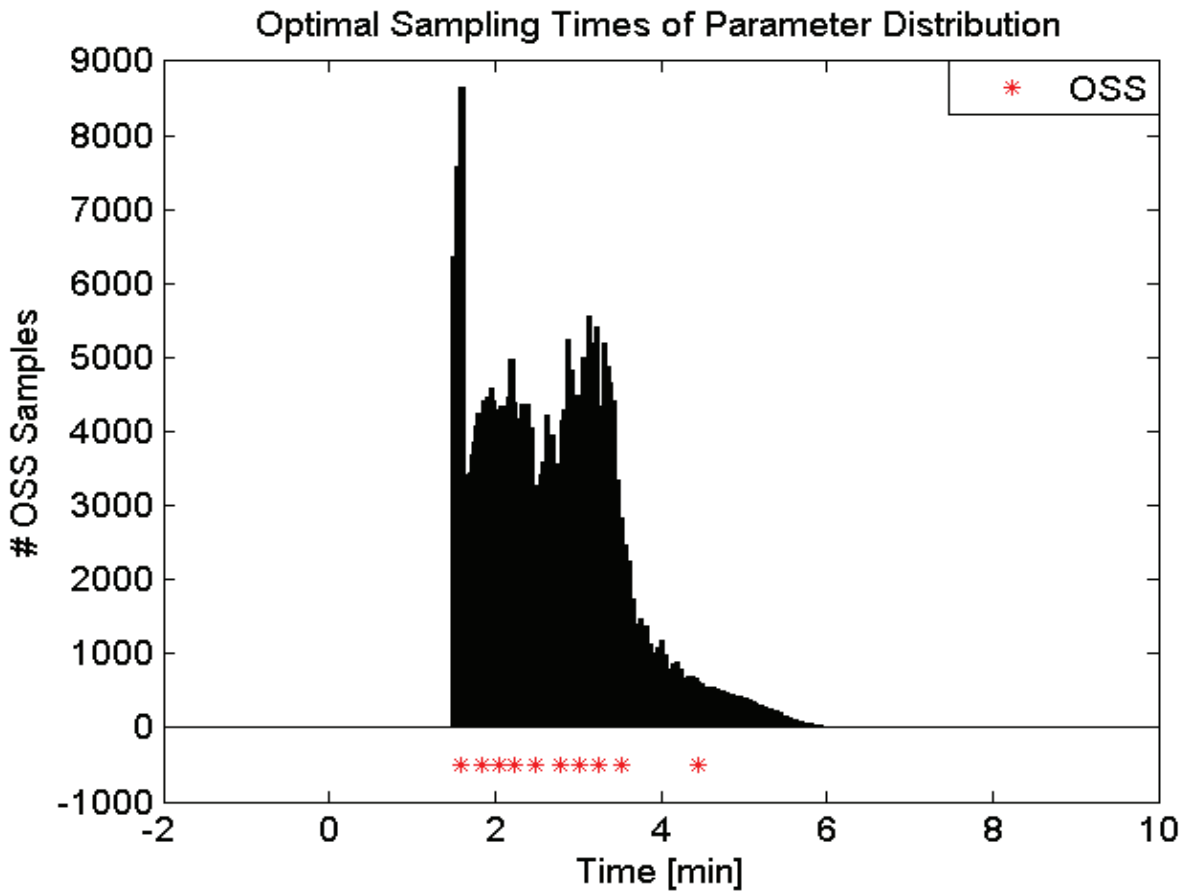

Figure 4.9: Histogram D_{OSS} (black) of optimal sampling points for PK parameter set distribution δ and resulting optimal sampling scheme (red).

- The amplitude of the sensitivity function during the interval of high magnitude is small. In this case, fast sampling is required since the fitting parameter is unstable.

The first peak in $\zeta_\tau(t)$ has a very high amplitude, however a narrow width, making τ a robust fitting parameter when sampled at the relevant times. Therefore, for accurate τ fitting, high frequency sampling is required during the interval $[\tau, \tau + 0.5 \text{ min}]$ in order not to miss relevant time points. The second peak of $\zeta_\tau(t)$ has a low magnitude and a relatively narrow width. Therefore to additionally increase τ-fitting, fast sampling during the interval $[\tau + 0.5 \text{ min}, \tau + 1.5 \text{ min}]$ is advantageous.

$\zeta_K(t)$ has a peak with a low amplitude and a narrow width. Consequently, K^{trans} is an unstable fitting parameter. For optimal K^{trans} fitting, fast sampling is needed during the interval $[\tau, \tau + 1.5 \text{ min}]$.

The sensitivity function $\zeta_v(t)$ has a peak with high amplitude and a very broad width, making v_e a robust fitting parameter. Here, it is suggested to sample with high temporal resolution during the time interval $[\tau, \tau + 2 \text{ min}]$ to acquire data in the area of the

maximum of ζ_v(t).

In summary, to enable accurate fitting of all parameters K^{trans}, v_e and τ, fast sampling is suggested during the interval $[\tau, \tau + 2$ min$]$. However, these time intervals are only valid for the underlying parameter sets. More general, fast sampling is required during to the upslope, the peak and the initial fast downslope of the concentration time curve $C(t)$. For all parameter sets, it is important to begin fast sampling directly after the onset time. Later phases of the curve, during the slow wash-out can be exploited for high spatial resolution images at low temporal resolution.

The sensitivity functions of typical benign and malignant curves show a similar behavior. This can be of advantage since the same time intervals are relevant for accurate model fitting. This can potentially contribute to a good distinction between benign and malignant PK parameter values.

Investigating the sensitivity functions does not deliver exact optimal sampling time points, only approximate time intervals. However, it provides a useful first estimate of parameter robustness and for sampling relevant time intervals.

OSS for Single Parameter Sets Using D-optimality

For a certain value of N, the times acquired for N-1 samples are kept and a new time point is added. Therefore, the resulting optimal sampling schemes with increasing number of samples N exhibit a 'ranking of the importance' of sampling points. For both parameter sets, the sampling times within the interval $[\tau, \tau + 2.5$ min$]$ are collected with the highest priority, followed by those within the interval $[\tau + 2.5$ min$, T_{max}]$. Data on the baseline are placed last, having the least importance.

This behavior is in good agreement with the estimates from the sensitivity functions. During the interval $[\tau, \tau + 2.5$ min$]$ the parameters are the most sensitive to the fitting process. Time points within the interval $[\tau + 2.5$ min$, T_{max}]$ mainly contribute to the accuracy of v_e, which can be determined already accurately from earlier time points. The baseline values are not relevant for fitting since the model states that the initial concentration before CA injection is zero. However, this would change for example if a prebolus was administered in order to measure the AIF.

In this work a constraint of $\Delta t_{min} = 10$ s is assumed. This value can be adjusted to the temporal requirements of the imaging process.

When no constraints are set, the sampling points are distributed only at three different time points being $t_1 = 1.5$ min, $t_2 = 1.76$ min and $t_3 = 3.1$ min for $\vec{p}_B$ and $t_1 = 1.6$ min, $t_2 = 1.73$ and $t_3 = 2.72$ for $\vec{p}_M$. With given constraints, the algorithms locates the sampling points as close as possible to these optimal time points, approaching them from the side of the lower inverse cost function.

The used algorithm does not cover all possible permutations. By fixing previous time points, set at smaller N, and keeping the constraints, certain combinations of time points are missed. For more accurate results all possible permutations should be compared in terms of cost optimization. However, a more efficient way of calculation has to be developed first, which was beyond the scope of this work.

Comparison of the Performance of the OSS and the EDS

It can be seen that the results obtained from methods (i) and (ii) are consistent. The measured parameter standard deviations from fitting are in general slightly larger than the theoretical ones. This might be due to the fact that the theoretical standard deviations of method (i) are always evaluated at the true parameter set, whilst for the fitting results systematic errors of the mean increase the measured standard deviations.

The results of the EDS follow a periodic zig-zag pattern. This pattern arises since relevant time points needed for accurate τ-fitting are repeatedly missed, leading to an overestimation of τ. Consequently, K^{trans} is also overestimated. That is the reason why EDS sampling schemes with lower N can perform better than others with higher N, dependent on the location of the time points within the period.

The resulting parameter accuracy is in good agreement with what is expected from the sensitivity functions. K^{trans} is the least robust parameter, whilst v_e is the most stable. τ is fitted accurately when the correct time points are sampled. It is a large disadvantage that K^{trans} is an unstable parameter since it is the parameter with the highest clinical relevance [Leach2005].

The parameter accuracy is strongly governed by the noise standard deviation σ. After a certain number of samples, increasing N does not further improve the parameter accuracy. Therefore, a minimal number of samples N_{min} can be determined such that no information is gained by using $N > N_{min}$. For the OSS, N_{min} is smaller than for the EDS. For high parameter accuracy it should be taken care of good image quality with high SNR and few artifacts, as for example caused by motion.

In general, it can be seen that the OSS performs better than the EDS at low N. For a few single values of N, the schemes are comparable when, by chance, the correct time points are sampled with the EDS. However, it cannot be guaranteed these points are acquired during imaging and it is more likely to sample the incorrect time points which will lead to large errors. For larger values of N, the EDS approaches the accuracy of the OSS.

The χ^2-function shows clearly why the OSS results in better fitting accuracy than the EDS. The optimal fit of the Levenberg-Marquardt-algorithm is obtained by finding the parameter set of the minimum of the χ^2-function. The steeper the slopes of the minimum valley are, the more stable are the fitting results. Since the OSS shows clearer minima than the EDS, the fit becomes more accurate.

Optimal Sampling Scheme for a Distribution of Parameter Sets

The results of the optimal sampling scheme for a parameter distribution show that high temporal resolution is required for the first two minutes after contrast agent onset. Afterwards, low temporal resolution is sufficient and high spatial resolution images can be acquired without a relevant loss in fitting accuracy. These results are in good agreement with clinical studies, for example [Mann2006], using combined high temporal/high spatial resolution schemes.

When compared to the sensitivity functions, the three peaks in the histogram corre-

spond to the times of the sensitivity function maxima for the parameters K^{trans}, v_e and τ.

Here, a distribution of equally weighted benign and malignant values is chosen. This choice can be adapted to the clinical question of interest. For example if only the malignant PK parameters are of interest for better tumor characterization, then the distribution can be tailored.

Other Considerations

The results of the optimal sampling scheme indicate that only the approximate time interval $[\tau, \tau + 2.0 \text{ min}]$ is relevant for high fitting accuracy. Afterwards a high spatial resolution image can be acquired, taking normally about 1.0-1.5 min. Therefore, imaging can potentially be stopped before the 8 min used in clinical routine without information loss. It is still a topic of current research to determine whether high temporal resolution images are sufficient to distinguish between benign and malignant lesion. If high temporal resolution would be found to be sufficient, imaging only 2.5 min after τ would provide a decrease in total imaging time and would be a step in the direction of using MR as feasible screening method.

In these investigations, the Tofts model is chosen to describe the underlying pharmacokinetic behavior. It is employed in many studies with many literature values and is relatively easy to apply due to only three free fitting parameters. It has to be kept in mind though that the Tofts model is only an approximation and does not describe reality correctly. A different model might be more suitable.

To use the Tofts model, the AIF has to be known. Here, a population-averaged AIF is assumed. In many studies, the AIF is measured within a large artery. If this is intended, the OSS calculation can be extended to additionally measure the AIF parameters accurately.

For OSS calculation *a priori* PK parameter values are required. The literature review yields values, however these values have to be regarded critically. Even if many lesions are taken into account, only a few studies in total are considered. All found values have in common an order of magnitude and the tendency of higher parameter values with increasing malignancy. However, the PK parameters from all presented studies show partly a large overlap between benign and malignant values and the chosen ranges are just a compromise. If this is due to the true overlapping nature of the physiology or if the reason for the discrepancy is different study designs, varying MR scanners and temporal resolution, remains unsolved. In addition, only PK values derived from breast MRI are considered here. A broader literature review comprising of other organs could potentially given better suitable parameter values. In any case, the general underlying problem of a lacking ground truth for PK parameter values makes it difficult to judge the obtained results. However, even if the used PK parameters turn out to be an unrealistic choice, the methods shown here can be straightforwardly applied to other parameter values.

In the distribution δ a variation of the onset time τ within the lesion of $\Delta\tau = 0.1$ min is assumed. This is set just as a rough estimate. The results would be more accurate if

actually measured values of $\Delta\tau$ would be used.

The OSS states that high temporal resolution is required during the first 2 min after contrast agent arrival. In general, acquiring images at higher temporal resolution has the consequence that spatial resolution or image quality has to be sacrificed. This introduces an additional measurement error which again decreases fitting accuracy. It has to be tested if the gain of more sampling points at sensitive locations outweighs the error introduced to achieve a high sampling rate.

According to the optimal sampling scheme, high temporal sampling begins approximately with the onset time τ of contrast agent. However, it is not *a priori* known when CA arrives in the lesion. The onset time can vary with the CA injection technique, the physiological condition of the patient and the timing of imaging. Therefore, an onset detection mechanism would be beneficial for fitting accuracy.

Here, a compromise to handle the missing *a priori* knowledge about the underlying parameter distribution is found by taking all possible values into account. However, this can be a very crude trade-off. The more information about the underlying parameter distribution is known the better the OSS can be tailored. Information about the underlying distribution could be for example obtained in real-time during imaging from already acquired data sets. Another approach could be to sample data in a way they can be reconstructed in retrospective at needed time points.

5 Comparison of Signal-adaptive *k*-space Acquisition Schemes in Quantitative DCE MRI

5.1 Introduction and Motivation

In chapter 4 it has been shown that, for typical breast DCE MRI data, fitting accuracy is improved when data are acquired at high temporal resolution during approximately the first 2 minutes after the onset time. At later times, during wash-out, rapid sampling is not required and high spatial resolution images can be exploited for morphological analysis. This is visualized in figure 5.4, where additionally the baseline is acquired with high temporal resolution sampling.

A decrease in acquisition time during the initial kinetics phase can be achieved by omitting certain k-space data. This may degrade image quality in the form of either lower spatial resolution, loss of SNR, aliasing artifacts or temporal blurring from view-sharing methods. Consequently, fitting errors are introduced due to this image degradation. A compromise between the gain in fitting accuracy due to accelerated imaging and the accompanying image degradation has to be found.

The aim of this study is the comparison of different view-sharing strategies to achieve a high temporal resolution during the initial kinetics interval. Using a numerical dynamic phantom, acquisitions with different k-space sampling strategies are simulated and their influence on K^{trans}, v_e and τ is studied.

5.2 State of the Art

In the following section, common DCE MRI acquisition techniques and view-sharing methods relevant for this chapter, which were partly already introduced in chapter 3, are described.

Imaging Contrast Changes with a GRE-Sequence

When contrast agent of the concentration $C(t)$ arrives in tissue, it has the effect of shortening the T_1-relaxation time as given by [Rosen1990]:

$$T_1(t) = \frac{1}{\frac{1}{T_1(0)} + r_1 C(t)}, \tag{5.1}$$

where r_1 is the relaxivity of the contrast agent and $T_1(0)$ is the T_1-relaxation time prior to CA arrival. The resulting steady-state signal $S(t)$ measured with a T_1-weighted spoiled GRE-sequence, can be expressed according to equation 2.51 as:

$$S(t) = M_0 \frac{(1 - e^{-\frac{TR}{T_1(t)}})sin(\theta)}{1 - cos(\theta)e^{-\frac{TR}{T_1(t)}}}, \tag{5.2}$$

when $TE << T_2^*$ is assumed. However, this equation is only a valid approximation when contrast agent changes occur slowly compared to the time to reach steady state.

Conversion from Signal to Concentration

To allow fitting of the Tofts model, the measured signal $S(t)$ has to be converted to the concentration time curve $C(t)$. An accurate estimate of $C(t)$ is achieved by using the variable flip angle method [Wang1987]. For this conversion, an additional proton density weighted (ρw) image prior to contrast administration is acquired. The T_1-weighted and ρ-weighted images only differ in the choice of flip angle of $\theta_{T_1 w}$ and $\theta_{\rho w}$.

The signal $S_{\rho w}$ can be mathematically described using equation 5.2 with flip angle $\theta_{\rho w}$ and $T_1(t) = T_1(0)$. The signal $S_{T_1 w,pre}$ of the T_1-weighted image before contrast agent arrival can be expressed using equation 5.2 with flip angle $\theta_{T_1 w}$ and $T_1(t) = T_1(0)$. From these two equations, the two unknowns M_0 and $T_1(0)$ can be extracted.

After contrast agent arrival, the signal $S_{T_1 w,post}$ is described using equation 5.2 with flip angle $\theta_{T_1 w}$. With the knowledge of M_0, $T_1(t)$ can be determined. Rewriting equation 5.1, $C(t)$ can be obtained from $T_1(t)$ by the relation:

$$C(t) = \frac{\frac{1}{T_1(t)} - \frac{1}{T_1(0)}}{r_1}, \tag{5.3}$$

where the previously calculated value of $T_1(0)$ is employed. The exact formulae of this conversion are given in appendix D.

Common Dynamic View-Sharing Methods

One way to increase acquisition speed during the initial kinetics is to omit certain *k*-space data. In this work, the following *k*-space view-sharing schemes, which have been introduced in section 3.5, will be employed:

- The keyhole technique [Vaals1993] can be used to reduce *k*-space data after a fully sampled reference image has been acquired. The keyhole technique is visualized in figure 5.1 a). The concept is to acquire a high spatial resolution reference image at baseline and update only the low *k*-space frequencies during contrast agent kinetics. The missing high *k*-space frequencies are copied from the reference image.

- Time resolved imaging of contrast kinetics (TRICKS) [Korosec1996] is used for data reduction after having acquired a fully samples reference image. The TRICKS

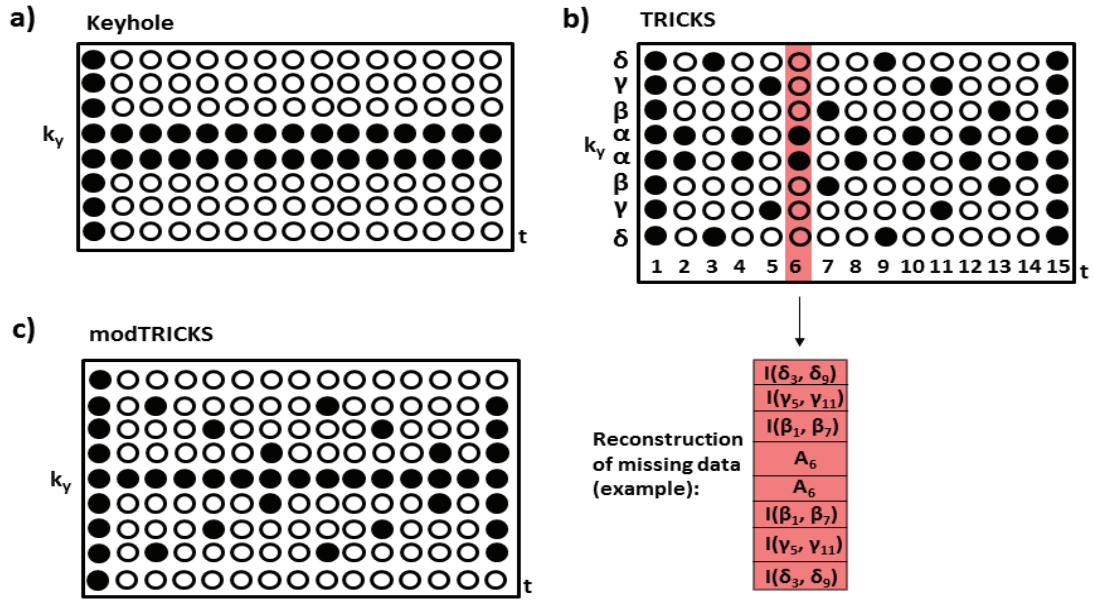

Figure 5.1: Schematic illustration of the accelerating sampling schemes during initial kinetics in k-space: a) Keyhole, b) TRICKS, c) modTRICKS. The black dots indicate data sampling. For TRICKS, an example of the interpolation is given for the 6th time frame, where $I()$ denotes linear interpolation. (adapted from [Taso2010] and [Korosec])

technique is shown in figure 5.1 b). k-space is divided into 4 regions denoted by α, β, γ and δ. Images are acquired according to the scheme α-δ-α-γ-α-β-α-δ-..., acquiring the k-space center section α at a higher frequency than the outer regions. The missing k-space sections are filled by linear interpolation between the neighboring time frames.

- A modified version of TRICKS (modTRICKS) can be used. This technique is a compromise between keyhole and TRICKS. Few low-frequency lines acquired at each time frame at the cost of applying keyhole for the highest frequencies. This is visualized in figure 5.1 c).

5.3 Methods

The aim is to investigate the influence of combined high/low temporal resolution sampling schemes using different acceleration techniques on PK parameter fitting accuracy. An overview of the employed methods is given in the flow chart in figure 5.2. First, a numerical dynamic phantom is generated. Data acquisition is simulated for different sampling schemes and the Tofts model is fitted to the data. For all schemes, the resulting mean PK values and parameter maps are compared. All of the methods are implemented

using Matlab 2012b (The MathWorks, Inc., Natick, Massachusetts, United States).

5.3.1 Numerical Phantom

Pharmacokinetic Parameter Maps

A numerical dynamic phantom simulating a tumor embedded in healthy tissue is created. Two-dimensional parameter maps of pixel-dimensions 64x64 of the parameters K^{trans} and v_e are created. Both maps can be seen in figure 5.3 a) and b). The onset time is set to $\tau = 1.5$min for all pixels. The mean PK parameter values $\bar{K}^{trans}$ and $\bar{v}_e$ are chosen such that they mimic the following structures: healthy tissue background ($\bar{K}^{trans} = 0.3\mathtt{min}^{-1}$, $\bar{v}_e = 0.3$), a tumor background with PK values of intermediate malignancy ($\bar{K}^{trans} = 1.2\mathrm{min}^{-1}$, $\bar{v}_e = 0.5$) and imbedded in the tumor structures of higher malignancy ($\bar{K}^{trans} = 2.0\mathtt{min}^{-1}$, $\bar{v}_e = 0.8$). A Gaussian variation of standard deviation (SD) $\sigma_{Map,K} = 0.1$ is added to the K^{trans}-map and of $\sigma_{Map,v} = 0.05$ to the v_e-map to produce ranges of varying PK parameters throughout the maps, making the distribution more realistic.

Dynamic Concentration Curves

Based on these PK parameter maps, concentration time curves $C(t)$ are generated for each pixel. This is performed using the Tofts model as given in equation 3.16. The parameters of the arterial input function (AIF) are assumed to be population-averaged as measured by [Walker-Samuel2007]. The assumed dose is $D = 0.1\mathrm{mMol{\cdot}kg}^{-1}$.

Simulating Imaging with a GRE-Sequence

For each pixel, $C(t)$ is converted to a signal intensity time curve $S(t)$ by calculating $T_1(t)$ according to equation 5.1, and simulating spoiled GRE imaging using equation 5.2.

The assumed parameters for tissue, contrast agent and the sequence are summarized in table 5.1. A series of T_1-weighted (T_1w) images, starting at baseline, is simulated for the dynamic imaging time T_{dyn}. Additionally, a single proton density weighted (ρw) image prior to contrast administration is generated for conversion from signal to concentration as described in section 5.2. The T_1w and ρw images only differ in the choice of flip angle of θ_{T_1w} and $\theta_{\rho w}$.

Regions Of Interest

Four regions of interest (ROI) of different sizes are chosen in areas of high malignancy, which are shown in figure 6.4 d). The sizes of the ROIs are: $\mathrm{ROI}_1 = 192$ pixels, $\mathrm{ROI}_2 = 64$ pixels, $\mathrm{ROI}_3 = 16$ pixels and $\mathrm{ROI}_4 = 4$ pixels.

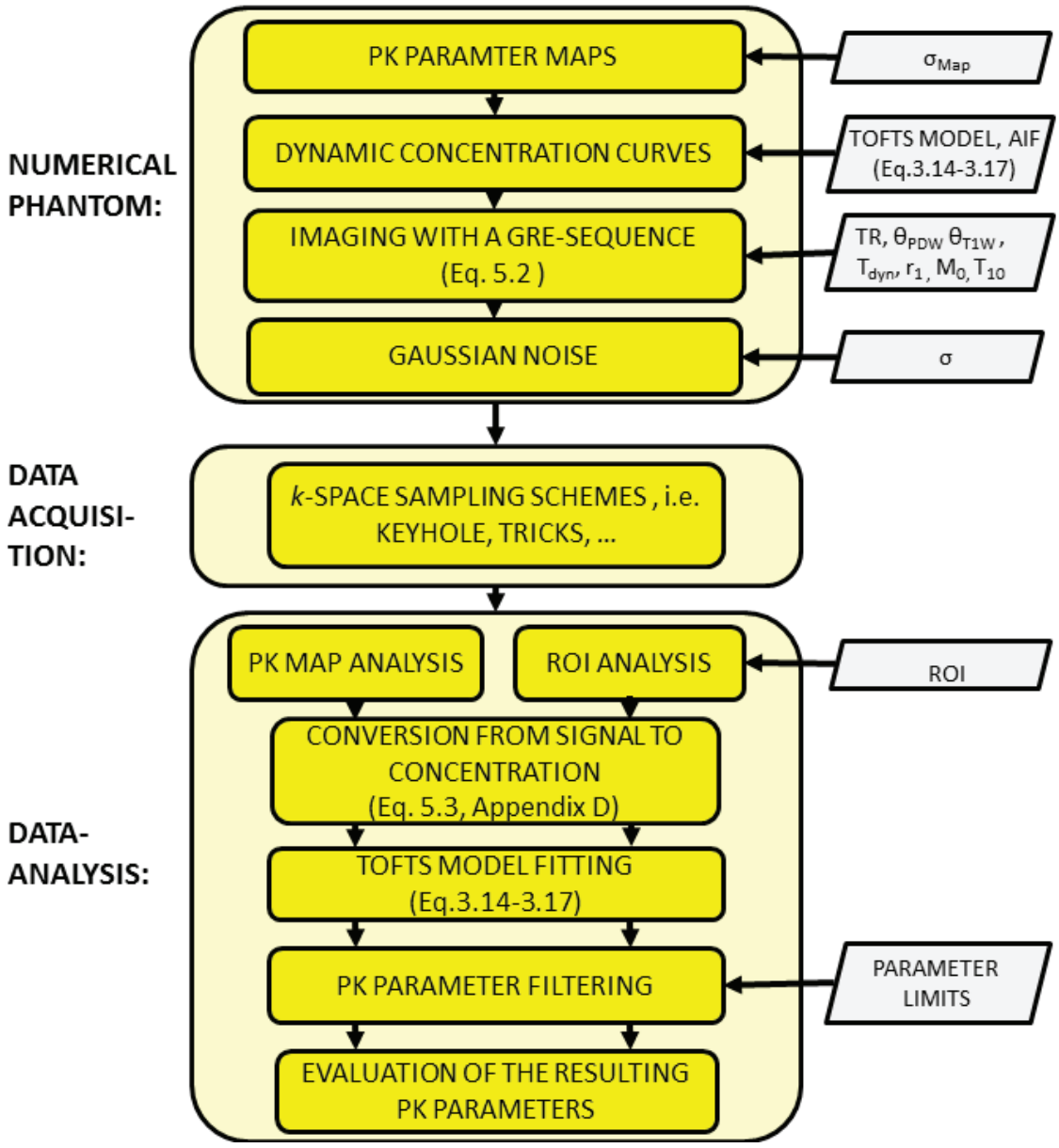

Figure 5.2: A dynamic numerical phantom is generated and acquisition with different k-space acquisition strategies is simulated. During data analysis, PK modeling is performed and the resulting PK parameters of the different schemes are evaluated and compared.

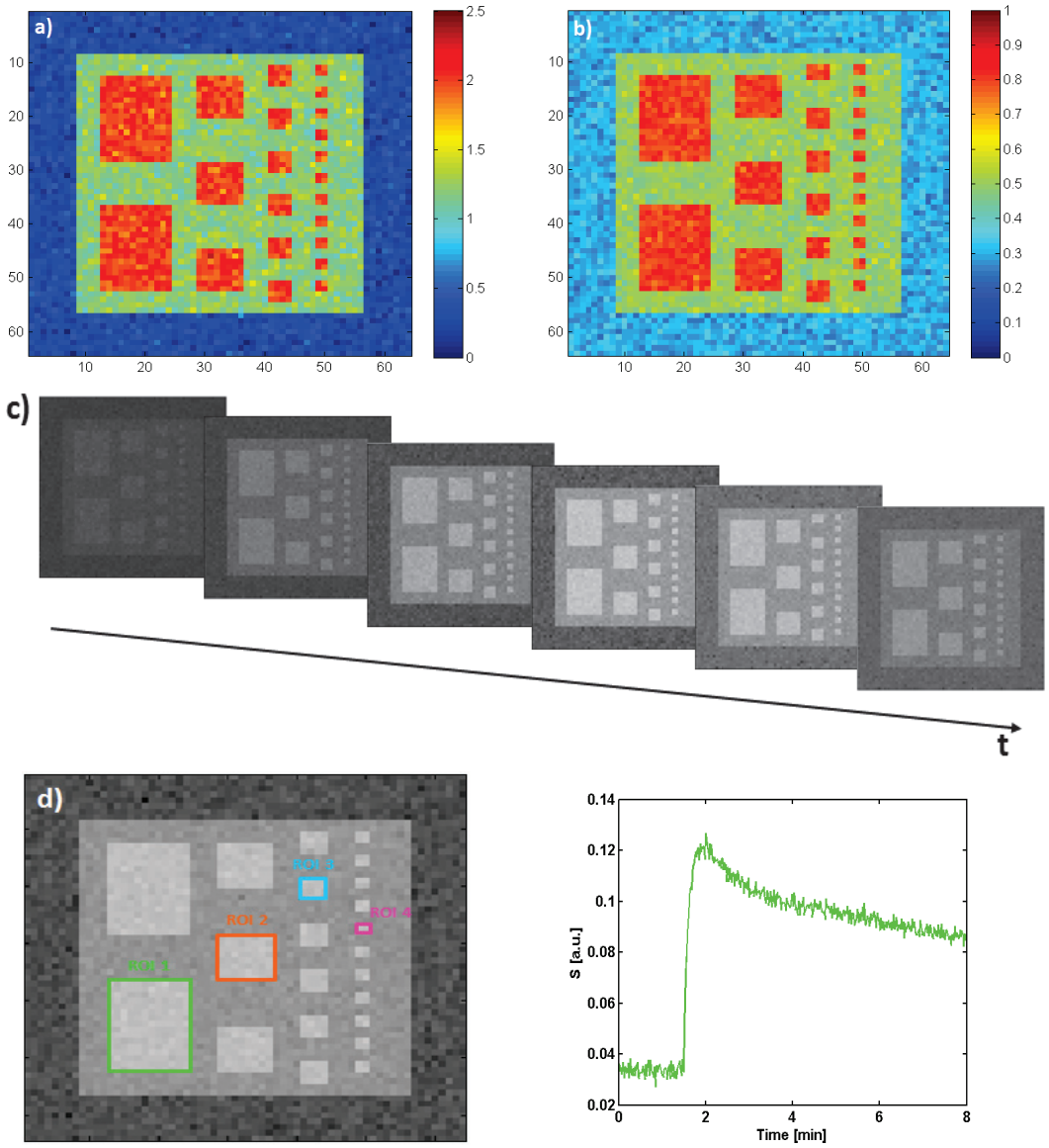

Figure 5.3: Pharmacokinetic parameter maps of a) K^{trans} and b) v_e used to create the numerical dynamic phantom. c) Example images of a phantom time series. d) ROI_1-ROI_4 used for data analysis. e) Example signal time curve from a pixel within ROI_4.

TR	5ms
T_{dyn}	8min
$\theta_{T_1w}/\theta_{\rho w}$	15°/2°
r_1	3.7mMol·s^{-1}
M_0	1
$T_1(0)$	1000ms

Table 5.1: Parameters of the simulated GRE-sequence, contrast agent and the phantom.

Gaussian Noise

Gaussian noise is added to the phantom to yield two different baseline signal-to-noise-ratios $\mathrm{SNR}_1 = 10$ and $\mathrm{SNR}_2 = 20$.

An example time series of the phantom is shown in figure 6.4 c), and the signal time curve $S(t)$ of a pixel within ROI_4 is shown in figure 6.4 e).

5.3.2 Simulated Data Acquisition

In this work, 5 different k-space acquisition schemes (A-E), amongst them the view-sharing methods described in section 5.2, are simulated and their influence on the resulting PK parameters is studied. In all schemes, a fully sampled Cartesian acquisition with high spatial and low temporal resolution Δt_{Cart} is used after the time $\tau + 2min$. This is schematically shown in figure 5.4. During the interval $[0, \tau + 2min]$, including baseline and initial kinetics, the following schemes are employed:

A) As a control, a fully sampled Cartesian scheme with equidistant temporal sampling at temporal resolution Δt_A throughout the whole dynamic imaging time is simulated.

B) The idealized, physically not possible case of fully sampled Cartesian imaging with an acceleration factor of 4 with $\Delta t_B = \Delta t_{Cart}/4$ is used as reference case for schemes C, D and E.

C) The keyhole technique is used to accelerate imaging by a factor of 4, leading to $\Delta t_C = \Delta t_{Cart}/4$.

D) The TRICKS technique is used to accelerate imaging by a factor of 4, leading to $\Delta t_D = \Delta t_{Cart}/4$.

E) A modified version of TRICKS (modTRICKS) is used to accelerate imaging by a factor of 4 leading to $\Delta t_E = \Delta t_{Cart}/4$.

In summary, the schemes B-E accelerate imaging during the interval $[0, \tau + 2min]$ by a factor of 4 in comparison to Δt_{Cart}.

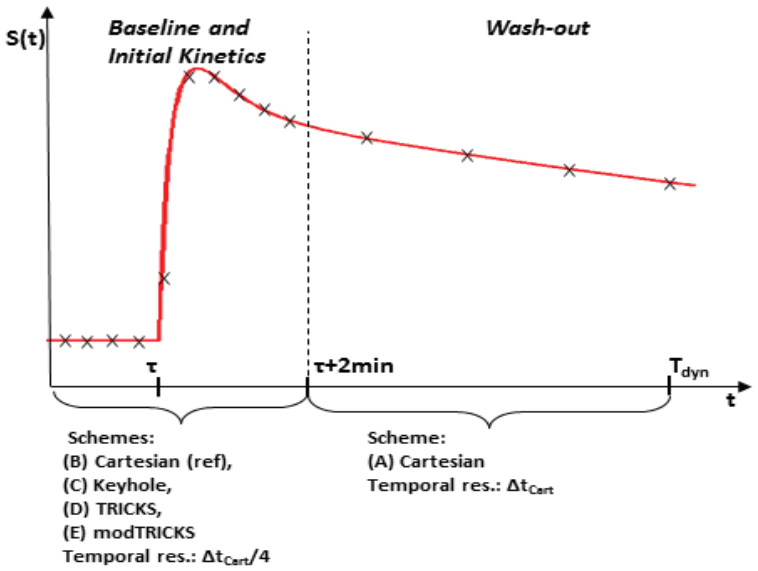

Figure 5.4: During the baseline and initial kinetics of the signal time curve phase, temporal resolution is increased by a factor of 4 in comparison to the wash-out phase. Different schemes (Cartesian (reference), Keyhole, TRICKS and modTRICKS are employed to accelerate imaging. Fully sampled Cartesian acquisition is used during wash-out.

5.3.3 Data Analysis

Tofts Model Fitting

To allow for Tofts model fitting, the measured signal $S(t)$ is converted to the concentration time curve $C(t)$ using the method described in section 5.2.

The Tofts model with fitting parameter set $\vec{p} = [K^{trans}, v_e, \tau]$ is fitted to the measured $C(t)$ using a Levenberg-Marquardt algorithm [Levenberg1944]. The initial estimates $\vec{p}_0$ are set to the original underlying PK parameter values.

PK Parameter Filtering

The resulting parameters are filtered for physiological plausible values as follows. Only results within the following ranges are considered as successful fits: $0\text{min}^{-1}<K^{trans}<4.0\text{min}^{-1}$, $0<v_e<1.0$. Values falling out of these ranges are classified as fitting failures and no value is assigned.

ROI Analysis

For schemes A-E, the mean signal intensity $S(t)$ of ROI_1 to ROI_4 is measured and converted to mean $C(t)$. The Tofts model is fitted to $C(t)$, yielding the mean parameters K^{trans}, v_e and τ of each ROI.

The temporal resolution Δt_{Cart} is varied from $\Delta t_{Cart} = 1$s to $\Delta t_{Cart} = 2$min in increments of 1s. The accelerated schemes have a corresponding temporal resolution of $\Delta t_{B,C,D,E} = \Delta t_{Cart}/4$. For each temporal resolution, the full procedure, including phantom generation, is repeated $N_{rep} = 50$ times. From the results of the N_{rep} repetitions, the relative mean $\bar{K}^{trans}_{rel}$, $\bar{v}_{e,rel}$ and $\bar{\tau}_{rel}$ and relative Standard deviations (SD) $\sigma_{K,rel}$, $\sigma_{v,rel}$, $\sigma_{\tau,rel}$ with respect to the original values is calculated. The process is repeated for SNR_1=10 and SNR_2=20. The resulting parameters $\bar{K}^{trans}_{rel}$, $\bar{v}_{e,rel}$ and $\bar{\tau}_{rel}$ along with $\sigma_{K,rel}$, $\sigma_{v,rel}$, $\sigma_{\tau,rel}$ are plotted against the temporal resolution Δt_{Cart}.

PK Map Analysis

For schemes A-E, PK maps of K^{trans} and v_e are generated at the fixed temporal resolution $\Delta t_{Cart} = 74s$ and $\Delta t_{B,C,D,E} = 18.5s$. For that, the same steps as for the ROI analysis are performed for each image pixel. Additionally, joint histograms of each map with the original PK maps are generated.

For each joint histogram, Pearson's correlation coefficient r, is calculated. Additionally, a linear function is fitted to the data in the joint histograms and its slope m is retrieved. Finally, for both, K^{trans} and v_e, the number of fitting failures f for each map is counted.

5.4 Results

ROI Analysis

The results of the ROI analysis can be seen in figure 5.5 for SNR = 10 and figure 5.6 for SNR = 20. The following behavior is observed:

- With increasing ROI size and increasing temporal resolution, systematic errors and standard deviations reduced.
- With increasing SNR, systematic errors and standard deviations decrease.
- K^{trans} exhibits the largest instability, showing the largest standard deviations and systematic errors amongst all schemes. v_e is the most stable parameter. τ is only unstable for scheme (A), otherwise it is a relatively stable parameter. A correlation between systematic errors in K^{trans} and τ can be seen.
- Comparison of scheme (A) and the reference scheme (B) shows that fast sampling during the initial kinetics phase improves fitting accuracy. Scheme (A) produces, following a zig-zag pattern, large systematic over-and underestimations in K^{trans} and a large σ_K. Using scheme (B), the relative mean K^{trans} for all Δt is centered around the original value and σ_K is significantly reduced. For v_e, small systematic errors can be seen for scheme (A), however for both schemes, the relative mean v_e value is close to 1 and σ_v is small. For scheme (A), large systematic over- and underestimation of τ with large σ_τ can be seen. Using scheme (B), the systematic errors and σ_τ are significantly reduced.

- The physically possible schemes (C), (D) and (E) reduce the standard deviations of the PK parameters, especially for K^{trans} and τ, compared to scheme (A) as well, however different systematic errors occur.

- Employing keyhole (C) leads to an increasing underestimation of K^{trans} with decreasing ROI size. For v_e the same effect can be seen, however on a smaller scale. τ shows similar results to those of scheme (B). For both K^{trans} and τ, an oscillating pattern can be detected, increasing in amplitude with increasing Δt_{Cart}.

- For TRICKS (D) abrupt changes can be seen with a tendency to underestimate K^{trans} and to overestimate τ, especially for large Δt_{Cart}. The results of v_e are comparable to those of scheme (B), showing only very small systematic underestimations.

- The modified TRICKS scheme (E) shows a combination of the effects of keyhole and TRICKS, but both are attenuated. A smaller underestimation than in scheme (C) and softer changes compared to scheme (D) are visible in K^{trans}. The results of v_e and τ are similar to those of scheme (B).

PK Map Analysis

The resulting PK parameter maps and joint histograms of K^{trans} are shown in figure 5.7 and of v_e in figure 5.8. The resulting values of r, m and the number of fitting failures f are summarized in table 5.2. The following behavior can be observed:

- With decreasing SNR, the maps become noisier and structures, especially small ones, are increasingly less recognizable. The joint histograms show a larger underestimation and the joint histogram clouds are more widely spread for the smaller SNR level. This leads leads to smaller values of r. Finally, fitting failures f increase with decreasing SNR. These effects are larger for K^{trans} than for v_e. For both SNR levels, all structures are visible in the v_e-maps. For K^{trans} at SNR_1=10, the two smallest structures disappear within the noise, even for the idealized scheme (B).

- v_e is found to be a more stable fitting parameter than K^{trans}. For v_e, the structures in the PK maps are better identifiable than for K^{trans}. The joint histograms of v_e display narrower clusters closer to unity, which leads to r values closer to 1. Furthermore, compared to K^{trans}, the v_e-fitting failures count f is smaller for the equidistant schemes and comparable for the adaptive schemes.

- Comparing the equidistant scheme (A) and the ideally accelerated scheme (B), a large improvement of the K^{trans} map quality is visible, especially for the higher SNR level. Whilst for scheme (A) many K^{trans} fitting failures occur, they are drastically reduced when using scheme (B). The joint histogram clouds of scheme (B) are narrower (r=0.99/0.84 at SNR 20/10) than for scheme (A) (r=0.76/0.77 at SNR 20/10). For SNR 20, the clouds of both schemes are oriented along unity ($m \approx 1$). At SNR 10, a tendency of underestimation can seen for scheme (A) with

m=0.96, which is reduced for scheme (B) with m=0.99. For v_e, there is only a small improvement, when scheme (B) is used at SNR 10. At SNR 20, a slightly larger improvement with respect to r (scheme (A): 0.86, scheme (B): 0.90) and m (scheme (A): 0.91, scheme (B): 0.96) is provided. Also the number of fitting failures is reduced.

- Using Keyhole (C), a blurring along the phase encoding direction is visible in both, the K^{trans} and v_e map. Due to that it is difficult to recognize the smallest squares as distinct structures. The parameter values of the small structures and the edges of the larger structures are underestimated. The joint histograms clusters are more blurred than those of scheme (B) (reduced r) with a slight underestimation tendency of the larger K^{trans} and v_e values (reduced m). f is reduced in comparison to scheme (A) and comparable to that of scheme (B).

- For the TRICKS scheme (D), the intermediate and malignant K^{trans} values are largely underestimated (small m). Nevertheless, the structures of all sizes are clearly visible. The underestimation shows as well in the joint histograms, where a systematic underestimation with narrow clusters (r close to 1 for SNR 20) can be seen. This effect is not observed in the v_e-maps. The number of fitting failures is comparable to scheme (B).

- In the resulting K^{trans}-maps of modTRICKS (E) a slight underestimation of small structures is visible, however it is less pronounced than for scheme (C). Blurring in phase-encoding direction is as well visible, but clearly reduced compared to scheme (C), showing all structures clearly delineated for the high SNR level. In comparison to schemes (C) and (D), modTRICKS provides the joint histograms with the largest similarity to scheme (B). The v_e-map is in good agreement with the original map. Of all three feasible accelerated schemes it is also the scheme with the value of both, r and m, being closest to that of scheme (B). For v_e, r and m are comparable to scheme (B). Finally, f is as well similar to that of scheme (B) for both parameters

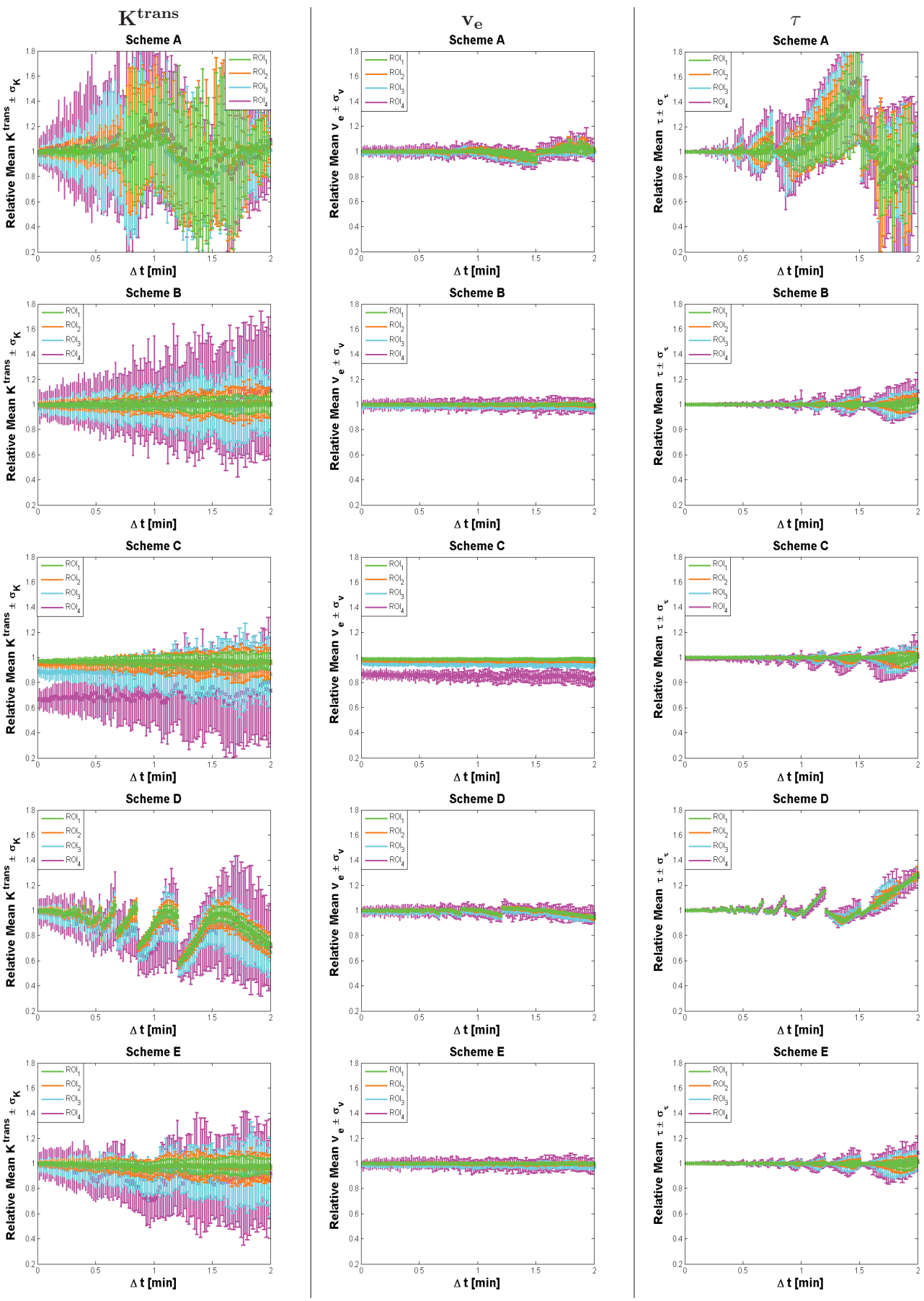

Figure 5.5: Relative mean K^{trans}, v_e and τ with standard deviations σ_K, σ_v and σ_τ versus Δt_{Cart} ($\Delta t_{B,C,D,E} = \Delta t_{Cart}/4$) for different acquisition schemes (A)-(E) of 4 ROIs at SNR_1=10.

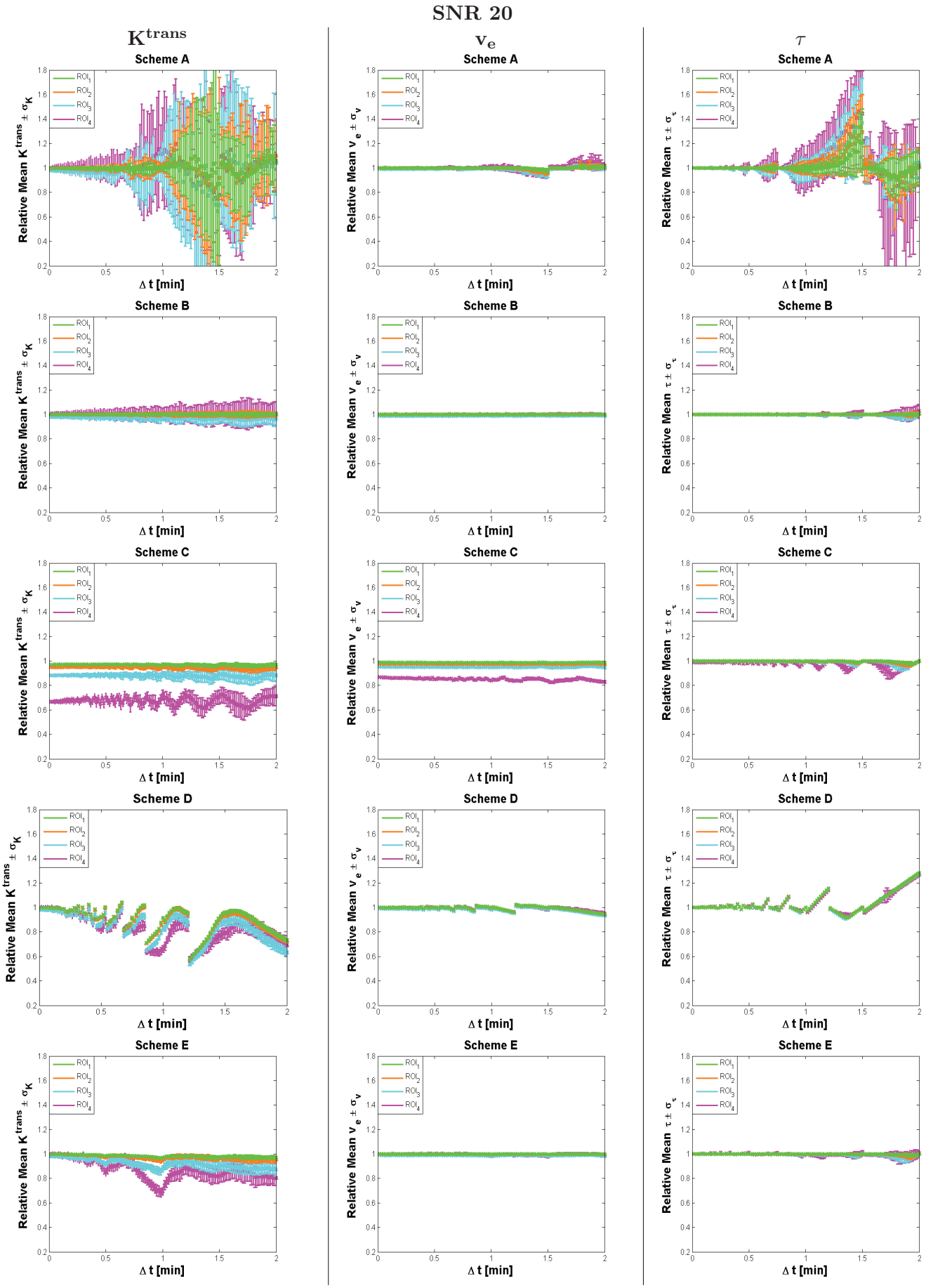

Figure 5.6: Relative mean K^{trans}, v_e and τ with standard deviations σ_K, σ_v and σ_τ versus Δt_{Cart} ($\Delta t_{B,C,D,E} = \Delta t_{Cart}/4$) for different acquisition schemes (A)-(E) of 4 ROIs at SNR_2=20.

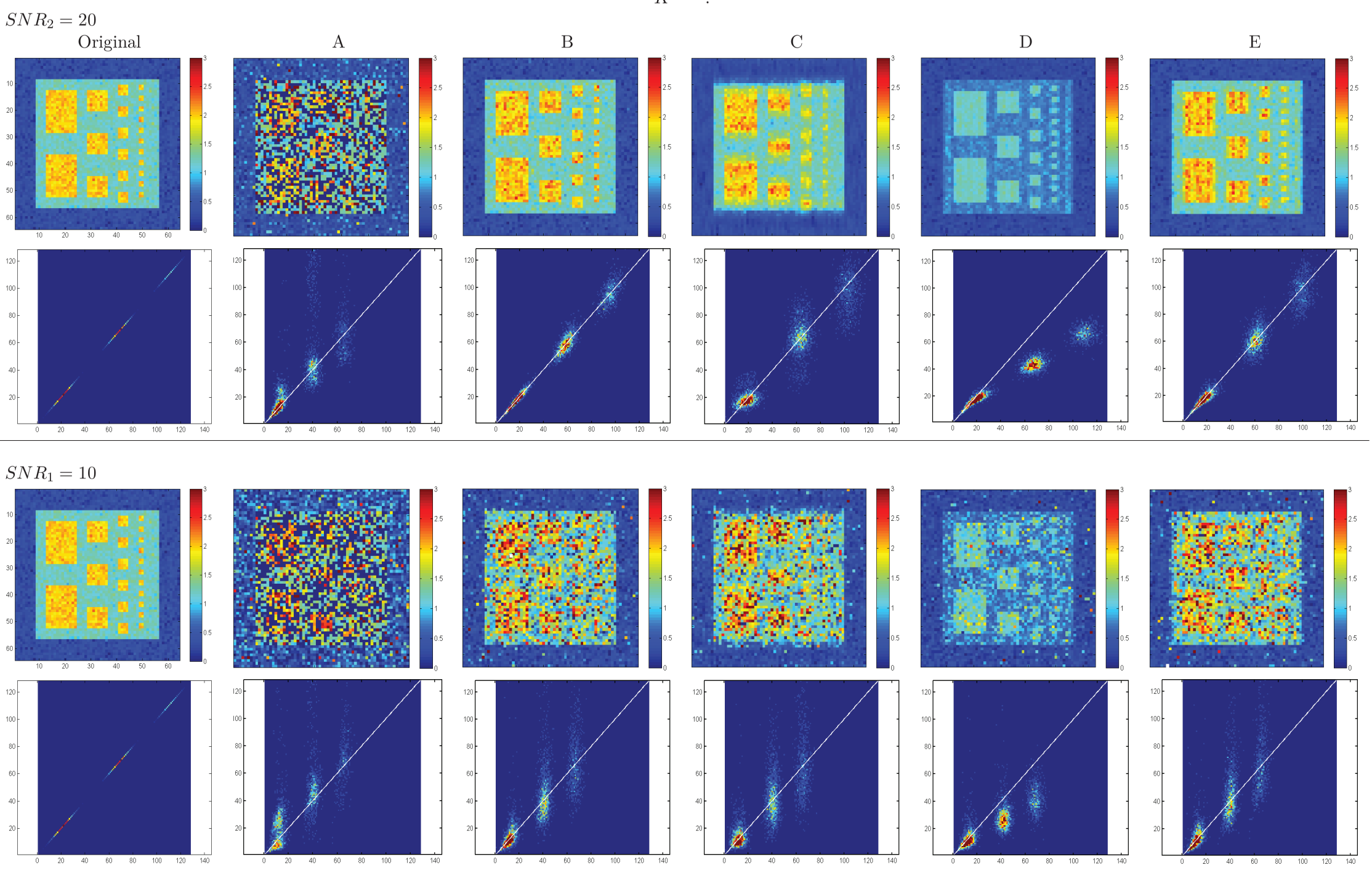

Figure 5.7: Resulting K^{trans} maps and joint histograms with original K^{trans} map for SNR_1 and SNR_2.

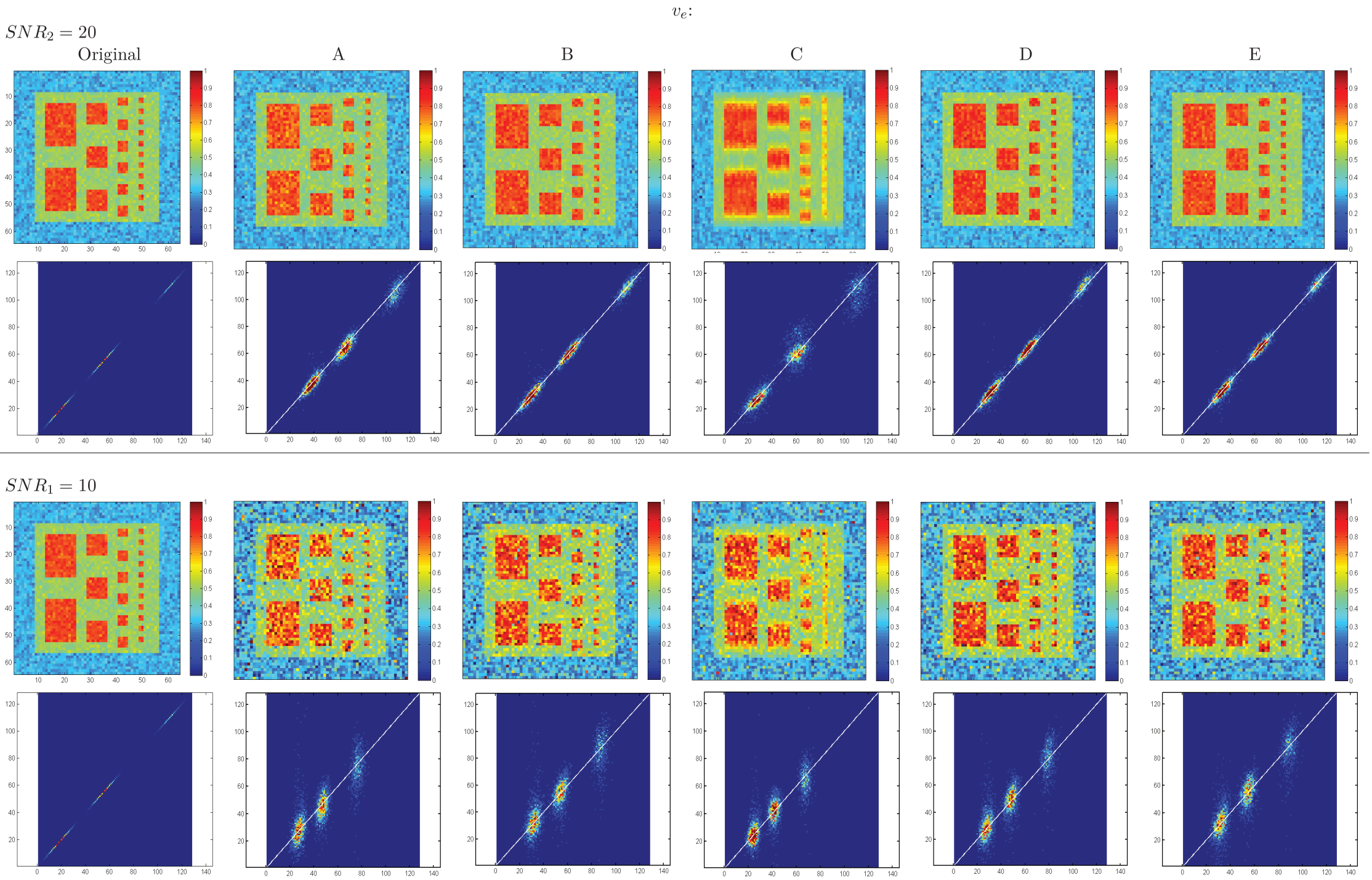

Figure 5.8: Resulting v_e maps and joint histograms with original v_e map for SNR_1 and SNR_2.

$SNR_2 = 20$		A	B	C	D	E
K^{trans}	r	0.76	0.99	0.94	0.98	0.97
	f	863	0	0	0	0
	m	1.01	1.00	0.92	0.54	0.98
v_e	r	0.98	0.99	0.97	0.99	0.99
	f	6	6	4	2	6
	m	0.97	0.99	0.95	1.01	1.00
$SNR_1 = 10$		A	B	C	D	E
K^{trans}	r	0.77	0.84	0.81	0.81	0.82
	f	1291	89	69	12	95
	m	0.96	0.99	0.94	0.52	0.96
v_e	r	0.86	0.90	0.88	0.90	0.91
	f	56	30	13	37	27
	m	0.91	0.96	0.95	0.98	0.97

Table 5.2: Pearson's correlation coefficient r and slope m of the joint histograms of K^{trans} and v_e and the number of fitting failures f in the PK maps for all schemes A, B, C, D, E at two different SNR levels.

5.5 Discussion

Other simulation-based studies have investigated the parameter accuracy in quantitative DCE MRI, for example [Henderson1998], [Heisen2010], [Laue2010]. However, this study is the first to investigate the effects of adaptive sampling schemes with changing temporal resolutions. In this work, the influence of different accelerated k-space sampling schemes during the initial kinetics phase on PK parameter fitting accuracy is investigated.

Using a dynamic numerical phantom, it has been shown that the PK parameter accuracy is improved when data are sampled with high frequency during the initial kinetics. Whereas with an ideally accelerated scheme only small systematic errors occur, feasible accelerated schemes introduce additional systematic errors, all having the tendency to underestimate K^{trans}. It is found that, of all evaluated schemes, the modTRICKS scheme shows the most accurate performance.

It is also observed that K^{trans} is an unstable fitting parameter, whilst v_e is more stable. The onset time τ is stable for all accelerated schemes and only shows large errors and standard deviations for the temporally equidistant scheme. Furthermore, it is found that the fitting accuracy is highly dependent on the data noise. In the following, the employed methods and obtained results will be discussed.

ROI and PK Map Analysis

The results of the PK map analysis are consistent with those of the ROI analysis.
It can be seen from both analysis methods, that the SNR has a high influence on the

parameter accuracy, for both, the equidistant and the accelerated schemes. The large discrepancy between the results of the two different SNR levels shows the important role played by SNR for improved fitting accuracy. This is in good agreement with the results from chapter 4. Also the fact that K^{trans} is the most sensitive parameter, whilst v_e is more stable and that, for large Δt_{Cart}, τ is only stable for the accelerated schemes, are consistent with the results from chapter 4.

Evaluating the ROIs, it was found for all schemes that the systematic errors and standard deviations decrease with increasing ROI size. This is due to more data averaging for larger ROIs.

When schemes (A) and (B) are compared, scheme (B) shows an improved fitting performance for K^{trans} and τ. For v_e, both schemes provide good fitting results and scheme (B) shows only a slight improvement. This is also in good agreement with the results of chapter 4. Dependent on the temporal location of the missing data points during the baseline and initial kinetics for scheme (A), the onset time can be over- and underestimated. This effect increases with decreasing temporal resolution. The combination of the false estimate of τ and the location of data sampling points during the upslope and the peak cause over-and underestimations of K^{trans}. In scheme (B), data are collected at many for fitting relevant time points, which leads to improved fitting accuracy.

When employing feasible sampling schemes, image quality is degraded compared to the idealized scheme. This introduces an additional source of fitting errors.

For small structures, the Keyhole technique (C) causes a systematic underestimation in K^{trans} and a smaller systematic underestimation in v_e. Since the high frequency data of the dynamic images are filled with the outer k-space areas of the baseline image, the signal in these areas is underestimated during contrast agent kinetics. The smaller the structure is, the more the signal is affected by the high frequencies. This leads to a high underestimation of K^{trans} and a small underestimation of v_e during fitting. The onset time is hardly affected by the underestimation of the signal and τ is therefore a stable fitting parameter.

Using TRICKS (D), missing k-space lines are linearly interpolated. Dependent on where sampling points are located, signal intensity during the initial kinetics is either enhanced or attenuated. Dependent on the location of these data points on the baseline, the upslope and the peak, this can abruptly change the fitting results of K^{trans} and τ. v_e is relatively uninfluenced since the wash-out phase of the curve is well recovered by linear interpolation due to slow signal changes. An overestimation of τ is correlated with an underestimation of K^{trans}. This occurs mainly when the signal intensity during the upslope is underestimated.

modTRICKS (E) shows combined effects of Keyhole and TRICKS, however both are attenuated. Even though it still produces a systematic underestimation of K^{trans}, it is the accelerated scheme which resembles scheme (B) most. Therefore, amongst the investigated schemes, scheme (E) shows the best performance.

A danger of all of the accelerated schemes investigated here is, that especially K^{trans} values are likely to be underestimated. In a clinical context this would mean that areas

of malignancy appear more benign in the PK maps. This could potentially lead to an erroneous classification of a tumor as being a benign lesion and should be considered when using accelerated schemes in practice, especially for small structures.

Limitations of the Simulation

In this work, an ideal numerical phantom and a simulated acquisition are employed. However, in a more realistic environment, many sources of errors will occur, which have not been taken into account here.

For example, B_0 and B_1 field inhomogeneities result in flip angle inaccuracies [Sung2013], leading to T_1 estimation errors and consequently causing errors in the calculated concentration. Other image artifacts, for example due to motion, also corrupt fitting accuracy.

Regarding the simulated sequence, k-space data of one temporal frame is assumed to be sampled instantaneously at a single time point. In reality, signal changes occur from one phase-encoding line to the next, causing temporal blurring. Heisen *et al* [Heisen2008] have shown that this fact should be considered in simulations. However, in Cartesian imaging, the k-space center predominantly determines the image contrast. Therefore, assuming instantaneous acquisition is at least a reasonable approximation.

As a large simplification, the same function is used for phantom simulation and model fitting. In reality this is not the case, since the Tofts model might not perfectly describe the dynamic curves.

Eventually, the currently employed numerical phantom takes only a narrow range of pharmacokinetic parameters and structures into account. If other parameter values are of interest, the methods of this chapter can be straightforwardly applied to other numerical phantoms.

Principal Limitations of the Used Methods

In the simulations, a constant onset time τ is assumed. However, in reality contrast agent can arrive at largely varying onset times within the tissue. In this case, the adaptive sampling is not optimized for regions of interest, in which τ deviates strongly from the expected value.

The Tofts model is assumed as underlying model. Within the scope of this chapter this is the known ground truth. However, with respect to organic tissue, the Tofts model is only a crude simplification of reality, which might not hold as an appropriate mathematical description. Furthermore, the Tofts model parameters used here are only based on literature values and could deviate from realistic parameter values. The methods of this chapter, however, can be straightforwardly repeated using a different model or underlying model parameters.

The employed Tofts model assumes a simplified population-averaged arterial input function. In an *in vivo* experiment, this can be potentially a large source of error for model fitting [Cheng2008]. A better approach is to measure an AIF estimate, for example in a large artery, which provides a more accurate description of the individual physiology.

Finally, the assumed relationship between concentration and T_1-changes is only an approximation. It is only true if contrast agent instantaneously interacts with all the water in the tissue. In reality, more complex exchange processes take place.

6 Perfusion Phantom

6.1 Introduction and Motivation

The optimization and validation of new sequences for DCE MRI require image acquisition of volunteers during contrast agent administration. This scenario is in a practical sense not always feasible due to ethical consideration, economical constraints, as well as the equipment and training required and potentially poor reproducibility. A good solution to these problems is to use a perfusion phantom. No ethical considerations are required here and a better repeatability is provided.

However, there is a lack of perfusion phantoms in the MR community. Only few publications exists presenting perfusion phantoms, such as [Ebrahimi2010], [Driscoll2011] and [Freed2011]. Few of them are commercially available and in general they are difficult to rebuild.

In this work, a perfusion phantom is developed. The main purpose of the phantom is to reproducibly generate dynamic signal curves with temporal changes in the order of typical breast DCE MRI data and to quantitatively describe these changes. The phantom is employed to assess and evaluate the sequences which will be the topic of chapter 7 and 8. The experimental setup, example data, a quantitative description of the pharmacokinetic properties of the phantom and a characterization of its reproducibility are presented in this chapter.

6.2 Methods

6.2.1 Experimental Setup

A perfusion phantom is constructed, which will be described here. The experimental setup is displayed in figure 6.1 a) and the phantom itself is schematically shown in figure 6.1 b).

A hose of external diameter d=8 mm is connected to a water source, and leads to the phantom inside the scanner. Water flow is turned on and regulated such that water has a flow velocity of approximately v=20 cm/s, which approximately resembles blood flow velocity through large arteries inside the human body [Gabe1969].
In close proximity to the phantom, two syringes join the main hose via a valve. One of the syringes is filled with contrast agent. Here, a copper sulfate ($CuSO_4 \cdot 5H_2O$) solution at a concentration of 60 mMol/kg is used as contrast agent. The administered dose is 50 ml. The other syringe contains water to flush the hose after contrast agent

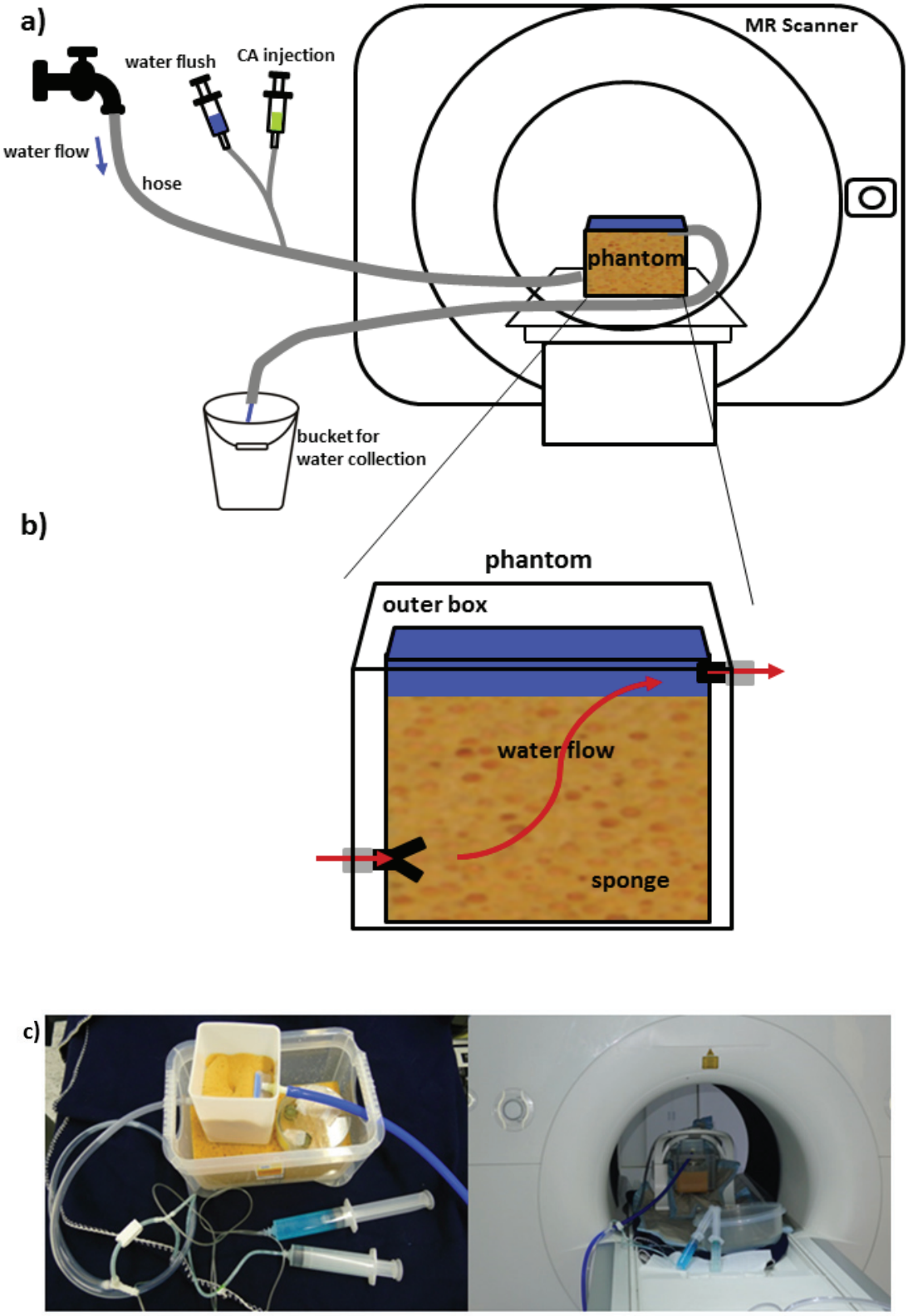

Figure 6.1: a) Experimental setup of the perfusion phantom experiment. b) The perfusion phantom. c) Images of the perfusion phantom and the installation inside the MR scanner.

TR [ms]	8.34
TE [ms]	3.99
α [°]	15
# Slices	1
Slice Thickness [mm]	20
Pixel Bandwidth [Hz/Px]	500
FOV [mm]	250 x 250
Spatial Resolution [mm]	0.78 x 0.78
Slice Orientation	coronal
Temporal Resolution [s]	2.67
Total Imaging Time [s]	216.3

Table 6.1: Sequence protocol used to acquire phantom data.

administration to counteract bolus dispersion. Both, contrast agent and flush bolus are administered manually.

The hose leads to the phantom inside the scanner. The phantom is surrounded by a plastic box, to which the hose is attached by a connector. To better distribute the incoming water, the connector is divided into two end-pieces at the inner side of the box. The phantom itself consists of a sponge, which fills a plastic box, leaving an unfilled area at the top of the box. On the opposite side of the box another connector is attached to a hose used for outward flow. Whilst the incoming connector is placed near the bottom of the box, the outgoing connector is located at a high level close to the top of the box. This arrangement guarantees that the water has to travel through the phantom before being washed out. The water that comes in travels through the sponge and is washed out by newly arriving water. The outflowing hose directs the water into a bucket outside the MR scanner, where it is collected. To prevent leakage into the scanner, a second plastic box is placed around the phantom for protection.

Images of the phantom and its installation inside the MR scanner can be seen in figure 6.1 c).

6.2.2 Acquisition of Phantom Data

All data is acquired on a commercially available 3T whole-body MRI system (Magnetom Skyra, Siemens Medical Solutions, Erlangen, Germany). Signal excitation is performed with the body coil and a 20 channel head coil is used to receive the resonance signal. Dynamic images of the phantom during contrast agent administration are acquired with a T_1-weighted GRE-sequence. The sequence protocol is summarized in table 6.1. Twenty example images of an acquired time series are displayed in figure 6.2.

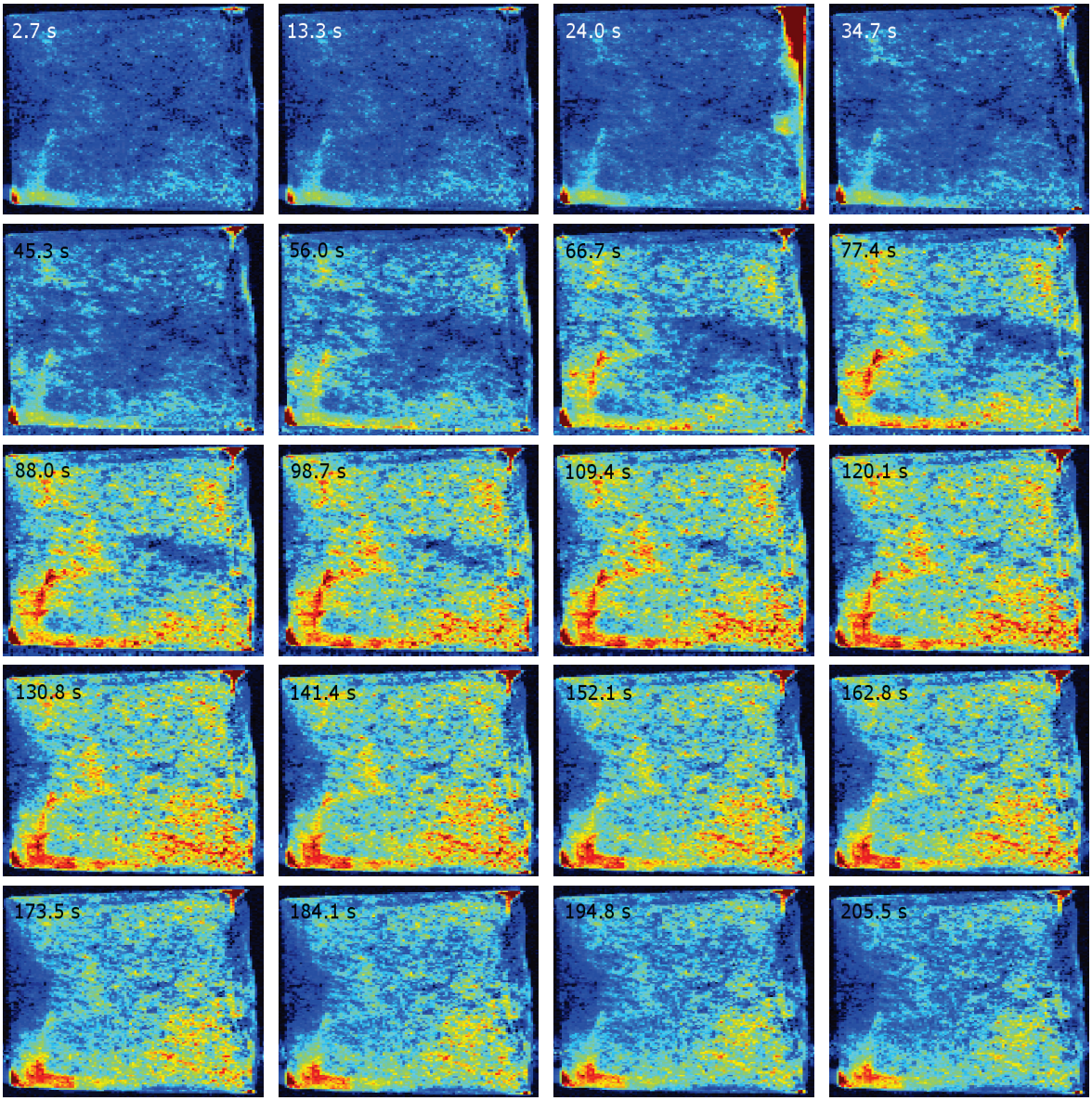

Figure 6.2: Dynamic series of a coronal slice of the perfusion phantom at various time points.

6.2.3 Quantitative Analysis

In previous studies, the gamma-variate function has been used to mathematically describe the pharmacokinetic behavior of a tracer. For example in [Zhu2011] the gamma-variate function is used to characterize the AIF for DCE MRI of the prostate. In [Benner1997], the gamma-variate function is fitted successfully to the concentration time curves from dynamic susceptibility-contrast enhanced MRI. Here, the gamma-variate function $\Gamma(t)$ is fitted to the signal time curves $S(t)$ of each image voxel using a Levenberg-Marquardt fitting routine. Examples can be seen in figure 6.3, where normalized signal time curves $S(t)$ of 6 randomly chosen image voxels are displayed. A simplified version of the gamma-variate function is used, which is more robust to fitting errors than the original formulation of the gamma-variate function [Chan2004]:

$$\begin{aligned} \Gamma(t) &= \epsilon && ,t \leq \tau \\ \Gamma(t) &= \epsilon + (\Gamma_{max} - \epsilon) e^{\alpha(1-\frac{t-\tau}{t_{max}-\tau})} (\frac{t-\tau}{t_{max}-\tau})^{\alpha} && ,t > \tau, \end{aligned} \tag{6.1}$$

where ϵ is the baseline signal value, τ is the onset time, Γ_{max} is the maximum of $\Gamma(t)$, t_{max} is the time of the maximum and α is a shape parameter. $\Gamma(t)$ is fitted to the normalized measured signal time curves $S(t)$ of each voxel in a chosen ROI to produce parameter maps of the parameters ϵ, τ, α, t_{max} and Γ_{max}.

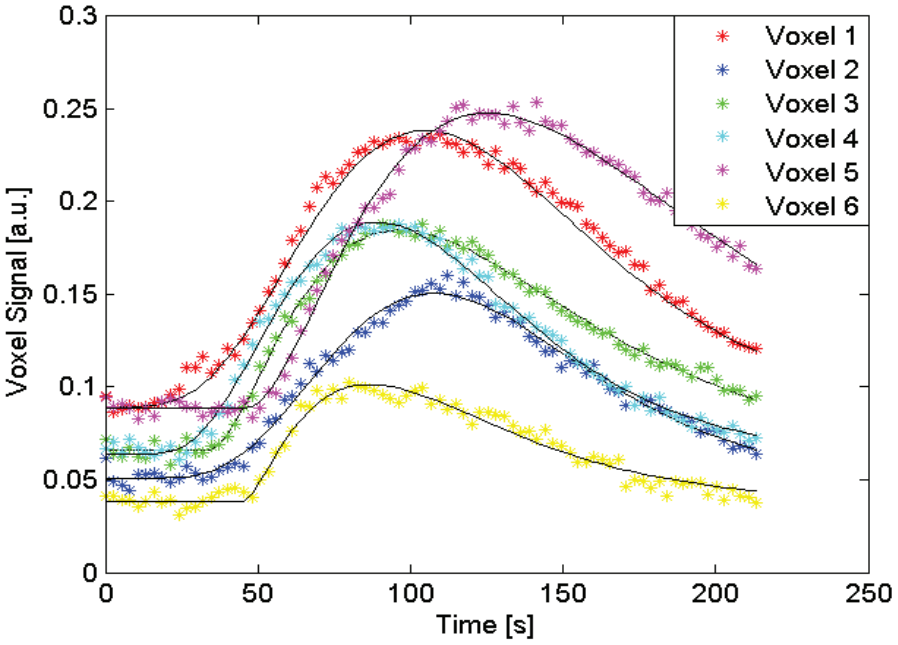

Figure 6.3: Normalized signal time curves $S(t)$ of example voxels and corresponding gamma-variate fits (black line).

The following steps are performed to provide initial parameter guesses $p_{j,init}$ for model fitting:

- ϵ_{init}: The initial baseline estimation is set to $\Gamma(t_3)$, where steady state has been reached.
- $\Gamma_{max,init}$: The initial maximum estimation is set to the maximum of all measured data along a curve.
- $t_{max,init}$: The initial maximum estimation is set to the time of $\Gamma_{max,init}$.
- τ_{init}: Going from $t_{max,init}$ towards decreasing times, the time τ_{init} is found at which $\Gamma(\tau_{init}) < \epsilon_{init} + 0.3 \cdot (\Gamma_{max,init} - \epsilon_{init})$. The value 0.3 is chosen based on experience from previous repetitions of the experiment, taking noise and motion artifacts during contrast agent administration into account.
- α_{init}: The initial estimation of α is set to 1. Testing different values, this has been shown to be a suitable starting parameter.

The resulting pharmacokinetic maps are filtered as follows to exclude fitting failures. Only values within the following ranges, which are assumed based on experience to provide reasonable fitting results, are taken into account:

- $0.0 \leq \epsilon \leq 0.2$
- $0.0 \leq \tau \leq 200.0$ ms
- $0.0 \leq \alpha \leq 150.0$
- $0.0 \leq t_{max} \leq 200.0$ ms
- $0.0 \leq \Gamma_{max} \leq 0.4$

If a value falls outside these ranges, the parameter is classified as 'fit failure' and no value is assigned.

6.2.4 Reproducibility Study

To be able to compare the results of repeated perfusion phantom experiments, it is indispensable that the phantom produces reproducible results.

Here, to test the reproducibility of the phantom experiment, the same experiment is repeated twice with the same sponge. For each repetition, PK maps are generated and joint histograms for the same parameters of each repetition are calculated.

For each joint histogram, Pearson's correlation coefficient r is calculated. r provides a quantitative measure for the reproducibility. The closer r is to 1, the better the reproducibility.

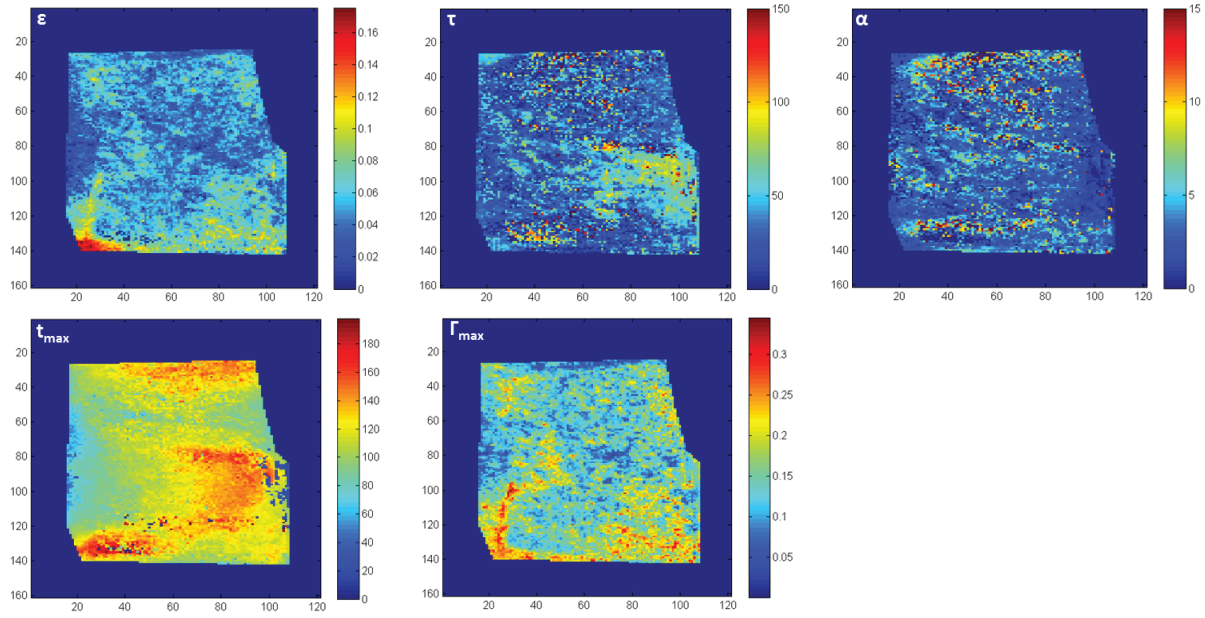

Figure 6.4: Resulting pharmacokinetic maps of the gamma-variate parameters ϵ, τ, α, t_{max} and Γ_{max}.

6.3 Results

6.3.1 Example Phantom Data and Quantitative Analysis

A dynamic series of a coronal slice of the perfusion phantom at various time points is presented in figure 6.2. Dynamic changes due to contrast agent arrival and wash-out are visible.

In terms of inter-voxel variability, large variations in curve shape are observed. This can be seen in figure 6.3 for 6 random voxels. However, all variations are accurately modeled by the gamma-variate function. The resulting filtered parameter maps of the parameters ϵ, τ, α, t_{max}, Γ_{max} are shown in figure 6.4. They show heterogeneous parameter distributions with clusters of similar PK parameter values.

6.3.2 Reproducibility

The joint histograms in figure 6.5 all have an orientation approximately along unity. For ϵ, the data cloud is very narrow and r is 0.97. The joint histograms of τ and α are largely spread out to both sides of the diagonal with r taking the values 0.79 and 0.81. For t_{max}, the cloud is very narrow with r being 0.99. The joint histogram of Γ_{max} is relatively narrow and points along the diagonal with r=0.95.

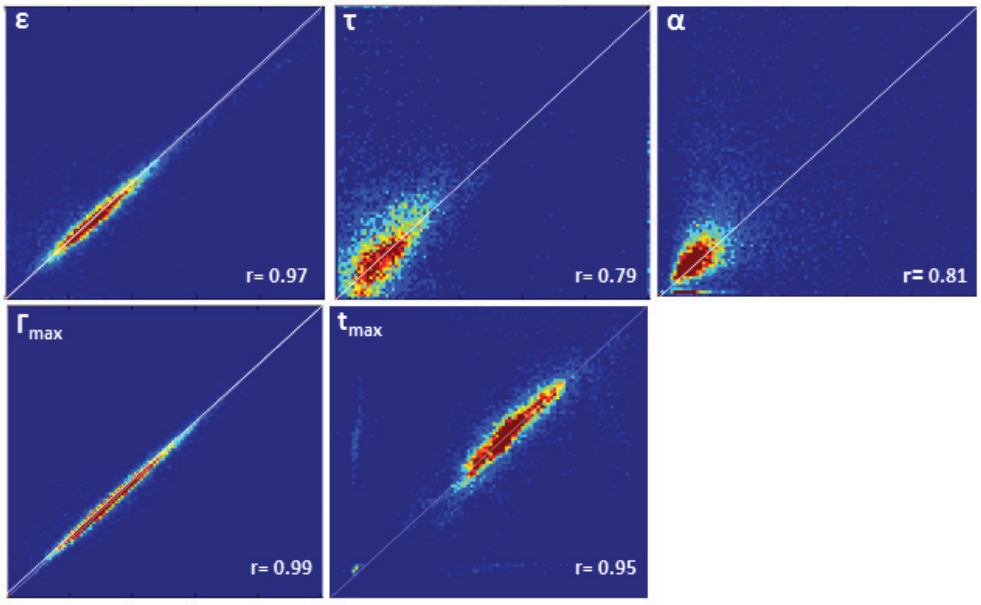

Figure 6.5: Joint histograms and Pearson's correlation coefficient r of the PK maps of ϵ, τ, α, t_{max} and Γ_{max} between two repetitions.

6.4 Discussion

In this work, a perfusion phantom allowing contrast agent administration is developed for sequence optimization and validation. The quantification, reproducibility, limitations and a comparison to *in vivo* data will be briefly discussed in the following.

Quantitative Analysis and Reproducibilty

The dynamic changes can be quantitatively described in good approximation using a gamma-variate function. For most voxels reasonable fitting results are achieved and PK maps can be produced. Only for some voxels the fitting procedure is not successful since the curve shape is distorted due to artifacts, mainly caused by motion during contrast agent administration.

From the joint histograms and the resulting values of r it can be seen that ϵ, t_{max} and Γ_{max} are well reproducible fitting parameters. τ and α are less reproducible, however still their reproducibility is still acceptable.

Limitations and Improvements

The experiment is relatively well reproducible. Deviations between the two repetitions arise from inaccuracies in the timing between contrast agent injection and the start

time of imaging. The boli are injected manually, making the injection rate not exactly reproducible. Furthermore, motion artifacts occur when the valve is opened and the syringes are lifted. An approach to overcome these errors could be the usage of a power injector as it is used in a clinical setup instead of manual injection. By that, the timing and the injection rate might be more accurately defined and motion artifacts would be avoided.

With multiple injection over time, contrast agent accumulates in the sponge, leading to a change in the baseline and the PK properties of the phantom. Finally, artifacts such as flow artifacts do not occur in the same way during each repetition.

Phantom Data Compared to *in vivo* Data

Performing the presented perfusion phantom experiment, dynamic changes are induced by contrast agent kinetics such as in organic tissue. By adjusting the velocity of inflowing water to a value similar to the blood flow in large arteries [Gabe1969], an approximately realistic time scale can be achieved. The time scale of a typical breast DCE MRI measurement is 5-8 min. The time scale of the phantom experiment is 3-4 min.

In reality, a tumor is a heterogeneous structure, displaying various physiological properties at different locations. With this perfusion phantom this is also the case due to varying densities of the sponge by compressing it during placement in the box. As with lesions, neighboring areas display similar PK properties.

The phantom data can be quantitatively described using a gamma-variate function. This is a function often encountered when modeling physiological processes. In MRI, gamma-variate functions are suitable to model measured arterial input functions [Zhu2011]. It is also used to describe signal changes measured with dynamic susceptibility contrast (DSC) MRI [Chan2004]. Therefore, with the perfusion phantom, physiologically realistic processes are mimicked. The gamma-variate is a typical function for models using one compartment such as the vascular space to describe underlying physiological processes.

However, as described in chapter 3, typical DCE MRI data can be better described using two-compartment models, such as the Tofts model, showing generally as slower wash-out than the gamma-variate function. This a large drawback of this phantom for DCE MRI investigations. To better simulate an DCE MRI experiment, typical tissue curves such as in the phantom from [Freed2011] would be more appropriate. However, for the scope of this thesis, where the phantom is used for sequence development and proof-of-principle studies, the current phantom is sufficient.

7 Real-time Automatic Resolution Adaption (AURA) for DCE MRI

7.1 Introduction and Motivation

In both, chapter 4 and 5, the importance of rapid data acquisition at the onset time and the upslope in terms of fitting accuracy has been shown. However, the onset time is dependent on the physiological condition of the patient and the timing of imaging relative to contrast agent injection, and therefore it is not *a priori* known when the initial kinetics starts.

Furthermore, the results of chapter 4 indicate that fast sampling should occur for 2 min after the onset time. However, this is just an estimate based on the assumed parameter distribution in chapter 4. In reality, this distribution of PK parameter might largely vary for different patients and it is not known prior to imaging when the wash out phase begins. If the sequence is switched too late to high spatial resolutions, contrast agent could be partially washed out, and important architectural features might be missed.

In the current clinical sequences, resolution changes occur at fixed predefined time points. These rigid implementations do not allow for adaption to patient-specific sampling requirements.

In previous studies, real-time automatic contrast agent (CA) bolus detection in vessels was introduced [Ho1999], [Goto2013]. In this work, this concept is extended to an automatic resolution adaption (AURA) sequence. Acquired dynamic data are analyzed in real-time to find the onset and the beginning of the washout and consequently temporal resolution is automatically adapted by alteration of spatial resolution.

In this study, the prototype of such an AURA sequence is developed and validated using the perfusion phantom described in chapter 6. Additionally, based on the perfusion phantom, the AURA sequence is compared to a fast sequence with only high temporal/low spatial resolution and to a slow sequence with only low temporal/high spatial resolution in terms of fitting accuracy and morphological information.

7.2 Methods

7.2.1 Hard- and Software

All experiments in this chapter are conducted on a commercially available 3T whole-body MRI system (Magnetom Skyra, Siemens Medical Solutions, Erlangen, Germany). Signal excitation is done with a body coil and a 20 channel head coil is used to receive the resonance signal.

Sequence and reconstruction are implemented in C++ inside the Integrated Development Environment for (MR) Applications (IDEA) and the image reconstruction environment (ICE) (Siemens Medical Solutions, Erlangen, Germany). Data analysis is done using Matlab R2012b (The MathWorks, Natick, MA, USA).

7.2.2 AURA Sequence Design

The AURA sequence can adapt to dynamic signal changes in real-time by varying the temporal/spatial resolution. Acquired data are evaluated in real-time during the dynamic imaging process and feedback how to adjust the resolution to signal changes is sent back to the sequence.

The underlying sequence for each time frame of the AURA sequence is a 2D T_1-weighted GRE sequence. The basic design of the AURA sequence is illustrated in figure 7.1 a)- c).

Schemes

As can be seen in figure 7.1 a), the sequence comprises of four different schemes which are concatenated in a single sequence, having each characteristic temporal and spatial resolutions. The schemes are adapted to signal changes as follows:

- 'Baseline' (BL): The baseline scheme acquires N_{BL} low temporal/high spatial resolution baseline images before CA injection. No high temporal resolution is required since no dynamic changes occur yet. The aim is to acquire one native high spatial resolution image in the steady-state which can be subtracted from the contrast-enhanced images. Here, $N_{BL} = 2$ is set, the first image being a dummy scan to reach the steady-state.

- 'Onset Detection' (OD): This scheme is used for accurate CA onset detection. With each dynamic frame, very high temporal/very low spatial resolution images are acquired.

- 'Initial Kinetics' (IK): To improve model fitting, images are acquired with high temporal/low spatial resolution to monitor the fast initial CA kinetics.

- 'Wash-out' (WO): The purpose of the wash-out scheme is to capture the slow kinetic wash-out behavior in addition to acquire high spatial resolution images with CA present in the tissue for morphological evaluation. N_{wo} images are acquired.

The properties of all schemes are summarized in the table in figure 7.1 b).

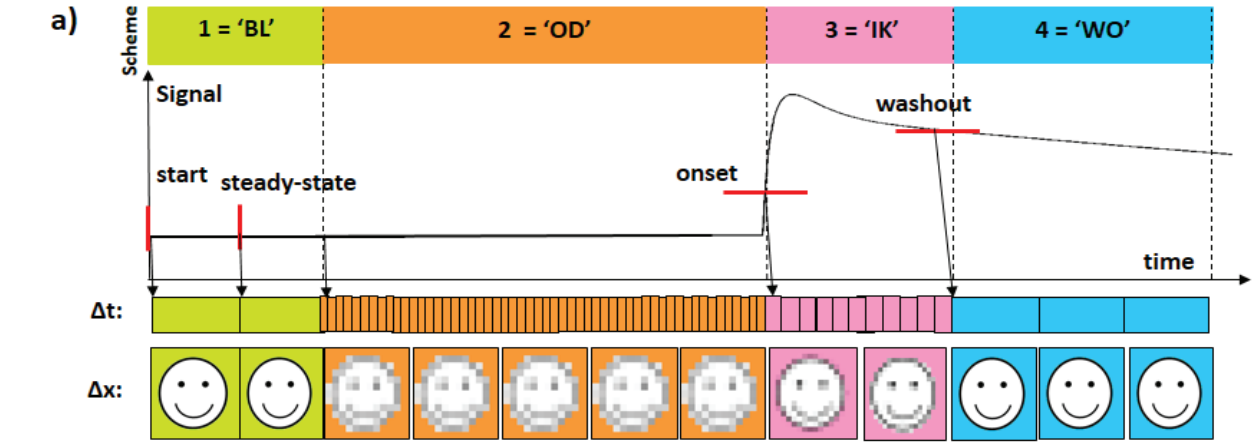

b)

	Scheme	Δt	Δx	Aims and remarks
1	'BL' = baseline	long	small	Acquisition of signal baseline, N_{BL}=2 images, the first to reach steady-state
2	'OD' = onset detection	very short	very large	Detection of CA onset
3	'IK' = Initial kinetics	short	large	Capture fast IK with to improve model fitting
4	'WO' = wash-out	long	small	Acquire high spatial resolution morphological images at high CA concentration and capture slow wash-out

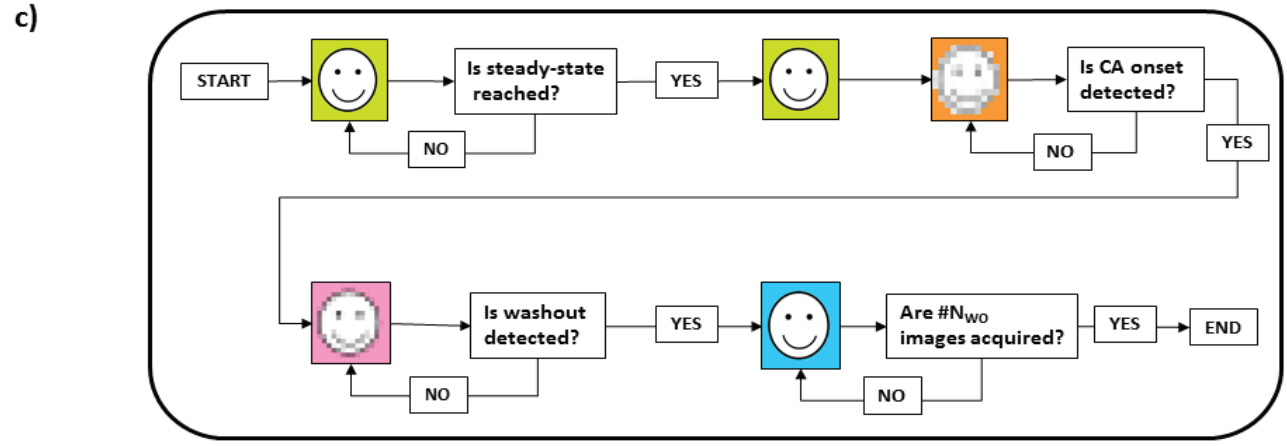

Figure 7.1: Sequence Design of AURA: a) AURA consists of four different schemes with varying temporal/spatial resolution. The switch from one scheme to the next is governed by the dynamic signal. b) Properties of the individual schemes BL, OD, IK and WO. c) Real-time resolution adaption mechanism.

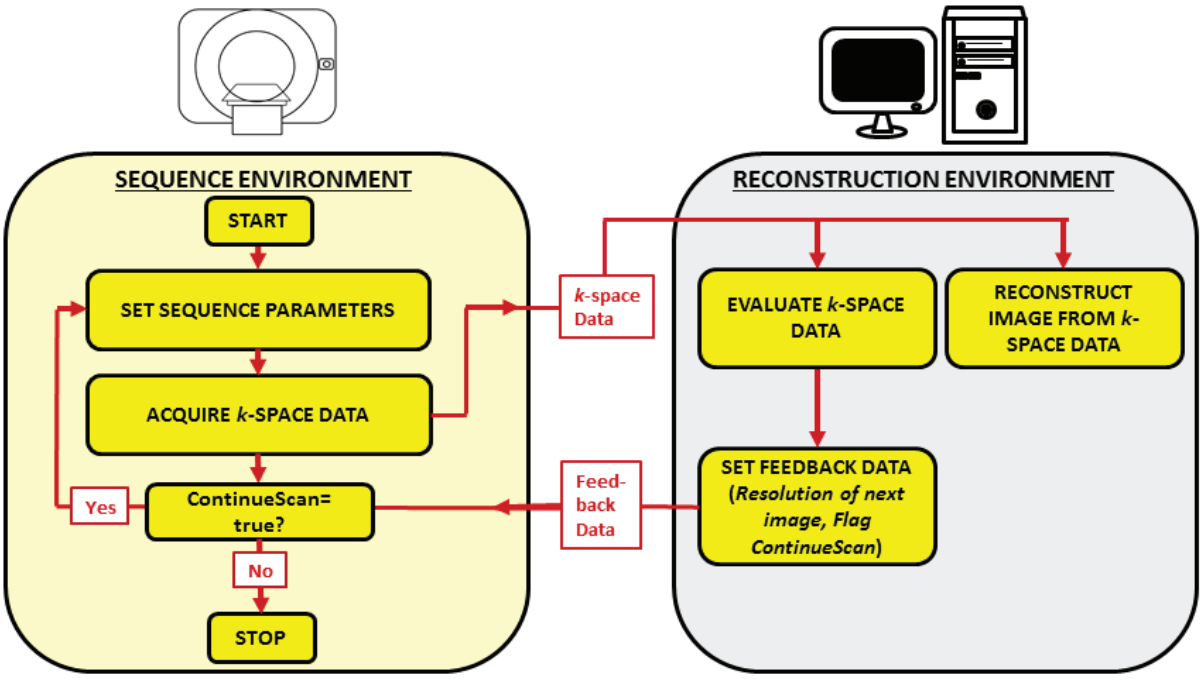

Figure 7.2: Implementation of the real-time resolution adaption mechanism on the MR scanner.

Real-time Resolution Adaption

The switch from one scheme to the next is determined by a real-time feedback mechanism, which is shown in the flow chart in figure 7.1 c). Acquired k-space data are analyzed for predefined signal-dependent switch criteria. The result of this analysis determines the resolution of the next image.

The first N_{BL} dynamic frames are acquired using the BL scheme. The first (N_{BL}-1) images are used to reach steady-state, the N_{BL}th image is used as native baseline image. After N_{BL} images have been acquired, the sequence automatically changes to scheme OD. Here, images at very high temporal/very low spatial resolution are acquired and evaluated for CA arrival. When the CA onset is detected, the sequence switches to scheme IK. Now imaging is performed at high temporal/low spatial resolution. The acquired data are monitored for the beginning of the wash-out phase. When it is detected, the sequence switches to scheme WO. Here, a predefined number N_{wo} of images is acquired at low temporal/high spatial resolution. When N_{wo} images are acquired, the sequence automatically stops.

Criteria for onset and wash-out detection have to be defined individually for each application. Examples of detection criteria will be given later in this chapter for a perfusion phantom.

The implementation of the real-time resolution adaption mechanism on the MR scanner is illustrated in figure 7.2. A more detailed description can be found in appendix

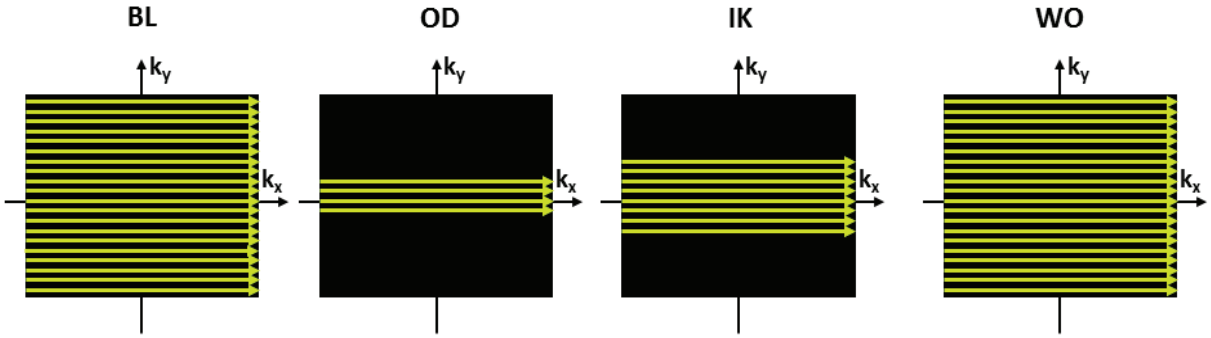

Figure 7.3: Reconstruction of multiple resolutions within a single sequence using zero-filling.

C. To enable the real-time feedback mechanism, a communication in both directions between the sequence environment and the reconstruction environment is required. In the beginning of imaging, initial sequence parameters are set in the user interface (UI) of the sequence and k-space data are acquired accordingly. These k-space data are forwarded to the reconstruction environment, where images are reconstructed. Additionally, the k-space data are evaluated for predefined signal-dependent criteria. The result of this analysis yields the resolution of the subsequent image and a boolean flag *ContinueScan*. These two properties are stored in the data struct *feedback data* which is sent back to the sequence. If *ContinueScan* is true, imaging continues and the sequence parameters are set according to the resolution given in the feedback data. This process is repeated until *ContinueScan* is set to false at the end of the WO scheme. Then the sequence automatically stops.

Multiple Resolutions Reconstruction

The reconstruction environment expects input data of a certain number of k-space lines which is set in the UI as initial parameter of the sequence. When k-space data of a deviating length are acquired, modifications have to be made to the reconstruction process. To be able to handle varying resolutions within a single sequence, the maximal expected number of lines M_{max} (as used in schemes BL, WO) are set in the UI. Each data set containing less k-space lines than M_{max} is zero-filled to M_{max}. For that, newly acquired lines are copied to the central part of the k-space matrix, which is initialized to zeros for all lines of matrix size M_{max}. This process is visualized in figure 7.3. In the frequency encoding direction, $2M_{max}$ data points are sampled for each line, independent of the resolution (including an oversampling factor of 2 applied by the scanner as default). This way the reconstruction environment can reconstruct all the incoming data in the same way using Fourier reconstruction.

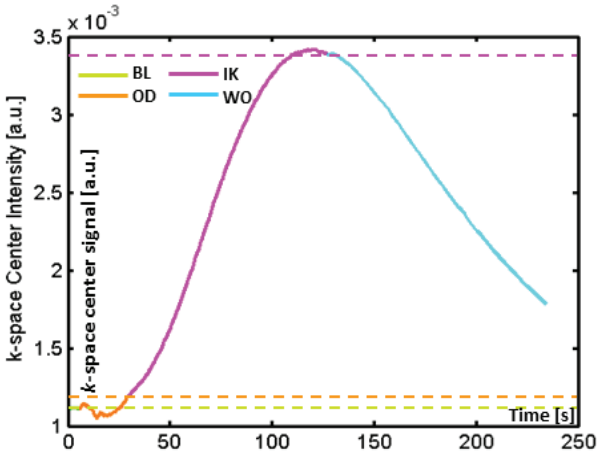

SWITCH	CRITERION: Switch to next scheme when
BL -> OD	N_{BL}=3 images are acquired
OD -> IK	Signal exceeds 5% of baseline signal
IK -> WO	Signal falls below 99% of peak signal
WO -> End	N_{WO}= 40 images are acquired

Figure 7.4: a) k-space center signal $S_k(t)$. The different schemes are color-coded. The percentage thresholds of the switch criteria are shown as dashed lines. b) Adaption criteria for the perfusion phantom based on the k-space center signal.

7.2.3 Validation of AURA Using a Perfusion Phantom

The AURA sequence is tested using the perfusion phantom described in chapter 6. At first, resolution adaption criteria are defined.

Definition of Adaption Criteria

The k-space center signal $S_k(t)$ consists of the sum of the signals throughout the whole image. Therefore, it can be used as a measure to detect global signal changes. Here, $S_k(t)$ is used for onset and wash-out detection. From the shape of measured example k-space curves, switch criteria are derived, which are shown in figure 7.4.

In the beginning, during the baseline scheme, $N_{BL} = 3$ images are acquired at high spatial resolution. Afterwards, the sequence automatically switches to scheme OD. A baseline intensity value S_{BL} is defined as the k-space center magnitude intensity of the third acquired image. The first two images are omitted since steady-state is not reached yet. For onset detection, a percentage p_{OD} is defined. When a k-space center value $S_k(t)$ is measured with $S_k(t) > S_{BL} \cdot (1 + p_{OD})$, the switch to the next scheme is triggered. Here, $p_{OD} = 5\%$ is chosen. For peak detection, all k-space center values during the initial kinetics scheme are saved and the current maximum S_{max} of all values is calculated for each new dataset. A wash-out percentage p_{wo} is defined. When a new value is measured with $S_k(t) < S_{max} \cdot (1 - p_{wo})$, the sequence changes to the wash-out scheme. Here, $p_{wo} = 1\%$ is set. Once the WO scheme is reached, $N_{wo} = 40$ images are acquires before the sequence stops.

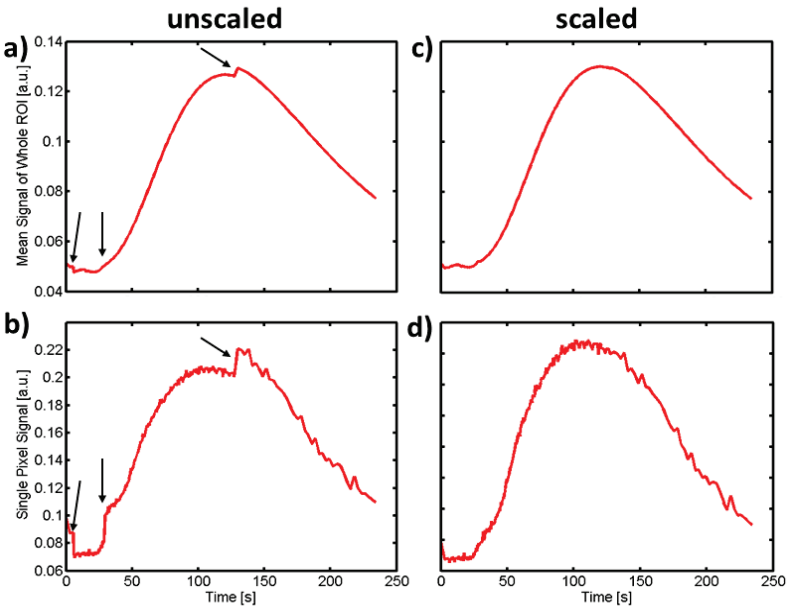

Figure 7.5: Unscaled a) mean signal of a ROI containing the whole phantom, b) signal of a single pixel within the phantom. c) and d) show the scaled curves from a) and b).

Retrospective Resolution Scaling

With the AURA sequence, various resolutions are acquired within a single sequence. Due to internal scanner scaling factors, the measured data are differently scaled for each scheme. This is shown in figure 7.5 a) for the mean signal of the whole phantom ROI and b) a single pixel signal of the phantom. At time points of resolution changes, the curves display discontinuities as indicted by the black arrows.

To handle this effect, the following scaling operations are performed for each pixel. It is assumed that the data acquired with high spatial resolution (BL, WO) are scaled with the reference scaling factors. It is furthermore assumed that neighboring time points are close enough in time to have similar signal intensity values. Therefore, the OD data are shifted by a constant value such that the first data point of the OD scheme has the same value as the last BL data point. The IK scheme data are scaled such that the first IK data point has the same value as the last scaled OD scheme data point and the last IK data point has the same value as the first WO scheme data point. The resulting curves of figure 7.5 a) and b) after scaling are shown in figures b) and d).

7.2.4 Comparison of a High Temporal, a Low Temporal Resolution and the AURA Sequence

Using the perfusion phantom, the performance of the AURA sequence is compared to an only low temporal/high spatial (*slow*) and an only high temporal/low spatial (*fast*)

resolution sequence. For each sequence, the phantom experiment is repeated under the same conditions. The data are compared with respect to parameter fitting accuracy of PK maps and the amount of morphological information near the CA peak concentration.

Flip angle θ [°]	15
Slice thickness [mm]	20
# slices	1
Pixel bandwidth [Hz/pixel]	500
FOV [mm]	250
TR [ms]	8.34
TE [ms]	3.99

Table 7.1: Common sequence parameters of the AURA, the fast and the slow sequence.

Sequence Protocols

The common imaging parameters for all three sequences are summarized in table 7.1. The sequences only vary regarding the matrix size and consequently the temporal and spatial resolution. The slow sequence has a temporal resolution of Δt_s=2.7 s and a spatial resolution of Δx_s=0.78 mm throughout the whole dynamic range. The fast sequence has a temporal resolution of Δt_f=0.54 s at a spatial resolution Δx_f=3.9 mm. AURA varies the temporal/spatial resolution according to the schemes: $\Delta t_{BL,WO}$=2.7 s, Δt_{OD}=0.27 s, Δt_{IK}=0.54 s and $\Delta x_{BL,WO}$=0.78 mm, Δx_{OD}=7.8 mm, Δx_{IK}=3.9 mm.

Generation of Pharmacokinetic Maps

As described in chapter 6, the dynamic changes of the perfusion phantom data can be mathematically described by a gamma-variate function $\Gamma(t)$, as given in equation 6.1. To generate pixel-by-pixel PK maps, the same steps as described for the perfusion phantom in section 6.2.3 were performed.

Ground Truth (GT) and Temporal Under-sampling (US)

PK maps of the slow sequence are generated and are assumed to be the ground truth, since they are acquired with high spatial resolution and a relatively high temporal resolution.

In all three data sets, only 1 slice is acquired. To mimic a multi-slice acquisition of 25 slices, all three data sets are temporally under-sampled by a factor of 25.

Data Analysis

The above described fitting procedure is repeated for the under-sampled data of the slow, the fast and the AURA sequence and PK maps are generated for each data set.

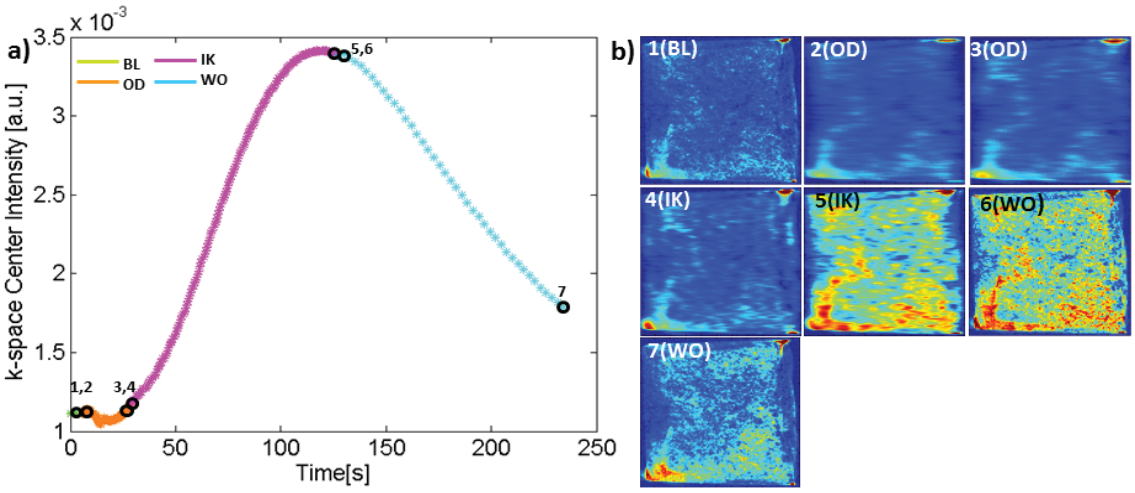

Figure 7.6: a) k-space center signal with color-coded schemes and b) corresponding phantom images at time points before and after resolution changes.

For comparison with the ground truth, joint histograms of the resulting pharmacokinetic maps with the ground truth pharmacokinetic maps are calculated for each parameter of the gamma-variate function. For each joint histogram, Pearson's correlation coefficient r is calculated.

Additionally, morphological images closest to the k-space signal peak are investigated for each of the under-sampled data sets. To obtain only the morphology of CA distribution and not the background signal, the baseline image is subtracted.

7.3 Results

7.3.1 Validation of AURA Using A Perfusion Phantom

The sequence switches resolutions according to the predefined criteria. For an example data set, the k-space center signal time curve, with schemes shown in varying colors, is shown along with phantom images at time points before and after resolution changes in figure 7.6.

7.3.2 Comparison of a High Temporal, a Low Temporal Resolution and the AURA Sequence

The resulting pharmacokinetic maps of the ground truth and the under-sampled AURA, fast and slow sequences are shown in figure 7.7. The baseline ϵ and the Γ_{max} maps are for all under-sampled maps similar to the ground truth. For Γ_{max}, the fast (US) map is more blurred.

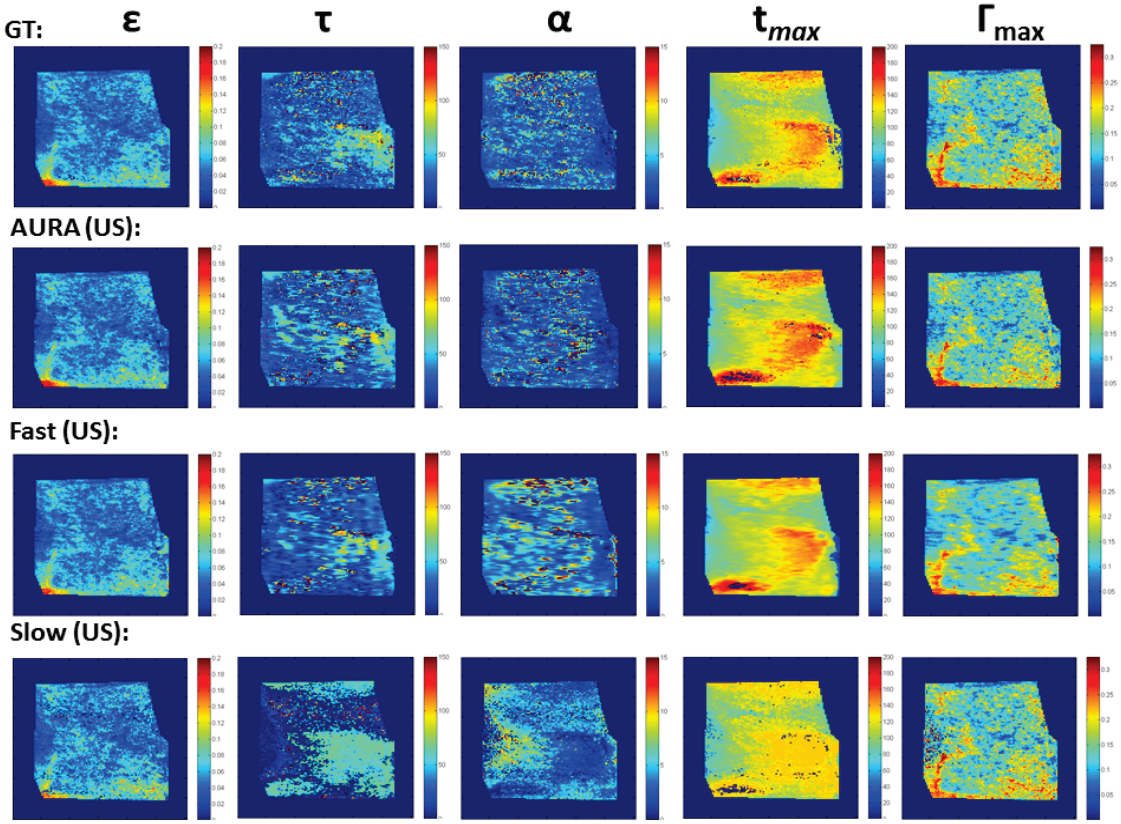

Figure 7.7: Resulting PK maps of the Γ-parameters ϵ, τ, α, t_{max} and Γ_{max} for the ground truth data and the temporally under-sampled data from the AURA, fast and slow sequence.

For the parameters τ, α and t_{max}, the AURA (US) and fast (US) maps are, with small variations, similar to the GT map, with the fast (US) maps being more blurred. The slow (US) maps deviate more from the ground truth maps.

The joint histograms of the AURA (US), fast (US) and slow (US) maps with the ground truth maps for the parameters ϵ, τ, α, t_{max} and Γ_{max} are shown in figure 7.8.

For AURA (US) and fast (US), the results are comparable for all parameters. Comparing slow (US) to AURA, r is lower for τ and α and systematic errors are visible for τ, α and Γ_{max}. The joint histograms of ϵ and t_{max} of slow (US) and AURA (US) are comparable.

The subtraction images closest to the k-space center peak of each of the under-sampled sequences are shown in figure 7.9 along with the corresponding time points. AURA (US) provides a high spatial resolution image shortly after the peak, whilst for slow (US), the peak is missed and less CA is present, for example in the region indicated by the arrows. Fast (US) provides an image close to the peak, however at lower spatial resolution.

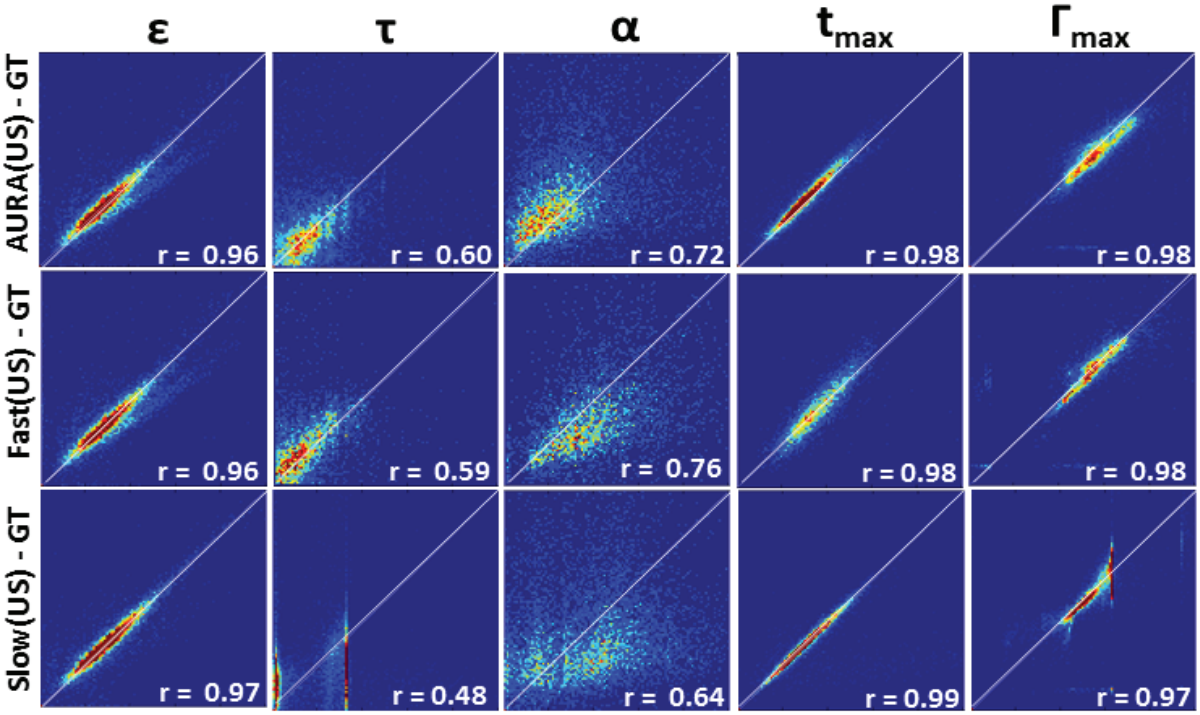

Figure 7.8: Joint histograms between resulting maps of AURA (US), fast (US), slow (US) and the ground truth PK maps for the parameters ϵ, τ, α, t_{max} and Γ_{max}.

7.4 Discussion

In summary, an 'intelligent' sequence is developed for DCE MRI, which automatically adapts the resolution to signal changes without user-interaction and is capable of reconstructing multiple resolutions within a single dynamic scan. For a perfusion phantom, robust adaption criteria based on the k-space center intensity are found. For the perfusion phantom, the AURA sequence yields comparable fitting performance to a high temporal/low spatial resolution sequence, whilst the spatial resolution of the PK maps is higher. Additionally, the AURA sequence reliably provides high spatial resolution images near the CA peak concentration, which can be used for mophological analysis of CA distribution.

In all previous studies using adaptive sequences, the resolution changed at fixed time points. However, contrast kinetics are dependent on the tumor, the physiological conditions of the patient and the injection timing. Therefore, rigid switching times bear the potential of information loss, for example by missing the onset time or the CA peak, leading to fitting inaccuracies as shown in the simulations in chapter 5. The newly developed AURA prevents this loss by flexibly reacting to the acquired data in real-time.

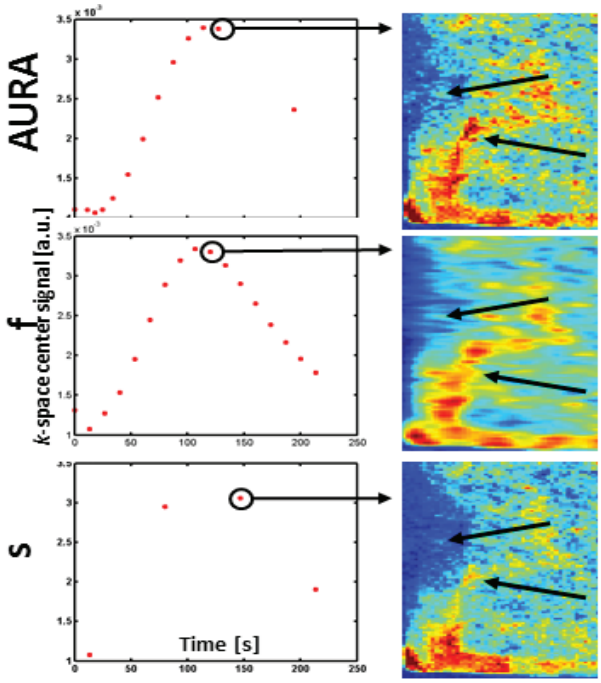

Figure 7.9: Morphological images close the k-space center signal peak.

The employed perfusion phantom, which is described in detail in section 6, is built in-house and is not perfectly reproducible in terms of fitting results. This is especially true for the parameters τ and α, which are very sensitive to even slight curve changes. Furthermore, for some pixels within the phantom gamma-variate fitting fails, mainly due to motion artifacts during contrast agent administration. When comparing the joint histograms of the AURA sequence with those from the phantom reproducibility investigation in chapter 6, it can be seen that the errors introduced by the AURA (US) and fast (US) sequence are in the order of the reproducibility errors of the phantom. However, for the slow (US) sequence the effects of fitting errors due to under-sampling still prevail phantom inaccuracies. The large fitting errors of the slow (US) data arise from the low temporal resolution which causes a false estimate of the onset time. Consequently, systematic errors, mainly in τ and α are introduced.

For the employed phantom the fitting function describing the data best is a gamma-variate function. However, tissue signal of clinical DCE MRI data is usually described by other models than the gamma-variate function. Instead, multi-compartment models such as [Tofts1991] are used, which exhibit a slower wash-out. In this case, the wash-out could be exploited further to acquire high spatial resolution images. However, for this work neither clinical data nor a phantom describing multi-compartmental model curves were available. For the scope of this thesis however, which was to implement a prototype of the AURA sequence and to show that it outperforms equidistant schemes, the used

phantom is sufficient.

A problem which is not solved in this thesis, but is required to be fixed before clinical applications, is the varying scaling factors of different resolutions. Even if the raw data are taken from the MR scanner and are off-line reconstructed, an internal data scaling by the scanner is already imposed. In this work, the problem is avoided by assuming the high spatial resolution scaling as ground truth and close time points to have similar intensity values. By that, partial volume effects due to blurring at low spatial resolutions are as well omitted. In this work, this approach yields a good approximation, since only one slice is acquired and time points are relatively close together for all schemes. However, this is not possible anymore for multi-slice or 3D acquisitions with longer scan times per dynamic frame. Yet, in other adaptive imaging studies scanner scaling factors are even more problematic since different resolutions are acquired using different sequences. By that, even more internal scaling operations are introduced compared to the ones of changing resolutions within a single sequence.

The chosen switch criteria work for the perfusion phantom and the k-space center signal provides a robust measure to adapt to global signal changes. For the onset detection criterion, a relatively high percentage of 5% is chosen since motion artifacts and overflow during CA injection cause irregularities in the signal time curve at baseline. For wash-out the curve is smooth and a percentage of 1% is sufficient.

In general, the measure of the k-space center signal is relatively crude, containing no spatial information. For clinical applications this might not be sufficient and more refined adaption criteria would be required, such that for example enhancement outside the organ of interest can be taken into account. In that case it might be better to use bolus tracking methods such as for example Kalman filters [Kalman1960] applied to reconstructed, potentially post-processed, images.

For the comparison of the high spatial resolution images close to the peak, the undersampling of data from the slow sequence is performed in such a way that the peak is missed. How close the high spatial resolution images are to the peak depends on the timing of the sampling relative the CA kinetics. It could as well be the case that the peak signal is perfectly acquired. However, this timing is not controlled and therefore unreliable. Using the AURA sequence, the timing is performed in a controlled way and images close to the peak are reliably provided.

A limitations of the AURA sequence is that the adaption reacts only to global signal changes. In reality, contrast curves of individual voxels within a region of interest can vary largely, especially the onset time. The AURA sequence is not optimized for each individual voxel, only for mean signal changes. This may cause missing time points during the onset and upslope and consequently lead to fitting errors as was shown in the simulations in chapter 5. It has to be investigated on *in vivo* data how large deviations from the mean signal time are typically.

Another disadvantage of the AURA sequence is that in case of automatic adaption failure, which can for example occur due to motion artifacts, information, for example from high spatial resolution images, is lost and cannot be recovered. This could be prevented by implementing the additional backup option to manually switch resolutions.

8 Retrospective Resolution Adaption for DCE MRI Using 3D Golden Angle Radial Acquisition

8.1 Introduction and Motivation

It has been previously shown in chapter 4 that increasing temporal resolution during the upslope of the signal-time curve improves model fitting and that images during the wash-out can be exploited for higher spatial resolution. However, as described in chapter 7, a key problem of adaptive sequences is that contrast agent is administered only once and that the underlying kinetic curves $S(t)$ are not known prior to imaging. Hence, it is not known when the initial kinetics and the wash-out begin and what the maximum allowed spatial resolutions are to assure accurate model fitting. Therefore, current clinical adaptive sequences which employ fixed time points to switch between predefined resolutions, might not be optimized to patient-specific sampling requirements.

In chapter 7, prospective resolution adaption has been shown to be feasible using the AURA sequence. In this chapter, as an alternative to AURA, retrospective adaption is investigated. As discussed in chapter 7, a principal limitation of prospective adaptive sequences is that the adaption is a global process. However, $S(t)$ may vary largely from voxel to voxel in heterogeneous lesions. Using retrospective adaption, the optimal temporal and spatial resolution throughout the curves can be adapted in principle for each voxel individually.

A 3D golden angle (GA) radial sequence [Chan2009] acquires k-space center, and therefore contrast information, with each projection. Additionally, due to the golden angles, images can be reconstructed at arbitrary time points with arbitrary spatial resolutions. In this study, 3D GA radial imaging is used to retrospectively adapt the spatial resolution to $S(t)$ throughout the time interval for individual voxels to achieve the maximal feasible spatial resolution whilst preserving fitting accuracy. The feasibility of employing the 3D GA radial sequence for retrospective resolution adaption is investigated using the perfusion phantom described in chapter 6.

8.2 Methods

In the following, the employed sequence, image reconstruction and corrections of the acquired data are described. Eventually, the process of retrospective resolution adaption is applied to acquired phantom data.

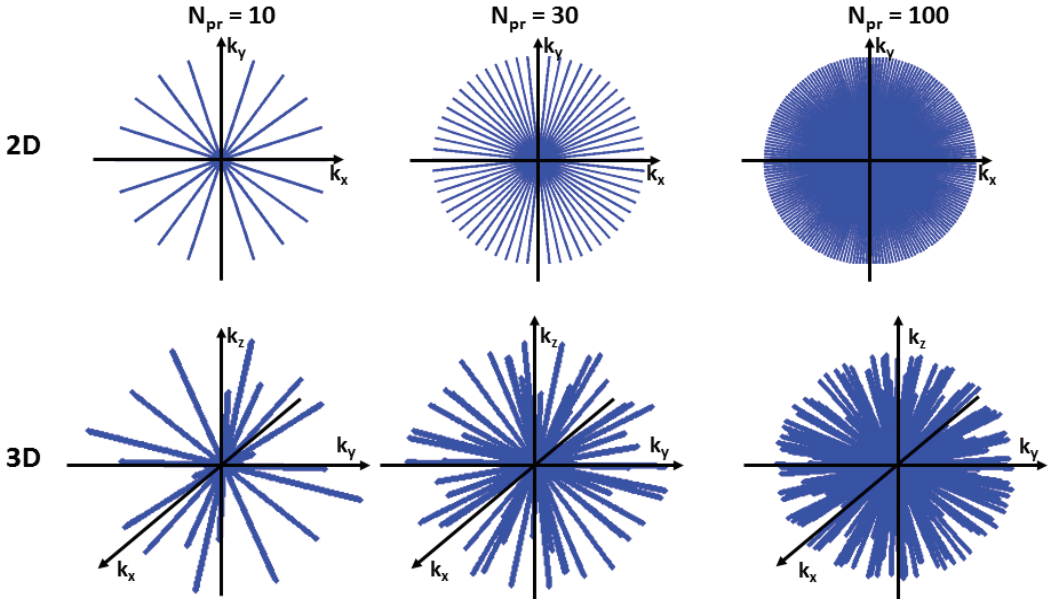

Figure 8.1: Using the golden angles, an approximately uniform distribution indepedent of the number of profies N_{pr} can be achieved in 2D and 3D.

8.2.1 Hardware and Software

All experiments in this chapter are conducted on a commercially available 3T whole-body MRI system (Magnetom Skyra, Siemens Medical Solutions, Erlangen, Germany). Signal excitation is done with a body coil, a 20 channel head coil is used to receive the signal.

The sequence development is done in the language C++ inside the Integrated Development Environment for (MR) Applications (IDEA)(Siemens Medical Solutions, Erlangen, Germany). The reconstruction, sequence corrections and and data analysis is implemented in Matlab 2012b (The MathWorks, Inc., Natick, Massachusetts, United States).

8.2.2 Concepts of the 3D Golden Angle Radial Sequence

In the following, the concepts of the work by Chan *et al* [Chan2009], on which the sequence used in this chapter is based, are summarized. For conventional 3D radial sequences the vector tips of the radial profiles follow a spiral on the surface of a sphere. A predefined number of profiles is needed to cover the whole 3D k-space. However, if the polar and azimuthal angles are chosen to be the *golden angles* Φ_{GA} and Θ_{GA}, it can be achieved that the angular distribution of profiles is always approximately uniform, independent of the number of profiles. This is the 3D analogy of the 2D golden angle method using $\Theta_{2D,GA} \approx 111°$ [Winkelmann2007]. For both, 2D and 3D, the spatial distribution of the radial profiles for a varying number of profiles N_{pr} using golden angles

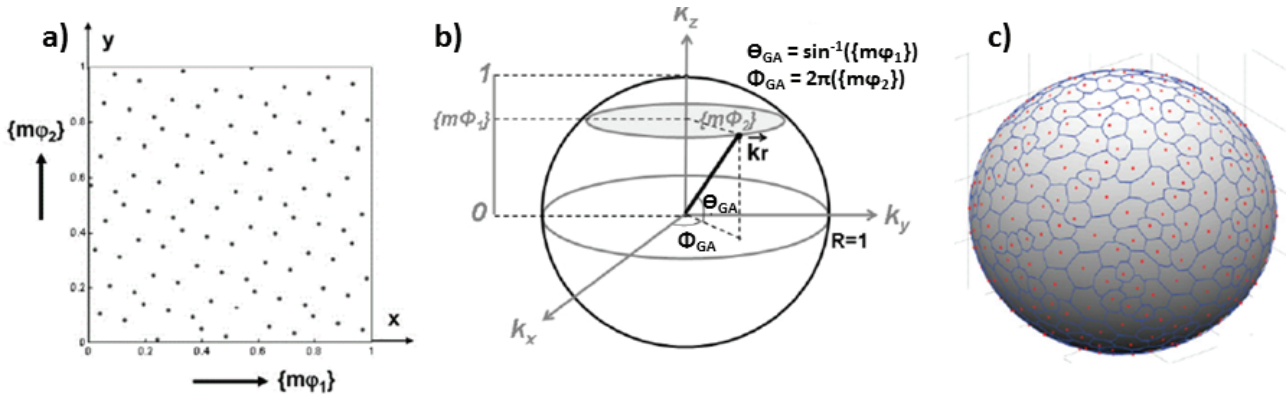

Figure 8.2: a) Using the two-dimensional golden means φ_1 and φ_2, points can be distributed relatively uniformly on a unit sphere. b) By a change in topology, the 2D golden means can be used to uniformly distribute points across the surface of a sphere. c) Resulting vector tips of the radial profiles. (adapted from [Chan2009])

is shown in figure 8.1. The multidimensional *golden angles* for 3D radial imaging were derived by Chan *et al* from a modified Fibonacci sequence. They found the resulting two-dimensional golden means φ_1 and φ_2 to be:

$$\varphi_1 = 0.4656 \ , \ \varphi_2 = 0.6823. \tag{8.1}$$

Using φ_1 and φ_2, points can be uniformly distributed on a unit square, as shown in figure 8.2 a). The coordinates of the points are placed according the following iterative process: The x-coordinate of the first point is set to be φ_1. The x-coordinate of the next point is placed by incrementing the previous value by φ_1 and taking the modulus 1. This is iteratively repeated for all following points. The corresponding y-coordinates are calculated analogously using φ_2. This process can be denoted by $(x, y) = (\{m\varphi_1\}, \{m\varphi_2\})$ with $m = 1, 2, ..., N_{pr}$.

By a change in topology, the result of the unit square is used to distribute the tips of the projections of the 3D radial k-space uniformly across the surface of the sphere surrounding the data. This is done by distributing the points along the k_z-axis using the one-dimensional golden mean φ_1. The second golden mean φ_2 is used to distribute the polar angle uniformly within the slices. This is illustrated in figure 8.2 b). The resulting distribution of the tips of the profiles is shown in figure 8.2 c).

The resulting golden azimuthal and polar angles Θ_{GA} and Φ_{GA} are given by:

$$\Theta_{GA} = sin^{-1}(\{m\varphi_1\}) \ , \ \Phi_{GA} = 2\pi(\{m\varphi_2\}). \tag{8.2}$$

8.2.3 Sequence Design

The design of the implemented 3D GA radial sequence implemented in this work will be addressed in the following. The sequence parameters used are listed in table 8.1.

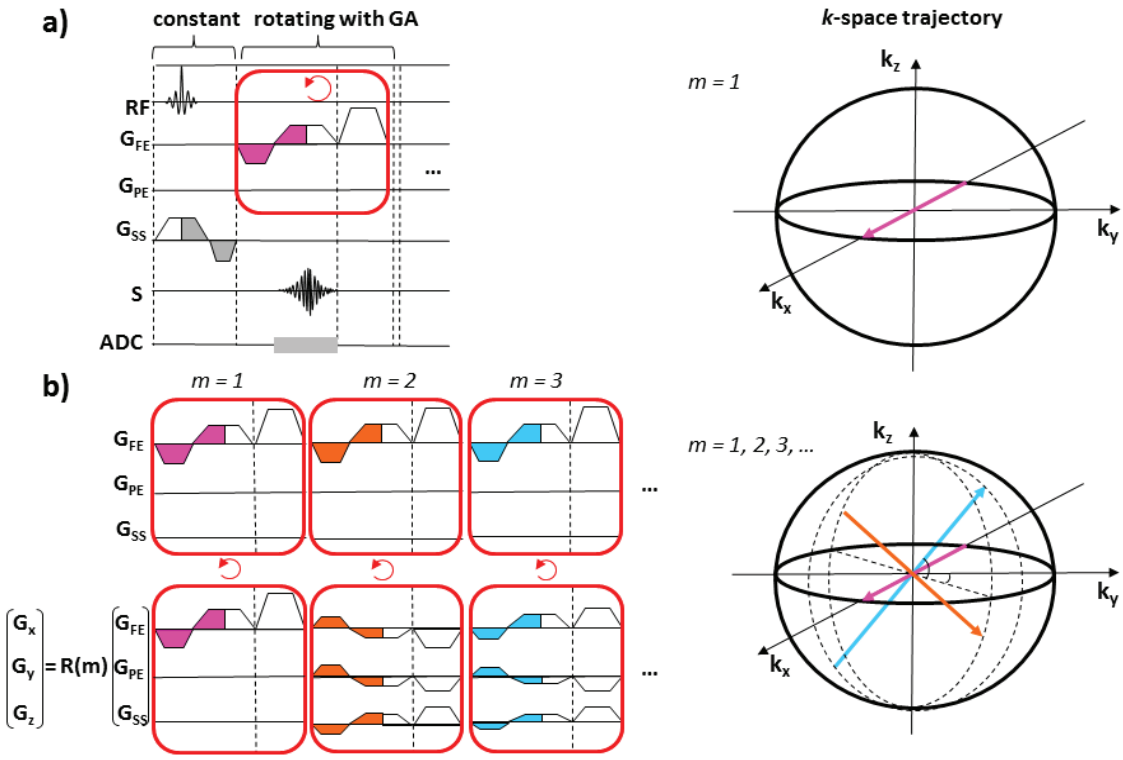

Figure 8.3: a) Sequence diagram of the first acquired profile and corresponding k-space trajectory. RF pulse and slab selection gradients have constant orientations, whilst the readout and spoiler gradients are rotated. b) Readout and spoiler gradients and corresponding k-space trajectories at three different repetition times, indicated by index m. The gradients of the first spoke are rotated with the current rotation matrix $\vec{R}$ to yield the subsequent profiles.

RF Pulse and Excitation Volume

A slab selection gradient is used to excite a large slab. The slab thickness is set to the same length as the FOV in in-plane direction. Additionally, a slab selection rephaser gradient is applied. For excitation, a *sinc*-shaped RF pulse is used. RF spoiling is used according to equation 2.56 with phase increment $\phi_0 = 117°$. The RF pulse and slab selection gradients are shown in the sequence diagram in figure 8.3 a).

Readout Gradients

The readout (RO) gradients are chosen such that data are sampled along a 3D GA radial k-space trajectory. Prior to each RO gradient, a prephaser gradient is played to start the readout at the k-space periphery.

In the sequence environment, a 3D rotation matrix $\vec{R}$ can be defined for each sequence element. It determines the orientation of the sequence element within the physical scan-

ner coordinate system. The MR scanner acquires images in the logical coordinate system, defined by the 'frequency-encoding' (FE), 'phase-encoding' (PE) and 'slice-selection' (SS) direction. To avoid specifying the amplitude for each of the gradients G_x, G_y, G_z in the logical coordinate system for every profile anew, $\vec{R}$ is exploited. The amplitude of the RO prephaser and the RO gradient is set for the first profile, which is aligned along the physical x-axis. All other profiles are determined by multiplication of the gradients of the initial profile with $\vec{R}$:

$$\vec{R}(m) = \begin{pmatrix} cos\Phi_m & -sin\Phi_m cos\Theta_m & sin\Phi_m sin\Theta_m \\ sin\Phi_m & cos\Phi_m cos\Theta_m & -cos\Phi_m sin\Theta_m \\ 0 & sin\Theta_m & cos\Theta_m \end{pmatrix}, \tag{8.3}$$

where the index m indicates the profile number ($m = 1, ..., N_{pr}$). This process is visualized for three profiles in figure 8.3 b).

Flip angle α	15°
BW$_{pixel}$ [Hz/px]	500
Spoiler moment A_{sp}[mTs/m]	0.0352
spoiler phase$\Delta\phi$ [rad]	3π
TR [ms]	5.19
TE [ms]	2.25
FOV [mm]	300

Table 8.1: Parameters used for the 3D GA radial sequence.

Data Acquisition and Pixel Bandwidth

Data acquisition is performed during the plateau of the trapezoidal RO gradients. The pixel bandwidth BW_{pixel} is the adjustable parameter in the sequence which characterizes the receiver bandwidth, defined as:

$$BW_{pixel} := \frac{BW_{read}}{N_x} = \frac{1}{T_s}, \tag{8.4}$$

where BW_{read} is the receiver bandwidth and T_s is the total data acquisition time during one readout period. N_x is the number of sampled data during readout, including an oversampling factor of 2 performed automatically by the scanner. The unit of BW_{pixel} used is Hertz/pixel (Hz/px). The chosen bandwidth, being a compromise of imaging speed and SNR, is listed in table 8.1.

Spoiler Gradients

Spoiler gradients, as described in section 2.7.1, are gradients with a large area used to spoil the residual magnetization from previous excitations.

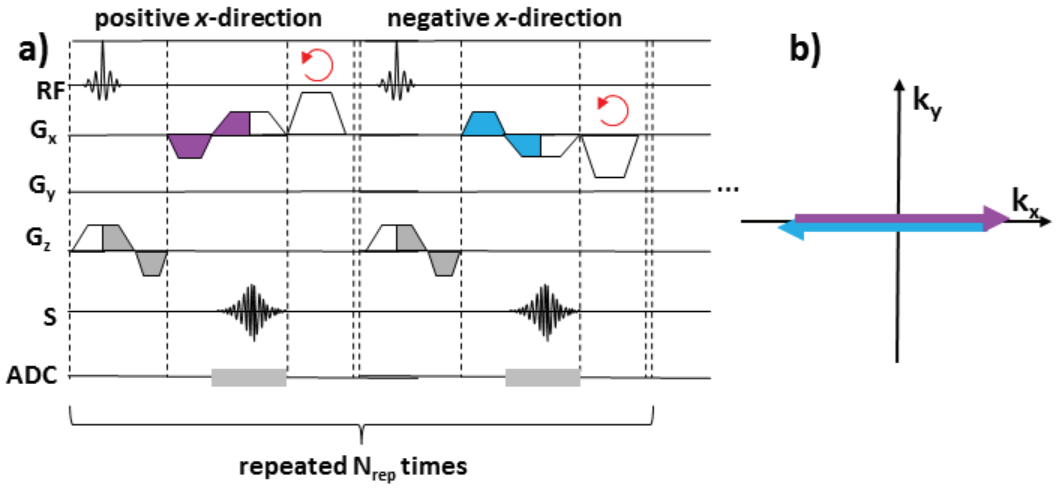

Figure 8.4: Diagram of sequence to measure gradient delays along the x-axis and corresponding k-space trajectory. Opposing lines along the axes in k-space are repeatedly acquired. To prevent stimulated echoes, the spoiler gradients are rotated with the 3D golden angles.

Since for each profile a RO gradient is played without a rephaser gradient, there is already dephasing of the spins present at the end of each RO gradient. To take advantage of this fact, the polarity of the spoiler gradient is chosen to be equal to that of the RO gradient. Since the RO gradient in a 3D radial golden angle sequence is changing direction with every acquired profile, the spoiler direction changes as well with every profile. This has the wanted effect to prevent artifacts due to the build-up of a residual steady-state magnetization. The chosen area A_{sp} and resulting phase $\Delta\phi$ across each voxel is listed in table 8.1.

8.2.4 Gradient Delay Measurements

Due to hardware imperfections and gradient-induced eddy currents a delay between the actual and the assumed starting time of a gradient can occur. This can potentially lead to image distortions since the expected k-space trajectory deviates from the true trajectory.

In this work, gradient delays along all three physical axes are measured using a method based on [Block2011]. Using an additional sequence, which is schematically shown in figure 8.4, data lines along opposing directions on each of the physical axes are acquired. To prevent the built-up of stimulated echoes, the spoiler gradient are rotated in 3D with the golden angles. In the ideal case of no gradient delays, the measured signal along opposing directions with one signal being mirrored, will be identical. If gradient delays are present, a translation between the two signals will be observed. From this translation, the delays can be determined as follows in detail and then be used to re-align the k-space trajectory. For simplicity, the process is only described for the x-axis (with

angles $\Theta = 0°$, $\Phi = 0°$ and 180°), however the other two axes are treated analogously.

(i) For both directions along the x-axis, N_{rep}=100 lines are acquired. The lines along the same direction are averaged and the magnitude is calculated. The resulting signal from lines with $\Phi = 0°$ shall be denoted as S_0 and the signal from opposite lines as S_{180}.

(ii) S_{180} is mirrored.

(iii) The shift distance d_{shift} between the two curves is calculated by cross-correlation on interpolated curves.

(iv) The k-space shift Δk_x due to gradient delays is given by $d_{shift}/2$.

(v) The time delay Δt_x is calculated by: $\Delta t_x = \frac{\Delta k_x}{N_{samples} \cdot BW_{pixel}}$, where $N_{samples}$ is the number of samples along the readout direction.

Examples of two opposing k-space center lines and the extraction of Δk_x is shown in figure 8.5. These steps are performed for each coil separately and then the average gradient delays of all coils is calculated.

In this work, gradient delays are measured for a water-filled spherical phantom. The re-alignment of the k-space trajectory based on the knowledge of Δk_x, Δk_y and Δk_z will be addressed in section 8.2.6. Images of two phantoms, a water-filled sphere and bottle are compared with and without gradient delay correction. To better visualize the effects of the correction, difference images for both phantoms are calculated. To quantify the effects of gradient delay correction, the ratio s of the mean background and the mean phantom signal for the 3D data is calculated.

8.2.5 Phase Corrections in the Presence of Gradient Delays

The phases of intersection points of two radial k-space projections under ideal conditions will be identical. However, due to B_0-field inhomogeneities and gradient induced B_0 eddy currents, phase errors along the profiles can occur. During gridding reconstruction this can lead to signal cancellation and hence image artifacts.

Without gradient delays, all profiles meet in the k-space center. If the phases are not consistent, they can be corrected for by measuring the phase φ in the k-space center, and multiplying the complex signal of the profile with the factor $e^{-i\varphi}$ such that all profiles have a phase of 0 radians in the center.

However, when data are affected by gradient delays, profiles will not intersect in the center. In the case of 3D data they might not intersect at all. In this work, a novel method is presented in which gradient delays are incorporated into 3D phase correction as follows:

- A reference profile p_0 is chosen and its complex data stored in the vector $\vec{p}_{ref}$.
- All projections $\{p_j\}$ are found for which the closest absolute distance d to p_0 is smaller than a given threshold t.

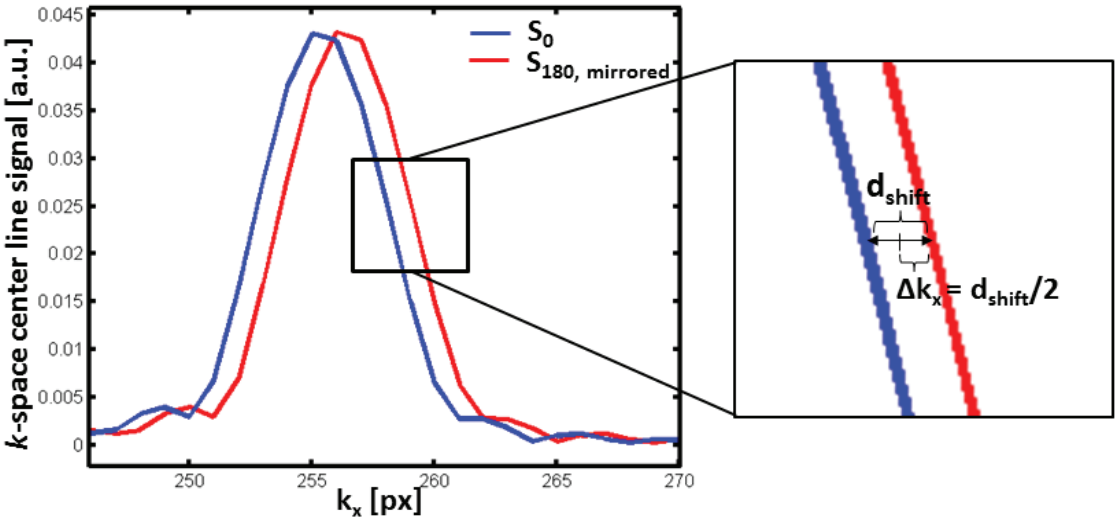

Figure 8.5: Measured k-space signals S_0 (blue) and S_{180} (red). The two curves exhibit a shift distance d_{shift}. The k-space shift Δk_x due to gradient delays is given by $d_{shift}/2$.

- The projections $\{p_j\}$ are phase corrected with respect to p_0 and also recorded in the vector $\vec{p}_{ref}$. A detailed description of the phase correction itself is given below.
- This procedure is repeated for the projections in $\vec{p}_{ref}$ one by one, where each corrected profile serves as a new additional reference projection.
- The algorithm is stopped, when all projections are corrected for.

The phase correction of profile p_2 with respect to reference profile p_1 is performed as follows. Both profiles are linearly interpolated and the points $\vec{r}_1$ on p_1 and $\vec{r}_2$ on p_2 with the closest distance d between both projections are determined. The phases φ_1 and φ_2 at the points $\vec{r}_1$ and $\vec{r}_2$ and their phase difference $\Delta\varphi = \varphi_1 - \varphi_2$ are calculated. Since for a small threshold t the distance between both points is small, the phases should be approximately the same, when no phase errors are present. With this assumption, the complex signal of p_2 is multiplied by the factor $e^{i\Delta\varphi}$, making both phases consistent.

For the water-filled spherical and the bottle phantom from the previous section, the gradient delay corrected images are additionally phase corrected. Difference images of the results with and without phase correction are generated. For the spherical phantom, the ratio of the mean background and the mean phantom signal is calculated for the phase corrected 3D images.

8.2.6 Data Reconstruction

The acquired 3D GA radial data lie on a non-Cartesian trajectory in k-space. In order to apply the FFT, the data have to be gridded onto a Cartesian grid, as it is described

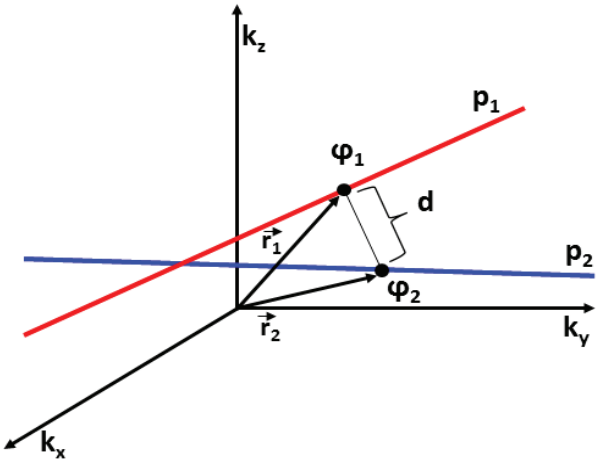

Figure 8.6: The shortest distance d between the skew projections p_1 and p_2 occurs between the points $\vec{r}_1$ and $\vec{r}_2$. At these points, the projections exhibit the phases φ_1 and φ_2.

in section 2.9.2. In the following, the gridding process as implemented in this work is described.

After data acquisition the complex raw data are exported from the scanner and reconstructed off-line.

k-space Trajectory and Gradient Delay Correction

The 3D k-space trajectory (k_x, k_y, k_z) of the acquired data is ideally given by:

$$k_x = r \cdot sin(\Theta_{GA})cos(\Phi_{GA}), \tag{8.5}$$

$$k_y = r \cdot sin(\Theta_{GA})sin(\Phi_{GA}), \tag{8.6}$$

$$k_z = r \cdot cos(\Theta_{GA}), \tag{8.7}$$

where Θ_{GA} and Φ_{GA} are the golden angles from section 8.2.2.

However, when gradient delays are present, the measured trajectory deviates from this ideal trajectory. For gradient delay correction, the measured delays Δk_x, Δk_y and Δk_z, which are described in section 8.2.4, are incorporated into the ideal k-space trajectory by shifting the whole profile in 3D k-space accordingly. Equations 8.5, 8.9 and 8.10 become:

$$k_x = (r + \Delta k_x)sin(\Theta_{GA})cos(\Phi_{GA}), \tag{8.8}$$

$$k_y = (r + \Delta k_y)sin(\Theta_{GA})sin(\Phi_{GA}), \tag{8.9}$$

$$k_z = (r + \Delta k_z)cos(\Theta_{GA}). \tag{8.10}$$

Density Compensation Function (DCF)

The density compensation function as described in section 2.9.2 is precalculated based on geometrical considerations. It is assumed that profiles are approximately uniformly distributed throughout k-space and that no gradient delays occur. To calculate the volume V of each sample, which is proportional to the DCF, the volume of spherical shells containing all the data points at radius r is determined. To obtain the volume occupied by a single sample point, the shell volume is divided by the number of profiles N_{pr} intersecting the shell. The resulting volumes are given by:

$$V(r) = \frac{4\pi(r^2 + r + 1/3)}{N_{pr}}. \tag{8.11}$$

Gridding Algorithm

The gridding algorithm was implemented as described in detail in section 2.9.2. The Kaiser-Bessel kernel is used as convolution kernel with width $w = 4$ and $\beta = 18.5547$, as recommended by [Jackson1991]. Data are gridded onto an oversampled grid by a factor 2. The gridding algorithm is performed for the real and imaginary components of the complex data separately and on a coil-by-coil basis.

Fourier Transform and Combination of Multiple Coils

The gridded Cartesian k-space matrix is 3D Fourier transformed for each coil separately. The different coil images are combined to form a magnitude image according to section 2.9.1 by calculating the square root of the sum of squares of all images.

Deapodization and FOV Cropping

As described in section 2.9.2, deapodization is performed by division by the FT of the Kaiser-Bessel kernel in each direction. Finally, the redundant periphery of the image due to oversampling is cropped.

8.2.7 Retrospective Resolution Adaption

In the following section, the previously described 3D GA radial sequence is applied to retrospectively reconstruct data at resolutions which are adapted to the measured signal time curves of a perfusion phantom.

Process of Resolution Adaption

The principle of retrospective resolution adaption is described in figure 8.7.

First, temporally equidistant images are reconstructed at low spatial/high temporal resolutions, such that the initial signal time curves $S_{init}(\vec{r},t)$ at voxel positions $\vec{r}$ are sampled sufficiently fast for high fitting accuracy. For each voxel within a chosen ROI, the pharmacokinetic model is fitted to $S_{init}(\vec{r},t)$, resulting in fitted curves $S_{fit}(\vec{r},t)$ and low spatial resolution PK maps $\vec{p}_{init}$.

From $S_{fit}(\vec{r},t)$ of each voxel, sampling times $\{t_i\}$ are derived which have the highest possible spatial resolution whilst preserving fitting accuracy. The choice of sampling times will be described in detail in the next section.

Finally, images are reconstructed at the time points $\{t_i\}$ and the PK model is fitted to generate the adaptive PK map $\vec{p}_{adapt}$. The resolution of $\vec{p}_{adapt}$ may vary for different parameters throughout the map.

Choice of Sampling Times and Corresponding Resolutions

It is assumed in this study that for accurate model fitting, the time points $\{t_i\}$ have to be distributed such that 4 equidistant time points are placed at baseline, upslope (including peak) and wash-out, respectively. This is visualized in figure 8.8.

Intervals of length Δt_i are defined such that the start and end points of each interval lie in the middle between adjacent t_i. The number of projections N_{pr} within each interval is determined by:

$$N_{pr} = \frac{\Delta t_i}{TR}, \tag{8.12}$$

where TR is the repetition time.

To determine the corresponding resolution for N_{pr} given projections, it is assumed that the GA radial profiles are approximately homogeneously distributed in k-space and that data under-sampled by 90% still yield acceptable image quality. The latter assumption is based on a work by Stehning *et al* [Stehning2004], in which it has been shown that for MR angiography 12.5% under-sampling is feasible.

Using equation 2.36, describing the Nyquist criterion of uniformly spaced 3D radial k-space data, the matrix size M can be derived, for which 10% of the Nyquist criterion is met:

$$M = \sqrt{10 N_{pr}/\pi}. \tag{8.13}$$

Since an integer value for M is required, the obtained value is rounded up. At a fixed FOV, the isotropic spatial resolution Δx is given by: $\Delta x = FOV/M$.

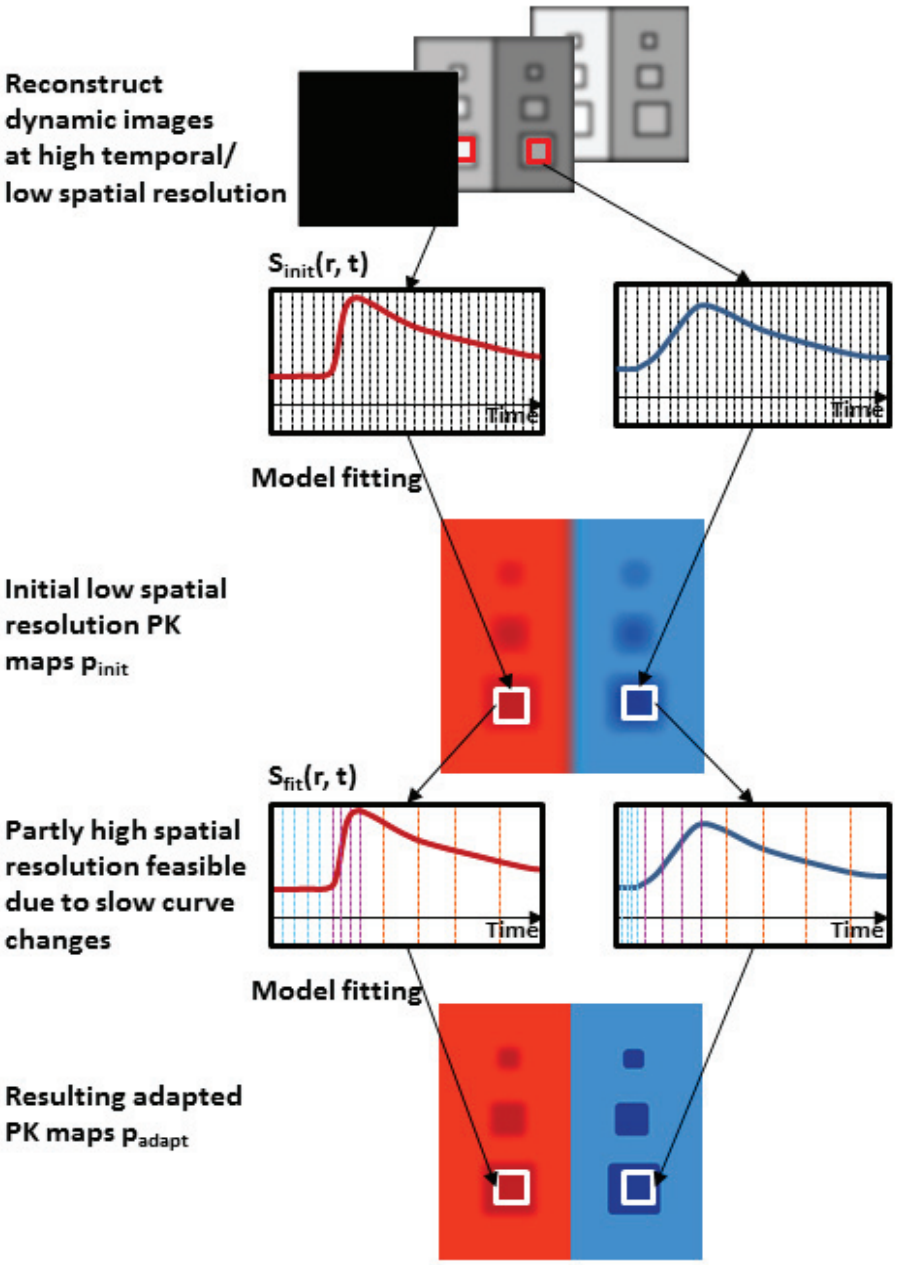

Figure 8.7: Process of resolution adaption: Equidistant low spatial/high temporal resolution images of voxel signal $S_{init}(\vec{r}, t)$ are reconstructed. The PK model is fitted to the data, providing fitted curves $S_{fit}(\vec{r}, t)$ and initial low spatial resolution PK maps $\vec{p}_{init}$. From the fitted curves $S_{fit}(\vec{r}, t)$, sampling times $\{t_i\}$ are derived which yield the maximal spatial resolution whilst preserving fitting accuracy. Data at times $\{t_i\}$ are reconstructed and PK maps $\vec{p}_{adapt}$ are generated.

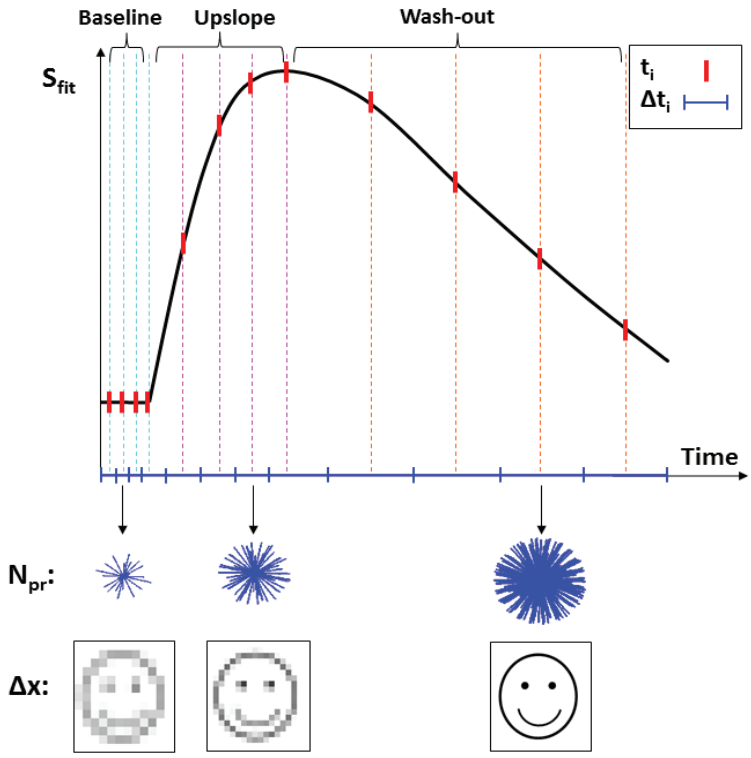

Figure 8.8: Sampling times and corresponding resolutions: It is assumed that 4 equidistant time points $\{t_i\}$ are required on the baseline, upslope and wash-out of S_{fit}, respectively. From the length of intervals Δt_i with start and end point between adjacent t_i, the number of projections N_{pr} and the corresponding feasible resolutions Δx are derived.

With the perfusion phantom used, some curves with large onset times are only partially acquired, such that large parts of the wash-out are missing. In that case, the number of required time points is adjusted such that the spatial resolution never falls below that of the initial low spatial resolution images.

Cluster Generation

To increase reconstruction speed, all curves $S_{fit}(\vec{r}, t)$ within the ROI are divided into clusters of similar onset times τ and peak times t_{max}. In increments of Δt=25 s, the time between 0 and the maximal possible τ-value is divided into intervals. The same is done for t_{max}. All curves falling into the same τ- and t_{max}-interval form a cluster. For each cluster, the mean curve $S_{mean}(t)$ is calculated. The sampling procedure as described above is done based on $S_{mean}(t)$. The resulting sampling times $\{t_i\}$ are used for PK map generation for all voxels having curves within the cluster. Two example clusters with mean curves $S_{mean}(t)$ can be seen in figure 8.9.

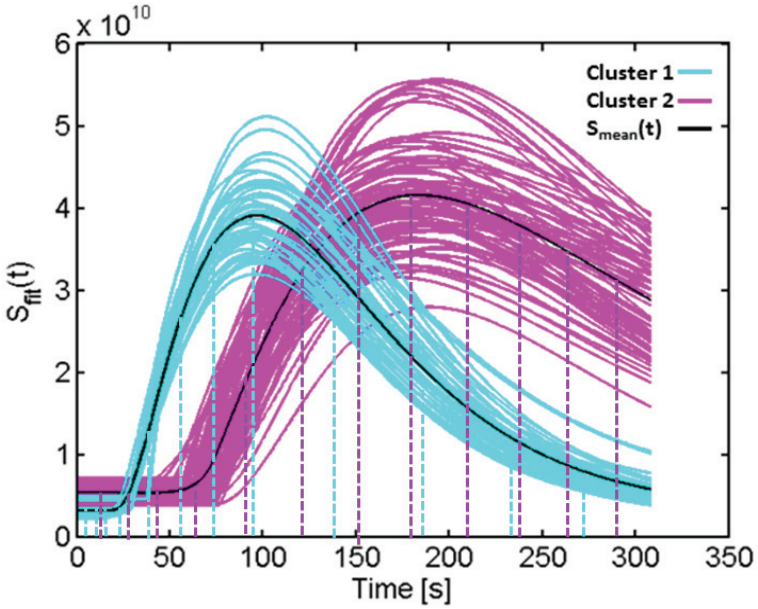

Figure 8.9: All fitted signal time curves S_{fit} of two clusters from perfusion phantom and the resulting mean curves $S_{mean}(t)$ and the resulting sampling schemes (dotted lines) for each cluster.

Image Scaling

Throughout the signal time curves, images are reconstructed at varying spatial resolutions. Since during gridding a resolution-dependent number of profiles N_{pr} is used, different scaling factors are imposed due to varying density compensation functions. To scale the signal intensity of image I_1 reconstructed with $N_{pr,1}$ profiles to image I_2 reconstructed with $N_{pr,2}$ profiles, the following rescaling has to be performed:

$$I_{1,sc} = I_1 \cdot \frac{N_{pr,2}}{N_{pr,1}}, \tag{8.14}$$

where $I_{1,sc}$ is the scaled image I_1.

This is investigated using phantom data of a water-filled sphere. Images with varying numbers of profiles N_{pr} = 625, 1000, 1250, 5000 at a constant spatial resolution (matrix size M=64 at a FOV of 300 mm) are reconstructed and scaled to the image with N_{pr}=5000. For each image, signal profiles denoted as S_{625}, S_{1000}, S_{1250} and S_{5000}, going through the center of the sphere are shown in figure 8.10 a) and b) without and with scaling.

Since a small shift is detected to remain in the phantom profiles after scaling, a constant shift s is empirically determined by calculation of the mean difference of the signal profiles to S_{5000} and division by the scaling factors given in equation 8.14. The scaled and shifted phantom profiles are given in figure 8.10 c).

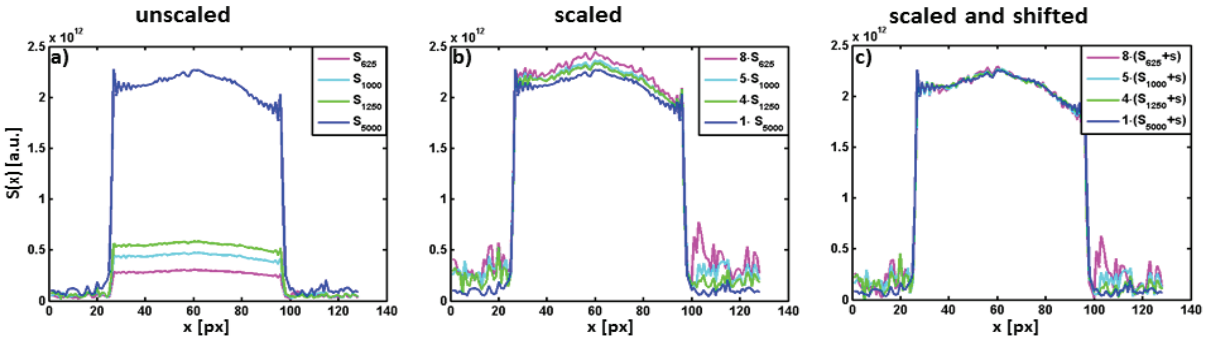

Figure 8.10: Signal profiles of images of a water-filled sphere for varying numbers of profiles N_{pr}= 625, 1000, 1250 and 5000 a) without scaling, b) scaled according to equation 8.14, c) scaled and shifted by the constant shift s.

8.2.8 Comparison of Adaptive and Equidistant Schemes Using a Perfusion Phantom

Using the sequence described in section 8.2.3, data of the perfusion phantom introduced in chapter 6 are acquired for a total dynamic imaging time of T_{dyn} = 311.4 s (60.000 profiles).

Retrospectively Reconstructed Schemes

The phantom data are dynamically reconstructed to yield the following sampling schemes:

- High temporal/low spatial resolution (*fast*) with temporal resolution of Δt=6.5 s and an isotropic spatial resolution of Δx=4.6 mm.
- Low temporal/high spatial resolution (*slow*) with temporal resolution of Δt=59.7 s and an isotropic spatial resolution of Δx=1.5mm.
- Adaptive temporal/spatial resolution as described in section 8.2.7 with a maximal temporal/spatial resolution of Δt=6.5 s/Δx=4.6 mm and a minimal temporal/spatial resolution of Δt=106.9 s/Δx=1.17 mm.

Generation of Pharmacokinetic Maps

As described in chapter 6, the dynamic changes of the perfusion phantom data can be modeled using a gamma-variate function $\Gamma(t)$, as given in equation 6.1. To generate voxel-by-voxel PK maps of the retrospectively reconstructed data, the same steps as described for the perfusion phantom in section 6.2.3 are performed.

Data Analysis

The resulting PK maps of the three schemes are visually compared. Additionally, for the model fit of each voxel, χ^2 as given in equation 4.2 with $\sigma_i = 1$, normalized by the

number of dynamic samples N, is calculated, and χ^2-maps are generated and visually compared.

8.3 Results

In the following, the results of the gradient delay measurement and correction, the phase correction and the retrospective resolution adaption are presented.

8.3.1 Gradient Delay and Phase Corrections

	x	y	z
Δk [pixel]	Δk_x=0.419	Δk_y=0.203	Δk_z=0.086
Δt [μs]	Δt_x=1.638	Δt_y=0.792	Δt_z=0.335

Table 8.2: Measured mean k-space shifts Δk and resulting gradient delays Δt along the x-, y- and z-axis.

The measured mean k-space shifts Δk_x, Δk_y and Δk_z for $N_{samples}$=512 and mean gradient delays Δt_x, Δt_y and Δt_z at a bandwidth of BW_{pixel}=500 Hz/px are summarized in table 8.2.

Images of a water-filled sphere and bottle without any corrections, with gradient delay corrections and with combined gradient delay and phase corrections are shown in figure 8.11. In addition, difference images are displayed. Artifacts are indicated by red arrows. A clear artifact reduction between uncorrected (a, f) and gradient delay corrected (b, g) images is visible for both phantoms. This is as well evident from the difference images (d, i). Only the artifacts marked by red arrows in b) and g) remain. Phase correction has less impact on the images than gradient delay correction. However, when phase correction is additionally applied to gradient delay corrected images (c, d), the remaining artifacts are mitigated. This can more clearly be seen in the difference images e) and j).

For the spherical phantom, the ratio of the mean background and the mean phantom signal of the whole 3D data set s is displayed in the images a), b) and c). A reduction of 5.3% between a) and b) and a smaller reduction of 0.4% between b) and c) is found. In the images, streaking artifacts are additionally visible due to undersampled data, especially for the bottle.

8.3.2 Comparison of Adaptive and Equidistant Schemes Using a Perfusion Phantom

The resulting pharmacokinetic maps for the parameters ϵ, τ, α, t_{max} and Γ_{max} are shown in figure 8.12 for the fast, slow and adaptive reconstruction.

It can be seen that fitting failures displaying very large values occur in the center the maps (indicated by a white arrow for parameter α) for τ, α, Γ_{max} and t_{max} for all schemes.

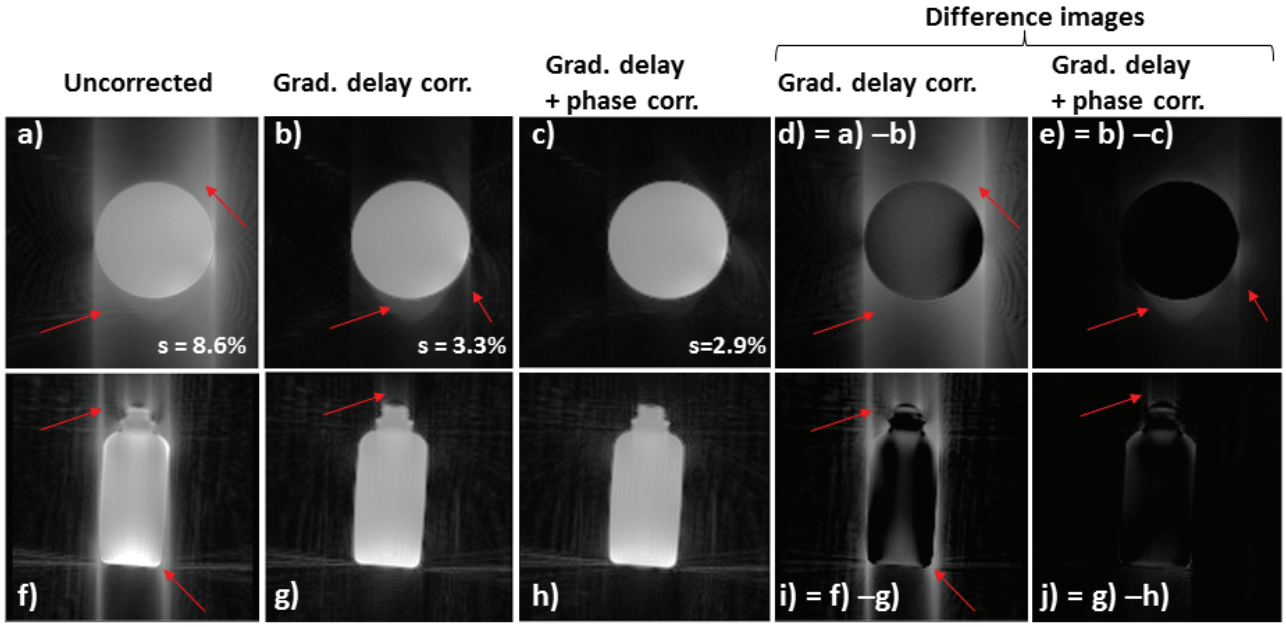

Figure 8.11: Images of a water-filled sphere and bottle a), f) uncorrected, b), g) with gradient delay correction, c), h) with gradient delay and phase correction, d), e), i), j) difference images. For both, gradient delay and phase correction, an artifact reduction in the regions indicated by the red arrows is visible. For the sphere, the ratio s of the mean background and mean phantom signal is given. Additionally, streaking artifacts are visible due to undersampling.

Comparing the fast and the adaptive maps, all parameters of the adaptive maps show a higher spatial resolution, displaying more fine structures. For τ, α, Γ_{max} and t_{max}, the adaptive reconstruction provides consistent results to the fast ones, the adaptive maps appearing sharper compared to the fast maps. For ϵ, the maps are similar, however structures vary more than for the other parameters.

For the slow data, significantly more fitting failures occur for the parameter maps of ϵ, τ and α, in which the structures are hardly recognizable. For Γ_{max} the results are consistent to the two other schemes with the highest spatial resolution. For t_{max}, the resolution is also highest, however, regions of very high peak times cannot be identified anymore.

The χ^2-maps of the fitted curves are shown in figure 8.13. It can be seen that χ^2 of the adaptive data is in average slightly higher but in general comparable to the ones from the fast data. For the slow data, the χ^2 map displays many very high values, indicating fitting failures.

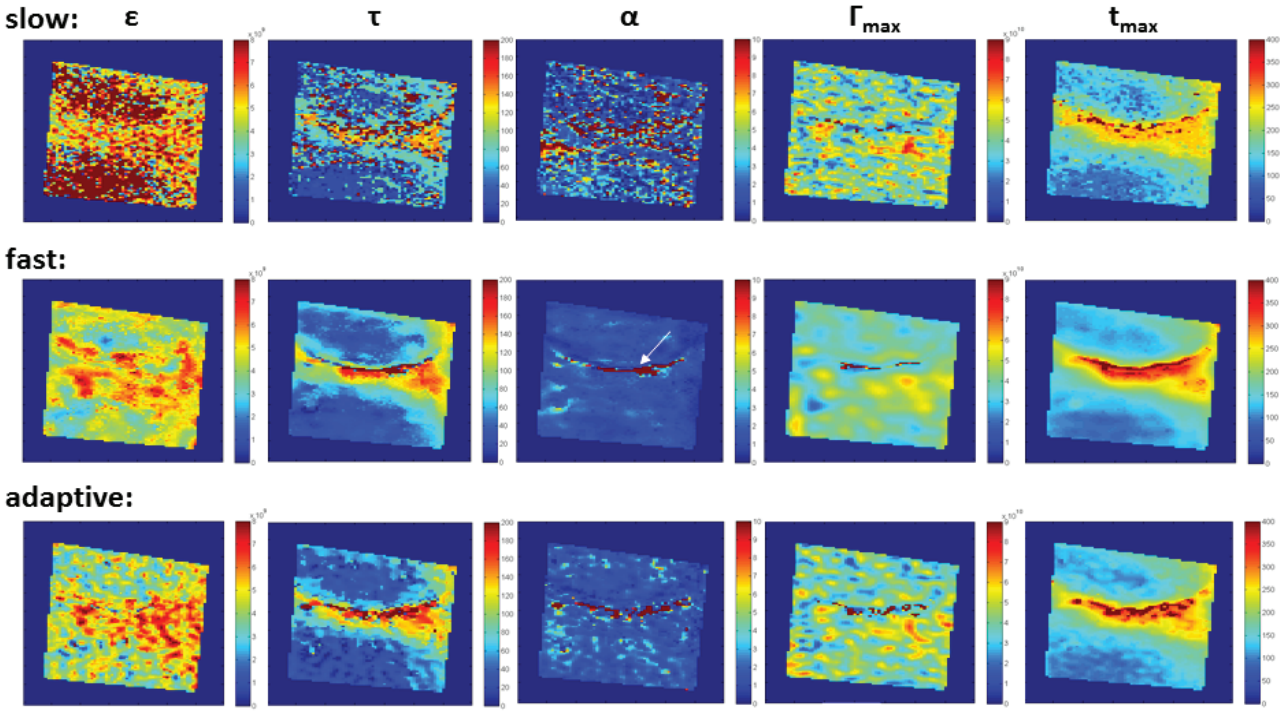

Figure 8.12: Resulting PK maps of the Γ-parameters ϵ, τ, α, t_{max} and Γ_{max} for the retrospectively reconstructed slow, fast and adaptive data.

8.4 Discussion

In this chapter, a 3D golden angle radial sequence is implemented and gradient delay and phase corrections are applied. Using the 3D GA radial sequence, data from a perfusion phantom are acquired and retrospectively the resolution is adapted to clusters of similar signal time curves. The resulting pharmacokinetic maps are compared to those obtained with equidistant reconstructions of low and high temporal resolution. In the following, the employed methods and results will be discussed.

8.4.1 Gradient Delay Corrections

Using an additional sequence, gradient delays are measured and used for k-space trajectory correction during gridding. The order of magnitude of the measured gradient delays is in agreement with those from other studies [Peters2003], [Robison2010]. Image artifacts are clearly reduced when gradient delays are corrected for. This is also in agreement with other works [Peters2003], [Robison2010], [Block2011].

These results suggest that the measured gradient delays can be used to correct for gradient delays is all directions. Inaccuracies may arise from the curve interpolation which is done in order to perform sub-voxel cross-correlation.

A drawback of the used method is that an additional sequence has to be run. However,

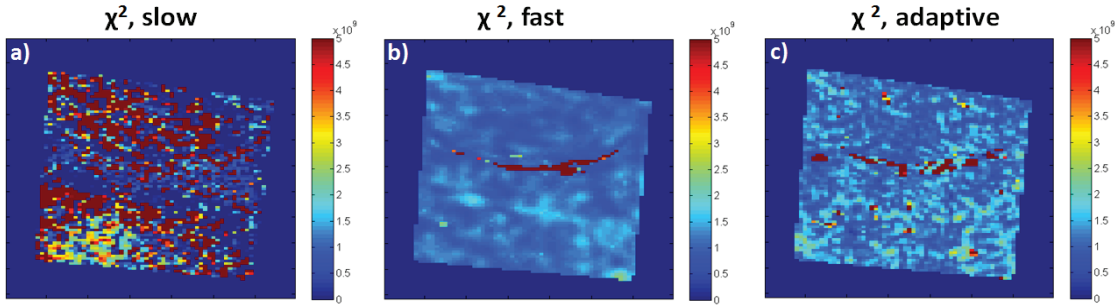

Figure 8.13: Normalized χ^2-maps of the a) slow, b) fast and c) adaptive data. It can be seen that χ^2 of b) and c) are comparable, whilst a) displays many very high values, indicating fitting failures.

since only few k-space profiles along the axes are acquired, the duration of the sequence is in the order of only a few seconds and, for the same scanner and sequence protocol, has to be run only once. Another approach would be to incorporate the gradient delay measurements into the imaging sequence, for example by acquiring each profile in both directions or starting data acquisition already during the pre-phaser gradient. From the additionally acquired information, gradient delays can be determined analogously to the method used here.

In this study, the measured gradient delays are incorporated into the trajectory during post-processing. However, this way k-space center is not exactly measured with each profile and some signal is lost. A more exact approach, yielding higher signal, would be to compensate for the delays when the gradients are played, as done by [Peters2003]. However, this was beyond the scope of this thesis.

When applying this method, it has to be furthermore kept in mind, that gradient delays may not be time-invariant, as for example caused by gradient coil heating. This was shown by [Brodsky2009]. Therefore, an improvement of the correction might be given when gradient delay measurements are regularly updated.

Eventually, the assumption that gradient delays along random directions are linear combinations of the delays along the x, y and z-axis might not be correct and lead to inaccurate gradient delay estimations.

8.4.2 Phase Corrections in the Presence of Gradient Delays

A novel method for phase error correction incorporating gradient delays has been implemented and shown to reduce image artifacts. In comparison to other works such as [Brereton1989], [Brodsky2013], no additional measurement coils or reference acquisitions are required. Instead, the needed information for correction are extracted directly from the raw data. The correction algorithm itself is simple and straightforward to apply. In a similar study, Moussavi *et al* [Moussavi2013] corrected 2D phase errors caused by gradient-induced B_0 eddy currents on the raw data, based on the assumption of a constant phase shift for a certain gradient field. However, during correction it was not taken

into account that profiles do no intersect in the center in the presence of gradient delays.

Since gradient delays are assumed to be exactly known in the used algorithm, the accuracy of gradient delay measurement affects the quality of the phase correction. The few artifacts which are still present after phase correction might arise from inaccurately measured gradient delays. Another source of the remaining artifacts could be the approximations used during the calculation of the density compensation function, which will be discussed below in more detail.

In the performed experiment, phases errors were relatively small compared to gradient delay errors. In general, B_0 effects are small for field strength $\leq$3T [Moussavi2013]. However, when going to higher field strengths, B_0 effects increase. In that case, phase error corrections might become more relevant. In a future work, the effects of the presented method could be investigated for data acquired at higher field strengths.

The presented algorithm is based on the assumption that two points at very similar spatial locations have the same phase. In the case of locally fast changing phases, this approximation becomes invalid and the phase correction is not accurate. This problem is enhanced by error propagation when a projection with erroneous phase is used as reference profile.

It has to be furthermore noted that the result of the algorithm depends on the choice of the initial reference profile. If multiple dynamic images are reconstructed, it is therefore important to always employ the same initial reference projection. To optimize the phase correction, it could be performed for various initial reference projections and the optimal phase distribution could be determined by using for example maximum likelihood estimators [Bevington2002]. This could be investigated in a future work.

8.4.3 Retrospective Resolution Adaption

In summary, retrospective resolution adaption of 3D GA radial data has been shown to be feasible using a perfusion phantom. The fitting accuracy of the adaptive data is comparable to those of a high temporal/low spatial resolution reconstruction. Compared to a low temporal/high spatial resolution reconstruction, the adaptive data show better fitting performance. The poor fitting accuracy of the slow data arises from missing important time points as it was shown in simulation is chapter 5. With the adaptive schemes, onset time and upslope are sampled correctly, improving fitting stability. The mean spatial resolution of the adaptive data lies between those of the two other reconstructions.

In a similar study, Grimm *et al* [Grimm2014] reconstructed dynamic DCE MRI golden angle "stack of stars" data at two different temporal resolutions to save computational time. They found that reconstruction time was significantly reduced at a preserved fitting accuracy. Here, this approach is extended to arbitrary resolutions to regionally optimize fitting accuracy. Furthermore, instead of "stack of stars", a true 3D radial trajectory is employed.

Retrospective resolution adaption is performed on data which are acquired from the perfusion phantom described in chapter 6. The model used to quantify the phantom is a gamma-variate function, which shows relatively fast changes during upslope and washout. Consequently, not a large amount of spatial resolution can be exploited. Typical DCE MRI data, which are for example modeled using [Tofts1991], exhibit a slower washout. In that case, higher spatial resolutions probably could be achieved due to partially slower curve changes. In a future work, this could be investigated using clinical data or a phantom, in which tissue curves are more realistically modeled.

For large onset times, the phantom curves are only partially sampled, only acquiring the baseline and parts of the onset. Here, the fitting fails because of the missing data. However, this limitation is only caused by the timing of the phantom and data acquisition, and should not be relevant for clinical applications.

In the used gridding reconstruction, the density compensation function is just an approximation based on simplifications of the distribution of profiles used for fast and easier calculation. The assumption that profiles show a perfectly uniform distribution is not true for golden angles. Especially for a small number of profiles, this may cause errors. Another assumption is that no gradient delays occur, which is also not true and might change the density compensation function, mainly in the k-space center. To prevent these errors, Voronoi diagrams could be used instead for density compensation calculation. However, due to very long calculation times of Voronoi algorithms for a large number of samples, the geometric approximation is used here.

For image reconstruction, gridding is employed which is a very basic reconstruction technique. For under-sampled data, aliasing manifests itself as streaking artifacts which may corrupt fitting accuracy. To guarantee acceptable image quality at higher spatial resolutions, a relatively large amount of profiles is required. When contrast changes occur during acquisition, this may lead to temporal blurring. Therefore, a compromise between temporal blurring, image resolution and streaking artifacts has to be found and can be freely chosen.

However, gridding can be replaced by more advanced reconstruction techniques such as non-Cartesian parallel imaging [Pruessmann1999] or compressed sensing [Donoho2006]. They allow for a reduction of aliasing artifacts and acceleration of imaging. Due to faster imaging, these methods also prevent temporal blurring. Another approach would be to post-process k-space data similar to as it is done using KWIC [Song2004]. A filter is applied such that only profiles close to the time point of interest contribute to image contrast. A trade-off between degree of temporal blurring and loss in SNR can be chosen flexibly.

The origin of the reported scaling problem of the shift for different profile numbers has not been solved in this work. Since it causes only a small discontinuity in the signal time curves, it is tolerated here. However, for future works it should be more thoroughly investigated.

To save computation time during retrospective reconstruction, the algorithm is applied to clusters of similar curves. In this study, clusters are chosen based on similar onset and peak times. This is a very basic method and is chosen because of its straightforwardness.

However, since the step size of the intervals are relatively large with Δt=25 s, the deviations of the onset and peak times with respect to the mean curves can potentially be large. Instead, more advanced algorithms for cluster generation such as k-means [Everitt2011] could be chosen.

The choice of sampling times being 4 time points each on baseline, upslope and washout are considered as required sampling scheme here. However, this is just an estimation based on experience from previous fitting testing. A better approach would be to employ optimal sampling design as it was done for the Tofts model in chapter 4.

In the current experiment, no ground truth for PK maps is available. Fitting accuracy is estimated by comparing the χ^2 maps to the one calculated from the slow temporal resolution data, which is assumed to provide accurate fitting. Spatial resolution can only be evaluated by investigating the amount of details in the maps and the data consistency. For an analysis with a known ground truth, the simulations of chapter 5 could be repeated with the 3D GA radial sampling schemes.

A general advantage of the 3D GA radial sequence is that central k-space is acquired with each projection and therefore a large amount of contrast information is present in the dynamic data. In comparison, for Cartesian data only comparably few lines cross k-space center and contrast information cannot be recovered once it is missed.

The golden angles allow for flexible reconstruction at arbitrary time points which is a large advantage in order to optimally sample signal time curves. Especially the fact that optimal sampling can be regionally adapted is of importance in situations of tumors with largely heterogeneous pharmacokinetic properties, as for example varying onset times. Another scenario would be multiple lesions within the FOV. This is an advantage over the AURA sequence described in chapter 7, in which the resolution is adapted only to the mean signal time curve. For single voxels, sampling of the AURA data might be still unsuitable for fitting, for example due to missing the onset time.

Another benefit of radial compared to Cartesian sequences is that relatively fast dynamic imaging is feasible since a high degree of under-sampling is normally tolerable. For example using the acquired data, model fitting is possible despite an under-sampling of 90%. This is the case since in many applications streaking artifacts corrupt image quality less than the Cartesian wrap-around artifacts as for example shown by [Peters2000], [Peters2001], [Shankaranarayanan2001]. With the current sequence, a 3D volume with a FOV of 300 mm can be acquired at an isotropic spatial resolution of Δx=4.6 mm in 6.5 s and at Δx=2.3 mm in 26 s. The given numbers are still without the usage of parallel reconstruction, which will yield an acceleration factor of 8 or more. Furthermore, radial sequences are relatively insensitive to motion artifacts. Additionally, the profile going through k-space center each time can be used for self-navigated motion correction [Welch2004].

However, radial sequences also require more data by a factor of π to satisfy the Nyquist criterion compared to Cartesian images. Additionally, artifacts typical for radial imaging need to be taken care of such as gradient delay and phase errors, which was investigated in chapter 8.2.4 and 8.2.5. They can be corrected for, however, additional measurements

and reconstruction steps are necessary. Finally, non-Cartesian reconstruction is more complicated and time-consuming than Cartesian data reconstruction.

A general problem of concatenating different resolutions are varying partial volume effects. They could adversely affect fitting accuracy.

In clinical routine, one of the advantages of the 3D GA radial sequence would be that exact timing of sequence starting time and contrast agent injection are not important anymore, since the onset time can be retrospectively recovered.

To bring the 3D GA radial sequence into clinical usage, however, first some further steps need to be completed. Example patient data need to be acquired to determine the SNR and amount of under-sampling tolerable in clinical data to preserve acceptable image quality. Probably parallel reconstruction will be inevitable to yield sufficient imaging speed. As for now, the computational reconstruction time is too high for clinical routine. To speed up the reconstruction process, the calculation could be implemented on a graphics processing unit, for example as done by [Nam2013].

9 Discussion and Conclusions

DCE MRI is used in oncology for lesion diagnosis and classification, and is still a topic of active research. Especially for breast lesions, a standard method for diagnosis is not yet established. One approach is to apply pharmacokinetic modeling to the data to obtain quantitative and physiologically-relevant parameters that reflect the underlying vasculature [Jackson2005]. For accurate fitting results, a high temporal resolution is required [Henderson1998]. However, tumors are inherently heterogeneous and therefore high spatial resolution is also desirable to depict spatial variations within the lesion. An alternative approach is to acquire high spatial resolution images to extract morphological features, which play an important role in diagnosis [Kuhl2005]. However, in MRI high temporal and spatial resolution are inherently not compatible and a compromise has to be found.

Most studies acquire images at a constant temporal resolution. However, different phases of the dynamic signal time curves are governed by different physiological processes. Some time points have more relevance than others for the determination of certain pharmacokinetic parameters. Therefore, a compromise between high spatial and temporal resolution can be found by using adaptive schemes, which sample data faster during intervals which are important for accurate model fitting, and otherwise exploit high spatial resolution.

Some studies exist which indicate that combining high and low temporal resolution acquisitions within the same DCE MRI investigation can be of advantage for diagnostic accuracy [Vomweg2004], [Veltman2008], [Pinker2009], [Jansen2010], [Mann2011]. All of these studies have in common that rapid sampling occurs during the fast early contrast agent kinetics. At later time points, during contrast agent wash-out, the sampling schemes switch to low temporal resolutions to allow for morphological evaluation when there is still a large amount of contrast agent present in the lesion. However, these adaptive sequences are still a relative new area of research and many questions remain unanswered. In this thesis, different problems of adaptive sequences are addressed, which are related to the accuracy of model fitting and the spatial resolution which can be achieved. The investigated aspects are summarized, the main issues are discussed and the works are concluded one by one in the following.

In previous clinical studies the temporal resolutions were changed at intuitively chosen time points based on experience. The key problem addressed in chapter 4 was to derive, using optimal sampling theory, where fast sampling is needed for accurate Tofts model [Tofts1991] fitting and where slower sampling is sufficient.

For typical breast DCE MRI parameters, it was found that high temporal resolution during the first 2 min after the onset time of contrast agent is advantageous for high

fitting accuracy, whilst images at later time points can be exploited for morphological imaging at high spatial resolution. It was shown as well that optimized sampling schemes perform better in terms of model fitting than equidistant sampling schemes for a small number of samples and comparable for a large number of samples. Additionally, it was found that for the number of samples being higher than a certain number, the parameter accuracy is mainly governed by the noise standard deviation of each data point.

The used methods have previously been applied to Arterial Spin Labeling [Xie2008]. However, with Arterial Spin Labeling, data can be repeatedly sampled at all time points throughout the curve. The novelty of this work lies in the adaption to DCE MRI, which imposes the constraints that time points have to be acquired in a chronological order with a minimal time interval between them. It is important to notice that the obtained results are only valid for the Tofts model and the assumed underlying parameter distribution. However, this method can potentially be applied straightforwardly to different parameter sets and models. Yet, with the parameters assumed in this study, the results are in good agreement with the improved diagnostic performance of clinical studies for similar sampling schemes [Pinker2005], [Jansen2010], [Mann2011].

In conclusion, as an estimate, fast sampling during the initial 2 min after the onset time is recommended for breast DCE MRI, slow acquisition high spatial resolution during later time points. The more information about the underlying model and parameter distribution are available, the better the optimal sampling scheme can be tailored. Data noise has a high influence on fitting accuracy and should be kept as small as possible.

After having derived in chapter 4 *where* fast sampling is required, one of the natural following question is *how* to optimally achieve fast sampling during these intervals. This problem is addressed in chapter 5. A common way to decrease acquisition time during the initial kinetics phase is to omit certain k-space data and employ view-sharing methods as described in chapter 3 to estimate the missing data. This potentially degrades image quality in the form of temporal blurring from the view-sharing methods. Consequently, fitting errors are introduced due to this image degradation. A compromise between the gain in fitting accuracy due to accelerated imaging and the accompanying image degradation has to be found. In this simulation study using a numerical phantom, different view-sharing acceleration strategies to achieve a high temporal resolution during the onset time and initial kinetics are compared in terms of their influence on the Tofts model parameters K^{trans}, v_e and τ.

First, the results from chapter 4 could be confirmed by implementing an idealized acquisition scheme providing acceleration but no image degradation. Sampling during the onset and initial kinetics significantly yielded improved fitting accuracy with few systematic errors. All realistic view-sharing methods imposed larger systematic fitting errors, characteristic for each scheme. All schemes showed the common tendency to underestimate K^{trans} especially for small structures, which bears the danger of underestimation the malignancy of a small tumor and misclassifying it as benign lesion. For the employed phantom the scheme called modTRICKS, a combination between TRICKS [Korosec1996] and Keyhole [Vaals1993] provided the best fitting performance, being clos-

est to the idealized case. It was additionally found that data noise has a high impact on fitting accuracy which is in good agreement with the results from chapter 4.

Other studies have investigated fitting accuracy based on simulations [Laue2010], [Heisen2010], however this was the first work to investigate the effects of different k-space view-sharing methods on fitting accuracy of adaptive schemes. It should be kept in mind that this is only a simulation study, not taking into account many factors of a realistic environment which may further influence fitting accuracy. Yet, estimates and tendencies can be obtained from these simulations.

In conclusion, it was found that different view-sharing methods impose different systematic fitting errors which all have the potential to underestimate K^{trans}. This should be kept in mind during diagnosis. From the compared schemes, modTRICKS is recommended. Furthermore, for accurate fitting, noise should be kept as low as possible.

In chapters 7 and 8, sequences were developed which will be described in the following paragraphs. Due to ethical constraints, the investigation of these sequences could not be performed in patients. For that purpose, a phantom was designed in chapter 6. The main demands to the phantom were the possibility to inject contrast agent, to yield quantifiable signal time curves with temporal changes in the order of typical breast DCE MRI data, to show a heterogeneous parameter distribution and to provide reproducible results. This could be achieved by employing a sponge, which was connected via a hose to an inflowing water source of constant flow velocity and a second hose allowing outflowing water to leave the sponge. Contrast agent was manually injected into the inflowing hose. Signal time curves could be quantified using a gamma-variate function [Chan2004] and a heterogeneous behavior of the parameters was monitored due to different densities of the sponge. Dynamic changes were in the order of approximately 3-4 min and fitting results were found to be relatively reproducible.

In general, there is a lack of reliable and useful perfusion phantoms in the MR community. Only few publications exist such as [Ebrahimi2010], [Driscoll2011], [Freed2011] and even fewer phantoms are commercially available and are generally difficult to rebuild. Yet, perfusion phantoms are very important for sequence development. The presented phantom here has the advantage to be very cheap and easy to implement. However, the largest drawback of the phantom for the current application is that quantitative description is not given by a multi-compartment model such as the Tofts model showing a slower wash-out typical for DCE MRI tissue curves. However, for sequence investigation and providing proofs of principle, a phantom with the given properties was sufficient.

In both, chapter 4 and 5, the importance of rapid data acquisition at the onset time and the subsequent upslope has been highlighted. However, the onset time is dependent on the physiological condition of the patient and the timing of imaging relative to contrast agent injection, and therefore it is not know prior to imaging when to start fast sampling. The same applies to the beginning of the wash-out phase. The results of chapter 4 indicate that fast sampling should occur for 2 min after the onset time. However, this is just an estimate for the assumed underlying parameter distribution in chapter 4, which

can largely vary from tumor to tumor. If the sequence switches too late to high spatial resolutions, contrast agent could be partially washed out, and important architectural features might be missed. In the current clinical sequences, resolution changes occur at fixed predefined time points. These rigid implementations do not allow for adaption to patient-specific sampling requirements.

In chapter 7, this problem was addressed by developing an automatic resolution adaption (AURA) sequence, which can react to individual patient sampling curves. Acquired dynamic data are analyzed in real-time to find the onset and the beginning of the washout and consequently temporal resolution is automatically adapted by alteration of spatial resolution. Using the perfusion phantom described in chapter 6, adaption criteria could be defined, which successfully worked for onset and peak detection. Acquiring phantom data, the AURA sequence was compared to two equidistant sequences, one acquiring only high temporal, the other only high spatial resolution. It could be shown that the fitting performance of the AURA sequence provided comparable results to that of the fast sequence. Additionally, using AURA, high spatial resolution images could be reliably acquired directly after the contrast agent peak, whilst contrast agent was partially washed out using the slow sequence.

In a previous study, real-time automatic contrast agent bolus detection in vessels was introduced [Goto2013]. In this work, this concept was for the first time extended to the application of adaptive DCE MRI sequences. The retrieved information from bolus tracking were used for real-time resolution adaption. A principal drawback of the AURA sequence is that resolutions are only globally adapted to the mean signal time curves. However, in heterogeneous lesions, the onset and peak times might show regional variations. In that case, important time points during the initial kinetics might be missed in some regions, leading to fitting inaccuracies, as was shown in chapter 5.

To conclude, an "intelligent" resolution adaptive DCE MRI sequence was developed, which provides both, high fitting accuracy and high spatial resolution images close to the signal peak. The promising phantom results suggest that this approach should be extended to *in vivo* applications.

As discussed in chapter 7, an inherent problem of globally adapted sequences is that imaging might be not optimized for all signal times curves within a heterogeneous lesion. The onset and peak times may vary from voxel to voxel, leading to different optimal time points of resolution changes. Additionally, the highest possible allowed resolutions whilst still preserving fitting accuracy may regionally vary for different signal time curves. Therefore, an alternative approach to the AURA sequence to overcome this problem is investigated in chapter 8 using retrospective resolution adaption. A 3D golden angle radial sequence [Chan2009] acquires k-space center and hence contrast information with each profile. Additionally, due to the golden angles, images can be reconstructed at arbitrary time points with arbitrary spatial/temporal resolution. In this work, a 3D golden angle radial sequence is used to adapt the spatial resolution to the signal time curves on a voxel-specific basis to achieve the maximal feasible spatial resolution whilst preserving fitting accuracy.

Using the perfusion phantom described in chapter 6, it could be shown that retrospective resolution adaption is feasible. The fitting accuracy of the adaptive reconstruction was comparable to that of a reconstruction with low spatial and high temporal resolution. However, an improvement of the spatial resolution for all parameters was achieved.

A 3D sequence based on 2D golden angle "stack of stars" DCE MRI was used in a recent study, in which data were reconstructed at two different temporal resolutions to save reconstruction time [Grimm2014] with unchanged fitting accuracy. In this work, this approach was extended to arbitrary resolutions with the aim to regionally optimize spatial resolution whilst preserving fitting accuracy. Furthermore, instead of "stack of stars", a true 3D radial trajectory was employed. Drawbacks of the method are long reconstruction times, artifacts which are not problematic in Cartesian imaging such as gradient delay and phase errors and more required data to fulfill the Nyquist criterion than for Cartesian imaging. Due to these reasons, the employment of sequences such as the AURA sequence might be more practical and it has to be investigated if the error caused due to regional pharmacokinetic differences justifies the drawbacks of 3D radial sequence.

In conclusion, in a proof-of-concept study, the retrospective resolution adaption using a 3D golden angle sequence has been shown to be a promising method to optimize spatial resolution whilst preserving fitting accuracy, especially for heterogeneous parameter distributions. Based on the results it is suggested that this method should be further investigated.

Future Work

This work should be seen as basic research and is by no means a finished project. Rather, the foundation for many interesting and promising future projects was laid with the potential to be one day ready for clinical applications. But until then, remaining problems still need to be solved and methods need to be refined.

The adaptive simulations in chapter 5 could be extended and improved. The used methods could be straightforwardly applied to view-sharing methods which were not taken into account in this work. The effects of the 3D radial sequences used in chapter 8 could be simulated to compare the results of the employed radial reconstruction to a known ground truth. Instead of using view-sharing methods, which are relatively basic techniques to speed up imaging, more advanced methods such as parallel imaging or compressed sensing could be simulated. By better mimicking realistic processes, the effects of other sources of fitting errors such as field inhomogeneities, motion, temporal blurring during imaging, or varying onset times throughout the phantom could be investigated.

The signal time curves of the perfusion phantom described in chapter 6 were modeled using a gamma-variate function. The next steps could be to extend the phantom set up such that typical multi-compartmental DCE MRI signal time curves are provided. This could be for example done by adding a filter on top of the sponge, mimicking a

permeable wall between two compartments.

A large drawback of the current phantom is that no ground truth is provided. A very interesting future project would be to replace the sponge with a more refined known structure for which the ground truth can be derived. This could be achieved for example using 3D printers, as suggested by [Oliver-Taylor2011]. However, as for today, printing structures as small as capillaries is still impossible on commercially available printers. However, 3D printing technologies are in rapid development and might be very promising for phantom generation in the near future.

For the AURA sequence, first of all, the remaining internal scaling problem needs to be solved. The next steps could be to implement better acceleration techniques instead of just changing the spatial resolution and using zero-filling. For example, the view-sharing method modTRICKS, which showed the best performance in terms of model fitting out of the compared schemes in chapter 5, could be implemented. As well, more advanced acceleration techniques such as parallel imaging or compressed sensing could be employed. So far, adaption criteria were only found for the perfusion phantom. These criteria should be extended to *in vivo* applications. For that, more refined bolus tracking methods need to be investigated. Since spatial information needs to be taken into account due to enhancing regions outside the region of interest, analysis should be done on reconstructed images rather than on k-space data. For example Kalman-filters could be considered as tracking algorithms [Kalman1960]. Furthermore, for first clinical experiments, until reliable adaption criteria are found, a manual "switch button" should be implemented to prevent data loss in case of automatic adaption failure. Another future work could be to employ a larger choice of possible resolutions rather than only the three given options. This way, adaption could be done in a better tailored fashion.

For the retrospective radial reconstruction, the remaining scaling problem should solved. The next steps towards acquiring *in vivo* data could be to implement parallel reconstruction, yielding a minimal acceleration factor of 2 in each direction or allowing higher spatial resolutions. Finally, more sophisticated algorithms for cluster generation, such as k-means [Everitt2011] could be employed. The problem of very long reconstruction times could be improved by using a graphics card implementation of the reconstruction process as done by [Nam2013].

Appendix A

For the literature search for physiologically realistic Toft model parameters only publications are taken into account which fulfill the following criteria:

- The values are measured in humans.
- The organ of interest is the breast.
- Absolute PK parameter values are given.
- Images are acquired with high temporal resolution(<20s).
- Many patients or lesions are taken into account(#>10).

A summary of the included publications can be found in table 9.1, which contains the reference, the number of patients and lesions, the measured PK parameter values, the model, the temporal resolution and the year of publication. *Cut-off* values are values which separate benign and malignant parameter ranges.
The results from table 9.1 are briefly summarized here.

K^{trans}:
Taking all publications into account, the overall range of measured values is $0.07 \leq K^{trans} \leq 4.0$. A distinction is made between healthy, benign and malignant tissue. Only one publication measuring healthy tissue values is found with a mean of $K^{trans} = 0.07$. Benign values range from $0.22 \leq K^{trans} \leq 1.5$, malignant values from $0.5 \leq K^{trans} \leq 4.0$. In all publications the mean value of malignant lesions is higher than that of benign lesions.
v_e:
The overall range of measured values is $0.08 \leq v_e \leq 0.9$. As for K^{trans} a distinction between benign and malignant values is made. Only one publication measured healthy tissue values with $v_e = 0.08$. Benign values range from $0.2 \leq v_e \leq 0.6$. Malignant values range from $0.4 \leq v_e \leq 0.9$. In all publications the malignant values are higher than the benign and healthy values. Fewer values are found in comparison to K^{trans}.

Ref	#Patients and Lesions	K^{trans}	v_e	PK model	Δt	Year
[Jena2013]	36 patients, 36 lesions (16 ben, 20 mal)	ben:0.33, mal:1.45, cut-off: 0.56	cut-off = 0.2	TK	4s	2013
[Khouli2011]	95 patients, 101 lesions (33 ben ,68 mal)	ben: 0.22, mal: 0.5	ben: 0.25, mal: 0.8	TK	15s	2011
[Veltman2008]	96 patients, 102 lesions (34 ben, 68 mal)	ben: 0.5-1.5, interm:1.5-2.0, mal: 2.0-4.0	ben: 0.2-0.4, interm:0.4-0.6, mal: 0.6-0.9	TK	4.1s	2007
[Padhani2003]	15 patients	healthy: 0.07	healthy: 0.08	TK	9s	2003
[Hayes2002]	15 patients	ben: 0.0-0.8, mal: 0.0-2.5	none	TK	10s	2001

Table 9.1: Summary of measured PK parameter mean values K^{trans} and v_e.

Appendix B

Tofts Model Sensitivity Functions

The sensitivity functions $\zeta_K(t)$, $\zeta_v(t)$ and $\zeta_\tau(t)$ of the Tofts model are the first partial derivatives of the concentration time curve $C(t)$ with respect to the parameters K^{trans}, v_e and τ are given by:

$$\zeta_K = \frac{\partial C(t)}{\partial K^{trans}}, \zeta_v = \frac{\partial C(t)}{\partial v_e}, \zeta_\tau = \frac{\partial C(t)}{\partial \tau}. \tag{9.1}$$

The derivatives are calculated using Mathematica 8 [Wolfram Research, Inc., Champaign, Illinois, USA]. The analytical solutions of the sensitivity functions are shown in the following.

$\zeta_K(t)$:

$$\begin{aligned}
&\text{if } t < \tau : \frac{\partial C(t)}{\partial K^{trans}} = 0 \\
&\text{if } t \geq \tau : \\
&\frac{\partial C(t)}{\partial K^{trans}} = D \cdot [\frac{a_1 e^{-m_1(t-\tau)}}{\frac{K^{trans}}{v_e} - m_1} + \frac{a_2 e^{-m_2(t-\tau)}}{\frac{K^{trans}}{v_e} - m_2} - e^{-\frac{K^{trans}(t-\tau)}{v_e}} \\
&\cdot (\frac{a_1}{\frac{K^{trans}}{v_e} - m_1} + \frac{a_2}{\frac{K^{trans}}{v_e} - m_2} - \frac{a_1 K^{trans}}{(\frac{K^{trans}}{v_e} - m_1)^2 v_e} - \frac{a_2 K^{trans}}{(\frac{K^{trans}}{v_e} - m_2)^2 v_e}) \\
&- \frac{a_1 K^{trans} e^{-m_1(t-\tau)}}{(\frac{K^{trans}}{v_e} - m_1)^2 v_e} - \frac{a_2 K^{trans} e^{-m_2(t-\tau)}}{(\frac{K^{trans}}{v_e} - m_2)^2 v_e} + \\
&te^{-\frac{K^{trans}}{v_e}(t-\tau)} \frac{a_1 K^{trans}}{\frac{K^{trans}}{v_e} - m_1} + \frac{a_2 K^{trans}(t-\tau)}{(\frac{K^{trans}}{v_e} - m_2) v_e}]
\end{aligned} \tag{9.2}$$

$\zeta_v(t)$:

$$\begin{aligned}
&\text{if } t < \tau : \frac{\partial C(t)}{\partial v_e} = 0 \\
&\text{if } t \geq \tau : \\
&\frac{\partial C(t)}{\partial v_e} = D \cdot [-e^{-\frac{K^{trans}}{v_e}(t-\tau)} (\frac{a_1 (K^{trans})^2}{(\frac{K^{trans}}{v_e} - m_1)^2 v_e^2} + \frac{a_2 (K^{trans})^2}{(\frac{K^{trans}}{v_e} - m_2)^2 v_e^2}) + \\
&\frac{a_1 e^{-m_1(t-\tau)} (K^{trans})^2}{(\frac{K^{trans}}{v_e} - m_1)^2 v_e^2} + \frac{a_2 e^{-m_2(t-\tau)} (K^{trans})^2}{(\frac{K^{trans}}{v_e} - m_2)^2 v_e^2} - \\
&e^{-\frac{K^{trans}}{v_e}(t-\tau)} K^{trans} (\frac{a_1 K^{trans}}{\frac{K^{trans}}{v_e} - m_1} + \frac{a_2 K^{trans}}{\frac{K^{trans}}{v_e} - m_2}) \frac{(t-\tau)}{v_e^2}]
\end{aligned} \tag{9.3}$$

$\zeta_\tau(t)$:

$$\text{if } t < \tau : \frac{\partial C(t)}{\partial \tau} = 0$$

$$\text{if } t \geq \tau :$$

$$\frac{\partial C(t)}{\partial \tau} = D \cdot [\frac{a_1 K^{trans} m_1 e^{-m_1(t-\tau)}}{\frac{K^{trans}}{v_e} - m_1} + \frac{a_2 K^{trans} m_2 e^{-m_2(t-\tau)}}{\frac{K^{trans}}{v_e} - m_2} + \tag{9.4}$$

$$\frac{1}{v_e} e^{-\frac{K^{trans}}{v_e}(t-\tau)} (t-\tau) K^{trans} (\frac{a_1 K^{trans}}{\frac{K^{trans}}{v_e} - m_1} + \frac{a_2 K^{trans}}{\frac{K^{trans}}{v_e} - m_2})]$$

Appendix C

In the sequence environment data with the matrix size of the current scheme are acquired and forwarded to the reconstruction environment, where they are evaluated and reconstructed. The real-time feedback mechanism within the reconstruction environment evaluates the incoming k-space for predefined feedback criteria. The result of the evaluation determines the scheme to be used for the next dynamic acquisition.
A detailed implementation is visualized in the flow chart in figure 9.1 and will be explained in the following step by step.
The following variables are used in the flow chart:

- *currScheme* describes the current scheme, which can take values 1-4 and represent the schemes BL, OD, IK and WO described in section 7. They vary regarding the temporal/spatial resolution.
- *rep* is an index which keeps track of the current repetition, starting at 0.
- *FBReceive* is a boolean flag within the sequence environment, which takes the value $false$ when feedback has not been received from the reconstruction environment and $true$ if feedback has been received.
- *currCond* is an boolean flag in the reconstruction environment which is $true$ when a certain if-condition is fulfilled and $false$ if it is not. The if-condition is applied to the acquired k-space data is dependent on *currScheme*.
- *continueScan* is a boolean flag set in the reconstruction environment which is $true$ if imaging continues after the current acquisition and $false$ if the currently evaluated image is the last acquired image in the dynamic scan.
- *Matrix size* defines the matrix size of the next image to be acquired. It is dependent on the current scheme.
- *RTFBData* is a data struct which is sent from the reconstruction environment to the sequence environment. It contains the variable *currScheme* and the flag *continueScan*.

Initially, the current scheme is set to $currScheme = 1$, which correspond to a matrix size of M_{BL}xM_{BL}. The repetition index is $rep = 0$ and the boolean flag $FBReceive$, which indicates that feedback has been received from the reconstruction environment, is $false$. In the next step data are acquired based on these settings. Afterwards the sequence pauses and waits for a wakeup signal from the RTFB mechanism, whilst the acquired k-space data are forwarded line by line to the reconstruction environment.

Within the reconstruction environment, the incoming k-space data are evaluated if they fulfill the condition $currCond = 1$. For scheme 1, $currCond = true$ if $rep > N_{BL}$. For $rep = 0$, $corrCond$ is $false$. Consequently, $currScheme$ and $currCond$ remain unchanged for the next acquisition. Additionally to real-time evaluation, the data are reconstructed according to the reconstruction required for data acquired with scheme 1.

The $RTFBData$ send the information $currScheme = 1$, which corresponds to a matrix size of M_{BL}xM_{BL}, for the next acquisition back to the sequence environment. Additionally, since this is not the last dynamic aquisition, $continueScan = true$ is forwarded as well to the sequence environment.

Upon arrival of the $RTFBData$ within the sequence environment the flag $FBReceive$ is updated to $true$. The repetition index is incremented by 1 and the sequence is prepared anew for data acquisition according to scheme 1.

This process is repeated until $currCond = 1$ is $true$ which is the case when N_{BL} images have been acquired. In that case, $currScheme$ and $currCond$ are each incremented by 1. $RTFBData$ are updated to $currScheme = 2$ with corresponding matrix size of M_{OD}xM_{BL}. The flag $continueScan$ remains $true$. Again, $RTFBData$ are received in the sequence environment and rep is incremented. This time the sequence is prepared according to scheme 2.

Again, after data acquisition the k-space data are evaluated, this time according to $currCond = 2$, which is used for onset detection. As long as $currCond = 2$ is $false$, images are continued to be acquired with scheme 2. If $currCond = 2$ is $true$, $currScheme$ and $currCond$ are incremented by 1 and $continueScan = true$ remains. Scheme 3 and scheme 4 are handled analogously, using the $RTFBData$ defined in the lower part of the reconstruction environment box in figure 9.1.

When the last image of scheme 4 has been acquired, the flag $continueScan$ is switched to $false$ and sent via the RTFBData back to the sequence environment. In this case the sequence stops the dynamic scan.

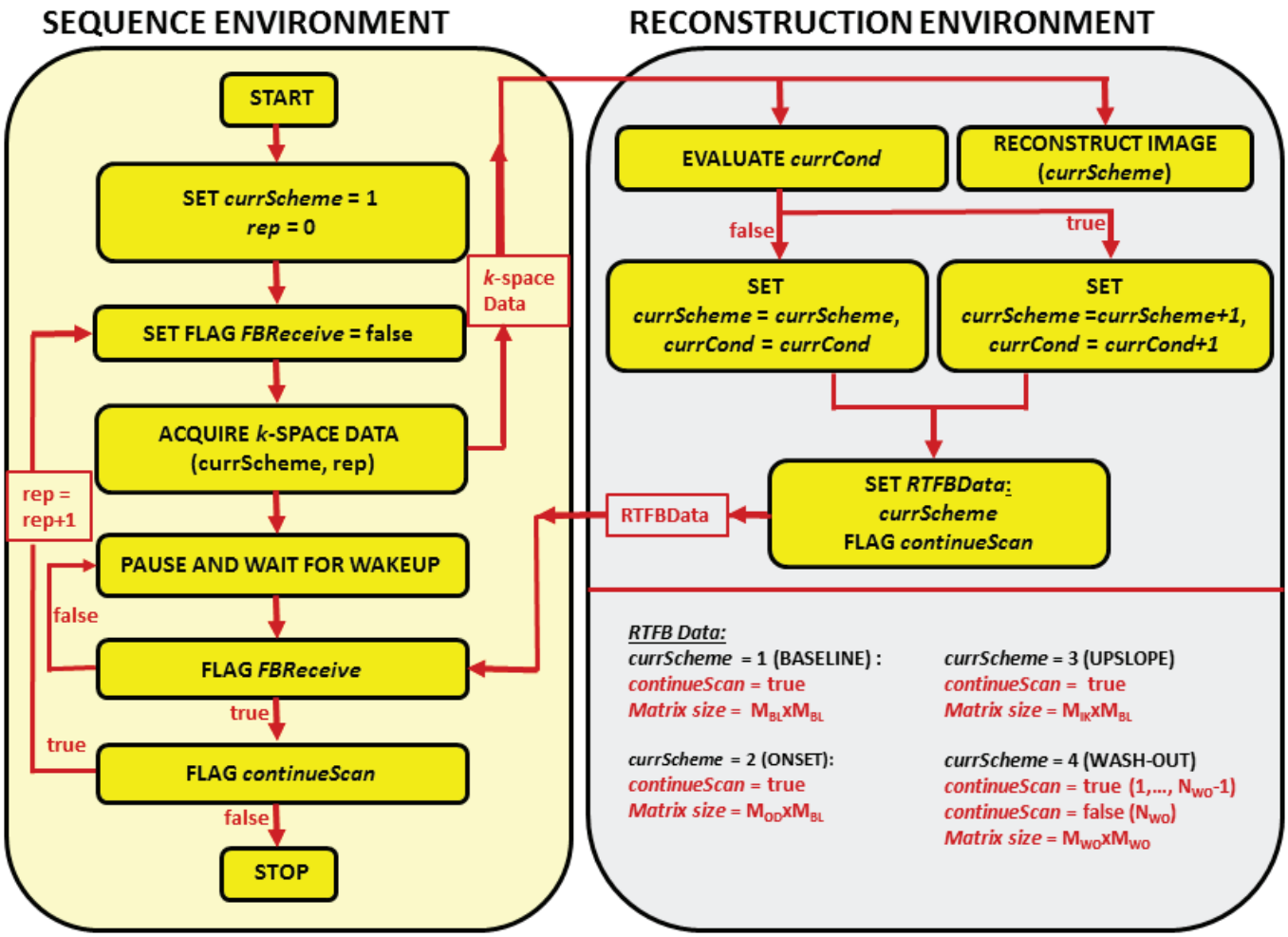

Figure 9.1: Detailed flow chart of the real-time resolution adaption process on the scanner.

Appendix D

Conversion from Signal Intensity to Concentration

The conversion from signal to concentration can be for example done using a variable flip angle approach as suggested by [Wang1987]. For that, before contrast agent administration, two baseline datasets are acquired, one being ρ-weighted with signal $S_{\rho w}$ and flip angle $\theta_{\rho w}$, the other being T_1-weighted with the signal $S_{T_1 w,pre}$ acquired at the flip angle $\theta_{T_1 w}$. The dynamic signal acquired after contrast administration is denoted by $S_{T_1 w,pre}$ and acquired at the same flip angle $\theta_{T_1 w}$.

In the following equations, the variables used are: M_0 is the equilibrium magnetization, TR is the repetition time, $T_1(0)$ is the native T_1-relaxation time before contrast agent, $T_1(t)$ is the dynamic relaxation time after contrast agent injection, r_1 is the relaxivity of contrast agent and $C(t)$ is the contrast agent concentration. TE is assumed to be very short and therefore T_2^* decay is assumed to be negligible.

The signal $S_{\rho w}$ of the ρ-weighted image can be written as:

$$S_{\rho w} = M_0 \frac{(1 - e^{-\frac{TR}{T_1(0)}}) sin\theta_{\rho w}}{1 - e^{-\frac{TR}{T_1(0)}} cos\theta_{\rho w}}. \tag{9.5}$$

The signal $S_{T_1 w,pre}$ of the T_1-weighted image prior to contrast agent arrival is given by:

$$S_{T_1 w,pre} = M_0 \frac{(1 - e^{-\frac{TR}{T_1(0)}}) sin\theta_{T_1 w}}{1 - e^{-\frac{TR}{T_1(0)}} cos\theta_{T_1 w}}. \tag{9.6}$$

These are two equations with two unknowns M_0 and $T_1(0)$, which can be resolved as follows. $T_1(0)$ is given by:

$$T_1(0) = -\frac{TR}{ln(b)}, \tag{9.7}$$

with

$$b = \frac{(a-1)}{acos\theta_{T_1 w} - cos\theta_{\rho}}, \tag{9.8}$$

and

$$a = \frac{S_{T_1 w,pre} sin\theta_{\rho}}{S_{\rho} sin\theta_{T_1 w}}. \tag{9.9}$$

With the derived $T_1(0)$, M_0 can be straightforwardly calculated for example from equation 9.5.

The signal $S_{T_1w,post}$ after contrast agent onset is given by:

$$S_{T_1w,post} = M_0 \frac{(1 - e^{-\frac{TR}{T_1(t)}}) sin\theta_{T_1w}}{1 - e^{-\frac{TR}{T_1(t)}} cos\theta_{T_1w}}. \tag{9.10}$$

With the knowledge of M_0, $T_1(t)$ can be determined according to:

$$T_1(t) = -\frac{TR}{ln(c)}, \tag{9.11}$$

with

$$c = \frac{S_{T_1w,pre} - M_0 sin\theta_{T_1w}}{S_{T_1w,pre} cos\theta_{T_1w} - M_0 sin\theta_{T_1w}}. \tag{9.12}$$

Finally, rewriting equation 5.1, $C(t)$ can be obtained from $T_1(t)$ by the relation:

$$C(t) = \frac{\frac{1}{T_1(t)} - \frac{1}{T_{1,0}}}{r_1}. \tag{9.13}$$

Abbreviations

2D Two-dimensional

3D Three-dimensional

AATH Adiabatic approximation tissue homogeneity

ADC Analog-to-digital converter

AIF Arterial input function

AUC Area under curve

AUGC Area under gadolinium curve

AURA Automatic resolution adaption

BL Baseline

BW Bandwidth

CA Contrast agent

CURE continuous update with random encoding

DCE Dynamic contrast-enhanced

DCF Density compensation function

DFT Discrete Fourier transform

DP Distribution parameter

DSC Dynamic susceptibility contrast

EDS Equidistant sampling scheme

EES Extravascular extracellular space

FE Frequency encoding

FFT Fast Fourier transform

FOV Field of view

FT Fourier transform

GA Golden angle

Gd-DTPA Gadopentetat-Dimeglumin

GRAPPA Generalized auto-calibrating partially parallel acquisition

GRE Gradient recalled echo

GT Ground truth

Hct Hematocrit

ICE Image Reconstruction Environment

ICS Intracellular space

IDEA Integrated Development Environment for MR Applications

IFT Inverse Fourier transform

IK Initial kinetics

IVPS Intravascular plasma space

IVS Intravascular space

KWIC k-space weighted image contrast

MRI Magnetic resonance imaging

NMR Nuclear magnetic resonance

OD Onset detection

OSS Optimal sampling scheme

PE Phase encoding

PK Pharmacokinetic

PR Projection reconstruction

PSF Point spread function

RF Radio frequency

RO Read out

ROI Region of interest

RR Reference region

SENSE Sensitivity encoding

SNR Signal-to-noise ratio

ss Slice selection

SSFP Steady-state free precession

T_1 Longitudinal relaxation time

T_2 Transverse relaxation time

TE Echo time

TH Tissue homogeneity

TP Time point

TR Repetition time

TRICKS Time-resolved imaging of contrast kinetics

US Under-sampled

WO Wash-out

TWIST time-resolved angiography with stochastic trajectories

Units:

C Coulomb

eV Electron volt

g Gram

Hz Hertz

J Joule

K Kelvin

l Liter

m Meter

min Minute

Mol Mol

px Pixel

s Second

sr Steradiant

T Tesla

List of Figures

List of Tables

Bibliography

[AGILE2011] http://cai2r.net/resources/software/agile-gpu-image-reconstruction-library.

[biologie.oncampus2013] http://biologie.oncampus.de/mediawiki.

[DKFZ2014] http://www.krebsinformationsdienst.de/grundlagen/krebsstatistiken.php.

[IARC2014] http://globocan.iarc.fr

[mri-info] http://mri-info.net

[Beatty2005] Beatty, P. J., Nishimura, D. G., and Pauly, J. M. (2005). Rapid gridding reconstruction with a minimal oversampling ratio. *IEEE Trans Med Imaging*, 6:799–808.

[Benner1997] Benner, T., Heiland, S., Erb, G., Forsting, M., and Sartor, K. (1997). Accuracy of gamma-variate fits to concentration-time curves from dynamic susceptibility-contrast enhanced MRI: Influence of time resolution, maximal signal drop and signal-to noise. *Magn Reson Imaging*, 3:307–317.

[Bernstein2004] Bernstein, M. A., King, K. F., and Zhou, X. J. (2004). *Handbook of MRI pulse sequences*. Elsevier Academic Press.

[Bevington2002] Bevington, P. and Robinson, D. K., editors (2002). *Data reduction and error analysis for physical sciences*. McGrw-Hill.

[Bishop1997] Bishop, J. E., Santyr, G. E., Kelcz, F., and Plewes, D. B. (1997). Limitations of the keyhole technique for quantitative dynamic contrast-enhancednhanced breast MRI. *J Magn Reson Imaging*, 7:716–723.

[Bloch1946] Bloch, F. (1946). Nuclear induction. *Phys Rev*, 70:460.

[Block2011] Block, K. and Uecker, M. (2011). Simple method for adaptive gradient-delay compensation in radial MRI. In *Proc Intl Soc Mag Reson Med 19*.

[Brereton1989] Brereton, I. M., Field, J., Moxon, L. N., Irving, M. G., and Doddrell, D. M. (1989). Water suppression with B0 field gradient homospoil pulses in high-resolution NMR spectroscopy. *Magn Reson Med*, 9:118–25.

[Brix1991] Brix, G., Semmler, W., Port, R., Schad, L. R., Layer, G., and Lorenz, W. J. (1991). Pharmacokinetic parameters in CNS GD-DTPA enhanced MR imaging. *J Comput Assist Tomogr*, 15:621–628.

[Brix2004] Brix, G., Kiessling, F., Lucht, R., Darai, S., Wasser, K., Delorme, S., and Griebel, J. (2004). Microcirculation and microvasculature in breast tumors: pharmacokinetic analysis of dynamic MR image series. *Magn Reson Med*, 2:420–429.

[Brockhaus1989] Brockhaus, F. (1989). *Brockhaus-Enzyklopädie: in 24 Bd.* Brockhaus, Mannheim.

[Brodsky2009] Brodsky, E. K., Samsonov, A. A., and Block, W. F. (2009). Characterizing and correcting gradient errors in non-cartesian imaging: Are gradient errors linear-time-invariant? *Magn Reson Med*, 62(6):1466–76.

[Brodsky2013] Brodsky, E. K., Klaers, J. L., Kijowski, A. A. A. A. S., and Block, W. F. (2013). Rapid measurement and correction of phase errors from B0 eddy currents: impact on image quality for non-cartesian imaging. *Magn Reson Med*, 69(2):509–15.

[Buckley2002] Buckley, D. L. (2002). Uncertainty in the analysis of tracer kinetics using dynamic contrast-enhanced T1-weighted MRI. *Magn Reson Med*, 47:601–606.

[Chan2004] Chan, A. A. and Nelson, S. J. (2004). Simplified gamma-variate fitting of perfusion curves. *IEEE Trans Med Imaging*, pages 1067–1070.

[Chan2009] Chan, R. W., Ramsay, E. A., Cunningham, C. H., and Plewes, D. B. (2009). Temporal stability of adaptive 3D radial MRI using multidimensional golden means. *Magn Reson Med*, 61:354–363.

[Cheng2008] Cheng, H. M. (2008). Investigation and optimization of parameter accuracy in dynamic contrast-enhanced MRI. *J Magn Reson Imaging*, 28:736–743.

[Cooley1965] Cooley, J. W. and Tukey, J. W. (1965). An algorithm for the machine calculation of complex fourier series. *Math Comput*, 19:297–301.

[Dale2003] Dale, B. M., Jesberger, J. A., Lewin, J. S., Hillenbrand, C. M., and Duerk, J. L. (2003). Determining and optimizing the precision of quantitative measurements of perfusion from dynamic contrast enhanced MRI. *J Magn Reson Imaging*, 18:575–584.

[Donoho2006] Donoho, D. L. (2006). Compressed sensing. *IEEE Transactions of Information Theory*, 52:1289–306.

[Dougherty2007] Dougherty, L., Isaac, G., Song, H. K., Rosen, M. A., Nunes, L. W., Moate, P. J., Boston, R. C., and Schnall, M. D. (2007). High frame-rate simultaneous bilateral DCE-MR breast imaging. In *Proc Intl Soc Mag Reson Med*.

[Driscoll2011] Driscoll, B., Keller, H., and Coolens, C. (2011). Development of a dynamic flow imaging phantom for dynamic contrast-enhanced CT. *Med Phys*, 38:4866–4880.

[Ebrahimi2010] Ebrahimi, B., Swanson, S. D., and Chupp, T. E. (2010). A microfabricated phantom for quantitative MR perfusion measurements: Validation of singular value decomposition deconvolution method. *IEEE Transactions on Bio-Medical Engineering*, 57:2730–2736.

[El-Khouli2008] El-Khouli, R. H., Jacobs, M., Wei, J., Barker, P. B., Macura, K. J., and Bluemke, D. A. (2008). Dynamic contrast enhanced MRI of the breast: Kinetic curve analysis to determine the optimal temporal resolution. In *Proc Intl Soc Magn Reson Med*.

[El-Khouli2009] El-Khouli, R. H., Macura, K. J., Barker, P. B., Habba, M. R., Jacobs, M. A., and Bluemke, D. A. (2009). The relationship of temporal resolution to diagnostic performance for dynamic contrast enhanced (DCE) MRI of the breast. *J Magn Reson Imaging*, 30:999–1004.

[Everitt2011] Everitt, B. S., Landau, S., Leese, M., and Stahl, D. (2011). *Cluster analysis*. 5th ed. London: Oxford University Press Inc.

[Fessler2004] Fessler, J. A. and Noll, D. C. (2004). Iterative image reconstruction in MRI with separate magnitude and phase regularization. In *In Proc IEEE Intl Symp Biomed Imag*.

[Fluckiger2012] Fluckiger, J. U., Schabel, M. C., and DiBella, E. V. (2012). The effect of temporal sampling on quantitative pharmacokinetic and three-time-point analysis of breast DCE-MRI. *Magn Reson Imaging*, 30:934–943.

[Freed2011] Freed, M., de Zwart, J. A., Hariharan, P., Myers, M. R., and Badano, A. (2011). Development and characterization of a dynamic lesion phantom for the quantitative evaluation of dynamic contrast-enhanced MRI. *Med Phys*, 38:5601–5611.

[Furman-Haran2001] Furman-Haran, E., Grobgeld, D., Kelcz, F., and Degani, H. (2001). Critical role of spatial resolution in dynamic contrast-enhanced breast MRI. *J Magn Reson Imaging*, 13:862–867.

[Gabe1969] Gabe, I. T., Gault, J. H., Ross, J., Mason, D. T., Mills, C. J., Schillingford, J. P., and Braunwald, E. (1969). Measurement of instantaneous blood flow velocity and pressure in conscious man with a catherter-tip velocity probe. *Circulation*, 40:603–614.

[Goto2007] Goto, M., Ito, H., Akazawa, K., Kubota, T., Kizu, O., Yamada, K., and Nishimura, T. (2007). Diagnosis of breast tumors by contrast-enhanced MR imaging: Comparison between the diagnostic performance of dynamic enhancement patterns and morphological features. *J Magn Reson Imaging*, 25:104–112.

[Goto2013] Goto, T. and Kabasawa, H. (2013). Automated smartprep tracker positioning in liver mri scans. *Medical Imaging Technology*, 31(2):105–112.

[Grimm2014] Grimm, R., Nickel, D., Hutter, J., Forman, C., Kiefer, B., Hornegger, J., and Block, K. T. (2014). Variable temporal resolution reconstruction for golden-angle radial sparse parallel DCE-MRI. *Proc Intl Soc Mag Reson Med*, 22.

[Griswold2002] Griswold, M. A., Jakob, P. M., and Heidemann, R. M. (2002). Generalized autocalibrating partially parallel acquisition (GRAPPA). *Magn Reson Med*, 47:1202–1210.

[Gudbjartsson1995] Gudbjartsson, H. and Patz, S. (1995). The rician distribution of noisy MRI data. *Magn Reson Med*, 34(6): 910–914.

[Guenther1999] Guenther, M. (1999). *Nichtinvasive quantitative Perfusionsmessung mittels Magnetresonanz-Tomographie: Arterial-Spin-Labeling*. PhD thesis, Ruprecht-Karls-Universität Heidelberg.

[Haacke1999] Haacke, E. M., Brown, R. W., Thompson, M. R., and Venkatesan, R. (1999). *Magnetic Resonance Imaging: Physical Principles and Sequence Design*. John Wiley & Sons.

[Hayes2002] Hayes, C., Padhani, A. R., and Leach, M. O. (2002). Assessing changes in tumour vascular function using dynamic contrast-enhanced magnetic resonance imaging. *NMR Biomed*, 15:154–163.

[Heisen2010] Heisen, M., Fan, X., Buurman, J., van Riel, N. A. W., Karczmar, G. S., and ter Haar Romeny, B. M. (2010). The influence of temporal resolution in determining pharmacokinetic parameters from DCE-MRI data. *Magn Reson Med*, 63:811–816.

[Henderson1998] Henderson, E., Rutt, B. K., and Lee, T.-Y. (1998). Temporal requirements for the tracer kinetics modelling of breast disease. *Magn Reson Imaging*, 9:1057–1073.

[Hendrick2008] Hendrick, R. E. (2008). *Breast MRI - Fundamentals and Technical Aspects*. Springer Science+Business Media, LLC.

[Herrmann2011] Herrmann, K.-H., Baltzer, P. A., Deitzel, M., Krumbein, I., Geppert, C., Kaiser, W. A., and Reichenbach, J. R. (2011). Resolving arterial phase and temporal enhacement characteristics in DCE MRI at high spatial resolution twist acquisition. *J Magn Reson Imaging*, 34:973–982.

[Ho1999] Ho, V. B., Choyke, P. L., Foo, T. K., Hood, M. N., Miller, D. L., Czum, J. M., and Aisen, A. M. (1999). Automated bolus chase peripheral MR angiography: initial practical experiences and future directions of this work-in-progress. *J Magn Reson Imaging*, 10(3):376–88.

[Hu1994] Hu, X. and Parrish, T. (1994). Reduction of field of view for dynamic imaging. *Magn Reson Med*, 31:691–694.

[Jackson1991] Jackson, J. I., Meyer, C. H., Nishimura, D. G., and Macovski, A. (1991). Selection of a convolution function for fourier inversion using gridding. *IEEE Trans Med Imaging*, 10 (3):473–78.

[Jackson2005] Ah-See, M. A. W., Brasch, R. C., Buckely, D. L., Calamante, F., Evelhoch, J. L., Fournier, L. S., Gribbestad, I. S., Gjesdal, K. I., Hjelstuen, M. H. B., Jackson, A. ., Jayson, G. C., Knopp, M. W., Li, M. O. L. L., Lundgreen, S., Mayr, N. A., McMeekin, D. S., Montebello, J. F., Moonen, C. T. W., Nicholson, D. A., Nilsen, G., Noseworthy, M. D., Padhani, A. R., Parker, G. J. M., Pedersen, M., Reddick, W. E., Roberts, T. P. L., Taylor, J. S., van Gelderen, P., Waterton, J. C., Wu, D. H., Yuh, W. T. C., and Zhu, X. P. (2005). *Dynamic Contrast-Enhanced Magnetic Resonence Imaging in Oncology*. Springer Berlin Heidelberg New York.

[Jansen2010] Jansen, S. A., Fan, X., Medved, M., Abe, H., Shimauchi, A., Yang, C., Zamora, M., Foxley, S., Olopade, O. I., Karczmar, G. S., and Newstead, G. M. (2010). Characterizing early contrast uptake of ductal carcinoma in situ with high temporal resolution dynamic contrast-enhanced MRI of the breast: a pilot study. *Phys Med Biol*, 55:473–485.

[Jena2013] Jena, A., Mehta, S. B., and Taneja, A. (2013). Optimizing MRI scan time in the computation of pharmacokinetic parameters (Ktrans) in breast cancer diagnosis. *J Magn Reson Imaging*, 38:573–579.

[Johnson1966] Johnson, J. A. and Wilson, T. A. (1966). A model for capillary exchange. *Am J Physiol*, 210:1299–1303.

[Jones1993] Jones, R. A., Haraldseth, O., Müller, T. B., Rinck, P., and Oksendal, A. N. (1993). K-space substitution: A novel dynamic imaging technique. *Magn Reson Med*, 29:830–834.

[Kalman1960] Kalman, R. E. (1960). A new approach to linear filtering and prediction problems. *Transaction of the ASME, Journal of Basic Engineering*, pages 35–45.

[Kershaw2006] Kershaw, L. E. and Buckley, D. L. (2006). Precision in measurements of perfusion and microvascular permeability with T1-weighted dynamic contrast-enhanced MRI. *Magn Reson Med*, 56:986–992.

[Kershaw2010] Kershaw, L. E. and Cheng, H.-L. M. (2010). Temporal resolution and SNR requirements for accurate DCE-MRI data analysis using the AATH model. *Magn Reson Med*, 64:1772–1780.

[Kershaw2011] Kershaw, L. E. and Cheng, H. L. M. (2011). A general dual-bolus approach for quantitative DCE-MRI. *Magn Reson Imaging*, 29:160–166.

[Khouli2011] Khouli, R. H. E., Macura, K. J., Kamel, I. R., Jacobs, M. A., and Bluemke, D. A. (2011). 3-t dynamic contrast-enhanced MRI of the breast: Pharmacokinetic parameters versus conventional kinetic curve analysis. *American Journal of Roentgenol*, 197:1498–1505.

[Koh2011] Koh, T. S., Bisdas, S., Koh, D. M., and Thng, C. H. (2011). Fundamentals of tracer kinetics for dynamic contrast-enhanced MRI. *J Magn Reson Imaging*, 34:1262–1276.

[Korosec1996] Korosec, F. R., Frayne, R., Grist, T. M., and Mistretta, C. A. (1996). Time-resolved contrast-enhanced 3D MR angiography. *Magn Reson Med*, 36:345–351.

[Kovar1998] Kovar, D. A., Lewis, M., and Karczmar, G. S. (1998). A new method for imaging perfusion and contrast extraction fraction: input functions derived from reference tissues. *J Magn Reson Imaging*, 8:1126–1134.

[Krishnan2004] Krishnan, S. and Chenevert, T. L. (2004). Spatio-temporal bandwidth-based acquisition for dynamic contrast-enhanced magnetic resonance imaging. *J Magn Reson Imaging*, 20:129–137.

[Kuhl2005] Kuhl, C. K., Schild, H. H., and Morakkabati, N. (2005). Dynamic bilateral contrast-enhanced MR imaging of the breast: Trade-off between spatial and temporal resolution. *Radiology*, 236:789–800.

[Larsson1989] Larsson, H. B. W., Stubgaard, M., Frederiksen, J. L., Jensen, M., Henriksen, O., and Paulson, O. B. (1989). Quantitation of blood-brain barrier defect using MRI and gadolinium-DTPA in acute multiple sclerosis. In *Proc Ann Meeting Soc Magn Reson Med*.

[Laue2010] Laue, H., Hennemuth, A., Diehl, V., Harz, M. T., Hahn, H. K., and Peitgen, H.-O. (2010). Influence of contrast arrival time and temporal resolution in diagnosis of breast cancer with DCE-MRI. In *Proc Intl Soc Magn Reson Med*.

[Lawrence1998] Lawrence, K. S. S. and Lee, T.-Y. (1998). An adiabatic approximation to the tissue homogeneity model for water exchange in the brain: I. theoretical derivation. *J Cereb Blood Flow Metab*, 18:1365–1377.

[Leach2005] Leach, M. O., Brindle, K. M., Evelhoch, J. L., Griffiths, J. R., Horsman, M. R., Jackson, A., Jayson, G. C., Judson, I. R., Knopp, M. V., Maxwell, R. J., McIntyre, D., Padhani, A. R., Price, P., Rathbone, R., G. J, R., Tofts, P. S., Tozer, G. M., Vennart, W., Waterton, J. C., Williams, S. R., and Workman, P. (2005). The assessment of antiangiogenic and antivascular therapies in early-stage clinical trials using magnetic resonance imaging: issues and recommendations. *Br J Cancer*, 92:1559–1610.

[Levenberg1944] Levenberg, K. (1944). A method for the solution of certain problems in least squares. *Quart Appl Math*, 2:164–168.

[Li2005] Li, X., Rooney, W. D., and Springer, C. S. (2005). A unified magnetic resonance imaging pharmacokinetic theory: intravascular and extracellular contrast agents. *Magn Reson Med*, 54:1351–1359.

[Liang2000] Liang, Z.-P. and Lauterbur, P. C. (2000). *Principles of Magnetic Resoance Imaging*. IEEE Press.

[Madore1999] Madore, B., Glover, G. H., and Pelc, N. J. (1999). Unaliasing by fourier-encoding the overlaps using the temporal dimension (UNFOLD), applied to cardiac imaging and fMRI. *Magn Reson Med*, 42:813–828.

[Mann2011] Mann, R. M., Mus, R. D., Geppert, C., Barentsz, J. O., , and Huisman, H. (2011). Ultrafast dynamic imaging of the breast at diagnostic spatial resolution using TWIST. In *Proc Intl Soc Magn Reson Med*.

[Marquardt1963] Marquardt, D. (1963). An algorithm for least-squares estimation of nonlinear parameters. *SIAM J Appl Math*, 11:31–441.

[Martel2008] Martel, A. L., Chan, R. W., Ramsay, E., and Plewes, D. B. (2008). Removing undersampling artifacts in DCE-MRI studies using independent components analysis. *Magn Reson Med*, 59:874–884.

[Meier1954] Meier, P. and Zierler, K. L. (1954). On the theory of the indicator-dilution method for measurement of blood flow and volume. *J Appl Physiol*, 6:731–744.

[Moussavi2013] Moussavi, A., Untenberger, M., and Frahm, M. U. U. (2013). Correction of gradient-induced phase errors in radial MRI. *Magn Reson Med*, 71(1):308–12.

[Mukherjee2010] Mukherjee, S., editor (2010). *The emperor of all maladies: a biography of cancer*. Scribner, a Division of Simon&Schuster, Inc., New York.

[Nagel2009] Nagel, A. M. (2009). *Natrium-Magnetresonanztomographie: Entwicklung einer 3D radialen Messtechnik mit optimierter k-Raum-Abtastdichte und hoher SNR-Effizienz*. PhD thesis, Ruprecht-Karls-Universität Heidelberg.

[Nam2013] Nam, S., Akcakaya, M., Basha, T., Stehning, C., Manning, W. J., Tarokh, V., and Nezafat, R. (2013). Compressed sensing reconstruction for whole-heart imaging with 3D radial trajectories: A graphics processing unit implementation. *Magn Reson Med*, 69:91–102.

[Newbould2006] Newbould, R. and Bammer, R. (2006). Colored noise and effective resolution: Data considerations for non-uniform k-space sampling reconstructions. In *Proc Intl Soc Mag Reson Med*.

[Nichols1990] Nichols, W. W. and O'Rourke, M. F. (1990). *McDonald's blood flow in arteries*. E. Arnold, London, Melbourne, Auckland.

[Noll1991] Noll, D. C., Nishimura, D. G., and Macovski, A. (1991). Homodyne detection in magnetic resonance imaging. *IEEE Trans Med Imaging*, 10(2):154–63.

[Nyquist1928] Nyquist, H. (1928). Thermal agitation of electric charge in conductors. *Phys Rev*, 32:110.

[Oesterle2000] Oesterle, C., Strohschein, R., Köhler, M., Schnell, M., and Hennig, J. (2000). Benefits and pitfalls of keyhole imaging, especially in first-pass perfusion studies. *J Magn Reson Imaging*, 11:312–323.

[Oliver-Taylor2011] Oliver-Taylor, A., Ordidge, R., and Thomas, D. (2011). A perfusion phantom with distinct vascular territories. *Proc Brit Chap ISMRM*.

[OSulllivan1985] O'Sulllivan, J. (1985). A fast sinc function gridding algorithm for fourier inversion in computed tomography. *IEEE Trans Med Imaging*, MI-4:200–207.

[Padhani2003] Padhani, A. R., Yarnold, J., Regan, J., and Husband, J. E. (2003). Dynamic MRI of breast hardness following radiation treatment. *J Magn Reson Imaging*, 17:427–434.

[Parrish1995] Parrish, T. and Hu, X. (1995). Continuous update with random encoding (CURE): A new strategy for dynamic imaging. *Magn Reson Med*, 33:326–336.

[Pauly2005] Pauly, J. (2005). Reconstruction of non-cartesian data.

[Peters2000] Peters, D., Korosec, F. R., Grist, T., Block, W., Holden, J., Vigen, K. K., and Mistretta, C. A. (2000). Undersampled projection reconstruction applied to MR angiography. *Magn Reson Med*, 43(1):91–101.

[Peters2001] Peters, D. C., Epstein, E. H., and McVeigh, E. R. (2001). Myocardial wall tagging with undersampled projection reconstruction. *Magn Reson Med*, 45:562–67.

[Peters2003] Peters, D. C., Derbyshire, J. A., and McVeigh, E. R. (2003). Centering the projection reconstruction trajectory: Reducing gradient delay errors. *Magn Reson Med*, 50(1):1–6.

[Pinker2009] Pinker, K., Grabner, G., Bogner, W., Gruber, S., Szomolanyi, P., Trattnig, S., Heinz-Peer, G., Weber, M., Fitzal, F., Pluschnig, U., Rudas, M., and Helbich, T. (2009). A combined high temporal and high spatial resolution 3 tesla MR imaging protocol for the assessment of breast lesions: Initial results. *Invest Radiol*, 44:553–558.

[Planey2009] Planey, C. R., Welch, E. B., Xu, L., Chakravarthy, A. B., Gatenby, C., Freehardt, D., Mayer, I., Meszeoly, I., Kelley, M., Means-Powell, J., Gore, J. C., and Yankeelov, T. E. (2009). Temporal sampling requirements for reference region modeling of DCE-MRI data in human breast cancer. *J Magn Reson Imaging*, 30:121–134.

[Plewes1995] Plewes, D. B., Bishop, J., S., I., and Cohen, E. (1995). Errors in quantitative dynamic three-dimensional keyhole MR imaging of the breast. *J Magn Reson Imaging*, 5:361–64.

[Pruessmann1999] Pruessmann, K. P., Weiger, M., and Boesiger, M. B. P. (1999). Sense: Sensivitiy encoding for fast MRI. *Magn Reson Med*, 42:952–962.

[Ramsey2006] Ramsey, E., P. Causer, K. H., and Plewes, D. (2006). Adaptive bilateral breast MRI using projection reconstruction time-resolved imaging of contrast kinetics. *J Magn Reson Imaging*, 24:617–624.

[Rice1945] Rice, S. O. (1945). Mathematical analysis of random noise. *Bell System Technical Journal*, 24:46–56.

[Robison2010] Robison, R. K., Devaraj, A., and Pipe, J. G. (2010). Fast, simple gradient delay estimation for spiral MRI. *Magn Reson Med*, 63:1683–90.

[Roemer1990] Roemer, E. B., Edelstein, W., Hayes, C., Souza, S., and Mueller, O. (1990). The NMR phased array. *Magn Reson Med*, 16:192–225.

[Rosen1990] Rosen, B. R., Belliveau, J. W., Vevea, J. M., and Brady, T. J. (1990). Perfusion imaging with NMR contrast agents. *Magn Reson Med*, 14 (2):249–265.

[Schabel2010] Schabel, M. C., Morrell, G. R., Oh, K. Y., Walczak, C. A., Barlow, R. B., and Neumayer, L. A. (2010). Pharmacokinetic mapping for lesion classification in dynamic breast MRI. *J Magn Reson Imaging*, 31:1371–1378.

[Shankaranarayanan2001] Shankaranarayanan, A., Simonetti, O. P., Laub, G., L., J. S. L. J., and Duerk (2001). Segmented k-space and real-time cardiac cine MR imaging with radial trajectories. *Radiology*, 221:827–36.

[Siemens2003] (2003). *Magnete, Spins und Resonanzen: Eine Einführung in die Grundlagen der Magnetresonanztomographie*. Siemens AG, Siemens Medical Solutions.

[Sijbers1998] Sijbers, J., den Dekker, A. J., van Audekerke, J., Verhoye, M., and van Dyck, D. (1998). Estimation of noise in MR images. *Magn Reson Imaging*, 16(1):87–90.

[Song2001] Song, H. K., Dougherty, L., and Schnall, M. D. (2001). Simultaneous acquisition of multiple resolution images for dynamic contrast enhanced imaging of the breast. *Magn Reson Med*, 46:503–509.

[Song2004] Song, H. K. and Dougherty, L. (2004). Dynamic MRI with projection reconstruction and KWIC processing for simultaneous high spatial and temporal resolution. *Magn Reson Med*, 52:815–824.

[Song2009] Song, T., Laine, A. F., Chen, Q., Rusinek, H., Bokacheva, L., Lim, R. P., Laub, G., Kroeker, R., and Lee, V. S. (2009). Optimal k-space sampling for dynamic contrast-enhanced MRI with an application to MR renography. *Magn Reson Med*, 61:1242–1248.

[Spraggins1994] Spraggins, T. A. (1994). Simulation of spatial and contrast distortions in keyhole imaging. *Magn Reson Med*, 31:320–322.

[Stehning2004] Stehning, C., Börnert, P., Nehrke, K., Eggers, H., and Dössel, O. (2004). Fast isotropic volumetric coronary MR angiography using free-breathing 3D radial balanced FFE acquisition. *Magn Reson Med*, 52:197–203.

[Sung2013] Sung, K., Daniel, B. L., and Hargreaves, B. (2013). Transmit B1+ field inhomogeneity and T1 estimation errors in breast DCE-MRI at 3T. *J Magn Reson Imaging*, 38 (2):454–459.

[Tofts1991] Tofts, P. S. and Kermode, A. G. (1991). Measurement of the blood-brain barrier permeability and leakage space using dynamic MR imaging. 1. fundamental concepts. *Magn Reson Med*, 17:357–267.

[Tofts1997] Tofts, P. S. (1997). Modeling tracer kinetics on dynamic GD-DTPA MR imaging. *J Magn Reson Imaging*, 7:91–101.

[Tofts1999] Tofts, P. S., Brix, G., Buckley, D. L., Evelhoch, J. L., Henderson, E., Knopp, M. V., Larsson, H. B. W., Lee, T.-Y., Mayr, N. A., Parker, G. J. M., Port, R. E., Taylor, J., and Weisskoff, R. M. (1999). Estimating kinetic parameters from dynamic contrast-enhanced T1-weighted MRI of a diffusable tracer: Standardized quantities and symbols. *J Magn Reson Imaging*, 10:223–232.

[Tsao2003] Tsao, J., Boesinger, P., and Pruessmann, K. P. (2003). k-t blast and k-t sense: Dynamic MRI with high frame rate exploiting spatiotemporal correlations. *Magn Reson Med*, 50:1031–1042.

[Tsao2010] Tsao, J. (2010). Imaging reconstruction - exploiting spatiotemporal correlations for dynamic imaging. *Proc Intl Soc Mag Reson Med*, 18.

[Tudorica2012] Tudorica, L. A., Oh, K. Y., Roy, N., Kettler, M. D., Chen, Y., Hemmingson, S. L., Afzal, A., Grinstead, J. W., Laub, G., Li, X., and Huang, W. (2012). A feasible high spatiotemporal resolution breast DCE-MRI protocol for clinical settings. *Magn Reson Imaging*, 30:1257–1267.

[Vaals1993] van Vaals, J. J., Brummer, M. E., Dixon, W. T., Tuithof, H. H., Engels, H., Nelson, R. C., Gerety, B. M., Chezmar, J. L., and den Boer, J. A. (1993). Keyhole method for accelerating imaging of contrast agent uptake. *J Magn Reson Imaging*, 3:671–675.

[Vautier2012] Vautier, J., Tayara, N. E. T. E., Walczak, C., Mispelter, J., and ChanVolk, A. A. (2012). Radial multigradient-echo DCE-MRI for 3D Ktrans mapping with individual arterial input function measurement in mouse tumor models. *Magn Reson Med*, 70(3):823-8.

[Veltman2008] Veltman, J., Stoutjesdijk, M., Mann, R., Huisman, H. J., Barentsz, J. O., Blickman, J. G., and Boetes, C. (2008). Contrast-enhanced magnetic resonance imaging of the breast: the value of pharmacokinetic parameters derived from fast dynamic imaging during initial enhancement in classifying lesions. *Eur Radiol*, 18:1123–1133.

[Vogt 2007] Vogt, F. M., Eggebrecht, H., and Laub, G. (2007). High temporal and spatial resolution MRA (TWIST) in acute aortic dissection. In *Proc Itnl Soc Magn Reson Med*.

[Vomweg2004] Vomweg, T. W., Teifke, A., Kunz, R. P., Hintze, C., Hlawatsch, A., Kern, A., Kreitner, K. F., and Thelen, M. (2004). Combination of low and high resolution sequences in two orientations for dynamic contrast-enhanced MRI of the breast: more than a compromise. *Eur Radiol*, 14:1732–1742.

[Walker-Samuel2007] Walker-Samuel, S. (2007). *Evaluation of Dynamic Contrast-Enhanced MRI in the Functional Assessment of Response to Treatment of Cancer*. PhD thesis, University of London.

[Wang1987] Wang, H. Z., Riederer, S. J., and Lee, J. N. (1987). Optimization the precision in T1 relaxation estimation using limited flip angles. *Magn Reson Med*, 5:399–416.

[Wasser2002] Wasser, K., Klein, S., Fink, C., Junkermann, H., Sinn, H., Zuna, I., Knopp, M., and Delorme, S. (2002). Evaluation of neoadjuvant chemotherapeutic response of breast cancer using dynamic MRI with high temporal resolution. *Eur Radiol*, 13:80–87.

[Weinmann1984] Weinmann, H. J., Laniado, M., and W.Mützel (1984). Pharmacokinetics of GD-DTPA/dimeglumine after intravenous injection into healthy volunteers. *Phys Chem Phys Med NMR*, 16(2):167–72.

[Welch2004] Welch, E. B., Rossman, P. J., Felmlee, J. P., and Manduca, A. (2004). Self-navigated motion correction using moments of spatial projections in radial MRI. *Magn Reson Med. 2004 Aug;52(2):337-45.*, 52(2):337–45.

[Winkelmann2007] Winkelmann, S., Schaeffter, T., Koehler, T., Eggers, H., and Doessel, O. (2007). An optimal radial profile order based on the golden ratio for time-resolved MRI. *IEEE Transactions on Medical Imaging*, 26(1):68–76.

[Xie2008] Xie, J., Gallichan, D., Gunn, R. N., and Jezzard, P. (2008). Optimal design of pulsed arterial spin labeling mri experiments. *Magn Reson Med*, 59:826–834.

[Yang2004] Yang, C., Karczmar, C. S., Medved, M., and Stadler, W. M. (2004). Estimating the arterial input function using two reference tissues in dynamic contrast-enhanced MRI studies: fundamental concepts and simulations. *Magn Reson Med*, 52:1110–1117.

[Yankeelov2007] Yankeelov, T. E., Cron, G. O., and Addison, C. L. (2007). Comparison of a reference region model with direct measurement of an AIF in the analysis of DCE-MRI data. *Magn Reson Imaging*, 57:353–361.

[Zhu2011] Zhu, Y., Chang, M., and Gupta, S. N. (2011). Automated determination of the arterial input function for DCE-MRI of the prostate. *SPIE Proceedings*, 7963.

Acknowledgments

Writing this thesis has been an interesting, exciting, challenging and very educational experience. However, it was by no means an accomplishment I did on my own. Many great people, being colleagues, friends and my family, contributed to this work regarding its content and by supporting and encouraging me. I would like to thank the following people for their dedication.

First of all I would like to thank my supervisor Matthias Guenther for giving me the opportunity to do this PhD, for his support, his brilliant ideas, very productive discussions in our weekly meetings, sharing his vast knowledge, the scientific freedom he gave me, his trust in me and standing behind me at all times. He taught me to think scientifically and to critically ask the right questions, a valuable skill for life. He also gave me great opportunities to visit many conferences and workshops and getting to know the MR community. I appreciate all he has done for me in the past years a lot.

I am much obliged to Wolfgang Dreher, Monika Fritz and Matthias van Osch for taking time to read my thesis and coming the partially very the long way to Bremen to my defense.

Sincerely I would like to express my gratitude to Horst Hahn, Ron Kikinis and the "Kleines Gremium" for their great leadership. It was as well a huge honor to be working at MeVis whilst Heinz-Otto Peitgen, the founder of MeVis, was head of institute. I would like to thank him for being a role model, and for giving me inspiration to pursuit the projects I believe in.

I cannot thank Ben enough for his enormous help. He spend innumerable hours with scientific discussions, proofreading my English and keeping me on track when I got lost in details. He kept me company during the weekends at the scanner, making the time more enjoyable and patiently answered every possible question, especially about image reconstruction.

I am deeply grateful to the members of the MR group, namely Federico, Klaus, Sven, Johanna, Jochen, Cristoffer, Thorsten, Simon, Saulius, Dennis, Marco and David. They were always taking time out of their day for answering questions and helped me getting a deeper MR knowledge during our seminars and journal clubs. They also contributed to this thesis by making being at work a great pleasure. And I will never forget the fun times we had together at conferences! I especially would like to thank Federico for relaxing beers in the evenings in our "MR-WG", Federico and Klaus for their help with

the phantom, Cristoffer for simulation support, Sven for his bouldering initiatives, curing my thesis-writing-related back pain and Johanna for legendary "VL"-sessions when sharing a hotel room.

A lot I learned from being a supervisor myself, for which I a much obliged to Nora-Josefin Breutigam who implemented the 3D radial reconstruction on the scanner during her master thesis. She made my first supervision experience very pleasant and probably has given a hard time to all potential further students by being the "gold-standard".

A big "thank you" to all the members of the "MeVis-family". They were amazing colleagues and friends and have greatly contributed to my scientific and personal development during the past years. They instantly made me feel at home at the institute and it was a great experience to be part of this remarkable group.

A special thanks goes to Wolf for patiently answering all my programming questions but mainly for being the best Rock'n'Roll dance partner I could wish for. Our performances at the MeVis Christmas parties were one of the highlights of my time in Bremen. Thanks to my office mate Markus, and to Ashley, who joined us later, for a relaxed and fun atmosphere whilst sharing thoughts and tea and constructing cute dragons. I would like to thank Felix for (involuntarily) providing me with fresh fruit every day, Hendrik for sharing his broad DCE MRI knowledge, Stefan for helping me structuring and organizing my thesis during many trips to the coffee machine, and Christina, Caroline, Indra and Bianca for becoming friends without whom I would not have made it through my thesis. And of course thanks to the 12:30 Mensa group! Additionally, the former colleagues Andreas and Tim enriched my time at MeVis with a valuable friendship. Eventually, thanks to all the people from the office management, administration and IT administration for always being friendly, competent and helpful.

I would like to thank my colleagues at mediri Joe, Johannes, Juergen (JJ), Julia, Alba, Sigurd, Stefan, Doerte and Manuela for finding space for me whenever I was in Heidelberg, an incredibly relaxed working atmosphere, and enormous amounts of nuts, gummibears and coffee serving as "nerve food". Thanks to JJ for proofreading my chapters and abstracts. And a special thanks to my dear friend Joe for always making me laugh and for breaking the "vicious circle of stress" during lunches at the Indian restaurant around the corner.

I am deeply grateful to Tobias, Geoff and Claudia from King's College London for their help regarding the adaptive simulations, for giving me insight into an amazing group and for their kindness and understanding.

A big "thanks" goes as well to Volker Diehl, who helped me to acquire *in vivo* data at the Zentrum fuer moderne Diagnostik (ZEMODI) in Bremen, and to Ritse Mann and Suzan Vreeman from the Radboud University Nijmegen Medical Centre, who made it possible for me to acquire first data of screening patients with the 3D radial sequence.

Thanks to Peter for his good ideas and his enjoyable company at the scanner.

For their scientific spirit I am indebted to Tobias Block and Rachel Chan, who thoroughly answered all of my question regarding their work.

I would like to thank Benny for all of his love and amazing support, the best times ever and being there for each other during times in which we would “rather be in Patagonia”. Thanks for being an highlight of my life!

Finally, I would like to thank the best parents in the world who gave me more than I can express in words. To just name a few examples, their unconditional love and support throughout all of my life, sharing their knowledge and adventures with me and for being the kind of persons who would try to fly through the arc de triomphe if they were pilots.

THANK YOU!